

Fundamental Research and Functionalisation of Nanoemulsions in Respect to Low-Energy Formation Processes

vorgelegt von

Diplom-Chemikerin

Peggy Heunemann

(geb. in Berlin, Deutschland)

Von der Fakultät II – Mathematik und Naturwissenschaften –
der Technischen Universität Berlin

zur Erlangung des akademischen Grades

Doktor der Naturwissenschaften

– Dr. rer. nat. –

genehmigte Dissertation

Promotionsausschuß :

Vorsitzender: Prof. Dr. T. Ressler

Berichter/Gutachter: Prof. Dr. M. Gradzielski

Berichter/Gutachter: Dr. I. Grillo

Tag der wissenschaftlichen Aussprache: 23. September 2011

Berlin 2012

- D83 -

“ Le peu que je sais c’est à mon ignorance que je le dois. ”

“ Das Wenige, das ich weiß, verdanke ich meinem Nichtwissen. ”

Sacha Guitry (1885-1957)

Contents

| | | |
|----------|---|-----------|
| 1 | Introduction | 1 |
| 1.1 | Emulsion principles | 1 |
| 1.1.1 | Definition and stabilisation of emulsions | 1 |
| 1.1.2 | Types of emulsions | 3 |
| 1.1.3 | Emulsification methods | 4 |
| 1.1.3.1 | High Energy Input Methods | 4 |
| 1.1.3.2 | Low Energy Input Methods | 4 |
| | PIT | 5 |
| | PIC | 6 |
| | Ouzo-Effect | 7 |
| | PSQ | 8 |
| 2 | Motivation | 11 |
| 3 | Materials and Methods | 15 |
| 3.1 | Materials | 15 |
| 3.1.1 | Chemical compounds employed | 19 |
| 3.1.1.1 | The model system (Tego [®] Wipe DE) | 19 |
| 3.1.1.2 | PIC-Formulation studies | 20 |
| 3.1.1.3 | O/S-variation | 22 |
| 3.1.1.4 | NE-Kinetics | 22 |
| 3.1.1.5 | PIC-Mechanism | 23 |
| 3.1.1.6 | PIC-Encapsulation | 23 |
| 3.1.2 | Sample preparation for PIC-Systems | 24 |
| 3.2 | Methods | 26 |
| 3.2.1 | Density | 26 |
| 3.2.2 | Electric Conductivity | 26 |
| 3.2.3 | Viscosity | 26 |
| 3.2.4 | Refractivity measurements | 27 |
| 3.2.5 | UV-Vis transmittance and turbidity measurements | 27 |
| 3.2.6 | Long-time transmittance measurement | 28 |
| 3.2.7 | Surface Tension | 29 |
| | 3.2.7.1 cmc | 29 |
| | 3.2.7.2 Gordon Parameter | 30 |
| 3.2.8 | Interfacial Tension | 31 |
| 3.2.9 | Zeta-Potential Measurements | 31 |
| 3.2.10 | Nuclear-Magnetic-Resonance Measurements (NMR) | 32 |
| 3.2.11 | Cryogenic Transmission Electron Microscopy (cryo-TEM) | 32 |
| 3.2.12 | Stopped-Flow mixing | 33 |

| | | |
|----------|--|-----------|
| 3.2.13 | Small-Angle Neutron Scattering (SANS) | 35 |
| 3.2.13.1 | Scattering theory - Model independent methods | 37 |
| 3.2.13.2 | Scattering theory - Teubner Strey model | 38 |
| 3.2.13.3 | Scattering theory - Polydisperse Sphere Model with Log-normal Distribution | 39 |
| 3.2.13.4 | Scattering theory - Polydisperse Disk Model with Log-normal Distribution | 42 |
| 3.2.14 | Small-Angle X-Ray Scattering (SAXS) | 43 |
| 4 | Low Energy Emulsification of Nanoemulsions | 45 |
| 4.1 | PIC-method (Tego [®] Wipe DE) | 46 |
| 4.1.1 | Phase behaviour | 47 |
| 4.1.2 | Structural Characterisation | 50 |
| 4.1.3 | Conclusion | 59 |
| 4.2 | O/S-Modifications | 61 |
| 4.2.1 | Variable O/S-ratio: Exchange of concentrate components | 63 |
| 4.2.2 | Const. O/S-ratio: Nonic-Surfactant-Variation | 64 |
| 4.2.3 | Const. O/S-ratio: Ionic-Surfactant-Variation | 65 |
| 4.2.3.1 | Phase behaviour and stability | 65 |
| 4.2.3.2 | Small-Angle Neutron Scattering (SANS) | 72 |
| 4.2.4 | Const. O/S-ratio: Oil-Variation | 79 |
| 4.2.4.1 | Phase behaviour and stability | 80 |
| 4.2.4.2 | Small-Angle Neutron Scattering (SANS) | 81 |
| 4.2.5 | Conclusion | 83 |
| 4.3 | O/S-Variation (O:DEHC/K300, S:P4L/SS) | 85 |
| 4.3.1 | SANS-analysis | 87 |
| 4.3.1.1 | O/S-ratio: $0 < S \leq 15$ wt-% surfactant S | 88 |
| 4.3.1.2 | O/S-ratio: $15 < S \leq 65$ wt-% surfactant S | 89 |
| 4.3.1.3 | O/S-ratio: $65 < S \leq 100$ wt-% surfactant S | 92 |
| 4.3.2 | Conclusion | 97 |
| 4.4 | PIC-Kinetics | 98 |
| 4.4.1 | PIC-formation kinetics | 98 |
| 4.4.2 | Nanoemulsion interdroplet exchange dynamics | 104 |
| 4.4.2.1 | Additives influence | 109 |
| 4.4.3 | Conclusion | 112 |
| 4.5 | PIC-Mechanism | 114 |
| 4.5.1 | Experimental and theoretical studies | 114 |
| 4.5.1.1 | Nuclear Magnetic Resonance (NMR) measurements | 114 |
| 4.5.1.2 | Refractive index contrast matching | 120 |
| 4.5.1.3 | Small-Angle Neutron Scattering (SANS) | 123 |
| | Contrast variation | 123 |
| 4.5.2 | Conclusion | 129 |
| 4.6 | Encapsulation | 130 |
| 4.6.1 | NE-encapsulation by electrostatic assembly | 130 |
| 4.6.1.1 | SANS | 133 |
| 4.6.1.2 | cryo-TEM | 135 |
| | The system: SS^-/lys^+ | 135 |
| | The system: PGL^-/lys^+ | 137 |
| 4.6.2 | Conclusion | 139 |

| | | |
|----------|--|------------|
| 5 | Summary | 141 |
| A | Appendix | 145 |
| A.1 | Appendix of section 3.1.1 | 145 |
| A.1.1 | Composition of Euxyl [®] K300 | 145 |
| A.1.2 | Structures of Exchange studies | 146 |
| A.1.2.1 | Oil-Exchange | 146 |
| A.1.2.2 | Surfactant-Exchange (non-ionic) | 146 |
| A.1.2.3 | Surfactant-Exchange (cat- and anionically charged) | 148 |
| A.1.2.4 | O/S-variation: Composition | 149 |
| A.1.2.5 | Synthesis of d ₃₄ -diethylhexyl carbonate (d-DEHC) | 150 |
| A.2 | Appendix of section 4.1 | 153 |
| A.2.1 | Long-time turbidity measurements | 153 |
| A.2.2 | UV/Vis-Transmittance measurements | 153 |
| A.2.3 | TS-data: upper phases | 154 |
| A.2.4 | TS-data: lower phases | 155 |
| A.2.5 | Residua - mono vs. bimodal | 156 |
| A.3 | Appendix of section 4.2 | 157 |
| A.3.1 | Charged surfactant-physical properties | 157 |
| A.3.2 | Chemical degradation of AOT in O/S-mixture | 158 |
| A.3.3 | NE-analysis: Charged surfactant formulations | 159 |
| A.3.4 | Charge influence on NE - SANS: model-fits | 160 |
| A.3.5 | Charge influence on NE - SANS: TS-analysis | 160 |
| A.3.6 | NE-analysis: Oil formulations | 161 |
| A.4 | Appendix of section 4.3 | 163 |
| A.4.1 | SANS-Guinier analysis | 163 |
| A.4.2 | SANS-Teubner Strey of NE and μ E | 164 |
| A.4.3 | SANS-programming (disk vs. vesicle) | 165 |
| A.5 | Appendix of section 4.4 | 166 |
| A.5.1 | SANS-simulation of interdroplet exchange | 166 |
| A.5.2 | SANS-interdroplet exchange (additives) | 167 |
| A.6 | Appendix of section 4.5 | 168 |
| A.6.1 | Refractivities of glycerol/H ₂ O and sugar/H ₂ O mixtures | 168 |
| A.6.2 | Transmittance spectra of glycerol/H ₂ O and sugar/H ₂ O mixtures | 168 |
| A.6.3 | NMR reference spectra | 169 |
| A.6.4 | NMR-data of PIC dilution | 170 |
| A.6.5 | SANS-contrast match of NE | 171 |
| A.6.6 | Gibb's Adsorption Isotherm of P4L | 172 |
| A.6.7 | Volume fractions in NE-region | 172 |
| A.7 | Appendix of section 4.6 | 173 |
| A.7.1 | NE-encapsulation by polycondensation | 173 |
| A.7.2 | PH-measurements of NE-encapsulation attempts | 174 |
| A.7.3 | SANS: model fits (surfactant/lysozyme-complexes) | 175 |
| A.7.4 | SANS - Teubner Strey analysis (SS ⁻ /lys ⁺) | 175 |
| A.8 | Mathematical tools | 176 |
| A.8.1 | Moments of Log-normal distribution | 176 |
| A.8.1.1 | Areas-averaged radii | 176 |
| A.8.1.2 | Volume-averaged radii | 177 |

| | |
|---|------------|
| B List of abbreviations | 179 |
| B.1 General | 179 |
| B.2 Chemical substances | 181 |
| B.3 Greek letters and mathematical abbreviations and physical constants | 182 |
| Bibliography | 183 |

Chapter 1

Introduction

1.1 Emulsion principles

The main part of this thesis deals with the formation process of nanoemulsions. Therefore it is essential to understand the fundamental principles of emulsions; their definition and structural characteristics, stabilisation, way of formulation and driving forces.

1.1.1 Definition and stabilisation of emulsions

Emulsions are dispersed systems that macroscopically appear homogeneous while consisting of at least two immiscible liquids. In such colloidal mixtures one liquid (dispersed phase) is dispersed in the other (continuous phase), the degree of dispersion depends mainly on the interfacial tension of both liquids, and tends in a single two-component system (e.g. water / oil) to a macroscopic phase separation with time.

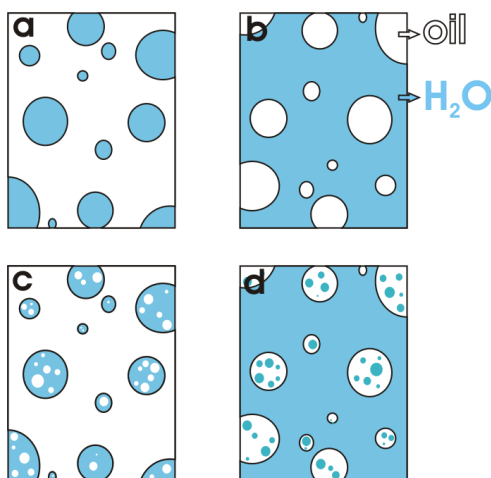


Figure 1.1: emulsion types: a) w/o-; b) o/w-; c) o/w/o-; d) w/o/w-emulsion

Most emulsion systems contain oil (o) and water (w) phases, are distinguishable according to the state of the dispersed phase in o/w- (e.g. milk) or w/o-emulsions (e.g. margarine). It should be noted that beside this simple emulsion phase even more sophisticated structures are known (e.g. w/o/w or o/w/o) that are irrelevant for this thesis (fig. 1.1).

Beside stepwise creaming, sedimentation, flocculation or aggregation - according to the polar properties of water molecules that tend to form hydrogen bonds while replacing the more unpolar oil molecules; break down processes of emulsions (fig. 1.2a) are mainly driven by processes of Ostwald ripening and coalescence. Ostwald ripening describes the growing of emulsion droplets at the expense of smaller ones via diffu-

sion. This phenomenon becomes more relevant to smaller particles due to their curvature and hence higher Laplace pressure. In case of coalescence dispersed droplets grow to bigger aggregates that finally merge due to the fact of minimising the interfacial energy with increasing the droplet volume.

However, to suppress break down processes **surface active agents**, known as surfactants, are required. Such compounds lower the surface tension between the dispersed and continuous phases; thus they favour the formation of kinetically stable emulsion droplets, according to the amphiphilic character of the surfactant molecules. Amphiphiles describe chemical compounds that possess both a hydrophilic (water-loving) and lipophilic (fat-loving) part in the overall molecular structure, whereas generally the hydrophilic head group is oriented in water- and the lipophilic tail in oil-direction (fig. 1.2b). Surfactants are usually classified by their head group as anionic, cationic, nonionic or amphoteric. With providing a small excess phase for defining the continuous phase of an emulsion, Bancroft's rule suggests that the type of emulsion (o/w vs. w/o) is dictated by the emulsifier properties; and that the phase, in which the emulsifier is more soluble, becomes the continuous one. In 1949 Griffin proposed the HLB-concept (hydrophilic-lipophilic-balances) for nonionic surfactants¹ that considers the coherency of the surfactant design and the curvature of the boundary surface. Generally the HLB-value of an emulsifier, which is given in numerical values of zero to 20, describes its solubility in rather hydrophilic or lipophilic media. Thereby the solubility depends on the free available space, an emulsifier provides, to bind water molecules. The more water is attached to the emulsifier the more hydrophilic it is and vice versa (tab. 1.1). Generally emulsifiers with very high HLB-values incorporate large amounts of water and hence tend to easily emulsion formation. To form stabilised emulsions, the applied surfactant fraction depends on the averaged particle size. It

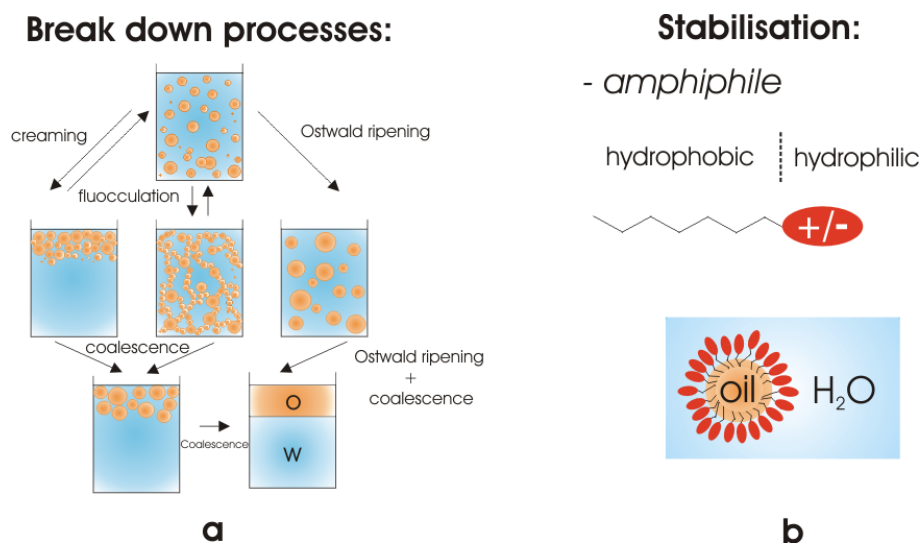


Figure 1.2: a) break down processes of emulsions that can occur; b) amphiphile concept of a surface active agent (surfactant)

¹An extension to ionic surfactants is accounted in the model of Davies (1957) [65, 135]

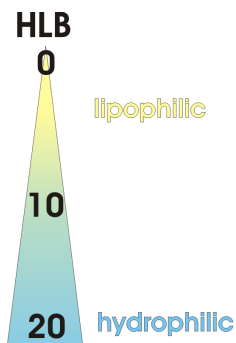


Figure 1.3: HLB-scale

| HLB-value | emulsifier properties |
|-----------|--|
| 1-4 | H ₂ O-insoluble - not water dispersible |
| 3-6 | clear, H ₂ O-soluble; solubiliser; w/o-emulsion |
| 6-8 | clear, mainly surfactants; w/o-emulsion |
| 8-10 | stable dispersion, whitish o/w-emulsion |
| 10-13 | opaque to clear, H ₂ O-soluble; o/w-emulsifier |
| 13 | clear, H ₂ O-soluble; detergents |
| 15-20 | clear, H ₂ O-soluble; solubiliser |

Table 1.1: HLB-values in relation to surfactant properties

is essential that the more dispersed an emulsion the bigger the boundary surface between inner and outer phase.

While decreasing the surface tension the formation of emulsions becomes more preferable. Therefore microemulsions, which possess a remarkably fine dispersion, are spontaneously formed at very low surface tensions and stay thermodynamically stable.

1.1.2 Types of emulsions

Emulsions are typically distinguished by their particle size and stabilisation in macro-, nano- and microemulsions. They appear more translucent the smaller the emulsion droplet size. Kinetically stable macroemulsions, that possess droplets ≥ 200 nm, appear strongly whitish (like milk or pastis), while thermodynamically stable microemulsions with particle sizes ≤ 10 nm occur completely clear or in maximum slightly bluish. Nanoemulsions, also referred as miniemulsions [34, 188], ultrafine emulsions [116], emulsoids [89], unstable microemulsions [116, 143] or submicrometer emulsions [13]; are structurally located between macro- and microemulsions, while linking their emulsion properties (tab. 1.2). The emulsion's appearance varies between translucent [168] and whitish [74] according to their possessed particle size (10 - 200 nm). The formation of a certain emulsion type depends on the composition the oil com-

| emulsion type | size | stability | coalescence | Ostwald-ripening | formation |
|---------------|------------------------------------|---|-----------------------------|---------------------------------|--|
| micro- | 5 - 10 nm, much cosurfactant | thermodyn. stable | Yes fusion/ fission | No thermodyn. stable | spontaneous formation |
| nano- | 10 - 200 nm few surfactant | kinetically stable | No kinetically stable | No osmotically stabilised | high pressure ultrasonic temp. (PIT) conc.(PIC) |
| macro- | >200 nm few surfactant | kinetically stable to coalescence | No kinetically stable | Yes very slow | shearing agitation mixing |

Table 1.2: Main distinction of micro-, nano- and macroemulsion

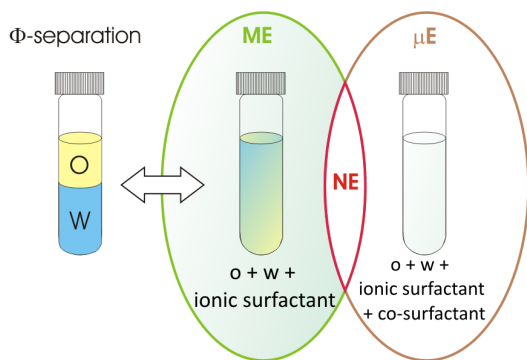


Figure 1.4: formation and stability of emulsion type (macro- (ME), nano- (NE) and microemulsion (μ E)) depends on initial components

nanoemulsions while providing still small particle sizes and long time stability simultaneously.

pond contains. A kinetically stable macroemulsion is formed if an amphiphile is added to the oil component that suppresses the immediately occurring phase separation, after oil and water phases are mixed. In the case of thermodynamic microemulsions, frequently one is using a further cosurfactant² beside this ternary system which affects the fluidity of the interface by interfering and disaggregating the surfactant layer [27]. Therefore microemulsions contain quite high amounts of surfactants [167, 177], which can be reduced in case of

1.1.3 Emulsification methods

The thermodynamically stable state of two immiscible liquids is their bulk form with a minimum of interface, the heavier phase lying below the lighter one [53].

The dispersion of a fluid into another one requires always a certain amount of energy for amplifying the boundary surface between both phases [41]. Since emulsions are widely used in food, cosmetics and pharmaceutical industry, versatile methods have been developed with time; concerning high and low energy emulsifications.

1.1.3.1 High Energy Input

One can either start from very tiny nuclei and then allow them to grow (condensation procedure [47, 165]) to the required size or more commonly break up large droplets of the bulk phase into smaller ones, which can be done in different manners using homogenisation, high pressure, shearing, ultrasonification, microfluidisation or et alii techniques [7, 35, 45, 66, 92, 95, 104, 148, 168, 183, 198]. These are demanding procedures and therefore low-energy methods are favoured.

1.1.3.2 Low Energy Input

While shrinking dispersion droplets during the emulsification process the specific surface area of both phases increases [91].

²systems for cosurfactant-free microemulsions are also known - e.g. via AOT [147]

Hence, the interfacial tension needs to be lowered for gaining new interfaces. As for emulsion systems this can be facilitated by applying surfactants, it is obvious that there should be a possibility of low energy emulsification just by using preferable oil/surfactant formulations.

In 1878 Gad [48] reported for the first time observations about a spontaneous emulsification³ of oil droplets, containing free fatty acids, in alkaline solutions [10] without any mechanical shaking. Thereby, the emulsion formation is initiated by the stored chemical energy of the individual components and released upon contact [59].

Phase Inversion Temperature (PIT) Method:

It is clear from the section 1.1.1 that the HLB-value of a nonionic⁴ surfactant, and therefore also the phase behaviour of an emulsion, is temperature dependent according to the change of interaction between water phase and hydrophilic head group or oil phase and lipophilic tail of the surfactant while varying the temperature. E.g., increasing the temperature of a nonionic surfactant correlates with a shortening of its hydrophilic part.

Generally an increase of temperature causes a reduction in viscosity of the continuous phase, as well as a decrease⁵ of the surfactant HLB-value. This affects the continuous phase in an amplification of the particle agitation and the emulsifier by a stronger preference for the dispersed phase [160].

As a consequence, it is obvious that at higher temperatures an assignment of the emulsion phase behaviour does not work if one applies the HLB-concept. In 1964 this relation was observed for the first time by Shinoda while using nonionic polyethylene glycol alkyl(aryl)ethers as emulsifiers in an emulsion formulation. Shinoda et al. noticed a reversible phase inversion from o/w- to w/o-emulsion (fig. 1.5-**bottom**) during temperature increase - which finally led to the expression of a so called Phase Inversion Temperature (PIT) [156]. Conductivity measurements⁶ can be used to trace the phase inversion of an emulsion system. The inversion of an o/w-emulsion by heating effects a zero conductivity due to the isolating properties of the resulting continuous (oil) phase. According to this the PIT is defined as the average value between the maximum and the spontaneously reached zero conductivity [62]. The size of particles, formed by the phase inversion temperature method depend mainly on their generation. Whereas the PIT itself relies on the emulsifier concentration, the length of the oxyethylene chain, the used oil phase, the overall HLB-value and the volume ratio. Close to the PIT dispersed emulsion systems are instable and bicontinuous structures (both phases coexist beside each other - no dispersion takes

³three mechanisms for spontaneous emulsification are known:

- diffusion-and-stranding (nonuniform diffusion) [28, 137, 145]
- intense interfacial turbulences [191]
- transient negative interfacial tension [133, 192]

⁴temp. effect on ionic surfactant solutions is small and the size of hydrophilic groups is fixed

⁵temperature conditioned decrease of HLB-value do not proceed in all cases

⁶Differential thermal analysis is also an option [103, 124]

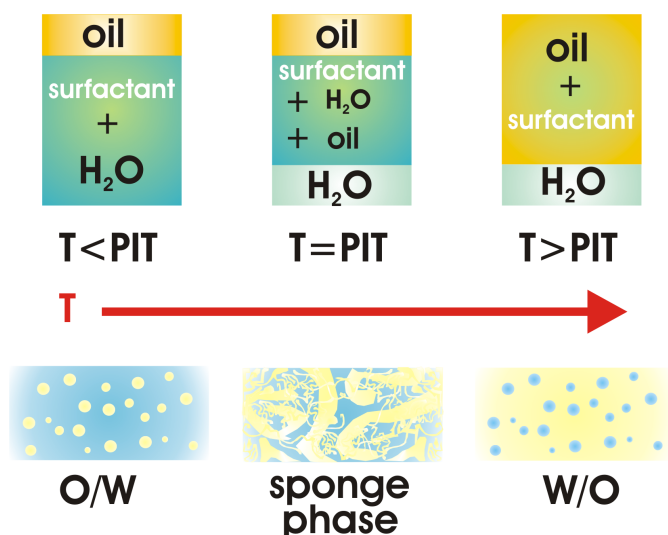


Figure 1.5: *top*: temperature dependent hydrophilic/lipophilic balance of ethoxylated nonionic surfactant which gets less water soluble with increasing temperature due to the decrease in strength of hydrogen bonds (particles exhibit higher movements and vibrations → hydrogen bondings are inhibited); *bottom*: Change of emulsion phase upon dilution [157].

place) are favoured due to the fact that the hydrophilic and lipophilic parts of the surfactant are balanced (fig. 1.5-*top*), which causes a rapid cooling to room temperature of the formulated dispersions [87, 156].

Phase Inversion Concentration (PIC) Method:

Contrary to the PIT-method, where the phase inversion temperature (PIT) is independent of a surfactant concentration while forming emulsions [15]; the phase inversion concentration method (PIC), also mentioned as Phase Inversion Composition [168, 171, 206] or Emulsion Inversion Point (EIP) [49], is affected by a change of surfactant concentration during the emulsification pathway. Nevertheless, the nanoemulsion formation via the PIC- and PIT methods resemble each other, so that former studies of the PIT-systems by Shinoda et al. [156], Solans et al. [80], Rybinski et al. [37, 46], Salager et al. [6] and others, also help in a better understanding concerning the PIC-emulsification process.

The nanoemulsion systems we are studying in this thesis are mainly based on the PIC-emulsification method. Thereby, the term phase inversion concentration (PIC) refers to the fact that simply a certain water concentration has to be added to a nanoemulsion qualified oil/surfactant composition for initialising their formation (fig. 1.8b). Emulsion systems which are finely dispersed and exhibit particle sizes in the nanoemulsion region are preferably generated close to liquid crystal (lamellar [113] or cubic [129]) or bicontinuous microemulsion like phases [44]. Upon emulsification such phases provide ultra low interfacial tensions which result in a spontaneous change of curvature, and hence facilitate the phase inversion [183].

This precondition, the passing of a phase with zero curvature (minimum interfacial tension), determines the suitable oil/surfactant/cosurfactant mixtures [171]. Concerning PIT-nanoemulsions, the formation process of nanoemulsions can be traced back to the change of solubility of polyoxyethylene-type surfactants (change of HLB value with temperature); whereas upon PIC-emulsification one presumes that the relative quantity of surfactant present in the water phase

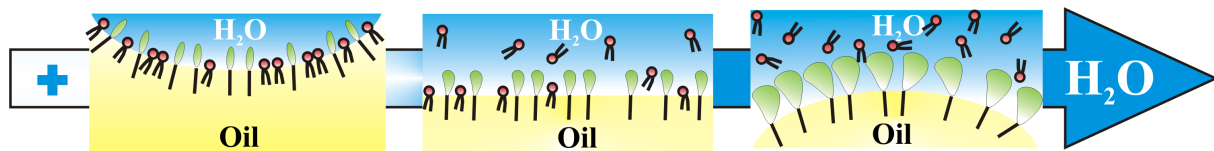


Figure 1.6: Assumed process of phase inversion concentration (PIC) method [110]; inversion of w/o-emulsion to o/w-nanoemulsion via passing of sponge like microemulsion phase with zero curvature during water addition

increases with dilution and thereby modifies the composition of the amphiphilic monolayer and results in a reversion of the curvature of the oil/water interface due to the increasing water solubility and hence extraction of the cosurfactant from the interface (fig. 1.6). Cosurfactants are interfacial active substances that do not form micelles on their own and do not stabilize emulsions. Consequently, for PIC -emulsification processes cosurfactants with a certain water solubility are needed [108]. However, so far especially for the PIC method, a systematic understanding about how to choose and optimise the hydrophobic/amphiphilic systems that work efficiently still has not been achieved. This also means that both the structural details of their formation process and the aspects relevant for their stability are still poorly understood.

The Ouzo-Effect:

At this stage we would like to point out the Ouzo-Effect [193] that describes the simple formation of milky turbid oil-in-water microemulsions by adding water to ouzo and other anise-flavored liqueurs and spirits, such as raki, sambuca, arak and absinth. Similar to the PIC-method the ouzo effect occurs due to the dissolution of a water-miscible solvent (eg. ethanol) upon dilution of a homogenous mixture of strongly hydrophobic essential oil of trans-anethole and water-miscible solvent.

Differently to all other high- and low-energy methods, the Ouzo-Effect slows

down droplet-coalescence dramatically without mechanical agitation, additional dispersing agents or other surfactant additions. It forms stable homogenous fluid dispersions by liquid-liquid nucleation [193]. Hence the droplet growth is only driven by Ostwald ripening processes whose effect diminishes with increasing ethanol concentration until the droplets stabilize with

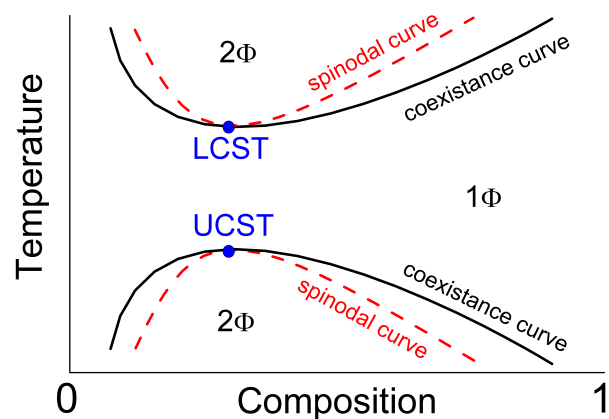


Figure 1.7: Phase diagram displaying spinodal and binodal (coexistence) curve. Lower- and upper critical solution temperature⁷ (LCST vs. UCST) are marked.

⁷Critical temperature below (LCST) or above (UCST) which the components of a mixture are miscible at all compositions.

an average diameter of 3 micrometer [166].

Based on thermodynamic considerations of the multi-component mixture, the emulsion derives its (meta)stability from trapping between the binodal⁸ and spinodal⁹ curves in the phase diagram [60]. However, the microscopic mechanisms responsible for the observed slowing of Ostwald ripening rates at increasing ethanol concentrations are not fully understood.

Phase Shift by Quenching (PSQ) Method:

Alternatively finely dispersed kinetically stable nanoemulsions can be formulated according to PIT-preferable oil/surfactant mixtures in combination with PIC-dilution process at room temperatures (fig. 1.8), using cosmotropic substances for shifting the complete phase diagram and hence also the phase inversion temperature.

At room temperature, mixtures of oil, water and emulsifiers form biphasic solutions. These are typical o/w-microemulsions with an oil-excess phase. Single phased microemulsions are obtainable at higher emulsifier concentrations and necessarily higher temperatures [24]. Upon heating, at a system dependent minimum temperature, a bicontinuous homogenous microemulsion phase, with zero bending of the amphiphilic film and hence minimal surface tension inside oil and water phases, is formed, before a phase inversion of o/w- to w/o-microemulsions occurs¹⁰ [159]. At this point, rapid cooling of the single w/o-microemulsion phase inverts the phase behaviour backwards and keeps it simultaneously "frozen" in a single metastable o/w-nanoemulsion state. See 1.8a.

Inside the Phase Shift by Quenching (PSQ) method cosmotropic substances lower the PIT to room temperature by replacing the temperature increase.

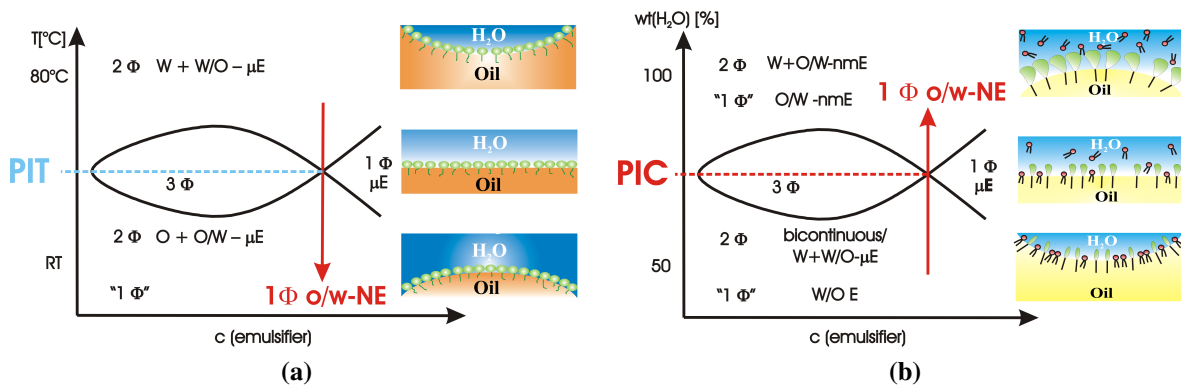


Figure 1.8: Emulsification process via **a** Phase Inversion Temperature (PIT) and **b** Phase Inversion Concentration (PIC) method

⁸Coexistence of two distinct phases.

⁹Stability limit of solution.

¹⁰Further increase of T leads to the inverted biphasic equilibrium (w/o- μE beside water excess phase).

Cosmotropic¹¹ substances favour, or enhance, the formation of hydrogen bonds in an aqueous solution and shift the hydrophilicity/hydrophobicity of an amphiphile to stronger hydrophobic properties.

A dilution of the cosmotropic affected oil/surfactant mixture with an adequate amount of water, simultaneously drops the concentration of the cosmotropes below the minimum concentration required for lowering the phase inversion temperature, so that the original temperature level (oil/surfactant mixture without cosmotropic additives) is restored. The dilution process equates the very rapid cooling inside PIT-procedure, and therefore results likewise in non phase separated meta stable fine dispersed nanoemulsions.

The Phase Shift by Quenching procedure is a two step method, where in a first stage the phase inversion temperature (PIT) is lowered by cosmotropic additives, preferably to the level of room temperature, and in a second stage finely dispersed nanoemulsions are obtained by diluting, and hence deactivating (quenching) the cosmotropic effect [51, 52, 111].

¹¹antonym: chaotropic substances - destruction of hydrogen bonds

There is a smooth transition between chaotropic and cosmotropic substances that is explainable with the Hofmeister effect. Thus phosphates, ammoniums, saccharoses and glycols are cosmotropic; sodium and chloride ions are neutral; thiocyanates and carbamides are chaotropic [26].

Chapter 2

Motivation

Emulsions are mixtures of at least two immiscible liquids; where one liquid is dispersed in the other one. Common structures are oil-in-water (o/w), water-in-oil (w/o) or multiple emulsion droplets (eg.: w/o/w or o/w/o). Without stabilising surfactants those systems tend to a macroscopic phase separation due to break down processes like creaming, coalescence or Ostwald ripening.

Depending on the components used and emulsification method, different emulsion types are accessible that are typically distinguished by their particle size and stability. They appear more translucent the smaller the particle size. Thereby metastable nanoemulsions that possess emulsion droplets in the range of 10 - 200 nm, are structurally located between smaller sized thermodynamically stable micro- (≤ 10 nm) and bigger sized unstable macroemulsions (> 200 nm). Emulsions are widely used in our daily life. Natural concepts, for the distribution of oil and water phases, can be found in milk or oil containing plants, like nuts, pulses (e.g. soy) or fruits (e.g. avocado). The better understanding and further enhancement of emulsions, concerning the physical properties of their ingredients, led to versatile applications in industry (food, pharmacy, cosmetics... [13, 116, 149, 202]). Although, specific conditions favour their use in fluidal and creamy, as alike in solid formulations.

During the 20th century many studies have been done concerning micro- and macroemulsions. Nanoemulsions require less surfactant than microemulsions and form, in comparison to macroemulsions, quite long-term stable emulsion droplets in an adequate size range, they have attracted more and more attention in the last years. They are formed by different high- and low-energy methods, as nanoemulsions formed by low-energy methods are particularly attractive, due to the mild conditions of preparation. However, so far their formation is still not well understood with respect to the oil/surfactant composition required and the structural pathway of formation.

The formation of metastable nanoemulsions by means of low energy input methods is a very interesting phenomenon, both from a fundamental scientific point of view but also for many

applications where nanosized dispersions of oil in water or vice versa shall be achieved by a simple experimental method.

Classically this is done by the well established phase inversion temperature (PIT) method that forms w/o-nanoemulsions due to a change of ethoxylated emulsifiers' hydrophilicity in a heating-cooling cycle.

More recently and even more appealing is the phase inversion concentration (PIC) method as it allows to obtain nanoemulsions by a simple dilution procedure (typically with water) of an appropriate oil/surfactant mixture in a spontaneous formation process, and therefore has also to be seen in the context of sustainable and green chemistry.

Hence, in this thesis we are therefore particular interested to investigate this novel method, as for the PIC method a systematic understanding about how to chose and optimise the hydrophobic/amphiphilic systems that work efficiently still has not been achieved. This also means that both the structural details of their formation process and the aspects relevant for their stability are still poorly understood.

Thus, we first of all investigated the formation of nanoemulsions based on a commercially available oil/surfactant formulation (Tego[®] Wipe DE) that is known to be suitable for the PIC method and extended these studies by systematic variations of the essential components of this model system. Whether a nano- or microemulsion is formed depends mainly on the dilution ratio, with nanoemulsions typically formed for larger dilution ratios. In order to obtain a more general understanding of the criteria required for the formation of nanoemulsions by the PIC method and their differentiation to similarly systems given in the literature [16, 44, 90, 101, 129, 142, 171, 172] we were highly interested in the structural progression upon dilution pathway and the structure and stability of the finally formed nanoemulsion droplets. We therefore employed different physico-chemical characterisation methods using conductivity, viscosity, density, UV/Vis-transmittance and zeta-potential measurements. Additionally small angle neutron and x-ray scattering (SANS/SAXS) examinations, and some complementary cryo-TEM micrographs led to a more refined structural understanding. As a consequence of contrast variation studies and NMR-experiments the PIC-mechanism could be partially resolved.

As nanoemulsions are metastable systems their structure is necessarily controlled by their formation process. Therefore detailed structural knowledge of this formation process and their dynamical behaviour during equilibration are central aspects for their understanding. The interdroplet exchange dynamics are not only important for a systematic understanding of ageing processes; they are also relevant with respect to the release properties of functionalised nanoemulsions. Time resolved SANS/SAXS and turbidity measurements, using the stopped flow technique, allowed us to follow the divers nanoemulsion dynamics in more detail.

However, another very interesting aspect is the functionalisation of such nanoemulsions in order to obtain modified functionalised nanoemulsion droplets that can be used to incorporate hydrophobic active substances. Thereby they may be employed as carrier systems in drug delivery or nanocontainers for the control of more complex chemical reactions. The encapsulation of PIC-formulated nanoemulsion droplets may be achieved by a modification of the oil/water interface using polymerisation reactions or oppositely charged molecules to form electrostatic interacting complexes. In particular we mainly investigated the latter one by SANS and cryo-TEM techniques, employing oppositely charged molecules, where one of the components (more lipophilic) will be contained in the oily nanoemulsion starting formulation and the second one (more hydrophilic) in the water used for its dilution.

In general, the study of such PIC nanoemulsions and their functionalisation constitutes a very interesting and innovative way to produce novel nanosized aggregates in a rather simple fashion. Our studies allowed us to draw some conclusions on the structures formed with this method, their stability and the requirements of the oil/surfactant mixtures employed. Furthermore, we got a more comprehensible understanding of the PIC principles that govern the spontaneous formation of nanoemulsions and their equilibration-dynamics. With this knowledge a rational design should become feasible. Additional encapsulation trials gave central aspects for further developments on the application-potential of such systems.

Chapter 3

Materials and Methods

3.1 Materials

| # | compound | commercial name | abbr. | Σ -formula | purity/grade | origin |
|-------------|-----------------------------------|---------------------------|--------|--|--------------|--|
| oils | | | | | | |
| 1 | | Tego [®] Wipe DE | TW | mix of # 2,9,11 and dilauryl citrate* | ind. | Evonik Goldschmidt (D) |
| 2 | diethylhexyl carbonate | Tegosoft [®] DEC | h-DEHC | C ₁₇ H ₃₄ O ₃ | ind. | Evonik Goldschmidt (D) |
| 3 | diethylhexyl carbonate-d34 | | d-DEHC | C ₁₇ D ₃₄ O ₃ | >98%D | synthesised at TUB |
| 4 | 2-ethylhexanol-d17 | | EH | C ₈ D ₁₇ OH | >99.5%D | Prof. R.K. Thomas (Oxford University,GB) |
| 5 | 2-ethyl carbonate | | | C ₅ H ₁₀ O ₃ | ≥99% | Merck (D) |
| 6 | 2-n-butyl carbonate | | | C ₉ H ₁₈ O ₃ | ≥98% | Merck (D) |
| 7 | 2-octyl carbonate | Cetiol [®] CC | CC | C ₁₇ H ₃₄ O ₃ | ind. | Cognis Europe (D) |
| 8 | octyloctanoate | | OO | C ₁₆ H ₃₂ O ₂ | ≥98% | Sigma-Aldrich (F) |
| 9 | phenoxyethanol / parabene mixture | Euxyl [®] K300 | K300 | C ₈ H ₁₀ O ₂ / C ₇ H ₅ O ₃ (C _n H _{2n+1}) n=1,2,3,4 | ind. | Schülke & Mayr |
| 10 | tetradecane | | | C ₁₄ H ₃₀ | ≥99% | Sigma-Aldrich (F) |

| # | compound | commercial name | abbr. | Σ -formula | purity/grade | origin |
|-----------------------------|--|-----------------------------------|-------|---|--------------|----------------------------------|
| nonionic surfactants | | | | | | |
| 11 | polyglycerol-4 laurate | Tego [®] Care PL4 | P4L | C ₂₄ H ₄₈ O ₁₀ | ind. | Evonik Goldschmidt (D) |
| 12 | polyglycerol-4 caprate | Hydriol [®] PGCL4 | | C ₂₂ H ₄₄ O ₁₀ | ind. | Hydriol AG (CH) |
| 13 | polyglycerol-4 oleat | Hydriol [®] PGO | | C ₃₀ H ₅₈ O ₁₀ | ind. | Hydriol AG (CH) |
| 14 | polyglycerol-4 oleat | Hydriol [®] PGMO.4 | | C ₃₀ H ₅₈ O ₁₀ | ind. | Hydriol AG (CH) |
| 15 | polyglycerol-4 oleat | Hydriol [®] PGHO.4 | | C ₃₀ H ₅₈ O ₁₀ | ind. | Hydriol AG (CH) |
| 16 | polyglycerol-4 isostearate | Hydriol [®] PGI | | C ₃₀ H ₆₀ O ₁₀ | ind. | Hydriol AG (CH) |
| 17 | polyglycerol-2 caprate | Hydriol [®] PG2 | | C ₁₆ H ₃₂ O ₆ | ind. | Hydriol AG (CH) |
| 18 | polyglycerol-3 caprate | Hydriol [®] PGC3 | | C ₁₉ H ₃₈ O ₈ | ind. | Hydriol AG (CH) |
| 19 | polyglycerol-10 laurate | SY-Glyster [®] ML-750 | | C ₄₂ H ₈₄ O ₂₂ | ind. | Sakamoto Yakuhin Kogyo (J) |
| charged surfactants | | | | | | |
| 20 | Di-Oleic Acidyl Isopropylester Dimethylammonium Methosulfate | Rewoquat [®] CR3099 | EQ | C ₄₃ H ₈₃ NO ₈ S | ind. | Evonik Goldschmidt (D) |
| 21 | Diocetyl Sodium sulfosuccinate | | AOT | C ₂₀ H ₃₇ NaO ₇ S | 98% | Sigma- Aldrich (D) |
| 22 | Sulfonated castor oil, Na-salt | Hydriosul [®] HRN100 | SCO | C ₁₈ H ₃₂ Na ₂ O ₆ S | ind. | Hydriol AG (CH) |
| 23 | Disodium Laureth Sulfosuccinate | Rewopol [®] SB FA 30 | SS | C ₂₂ H ₄₀ Na ₂ O ₁₀ S | ind. | Evonik Goldschmidt (D) |
| others | | | | | | |
| 24 | deuterium oxide | | | D ₂ O | 99.85%D | Euriso-top (D,F) |
| 25 | glycerol | | | C ₃ H ₈ O ₃ | ≥99% | Sigma- Aldrich (F) |
| 26 | triphosgene | | | C ₃ Cl ₆ O ₃ | 98% | Sigma- Aldrich (D) |

3.1 Materials

| # | compound | commercial name | abbr. | Σ -formula | purity/grade | origin |
|---------------|---|-----------------|-------|--------------------------|--------------|-------------------|
| others | | | | | | |
| 27 | 1,2-diacyl-sn-glycerol-3-phospho-L-serine sodium salt | | PGL | $C_{42}H_{81}NNaO_{10}P$ | $\geq 97\%$ | Sigma-Aldrich (F) |
| 28 | lysozyme | | lys | | | Sigma-Aldrich (F) |
| 29 | toluene 2,4-diisocyanate | | TDI | $C_9H_6N_2O_2$ | 95% | Sigma-Aldrich (F) |
| 30 | diethylenetriamine | | DETA | $C_4H_{13}N_3$ | 99% | Sigma-Aldrich (F) |
| 31 | triblock copolymer (PEO ₂ -PPO ₁₆ -PEO ₂) | Pluronic L31 | L31 | $C_{52}H_{105}O_{21}$ | ind. | BASF (D) |

Table 3.1: Oils, nonionic and charged surfactants, and other chemical compounds used in this thesis, with their commercial name, abbreviation, sum-formula, grade of purity and origin. *Pure charged surfactant dilauryl citrate (DC), contained in our model system Tego[®] Wipe DE, was not available.

3.1.1 Chemical compounds employed

A wide range of chemicals were used in this study, and are shown in table 3.1. They will be introduced in more detail at the pertinent point in the work.

3.1.1.1 The model system (Tego[®] Wipe DE)

The basic oil/surfactant (O/S) composition (Tego[®] Wipe DE (Evonik Goldschmidt) - $\rho(\text{TW}) = 0.954 \text{ g/cm}^3$) our work based on consists of $\sim 66 \text{ wt}\%$ diethylhexyl carbonate (TegoSoft[®] DEC (Evonik Goldschmidt)), $\sim 12 \text{ wt}\%$ of a preservative mixture consisting of phenoxyethanol

| name | synonym | abbr. | Σ -formula | Mw g/mol | $\rho^{25^\circ\text{C}}$ g/cm ³ | wt-% | SLD 10^{-6} \AA^{-2} |
|--|-----------------------------|-------|---|-------------|--|------------|-----------------------------------|
| deuterium oxide | | | D ₂ O | 20.2 | 1.1072 | | 6.370 |
| 2-ethylhexyl carbonate | Tegosoft [®] DEC | DEHC | C ₁₇ H ₃₄ O ₃ | 286.5 | 0.8925 | 66 | 0.061 |
| phenoxyethanol/ parabene mixture | Euxyl [®] K300 | K300 | (A.1) ¹ | 144.4 | 1.1219 | 12 | 1.45 |
| polyglycerol-4 laurate | Tego [®] Care PL 4 | P4L | C ₂₄ H ₄₈ O ₁₀ | 496.6 | 1.0944 | 21.1 | 0.505 |
| 4-dodecoxy-2-(dodecoxycarbonyl-methyl)-2-hydroxy-4-oxo-butanoic acid | Dilauryl Citrate | DC | C ₃₀ H ₅₆ O ₇ | 528.8 | 1.0110 | ~ 0.9 | 0.353 |

Table 3.2: Sum formula, densities ρ , weight fraction wt-% and scattering length densities SLD of the individual components of the oil/surfactant formulation in the model system Tego[®] Wipe DE -O/S-ratio: 78/22

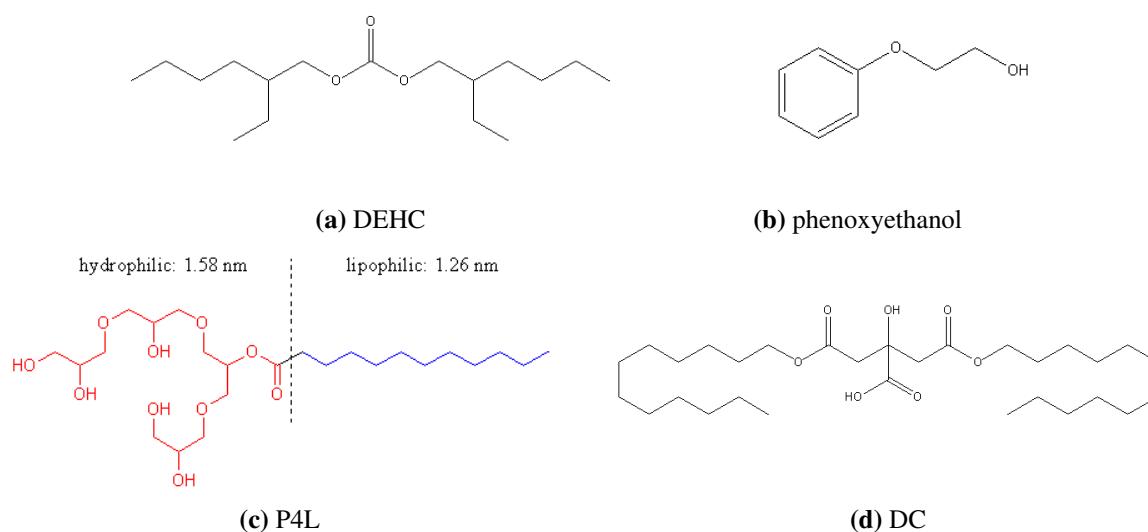


Figure 3.1: Molecular structure of Tego[®] Wipe DE composites

¹Detailed composition of preservative mixture Euxyl K300 is tabulated in the appendix A.1.

(main component (72 wt%)) and different parabens (methyl- (16 wt%), ethyl- (4 wt%), propyl- (2 wt%), butyl- (4 wt%) and isobutylparabene (2 wt%)); and 22 wt% polyglyceryl-4 laurate (TEGO[®] Care PL 4 (Evonik Goldschmidt)) containing a small amount (~ 0.9 wt%) of dilauryl citrate as anionic surfactants. It should be noted that at the given pH of 5.5-6 of the solutions the citrate is fully charged and contains one charge per surfactant molecule.

All components were obtained as gifts from Evonik Industries. Water was deionised and further treated by Milli-Q purification. D₂O for SANS-measurements was purchased from Euriso-top (99.85 %D).

3.1.1.2 PIC-Formulation studies - Exchange of single Oil/Surfactant compounds

While using a model system (see section 3.1.1.1), we modified the oil/surfactant (O/S) mixture at a constant O/S-ratio (78/22). At this given ratio we exchanged the main oil component and the charged surfactant, as for the nonionic surfactant and cosurfactant no alternatives have been found.

Alternative substances to exchange the main oil component, while keeping all other ingredients and the ratios, were chosen to be similar to the model one (2-ethylhexyl carbonate) as greater structural deviations prevent the formation of homogenous O/S-mixtures (eg. table 3.3). Their structures are given in table A.2 of the appendix. Some relevant characteristics for the charged surfactants employed are summarised in table 3.4. Their structures are given in table A.4 of the appendix.

Nonionic surfactants employed to exchange the main surfactant phase (polyglycerol-4 laurate) are listed in table A.3 of the appendix, as no homogenous O/S-concentrates could be formed and no further measurements were done.

| compound (oil) | commercial name | abbr. | Σ -formula | Mw g/mol | $\rho^{25^\circ\text{C}}$ g/cm ³ | H ₂ O _{solub.} mg/L ^{25°C} | homog. O/S-mix. |
|------------------------|---------------------------|-------|--|----------|---|---|-----------------|
| 2-ethylhexyl carbonate | Tegosoft [®] DEC | DEHC | C ₁₇ H ₃₄ O ₃ | 286.5 | 0.893 | 2.8 | y |
| 2-ethyl carbonate | | | C ₅ H ₁₀ O ₃ | 118.1 | 0.975 | 23 800 | n |
| 2-n-butyl carbonate | | | C ₉ H ₁₈ O ₃ | 174.2 | 0.92 ^{20°C} | 542 | n |
| 2-octyl carbonate | Cetiol CC | CC | C ₁₇ H ₃₄ O ₃ | 286.5 | 0.891 | 0.1 | y |
| octyl-octanoate | | OO | C ₁₆ H ₃₂ O ₂ | 256.4 | 0.859 | 4.6 | y |

Table 3.3: Oils used to form homogenous oil/surfactant (O/S) nanoemulsion (NE) qualified mixtures, their commercial name, sum-formula, density ρ , water solubility at 25°C and tendency to form a homogenous O/S-mixture and hence NE at high water concentrations (y - yes, n-no); (O/S-composition: oil/phenoxyethanol+parabens/polyglycerol-4 laurate/Rewoquat CR 3099 (66/12/21.1/0.9)) - (molecular structures of the oils are given in table A.2) - O/S-ratio: 78/22

| compound (charged surfactant) | commercial name | abbr. | Σ -formula | Mw g/mol | z | c mM | $\rho^{25^\circ\text{C}}$ g/cm ³ | cmc mM | HLB |
|---|----------------------|-------|--|-------------|----|---------|--|-----------|-----|
| 2-lauryl citrate | | DC | $\text{C}_{30}\text{H}_{56}\text{O}_7$ | 528.8 | -1 | 16.6 | 1.0110 | * | 5 |
| 2-oleic acyl isopropylester | | | | | | | | | |
| 2-methylam- monium Methosulfate | Rewoquat CR 3099 | EQ | $\text{C}_{43}\text{H}_{83}\text{NO}_8\text{S}$ | 773.6 | +1 | 11.4 | 0.9054 | 2.09 | 23 |
| 2-octyl sodium sulfosuccinate | AOT | AOT | $\text{C}_{20}\text{H}_{37}\text{NaO}_7\text{S}$ | 444.6 | -1 | 19.8 | 1.1002 | 7.07 | 15 |
| sulfonated castor oil, Na salt | Hydriosul HRN 100 | SCO | $\text{C}_{18}\text{H}_{32}\text{Na}_2\text{O}_6\text{S}$ | 422.2 | -2 | 20.9 | 1.0252 | 1.81 | 25 |
| 2-sodium laureth sulfo- succinate | Rewopol SB FA 30 | SS | $\text{C}_{22}\text{H}_{40}\text{Na}_2\text{O}_{10}\text{S}$ | 542.2 | -2 | 16.2 | 1.1217 | 0.32 | 35 |

Table 3.4: Charged surfactants in use (chem. structures are given in table A.4 of the appendix), to form homogenous oil/surfactant (O/S) nanoemulsion (NE) qualified mixtures, their commercial name, sum-formula, charge z, concentration c, density ρ , critical micelle concentration cmc (*raw material was not available) and hydrophilic-lipophilic balance (HLB) value (O/S-composition: 2-ethylhexyl carbonate/ phenoxyethanol+parabens /polyglycerol-4 laurate/charged surfactant (66/12/21.1/0.9)); all formulated mixtures generated a homogenous oil/surfactant concentrate whose dilution lead to a nanoemulsion formation at high dilution ratios - O/S-ratio: 78/22

Single compounds of the model system (tab. 3.2) were obtained as gifts from Evonik Industries, except for the charged surfactant dilauryl citrate which was not commercially available. The oils were obtained from Merck (diethylcarbonate ($\geq 99\%$), di-n-butylcarbonate ($\geq 98\%$)) and Cognis (Cetiol CC ($\geq 96\%$)) GmbH. Nonionic surfactants (eg. table A.3) of the Hydriol-series were obtained as gifts from Hydriol (Swiss) and polyglycerol-10 laurate by Sakamoto Yakuin Kogyo (Japan). Charged surfactants are gifts of Evonik Goldschmidt (Rewopol[®] SB FA 30

and Rewoquat[®] CR 3099) and Hydrior (Hydriosul[®] HRN.100). AOT (98%) and tetradecane ($\geq 99\%$) were acquired from Sigma Aldrich. Water for dilutions was deionised and further treated by Milli-Q purification. D₂O for SANS-measurements was purchased by Euriso-top (99.85%D)

3.1.1.3 The variation of the O/S-ratio at constant dilution ratio (95wt-% water)

The influence of a O/S-variation on the nanoemulsion phase formed at 95wt-% water was studied. For this purpose we employed O/S-mixtures based on 2-ethylhexyl carbonate (DEHC) and Euxyl[®] K300 (K300) as oil (O), and polyglycerol-4 laurate (P4L) and 2-sodium laureth sulfosuccinate (SS) or Rewoquat CR3099 (EQ) as surfactant (S) phase. More detailed information about the single components can be found in table 3.2 and 3.4 of the previous subsections. O/S-variations were accomplished for O/S-ratios of 100/0, 95/5, 90/10... to 0/100. Individual volume fractions or percentage compositions are given in table A.5 of the appendix. All components were obtained from Evonik Industries as gifts.

Water for dilutions was deionised and further treated by Milli-Q purification. D₂O for SANS-measurements was purchased by Euriso-top (99.85%D)

3.1.1.4 Dynamics observed in PIC-prepared nanoemulsions

Studies on the rapid formation kinetics of PIC formulated nanoemulsions have been done using the model system Tego[®] Wipe DE (eg. composition in table 3.2). Slower interdroplet exchange dynamics and SANS-contrast match measurements have been done with fully deuterated 2-ethylhexyl carbonate ($\rho^{25^\circ\text{C}}(\text{C}_{17}\text{D}_{34}\text{O}_3) = 0.893 \text{ g/cm}^3$, $\text{SLD}(\text{C}_{17}\text{D}_{34}\text{O}_3) = 6.69 \cdot 10^{-6} \text{ \AA}^{-2}$) that we synthesised with the help of Dr. M. Päch at the Fraunhofer IAP (Golm, Germany). The synthesis based on 2-ethyl hexanol ($\text{C}_8\text{D}_{17}\text{OH}$), which we purchased from Prof. R.K. Thomas (Oxford University) and triphosgene acquired from Sigma Aldrich (98%). More detailed information about synthesis work can be found in the appendix section A.1.2.5. The O/S-mixture used here was based on a slight modification of our model system, replacing the hydrogenated oil diethylhexyl carbonate ($\text{h}_{34}\text{-DEHC}$) by its fully deuterated equivalent ($\text{d}_{34}\text{-DEHC}$) and the nonionic surfactant dilauryl citrate by AOT. AOT was chosen due to its common commercial availability and its capability to replace the charged dilauryl citrate of the commercial O/S-mixture.

Additional triblock copolymer Pluronic L31 (ind. grade) was employed as additive that we obtained as a gift from BASF company, Germany. Some polymer properties are summarised in the following table 3.5.

²Cmc was taken from reference [150] where they measured the polymers cmc by surface tension studies, employing the bubble tensiometer method.

| compound (polymer) | commercial name | abbr. | Σ -formula | Mw g/mol | cmc ppm | HLB |
|---|--------------------|-------|--|-------------|------------------|-----|
| triblock copolymer (PEO _n -PPO _n -PEO _n) n = 2/16/2 | Pluronic L31 | L31 | C ₅₂ H ₁₀₅ O ₂₁ | ~ 1100 | 650 ² | 1 |

Table 3.5: Some properties (monomer units n, molecular weight Mw, critical micelle concentration cmc and hydrophilic lipophilic balance value HLB) of the triblock copolymer Pluronic L31 employed for the additives interdroplet exchange studies.

3.1.1.5 Experimental and theoretical considerations concerning the PIC-mechanism

For our studies of the phase inversion concentration (PIC) mechanism we used oil/surfactant mixtures based on our model system (Tego[®] Wipe DE, eg. section 3.1.1.1) and a slightly modified one -containing DEHC/K300/P4L/AOT (66/12/21.1/~0.9 wt-%; see beside section 3.1.1.1 also section 3.1.1.2). As the nonionic surfactant dilauryl citrate (DC) given in our model system Tego[®] Wipe DE was not accessible as a pure substance, we chose AOT due to its common commercial availability and its popularity in soft matter science to replace the DC. Glycerol ($\geq 99\%$, biomolecular grade), D(+)-glucose (99.5%) and D(+)-galactose ($\geq 99\%$, biomolecular grade) were obtained from Sigma-Aldrich and used as refractive index matching substances in formed nanoemulsions with 95wt-% H₂O.

3.1.1.6 Compounds used for nanoemulsion-droplets encapsulation

For our encapsulation trials of nanoemulsion droplets we used O/S-mixtures based on our model system (Tego[®] Wipe DE, eg. section 3.1.1.1) to form the nanoemulsion droplets by

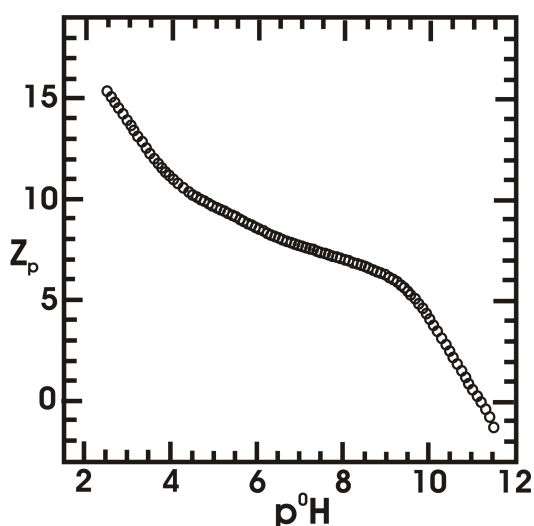


Figure 3.2: This plot is a copy of the experimental hydrogen ion titration for hen-egg-white lysozyme in a solution of potassium chloride at an ionic strength of 0.2 mol/L from reference [88]. Plotted is the net charge Z_p versus the pH-value.

the PIC-formation process. The encapsulations we studied, based on the attracting forces of counter charged molecules. The O/S-concentrate contained either anionic 2-sodium lauryl sulfosuccinate (SS^- , Evonik Goldschmidt - ind. grade) or 1,2-diacyl-sn-glycerol-3-phospho-L-serine sodium salt (PGL^- , Sigma Aldrich $\geq 97\%$ (TLC)). As counter charge lysozyme solutions (lys^+ , Sigma Aldrich $\sim 70\ 000$ units/mg) were always employed in proper concentrations to obtain charge ratios of $0 \leq z[\text{cation}^+/\text{anion}^-] < 1$, respecting its pH-dependent net charge [88]. At a given pH-value of 6.0 ± 0.5 (eg. section A.7.2 of the appendix) for our nanoemulsion solutions, studied at 95wt-% water, a lysozyme net charge of approximately +8 was established. A plot of

Encapsulation by electrostatic forces

| compounds | abbr. | Σ -formula | Mw / g/mol | z | $\Phi_{dissolv.}$ |
|---|-------|---------------------------|--------------|--------------|-------------------|
| 2-sodium laureth sulfo-succinate | SS | $C_{22}H_{40}Na_2O_{10}S$ | 542.2 | -2 | o |
| 1,2-diacyl-sn-glycerol-3-phospho-L-serine sodium salt | PGL | $C_{42}H_{81}NNaO_{10}P$ | 814.1 | -1 | o |
| lysozyme, from chicken egg white | lys | (eg. CAS 12650-88-3) | ~ 14500 | pH-dependent | w |

Encapsulation by polymerisation

| compounds | abbr. | Σ -formula | Mw / g/mol | ρ g/cm ³ | $\Phi_{dissolv.}$ |
|--------------------------|-------|-------------------|------------|--------------------------|-------------------|
| toluene 2,4-diisocyanate | TDI | $C_9H_6N_2O_2$ | 174.2 | 1.214 | o |
| diethylentriamine | DETA | $C_4H_{13}N_3$ | 103.17 | 0.955 | w |

Table 3.6: Components employed for nanoemulsion droplets encapsulation. Their chemical name, abbreviation, Sum-formula Σ , molecular weight Mw, molecular charge z and density ρ are listed. PIC-formed nanoemulsion droplets based on our model system Tego[®] Wipe DE (eg. chemical compounds in section 3.1.1.1) where either tried to encapsulate using the electrostatic forces of the employed components or by a polymerisation reaction. Indication in which phase the respective molecule was dissolved (either in the oil o or water w phase Φ .)

the pH-dependent net charge of lysozyme is given in figure 3.2. For some tests on the nanoemulsion droplets encapsulation by a polymerisation reaction toluene 2,4-diisocyanate (TDI, Sigma Aldrich 95%) and diethylentriamine (DETA, Sigma Aldrich 99%) were employed (eg. section A.7.1 in the appendix).

3.1.2 Sample preparation for PIC-Systems

Oil/Surfactant (O/S) mixtures of a constant O/S-ratio of 78/22 (wt-%) were formulated by adding all ingredients at room-pressure and -temperature, respecting the given weight fractions (oil/preservative mixture/surfactant/charged surfactant 66/12/21.1/0.9 (wt-%)), and incorporating them into a homogenous concentrate by mixing. For the given conditions (O/S-ratio, mass fractions, temperature and pressure) non-homogenous, and hence not nanoemulsion qualified concentrates were mainly formed in case of greater structural changes of the main oil component and generally for all non-ionic surfactants other than polyglycerol-4 laurate.

Homogenous oil/surfactant mixtures were used to form nanoemulsions by the phase inversion concentration (PIC) method, where at a certain dilution ratio upon emulsification, nanoemul-

sions are formed. The exact PIC depends thereby on the initial oil/surfactant formulation. Nanoemulsion phases and phases prior to the PIC were prepared by a one step dilution of a homogenous oil/surfactant concentrate. The formation process was typically initiated by vortex mixing but could also be done by simple hand mixing. The method of mixing (single-step or step-wise addition of oil or water; vortex or hand mixing) did not affect the final structure or behaviour.

Nanoemulsions appear as milky/white turbid, water viscous solutions with a more bluish or reddish tint depending on the angle of the incident light and dispersed droplet size (the lower the water content the more bluish the solutions). Flow birefringence was checked using polarisers while shaking the sample gently.

The age of the samples, as well as that of the starting formulation of surfactant/oil is relevant as ageing is an important issue in these systems and was always carefully registered. Measurements that are compared were always done on samples of identical age.

3.2 Methods

3.2.1 Density

Densities given in this thesis were either measured with the oscillating density meter DMA 4500 M by Anton Paar (TUB) or the DMA 58 by Anton Paar (ILL). The principle of the density meter is based on the natural frequency of an oscillatory system. The oscillation period is measured electronically for a certain volume fraction that is placed in a resonator (hollow U-shaped tube made of borosilicate). The oscillation period τ is correlated with the density via $\rho = A \cdot \tau^2 + B$, where A and B are device specific constants of the resonator.



Figure 3.3: Principle of flexural resonator for density measurements.

3.2.2 Electric Conductivity

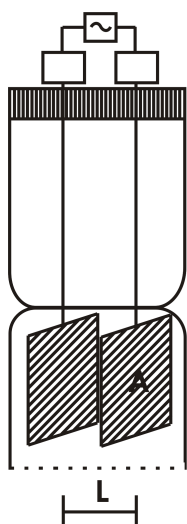


Figure 3.4: Principle setup of a conductivity cell.

For assigning the type of emulsion (i. e. water continuous or not), conductivity measurements were done. The electrical conductivity was measured at constant temperature ($25.0 \pm 0.1^\circ\text{C}$) using a conductometer 712 by Metrohm (TUB). In biphasic regions the previously separated phases were measured individually, provided adequate volumes ($> \sim 25$ vol-%) were available. The given conductivities are averaged values over four repeated measurements.

The electric conductivity is given by $\kappa = 1/R \cdot L/A = G \cdot z$, by the reciprocal value of the electrical resistance (conductance G) times the measurement-setup dependent cell constant z, that is given as the quotient of the electrode distance L and electrode surface A (cp. figure 3.4).

3.2.3 Viscosity

For measuring the kinematic viscosity of the Newtonian fluids, calibrated Ubbelohde capillary viscosimeters (Schott) were used at constant temperature ($25.0 \pm 0.1^\circ\text{C}$). The kinematic viscosity ν was measured by determining the capillary suction time t of a given volume ($V = 20$ mL), at a defined cross section (radius r), via the Hagen-Poiseuille equation and taking into account the Hagenbach-Couette correction ζ (eq. (3.2)), that accounts for the difference between theoretical and measured flow time due to the drop in pressure by fluid acceleration at the capillary entrance [154].

Here, K is a device-specific constant, given by calibration measurements of Schott (model: 0a ($\nu = 0.8 - 5 \text{ mm}^2/\text{s}$) / I ($\nu = 1.2 - 10 \text{ mm}^2/\text{s}$) / Ic ($\nu = 3 - 30 \text{ mm}^2/\text{s}$) / IIc ($\nu = 30 - 300 \text{ mm}^2/\text{s}$)), and η , the dynamic viscosity, which is connected via the sample density ρ with the kinematic viscosity ν (eq. (3.1)).

$$\nu = \frac{\eta}{\rho} = K \cdot (t - \vartheta) \quad (3.1)$$

$$\vartheta = \frac{0.00168 \cdot \sqrt[3]{V}}{l \cdot \sqrt{2 \cdot r} \cdot \sqrt[3]{K} \cdot t^2} \quad (3.2)$$

The flow time t was registered automatically by Viscoboy 2 (MWG Lauda). The given viscosities are averaged values of five consecutive measurements.

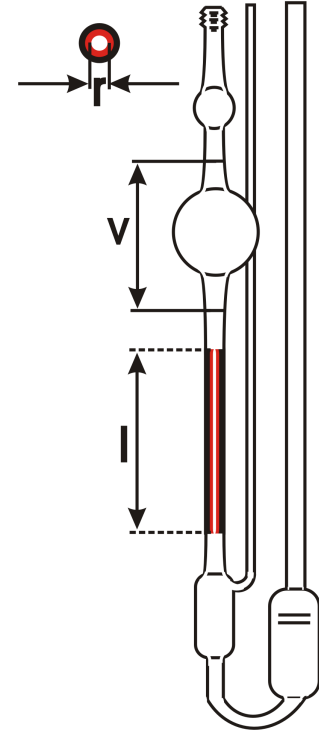


Figure 3.5: Ubbelohde capillary viscometer

3.2.4 Refractivity measurements

Refractivities have been measured with an Abbe refractometer (model G) of VEB Carl Zeiss (Jena) at $25.0 \pm 0.1^\circ\text{C}$ for non specific wavelengths. Expressed refractivities are averaged values of three repeated measurements.

3.2.5 UV-Vis transmittance and turbidity measurements

Dilution processes of oil/surfactant mixtures and nanoemulsion stabilities were followed either with a Clariant Cary 50 Tablet UV/Vis instrument (TUB) or a Jasco-V630 photometer (ILL) at $25.0 \pm 0.1^\circ\text{C}$, using Hellma cuvettes of 0.5 mm thickness. Transmittance spectra (300 - 800 nm) were measured for structures upon dilution pathway (0-100 wt% H_2O) statically and for nanoemulsions with an oil/water ratio of 95 wt-% (H_2O) time-dependently.

Assuming that at high wavelength the transmittance $T = T_T + T_S$ (given by the transmission- (T) and scattering-contributions (S) of the colloidal particles) can mainly be attributed to the scattering [126], we fitted the measured spectra, for samples in the nanoemulsion region, at high wavelengths (700-800 nm) using eq. (3.3),

$$T = T_0 \cdot \exp\left(-C \cdot d / \lambda^4\right) \quad (3.3)$$

where T is the transmission through a colloidal sample of thickness d , wavelength independent transmittance T_0 (= 100%) and the Rayleigh scattering coefficient C . Due to eq. (3.4) we also checked for full transmission at infinity wavelengths. Using the averaged transmission at 800

nm $T(\lambda = 800 \text{ nm})$ (eq. (3.3)), the turbidity coefficient τ was calculated according to:

$$\tau = -\frac{\ln T}{d} \quad (3.4)$$

where d is the thickness of the cuvette. From the value of the turbidity τ we calculated the molecular weight M_W of the colloidal particles according to eq. (3.5) and converted this value to obtain an approximate particle size R for spherical aggregates (eq. (3.6)).

$$M_W = \frac{\tau \cdot 3 \cdot N_{Av} \cdot \lambda^4}{32 \cdot \pi^3 \cdot n^2 \cdot c_g (dn/dc_g)^2} \quad (3.5)$$

$$R(M_W) = \left(\frac{M_W}{4/3 \cdot \pi \cdot \rho \cdot N_{Av}} \right) \quad (3.6)$$

Here N_{Av} is the Avogadro constant, λ the wavelength of light, n the refractive index of the solvent, c_g the mass concentration of the dissolved particles (assuming all surfactant and oil to be contained in the particles), dn/dc_g the refractive index increment, and ρ the density of the aggregates.

For our studies concerning the PIC-mechanism we used an averaged transmission T (due to eq. (3.3)) at 800 nm to calculate the turbidity coefficient τ which we then used to determine the matched refractivity $n_0(\sqrt{\tau} = 0)$ of the emulsified oil droplets in the nanoemulsions via:

$$\tau \propto \left(\frac{dn}{dc} \right)^2 \approx \left(\frac{n_S - n_0}{c_{total}} \right)^2 \rightarrow \sqrt{\tau} \approx \frac{n_S}{c_{total}} - \frac{1}{c_{total}} \cdot n_0 \quad (3.7)$$

with n_S and n_0 being the refractivity of the surfactant S and solvent mixture 0 (H_2O / glycerol and H_2O /sugar), and c_{total} the particle concentration contained in the solution.

The signal of a water filled cuvette was always subtracted to get the spectrum of the sample. Refractivity and densities of oil/surfactant concentrates and solvent (H_2O) were measured respectively.

3.2.6 Long-time transmittance measurement

Long-time transmittance (T) measurements were done at $25.0 \pm 0.1 \text{ }^\circ\text{C}$ and 633 nm with an in-house transmittance-setup; built-on a 4 mW He-Ne-Laser, a thermostated sample holder and a PH100-Si photodetector (Gentec-E0) connected to a Gentec-E0 SOLO PE Laser Power & Energy meter with an automatical PC-controlled readout 3.6.

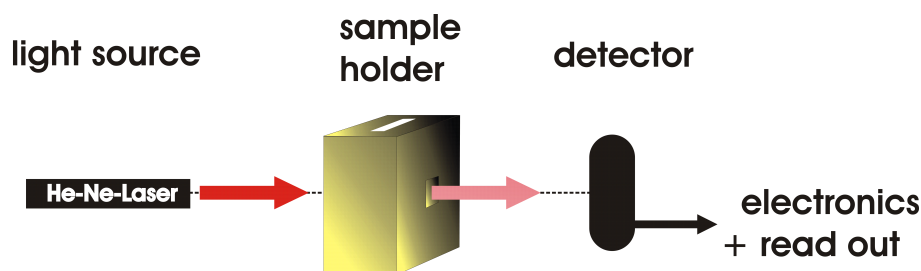


Figure 3.6: Scheme of the long-time transmittance setup

The signal of a water filled cuvette was always used as a reference to get the spectrum of the sample.

3.2.7 Surface Tension

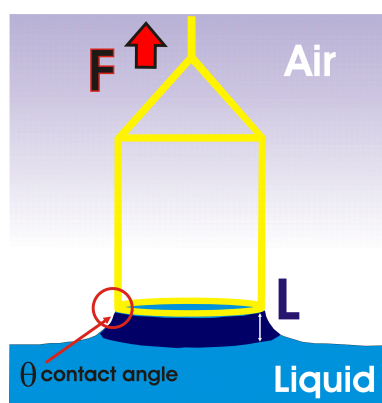


Figure 3.7: Scheme of Du Noüy ring method for surface tension measurements

Single surface tension measurements and the determination of the critical micelle concentration (cmc) for the different surfactants in use were done either with an automated Dataphysics DCAT 11 (TUB) or a Krüss K11 (ILL) tensiometer at $25.0 \pm 0.1^\circ\text{C}$, using the Du Noüy ring method. Here the surface tension of a liquid is measured by lifting a ring made of platinum, from its surface and detecting the maximum force that is required until the contact angle θ gets 0° (eg. fig. 3.7). It is calculated by:

$$\gamma = \frac{F_{max} - F_V}{L \cdot \cos \theta} \quad (3.8)$$

where γ is the surface tension concentration, F_{max} the maximum used force to lift the liquid film, F_V the weight of the lifted volume, L the stretching length and θ the contact angle. Prior to the surface tension measurements the platinum ring was always dipped into acetone and subsequently heated briefly by a gas torch for cleaning.

3.2.7.1 Determination of the critical micelle concentration (cmc):

Surface active agents adsorb to inter- and surfaces (eg. liquid/liquid or liquid/air), while lowering their tension. The change in surface tension $d\sigma$, at a constant temperature T and a surfactant concentration c of the solvent, is given by the Gibbs-Equation:

$$\begin{aligned} d\sigma &= -RT\gamma \cdot d \ln c \\ &= -\ln(10) \cdot RT\gamma \cdot d \lg c \end{aligned} \quad (3.9)$$

where R is the universal gas constant $R = 8.314 \text{ J}/(\text{mol} \cdot \text{K})$ and γ the surfactant concentration at the interface.

From a plot of the surface tension σ versus the common logarithm of the surfactant concentration $\lg c$ in the bulk phase, the surface concentration γ can be obtained by the slope of the given graph using eq. (3.10). The head group area a_h of a surfactant molecule is related to γ via the Avogadro constant according to equation (3.11).

$$\gamma = -\frac{1}{\ln(10)RT} \cdot \left(\frac{\partial \sigma}{\partial \lg c} \right)_T \quad (3.10)$$

$$a_h = \frac{1}{N_A \cdot \gamma} \quad (3.11)$$

As long as the surfactant concentration is increasing in the bulk phase, the surface concentration rises also linearly. However, in case of micellization the monomer concentration and hence the surface tension remains constant above the cmc. Thus, the cmc is determinable by observing the change in surface tension with increasing surfactant concentration [144]. The intersection point of two fit-lines, for the linear and constant parts, corresponds to the cmc [139].

3.2.7.2 Quantification of substance solubility/polarity via the Gordon and Hildebrand parameter:

A possible method to semi-quantify the solvents ability to dissolve non-polar molecules, is given by the so-called Gordon parameter $G = \gamma \cdot V_m^{1/3}$ [J/cm³], where γ is the surface tension concentration of the solvent and $V_m (= M_w / \rho \cdot N_A)$ its molar volume [55].

Water has a very high Gordon parameter, ≈ 234 J/cm³(25°C), while for example hexane has a very low value of ≈ 30 J/cm³(25°C). Thereby the hydrophobic interaction is largely due to the high cohesive energy density in water. Thus, the higher the Gordon parameter of a molecule the more polar it is. However, one has also to note that water is a 'better solvent' than its high Gordon parameter implies, which means that water to some extent is capable of compensating for the loss in cohesive energy when dissolving a non-polar solute [78].

This quantity, which was first introduced by Gordon [55], is analogous to the Hildebrand solubility parameter [70, 71], but permits in addition solvents with vanishingly small vapour pressures to be evaluated [114, 138].

However, the Hildebrand parameter δ is a numerical value that indicates the relative solvency behaviour of a specific solvent [201]. It is derived from the cohesive energy density c of the solvent and defined by the square root of its internal energy of vaporization ΔH_{vap} divided by the molar volume V_m :

$$\delta = \sqrt{c} = \sqrt{\frac{\Delta H_{vap} - RT}{V_m}} \quad (3.12)$$

These quantities are sometimes more easily accessible as the heat of vaporization is quite often

listed. It should be noted that Hildebrand took only dispersion interactions into account. As the solvent also interacts with the solutes by electron pair, donor-acceptor and hydrogen bonding interactions. Therefore Hansen proposed a practical extension of the Hildebrand parameter for polar and hydrogen bonding systems, which takes also the dispersive, polar and hydrogen bonding terms into account [67, 72].

3.2.8 Interfacial Tension

Interfacial tension measurements were done at $25.0 \pm 0.1^\circ\text{C}$ by means of a spinning drop tensiometer³ and using water as the continuous phase. The spinning drop principles are based on the theory derived by Vonnegut [194], where inside a horizontally positioned glass capillary, a lighter droplet (oil/surfactant mixture) is placed into a heavier outer phase (water) while rotation. The interfacial tension of the droplet can be calculated by the Vonnegut equation

$$\sigma = \frac{\Delta\rho \cdot \omega^2 \cdot a^2}{4} \quad (3.13)$$

at the equilibrium state, where the shape of the droplet is a balance between the interfacial ($\sim \gamma/a$) and centrifugal ($\sim \Delta\rho \cdot \omega^2 \cdot a^2$) stresses. $\Delta\rho$ is the difference in density of the phases, ω the frequency of rotation and a the radius of the droplet cross section [22, 83, 134].

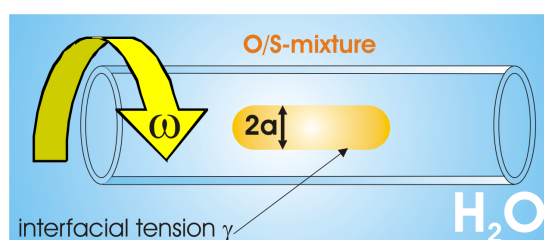


Figure 3.8: Main spinning drop setup for interfacial tension measurements

3.2.9 Zeta-Potential Measurements

| ZP / mV | Stability behaviour of colloids |
|---------------------------|-----------------------------------|
| from 0 to ± 5 | Rapid coagulation or flocculation |
| from ± 10 to ± 30 | Incipient instability |
| from ± 30 to ± 40 | Moderate stability |
| from ± 40 to ± 60 | Good stability |
| more than ± 61 | Excellent stability |

Figure 3.9: Colloids stability tendencies represented by their zeta potential ZP.

The zeta potential gives an indication about the stability of the studied system. In case of large negative or positive zeta potential for the dispersed aggregates, there is a bigger tendency of droplets repulsion and less opportunity of flocculation. However, if the particles exhibit low zeta potential values there is no force to prevent their convergency and hence flocculation.

The zeta potential of nanoemulsions were measured with a Malvern Zetasizer Nano ZS at $25.0 \pm 0.1^\circ\text{C}$. Thereby the electrophoretic mobility of the dispersed particles is measured in a spatially uniform electrical field by Laser Doppler Velocimetry (LDV). The magnitude of the zeta

³Model SITE04 from Kruss

3.2.10 Nuclear-Magnetic-Resonance Measurements (NMR)

^1H , ^{13}C and DEPT-NMR measurements were performed on a Bruker AC 200-MHz spectrometer. The reference was set to the solvent residual peak (CHCl_3 at 7.26 ppm, D_2O at 4.67 ppm) and the lock set via deuterium to 10 MHz. Acquisition setup was operated with DISNMR software.

3.2.11 Cryogenic Transmission Electron Microscopy (cryo-TEM)

Collaboration with University of Delaware, USA

Oil in water (o/w) samples were prepared as described in section 3.1.2 and arranged on Quantifoil carbon-coated copper grids with a 200 mesh. Grid samples were prepared in a Vitrobot machine by FEI CompanyTM (Tools for Nanotech). The grid was suspended between a pair of tweezers in a chamber with controlled temperature ($25.0 \pm 0.1^\circ\text{C}$) and humidity (100% humidity), where it was then dipped into a vial with the sample. The tweezers were then pneumatically lifted from the sample to an area between two blotting papers where the grid was blotted automatically with specified time of blotting and number of blots. After a given relaxation time, the grid was immediately plunged in liquid ethane where it was vitrified at the freezing point of ethane (165°C). The specifications of the blotting parameters were 2 blots held at 1 second for each blot, and the grid was allowed to relax in the chamber after blotting for 30 seconds. The blotting paper was kept at an offset of -1 where a positive offset gives a softer blot and a negative offset gives a harder blot. The sample was then viewed in a FEI Tecnai G2 12 Twin transmission electron microscope at a voltage of 120 kV. The sample was kept at -175°C or lower with a Gatan 626 cryo-specimen holder. The images were digitally recorded with a Gatan 794 CCD camera at about 12 micrometers of underfocus.

Cryo-TEM images (see figure 3.10) were taken by Christina Michelina Marino from the University of Delaware in 2008/2009.

Collaboration with Technion in Haifa, Israel

Solutions were examined by cryo-TEM. A small droplet of the solution was placed on a perforated carbon film supported on a TEM copper grid (Ted Pella, Inc., USA), held by tweezers. It was then blotted by a piece of filter paper, resulting in the formation of thin films of 100 – 300 nm thickness within the micropores in the carbon-coated lace-like polymer layer, supported on the grid. The specimen was then plunged into a reservoir of liquid ethane, cooled by liquid nitrogen, to ensure its vitrification (fast-freezing) and to prevent ice crystals formation. The vitrified specimen was transferred under liquid nitrogen and mounted on a cryogenic sample holder, cooled to -170°C . All samples were observed under low-dose conditions. Vitrified samples were examined in an FEI T12 G2 Cryo-TEM, operating at 120 kV, using a Gatan 626 cryo-holder. Images were recorded in a Gatan US1000 high-resolution cooled CCD camera and were processed with DigitalMicrograph version 3.3.1 software. The ramp-shaped optical den-

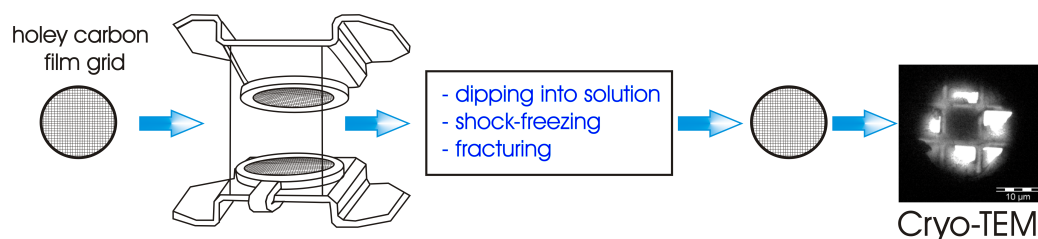


Figure 3.10: One-step sample preparation via freeze fracture direct imaging (FFDI [12])

sity gradients in the background were digitally corrected. Cryo-TEM images (see figure 3.10) were taken by group members of Dganit Danino at the Technion in Haifa (Israel) 2009/2010.

3.2.12 Stopped-Flow mixing

The stopped flow technique offers the possibility to measure very fast reaction kinetics of mixed solutions with appropriate detection methods (transmittance, fluorescence, conductivity and scattering methods).

Generally with a stopped flow apparatus small volumes of solutions are driven by high performance syringes through highly efficient mixers. The resulting mixture passes through a measurement flow cell (e.g figure 3.11). Then the flow is abruptly stopped by an electronically triggered shutter, which allows the observation of the mixed system about 1 ms after the mixing time. This dead time is mainly determined by the volume of the mixer and the connection between mixer and observation cell. Changes in the mixed solution af-

ter the mixing process, eg. mesoscopic structural changes, can be detected by transmittance, fluorescence, and conductivity measurements. In order to obtain more detailed structural information this technique can also be coupled to small-angle x-ray or neutron scattering [1, 11].

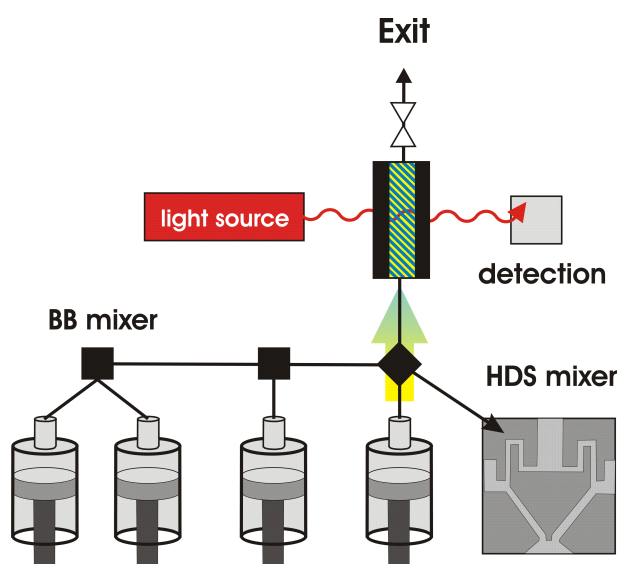


Figure 3.11: Stopped-Flow setup of a SFM-400 apparatus by BioLogic [1] with four syringes, berger ball mixer (BB) and high density mixer (HDS).

Stopped Flow turbidity experiments have been carried out at the TUB with a BioLogic SFM-400/S device. The SFM400/S is a four-syringe (10 mL) instrument in which all step-motor-driven syringes can be operated independently for either single- or double mixing, allowing suitable mixing ratios over a wide range. The stopped flow device was attached to a MOS-250 spectrometer and the transmitted wavelength adjusted to 626 nm. For the experiments a total flow rate of 6 mL/s was chosen with a total volume of either 500 μ L or 1000 μ L dependent on

the used mixing ratio, to ensure a proper mixing.

In respect to these conditions and the use of a FC-15 flow cell for the transmittance detection, the dead time was 6.1 ms [11].

Stopped flow SAXS experiments have been carried out at the ID02 beamline of the ESRF with a BioLogic SFM-400 device consisting of four motorized syringes interconnected through three mixers. The scattering cell, placed directly behind the last mixer, is made of a quartz capillary with a diameter of about 1.5 mm and 10 μm wall thickness. The flow is stopped by a hard-stop which consists of a solenoid valve placed at the end of the flow-line and is activated at the termination of the mixing sequence. The dead time of the device is primarily determined by the time to transfer the mixture from the last mixer to the beam crossing point on the capillary cell. This transfer time is about 2.2 ms for a flow rate of 6.7 ml/s while the turbulent mixing time is of the order of 0.1 ms. This means that the earliest time scale probed is about 2.3 ms [64]. The dead time and the quality of mixing are verified elsewhere [123].

For the fast kinetic SAXS experiments a total volume of 1000 μL was chosen with a total flow rate of ~ 6.7 mL/s, resulting in a dead time of 2.3 ms. Sample-to-detector distance was set to 8 m and X-ray wavelength (λ) to 1 \AA corresponding to a q -range of 0.01 - 0.7 nm^{-1} .

Due to the high brilliance of the beam ($\sim 5 \cdot 10^{13}$ photons per s) and high sensitivity of the CCD detector (FreLoN 4M) an acquisition time of 5 ms gave sufficient intensity statistics. Thereby the acquisition time is defined by the opening of a high precision tandem x-ray beam shutter. The first 5 ms frame is placed towards the end of the fast mixing phase such that the kinetic time is equal to the dead time (2.3 ms) of the stopped-flow device and the system ages after the cessation of flow. In the sequential data acquisition, the first frame of the next cycle is delayed by a desired time (typically 10 ms). The repetition of the mixing sequence and hence progressive increase of the initial delay time allows to cover the readout time gap of the CCD detector adequately. Further technical details are given elsewhere [64, 123].

Stopped flow SANS experiments have been carried out at the D22 instrument of the ILL with a BioLogic SFM-3 device consisting of three motorized syringes interconnected through two mixers. As neutrons possess a lower flux than x-rays larger sample volumes are required. Hence a rectangular quartz Hellma cell of 1 mm thickness with a total volume of 250 μL is used.

For the kinetic measurements a total volume of 750 μL was chosen with a total flow rate of 5 mL/s, resulting in a dead time of 3.1 ms. Sample-to-detector distance was set to 5 m, collimation to 5.6 m and neutron wavelength (λ) to 12 \AA covering a q -range of 0.03 - 1 nm^{-1} .

Further technical details are given elsewhere [4, 61].

3.2.13 Small-Angle Neutron Scattering (SANS)

All samples for SANS experiments were prepared by adding appropriate D₂O volumes to the oil phase at room temperature as described in section (3.1.2) for the H₂O-case, and stored in a bath thermostated at $25.0 \pm 0.1^\circ\text{C}$ before measuring them at the same temperature. D₂O was used instead of H₂O to increase the contrast and lower the incoherent background, accounting for the density difference, thereby keeping volumetric and molar compositions identical to the corresponding H₂O samples. In case of biphasic samples both phases were measured separately. Plots of SANS results, that are depicted as a function of D₂O-content, refer to the corresponding volume fraction of H₂O. SANS measurements were done on the small angle scattering instrument D11 or D22 at Institut Laue Langevin (ILL), Grenoble, France and the small angle scattering instrument V4 at Helmholtz Zentrum Berlin, Germany.

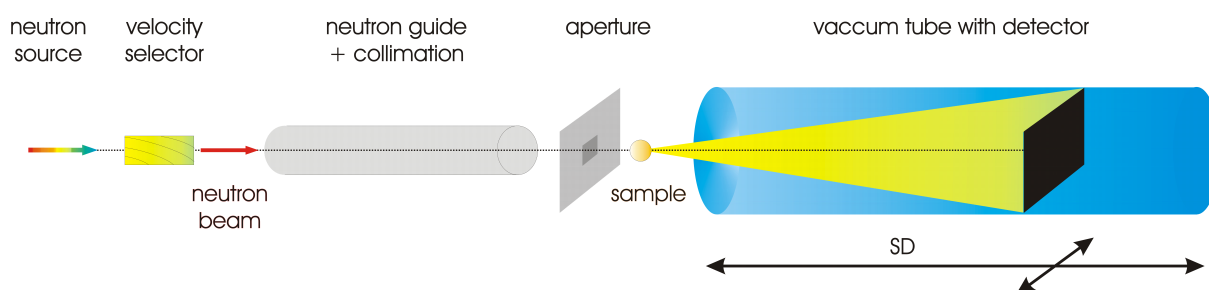


Figure 3.12: General setup for a Small-Angle-Neutron-Scattering (SANS) instrument

In a Small-Angle-Neutron (SANS⁴) experiment neutrons from a reactor source are monochromatized by a velocity selector to obtain the required wavelengths. Before entering the sample the neutron beam is further collimated and defined by an aperture whose shape is chosen to match the specific sample geometry. After entering the sample and subsequently being scattered, the neutrons are detected at a certain distance to the sample (sample-to-detector (SD) distance) due to the q -range of relevance. In the case of isotropic scattering the detector might be setup in an position offset, laterally to the neutron beam to cover a larger q -range (fig. 3.12). Several detector- collimation settings are usually combined to cover a preferably broad q -range of interest [175].

D11

Spectra were recorded on a 2-dimensional He³ gas detector of 128 x 128 pixels, 96 x 96 cm². The wavelength was always 6 Å (FWHM 10%), SD-distances of 1.2, 8, and 34 m (1.2, 6 and 39 m) were selected to cover a wide range of the wave vector magnitude $q = 0.02 - 5 \text{ nm}^{-1}$, where $q = 4\pi \cdot \sin(\varphi/2) / \lambda$ with φ being the scattering angle. Collimation lengths of 4, 8, and 34 m (8,

⁴World Directory of SANS instruments:

<http://www.ill.eu/instruments-support/instruments-groups/groups/lss/more/world-directory-of-sans-instruments/>, 02/2011

8 and 39 m) were chosen, respectively⁵.

D22

Spectra were recorded on a 2-dimensional He³ gas detector of 128 x 128 pixels of 0.8 x 0.8 cm². The wavelength was either 8 Å or 12 Å (FWHM 10%), a SD-distance of 1.4, 5, and 17 m were selected to cover a wide range of the wave vector magnitude $q = 0.02 - 5 \text{ nm}^{-1}$, where $q = 4\pi \cdot \sin(\varphi/2) / \lambda$ with φ being the scattering angle. Collimation lengths of 5.6, 8, and 17.6 m were chosen, respectively⁶.

V4

Spectra were recorded on a 2-dimensional He³ gas detector of 128 x 128 pixels of 5 x 5 mm². The wavelength was always 6 Å (FWHM 11%), a SD-distance of 1, 4, 12 and 16 m were selected to cover a wide range of the wave vector magnitude $q = 0.05 - 4.5 \text{ nm}^{-1}$, where $q = 4\pi \cdot \sin(\varphi/2) / \lambda$ with φ being the scattering angle. Collimation lengths of 4, 8, 12 and 16 m were chosen, respectively⁷.

Samples were kept in quartz cuvettes of QS quality (Hellma) of either 1 mm or 0.5 mm path length, which were placed in a thermostated ($25.0 \pm 0.1^\circ\text{C}$) sample-changer.

Raw data were corrected for the scattering of the empty cell. Pixel efficiency and solid angle variation were taken into account by dividing with the scattering pattern of pure water in a 1 mm cuvette. Background noise was accounted for by measurements with boron carbide (B₄C) at the sample position. The absolute scale was determined by the transmission of the water, assuming the ideal case where non-transmitted neutrons are scattered uniformly over the full solid angle of 4π and considering the Jacrot factor (6 Å (D11): 0.983 cm^{-1} ; 8 Å (D22): 1.089 cm^{-1} ; 12 Å (D22): 1.450 cm^{-1}) that accounts for the wavelength dependent forward scattering of water [82]. The reduced data obtained using either BerSANS ((in-house development of the HZB by U. Keiderling [84]) or LAMP software (in-house development of the ILL by D. Richard and M. Gonzales [140]), were always isotropic and consequently azimuthally averaged. Spectra from different configurations for each sample were merged with either no need of any scaling factor or just a scaling factor around ± 1.00 . The presented SANS curves still contain the incoherent background scattering of solvent and sample [23].

⁵D11-characteristics:

<http://www.ill.eu/instruments-support/instruments-groups/instruments/d11/characteristics/>, 02/2011

⁶D22-characteristics:

<http://www.ill.eu/instruments-support/instruments-groups/instruments/d22/characteristics/>, 02/2011

⁷V4-characteristics:

http://www.helmholtz-berlin.de/pubbin/igama_output?modus=einzel&sprache=en&gid=1706&typoid=8542, 02/2011

3.2.13.1 Scattering theory - Model independent methods

The scattering length densities (SLD) used in this work are tabulated for each component in the materials section 3.1.1. The calculation was done for each component of the oil/surfactant mixtures using the Scattering Length Density Calculator of the NIST web page⁸ according to equation (3.14), where b_{ci} is the bound coherent scattering length of each species of n atoms in a molecule, having a molecular volume v_m . The scattering length density of the nanoemulsion droplets used in model fits was calculated as an average of all scattering length densities in the formulation, weighted by their corresponding volume fraction.

$$SLD = \frac{\sum_{i=1}^n b_{ci}}{v_m} \quad (3.14)$$

For the range of $qR < 1$, the Guinier approximation can be employed according to which for the presence of individual, non-interacting particles the scattering intensity $I(q)$ depends only on the radius of gyration, R_G (eq. (3.15)) [63]. For emulsion droplets, an average sphere radius R can be obtained by the relation: $R_G^2 = 3/5 R^2$ (as in D_2O they can to first order be considered as being homogeneous). It should be noted that for polydisperse systems via the Guinier analysis a z -average for the radius of gyration is obtained.

$$\ln I(q) = \ln I(q=0) - \frac{R_G^2 \cdot q^2}{3} + I_{bkg} \quad (3.15)$$

However, the average particle size R can also be approached by using the extrapolated zero-angle intensity $I(q=0)$, which is given by the contrast ΔSLD (the difference between the scattering length densities of particle and matrix), the volume fraction Φ , and the volume of one scattering particle V_p , which can simply be used to calculate the radius of the corresponding sphere (eq. (3.16)/(3.17)).

$$\ln I(q=0) = \Phi \cdot V_p \cdot \Delta SLD^2 \quad (3.16)$$

$$R = \sqrt[3]{\frac{3}{4} \cdot \frac{I_0}{\pi \cdot \Phi \cdot \Delta SLD^2}} \quad (3.17)$$

It should be noted that for polydisperse systems the averages obtained for R differ, as by the Guinier analysis a z -average is obtained, while the value from $I(q=0)$ is a M_w -average. Accordingly the latter should always be somewhat smaller.

The invariant Q is a fundamental result of scattering theory [174], which states that independently of the structure of the system (shape, size, interactions), in a two-phase system its value

⁸Scattering Length Density Calculator
<http://www.ncnr.nist.gov/resources/sldcalc.html> , 06/2009

depends only on the volume fraction Φ and the scattering contrast ΔSLD .

$$\bar{Q}_{theo,homo} = 2\pi^2 \cdot \Phi \cdot (1 - \Phi) \cdot \Delta SLD^2 \quad (3.18)$$

The experimental invariant can be obtained by calculating the integral,

$$Q_{exp.} = \int_{q=0}^{\infty} I(q) \cdot q^2 dq \quad (3.19)$$

extrapolating the experimental data for the scattering vector q to zero and to infinity. However, for our experimental data, using respectively the Guinier and Porod approximations, which require in particular that intensity reaches or comes close to a plateau with the experimental low q region, both extrapolations to low and high q provided an empirical invariant which is in a good agreement to the theoretical one, with an error estimate of approx. $\pm 15\%$ ($\Delta Q_{extrapolation} = 10\%$; $\Delta Q_{data} = 5\%$). Differences between experimental and theoretical invariant would indicate a molecular dissolution of components.

3.2.13.2 Scattering theory - Teubner Strey model

A very useful model which is often used for the characterization of bicontinuous microemulsions is the Teubner-Strey approximation, which is based on Landau's free energy theory and Debey-Anderson-Brumberger's derivation of scattering by inhomogeneous domains [29, 186]. The scattering intensity is described by eq. (3.20), where $\langle \eta \rangle \equiv \Phi_o \Phi_w \langle \Delta SLD^2 \rangle$ and $\langle \Delta SLD^2 \rangle$ is the difference in scattering length density between oil (o) and water (w). a_2 , c_1 and c_2 are coefficients of various terms of order parameters in Landau's free energy. In the case of a microemulsion, c_1 indicates the tendency to form interfaces between different domains and is usually negative, whereas a positive a_2 favours the microemulsion formation. For a stable morphology the criterion of $4a_2c_2 - c_1 > 0$ with a positive c_2 is required [186].

$$I(q) = \frac{8 \cdot \pi \cdot c_2 \langle \eta^2 \rangle / \xi_i}{a_2 + c_1 q^2 + c_2 q^4} \quad (3.20)$$

$$\gamma(R) = \frac{\sin(\varepsilon \cdot R)}{\varepsilon \cdot R} \cdot \exp\left(-\frac{R}{\xi_i}\right) \quad (3.21)$$

The corresponding correlation function is given by eq. (3.21) and incorporates alternating regions of water and oil domains with $\varepsilon = 2\pi / D_S$ giving the quasiperiodic repeat distance (periodicity) D_S (eq. (3.23)). D_S can be associated with a peak in the SANS spectra at $2\pi/D_S$ in case of high densities and order. The number density 1N is given via the volume fraction through ${}^1N = \Phi/V = 1/D_S^3$ in case of a simple cubic packing assumption. Hence the correlation length

can also be extracted from SANS data as:

$$\xi_i = \frac{\pi}{Q} \cdot \int I(q) \cdot q \, dq \quad (3.22)$$

The correlation length ξ_i (eq. (3.24)) corresponds to a characteristic length for positional correlation, i.e. is related to a characteristic size of the structural domains contained.

$$D_s = 2\pi \cdot \left[\frac{1}{2} \cdot \sqrt{\frac{a_2}{c_2}} - \frac{1}{4} \cdot \frac{c_1}{c_2} \right]^{-1/2} \quad (3.23)$$

$$\xi_i = \left[\frac{1}{2} \cdot \sqrt{\frac{a_2}{c_2}} + \frac{1}{4} \cdot \frac{c_1}{c_2} \right]^{-1/2} \quad (3.24)$$

To describe the degree of ordering in a nano- or microemulsions the amphiphilicity factor f_a given by eq. (3.25) [152, 153] can be used, as demonstrated previously for bicontinuous microemulsions [58, 151].

$$f_a = \frac{c_1}{(4 \cdot a_2 c_2)^{1/2}} \quad (3.25)$$

The range of f_a reaches from 1 for a completely disordered solution to -1 for a superlattice which assumes in case of microemulsions a lamellar structure. When the Lifschitz line is crossed at $f_a = 0$ a peak at non zero wave vector can be observed. Therefore the amphiphilicity factor provides a useful scale for the quantification of the extent of ordering [164].

3.2.13.3 Scattering theory - Polydisperse Sphere Model with Log-normal Distribution

For emulsion systems containing homogeneous spheres, the form factor $F_{HS}(q)$ is given by eq. (3.26) through the magnitude of the scattering vector q , the sphere radius R and the difference in scattering length density $\Delta SLD = \Delta SLD_{sph} - SLD_{solv}$ of sphere and solvent. In case of polydisperse (pd) systems the form factor (eq. (3.27)) has to be averaged by a particle size distribution. This was done using a log-normal distribution $f(R, R_i, \sigma_i)$ (eq. (3.27)), where σ describes the polydispersity of a population.

$$F_{HS}(q, R) = 3 \cdot \frac{4}{3} \pi \cdot R^3 \cdot \Delta SLD \cdot \frac{\sin(qR) - qR \cdot \cos(qR)}{(q \cdot R)^3} \quad (3.26)$$

$$f_{pdS}(R, R_i, \sigma_i) = \frac{\exp\left(-\frac{\ln(R/u(R_i, \sigma_i))^2}{2v^2(R_i, \sigma_i)}\right)}{\sqrt{2\pi} \cdot Rv(R_i, \sigma_i)} \quad (3.27)$$

$$\begin{aligned} \text{with } u(R_i, \sigma_i) &= \frac{R_i^2}{\sqrt{\sigma^2(R_i, \sigma_i) + R_i^2}} \\ v(R_i, \sigma_i) &= \sqrt{\ln((\sigma^2(R_i, \sigma_i)/R_i)^2 + 1) + R_i^2} \\ \text{and } \sigma(R_i, \sigma_i) &= R_i \cdot \sigma_i \end{aligned}$$

The total scattering intensity of a polydisperse homogeneous spherical particle can be described hence by eq. (3.28), where 1N ($= N/V$) is the number density of particles and I_{Bkg} the incoherent background scattering.

$$I_{HS}(q) = \left(\frac{4\pi}{3}\right)^2 \cdot {}^1N \cdot \Delta SLD^2 \cdot \int_0^\infty f_{pdS}(R, R_0, \sigma_0) \cdot R^6 \cdot F_{HS}^2(q, R) \cdot dR + I_{Bkg} \quad (3.28)$$

In case of a bimodal lognormal distributed spherical model (BHS) a linear combination of both populations leads to eq. 18. Φ is the volume fraction of the particles, whereas A refers to the volume fraction of scattering material that is in the species with radius R_1 and $(1-A)$ to the species of radius R_2 .

$$\begin{aligned} I_{BHS}(q) = {}^1N \cdot & \left[\int_0^\infty A \cdot f_{pdS}(R, R_1, \sigma_1) \cdot F_{HS}^2(q, R) \cdot dR \right. \\ & \left. + \int_0^\infty (1-A) \cdot f_{pdS}(R, R_2, \sigma_2) \cdot F_{HS}^2(q, R) \cdot dR \right] + I_{Bkg} \end{aligned} \quad (3.29)$$

The experimental smearing (mostly determined by the spread of wavelength which in our case was given by a FWHM of 10%) was considered within the distribution function and the values given therefore refer directly to the polydispersity of the particles. Interparticle interferences were accounted for by a hard-sphere structure factor with a hard-sphere radius R_{HS} [9], using a monodisperse approximation that multiplies the size average form factor $P(q)$ with the structure factor $S(q)$, while assuming that the interaction potential between particles are spherical symmetric and independent of the particle size (eq. (3.30)).

$$I(q) = \Phi \cdot V_P \cdot P(q) \cdot S(q) \quad (3.30)$$

The interaction potential $U(r)$ for hard spheres of the diameter d and the position r_i is given pairwise by eq. (3.31):

$$U(r_i) = \begin{cases} \infty & r < d \\ 0 & r \geq d \end{cases} \quad (3.31)$$

The static structure factor $S(q) = (1 - \tilde{c}(q))^{-1}$ can be obtained in analytical form by Percus-Yevick approximation [125, 190]. $\tilde{c}(q)$ is the Fourier transform of direct correlation function $c(r)$.

A detailed algebraic solution, using the direct correlation function $c(r) = c_0 + c_1 r + c_3 r^3$ ($0 \leq r \leq 1$) and pair correlation function $g(r=1) = (r-1)(Q_0 + Q_1(r-1))$ for three dimensions with the two constants:

$$Q_0 = \frac{1 + f_P/2}{(1 - f_P)^2} \quad (3.32a)$$

$$Q_1 = \frac{1/2 + f_P}{(1 - f_P)^2} \quad (3.32b)$$

and $f_P = (\pi/6)\rho$ being the packing fraction, can be found elsewhere [127] - ρ is the particle number density.

The used structure factor S_{HS} , given in eq. (3.33f), is based on the interaction potential (eq. (3.31)) and the volume fraction f_P of the assumed dissolved spherical aggregates.

$$A = 2qR_{HS} \quad (3.33a)$$

$$\alpha = \frac{(1 + 2f_P)^2}{(1 - f_P)^4} \quad (3.33b)$$

$$\beta = -6f_P \frac{(1 + f_P/2)^2}{(1 - f_P)^4} \quad (3.33c)$$

$$\gamma = \frac{f_P \cdot \alpha}{2} \quad (3.33d)$$

$$c(q, R_{HS}, f_P) = \alpha \frac{\sin A - A \cos A}{A^2} + \beta \frac{2A \cdot \sin A + (2 - A^2) \cos A - 2}{A^3} \quad (3.33e)$$

$$+ \gamma \frac{-A^4 \cos A + 4[(3A^2 - 6) \cos A + (A^3 - 6A) \sin A + 6]}{A^5}$$

$$S_{HS}(q, R_{HS}, f_P) = \frac{1}{1 + 24f_P \cdot \frac{c(q, R_{HS}, f_P)}{qR_{HS}}} \quad (3.33f)$$

Besides the data treatment with mono- and bimodal polydisperse spherical models, we also employed the identical polydisperse model for a core-shell form factor, thereby accounting for the slight differences in scattering length density between surfactant shell and oil. However this model did not yield substantially improved fits of the experimental data and also had no systematic impact on the final fit parameters.

3.2.13.4 Scattering theory - Polydisperse Disk Model with Log-normal Distribution

For surfactant systems containing a collection of cylindrical particles (as given for disk-like structures), the form factor $F_{disk}(q)$ is given by eq. (3.34) through the magnitude of the scattering vector q , the total volume fraction of the dispersed material Φ , the disk-radius R_d , its thickness D the difference in scattering length density $\Delta SLD = \Delta SLD_{disk} - SLD_{solv}$ of disk and solvent. In case of polydisperse (pd) systems the form factor (eq. (3.34)) has to be averaged by a particle size distribution. This was done using a log-normal distribution $f(R, R_0, \sigma)$ (eq. (3.27)), where σ describes the polydispersity of a population.

The total scattering intensity of a polydisperse homogeneous cylindrical particle (disk) can be described hence by eq. (3.35), where ${}^1N (= N/V)$ is the number density of particles and I_{Bkg} the incoherent background scattering.

$$F_{disk}(q, R_d, D) = 16(\pi R_d^2 D)^2 \Delta SLD^2 \cdot \int_0^1 \left(\frac{J_1 \left(q R_d \cdot \sqrt{1 - \Phi^2} \right) \sin(q D \Phi / 2)}{q^2 R_d \sqrt{1 - \Phi^2} D \Phi} \right)^2 d\Phi \quad (3.34)$$

$$I_{disk}(q) = \int_0^\infty \left({}^1N \cdot F_{disk}(q, R_d, D) \right) f_{pdS}(R, R_0, \sigma_0) dR + I_{Bkg} \quad (3.35)$$

$$\text{with } {}^1N = \frac{\Phi}{\int_0^\infty \pi R_d^2 D \cdot f_{pdS}(R, R_0, \sigma_0) dR} \quad (3.36)$$

3.2.14 Small-Angle X-Ray Scattering (SAXS)

SAXS experiments have been carried out at the ID02-beamline of the ESRF, where we measured fast reaction kinetics using SAXS coupled to a stopped flow rapid mixing apparatus. Detailed information about the stopped flow technique can be found in section 3.2.12.

In SAXS experiments photons are provided by an electron beam that is accelerated close to the speed of light and then forced into a bent trajectory. In case of the ESRF, the electron beam is held in a circular particle accelerator in which the magnetic field (to turn the particles so they circulate) and the electric field (to accelerate the particles) are carefully synchronised with the travelling particle beam, hence the name synchrotron. The electrons are initially accelerated via a 200 MeV Linac and a 6 GeV synchrotron booster. Then they are injected into the storage ring at 10 Hz to keep the charging times short in comparison to the beam lifetime [128].

Inside the storage ring the particle energy is kept constant, acceleration is only done to compensate radiation losses. The X-rays are produced at the bending magnets or at special insertion devices (ID) of a few meters length where the magnetic field is rotated every few centimetres.

The ID02 beamline is located at a high- β section of the storage ring. Two undulators U21.4 and one U35 provide high photon flux with a low divergence. Only the central radiation cone of the undulator is used. Unless otherwise stated, all beam sizes correspond to 2.35-values (FWHM). The beamline optics consist of a cryogenic (liquid nitrogen) cooled Si-111 channel-cut monochromator and a focusing toroidal mirror. The standard beam size is $200 \mu\text{m} \times 400 \mu\text{m}$ (vertical and horizontal, respectively) with divergence of $20 \mu\text{rad} \times 40 \mu\text{rad}$. The beamline is optimised for experiments using a fixed wavelength around 0.1 nm (12.4 keV), but a wavelength range between 0.073 nm and 0.16 nm is accessible. There are two separate experimental stations one for combined SAXS/WAXS and the other for USAXS measurements. The maximum photon flux at the sample position is of the order of 10^{14} photons/sec/100 mA with $\Delta\lambda/\lambda = 0.015 \%$ at 12.4 keV [2].

The SAXS-setup consists of different slits along the beamline due to beam-collimation (not shown in the scheme of fig. 3.14). Two guard slits are located directly before the sample. Usually the slit apertures are set to twice the full width at half maximum (2 x FWHM)

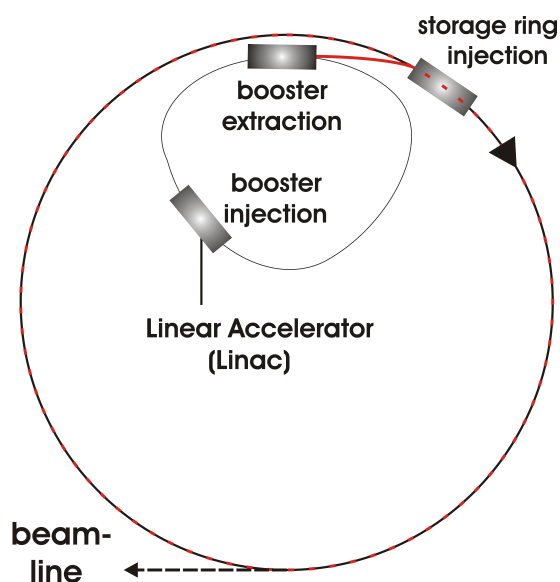


Figure 3.13: Synchrotron-layout of the ESRF, taken from source [128].

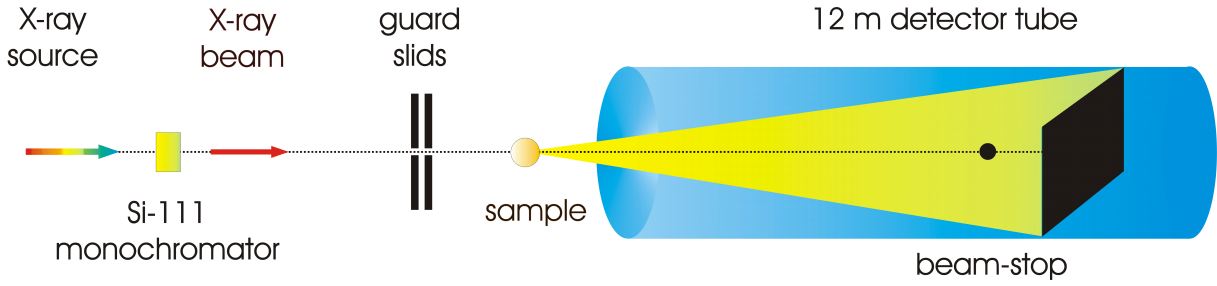


Figure 3.14: General setup of a Small-Angle-X-Ray-Scattering (SAXS).

of the focused monochromatic beam. The slits confine the region around the primary beam in which diffuse parasitic scattering from the optics is visible. This defines the minimum size of the beamstop and the minimum observable scattering angle.

The SAXS detector is mounted on a wagon inside the 12 m detector tube. The sample-to-detector distance can be varied from 1 m to 10 m covering a wide scattering wave vector q -range, $6 \cdot 10^{-3} \text{ nm}^{-1} < q < 6 \text{ nm}^{-1}$, where $q = (4\pi/\lambda) \cdot \sin(\Theta/2)$, with λ the wavelength ($\sim 0.1 \text{ nm}$) and Θ the scattering angle. The q resolution limited by the beam divergence ($\sim 25 \mu\text{rad}$) and size ($\sim 100 \mu\text{m}$) is about $3 \cdot 10^{-3} \text{ nm}^{-1}$. However, the smallest q reachable at 10 m detector distance is also limited by the detector point spread function and the parasitic scattering to about $6 \cdot 10^{-3} \text{ nm}^{-1}$. In normal operation, q is further curtailed to about 0.008 nm^{-1} due to the parasitic background and limited dynamic range of the detector. More detailed information about the beamline layout can be found elsewhere [3].

SAXS-data reduction was processed using the online data processing software provided by the ID02-beamline. The raw data is corrected for detector imperfections (subtraction of dark current and readout noise, division by flatfield, and spatial distortion correction) and normalized to absolute scattering intensities. The 2D spatial coordinates are transformed to polar coordinates and azimuthally integrated to obtain 1D scattering profiles as a function of scattering vector. Only the background of the solvent (water) had to be subtracted additionally by us. For further SAXS-data treatment (averaging, background subtraction... *etc.*) the SAXS-utilities program [181] was used.

SAXS-data analyses were proceeded similarly as for SANS, except that the scattering length density was calculated due to x-ray properties. For x-rays the scattering length density SLD_{SAXS} is given by a slight variation of equation (3.14) as the scattering is only due to electrons that are all identical. Hence, the x-rays scattering length density can be obtained by replacing b_c values by the expression of $Z \cdot r_e$, where $r_e = 2.81 \cdot 10^{-5} \text{ \AA}$ is the classical radius of the electron and Z the atomic number of the i^{th} atom in the molecular volume v_m .

$$SLD_{\text{SAXS}} = \frac{\sum_{i=1}^n Z \cdot r_e}{v_m} \quad (3.37)$$

Chapter 4

Low Energy Emulsification of Nanoemulsions

The surfactant aided dispersion of oil in water (or vice versa) often leads to the formation of more or less stable emulsions, where the size of the dispersed droplets is typically in the range of 0.1-10 μm [184]. They are thermodynamically unstable; i.e. will undergo macroscopic phase separation, where the time for this process to take place depends largely on the quality of kinetic stabilisation provided by the surfactant [185]. However it is also possible to form smaller sized emulsions in the size range of 10-200 nm, so-called nanoemulsions [35, 116, 168]. They often exhibit remarkably high kinetic stability, being relatively stable with respect to coalescence and Ostwald ripening [185], which renders them interesting for a variety of applications [183]. Of course, in general nanoemulsions are prone to Ostwald ripening but their frequent long-time metastability indicates that this process is often effectively slowed down. In addition, due to their small size they are intrinsically stable against creaming or sedimentation [20]. Typically such nanoemulsions are produced by high-energy input methods, such as high-pressure homogenisation or ultrasonic treatment [13, 18, 179, 187, 197, 199, 204]. However, apart from being energy intensive, such methods could also be damaging for sensitive ingredients (e.g. biomolecules, active agents, drug molecules, etc.) incorporated in such formulations. Therefore a highly interesting approach to the production of such finely dispersed emulsions is by means of low energy input methods, which are very appealing both from a fundamental scientific point of view but also for many applications, where nanosized dispersions of an oil in water or vice versa can be achieved by a simple preparation method.

In the following we investigated such nanoemulsions formed by means of the phase inversion concentration (PIC) method. The aim of these investigations was to correlate the phase behaviour of the surfactant/oil mixture as a function of water dilution with the ability to form nanoemulsions and also with the structure of the formed nanoemulsion droplets.

4.1 Studies of nanoemulsion formation by low energy phase inversion concentration (PIC) method

Classically the formation of nanoemulsions using low energy emulsification procedures was done by the method of phase inversion temperature (PIT) [155, 161, 162, 195], where typically one starts from a water-in-oil (W/O) microemulsion at high temperature and enters into a long time stable oil-in-water (O/W) nanoemulsion below the PIT by a rapid cooling process (1.1.3.2 - PIT). More recently an analogous strategy has been devised by the phase inversion concentration (PIC) method [90,98, 112, 146, 168]. In particular, the PIC method is very appealing from a practical point of view as it only involves a simple dilution with a solvent (typically water) to produce the nanoemulsion (1.1.3.2 - PIC).

While nanoemulsions are not thermodynamically stable systems, they can exhibit quite long term stabilities. The reasons for this are still largely unexplored with respect to the oil-surfactant composition required and the pathway of formation.

In the following, the PIC emulsification procedure is examined, especially with respect to the structural details of the nanoemulsion formation process and the aspects relevant for their stability, which are still poorly understood.

Our studies are based on a commercially available oil/surfactant (O/S) mixture, consisting of diethylhexyl carbonate, phenoxy ethanol, polyglyceryl-4 laurate and dilauryl citrate (Tego[®] Wipe DE) (e.g also section of sample preparation 3.1.2 and ingredients of oil/surfactant mixture Tego[®] Wipe DE in section 3.1.1.1). The system has been described previously [108] and forms o/w-nanoemulsions at a certain oil/water ratio, presumably due to the change of interfacial composition during dilution.

The aim of our study was to extend this phenomenological study in a more systematic and comprehensive way, in order to understand nanoemulsion formation by the PIC method from a fundamental point of view. For that purpose we studied the overall phase behaviour as a function of the addition of water, complemented by measurements of electric conductivity and viscosity. Particular emphasis was given to a detailed mesoscopic structural characterization of the PIC system and its structural evolution over the full range of dilution. Accordingly in our investigation we varied the oil/water-ratio concentration in the transitional composition range, i.e. dilutions less than those required to form nanoemulsions, and the more dilute region of the nanoemulsion. For that purpose the structure was determined by means of turbidity measurements, small-angle neutron scattering (SANS) and cryogenic-transmission electron microscopy (cryo-TEM).

4.1.1 Phase behaviour

As a first step we characterised the phase behaviour of the commercially available oil/surfactant mixture (Tego[®] Wipe DE, composition see section 3.1.1.1) as a function of the added amount of water at 15.0, 25.0, and 40.0 ± 0.1 °C which is depicted in fig. 4.1.

It should be noted that the phase characterisation given here does not refer to a proper phase diagram, because of the metastable properties of nanoemulsions. Therefore the "phases" depicted here are not really thermodynamically stable, but instead just more or less long time metastable states. Accordingly the samples were inspected after 2 and 10 days thereby giving the appearance of the samples at time scales relevant to our experiments. However, it should always be kept in mind that, depending on the location in the phase diagram, samples could still be evolving and changing substantially with time. In fact this can also be seen in the shift of the multiple phase regions that become larger with temperature and time, which can be attributed to the already mentioned metastability of nanoemulsions. Although the influence of temperature is greater than that of the time-dependence, both are controlling ageing processes like coalescence and Ostwald ripening (section 1.1.1). However, at room temperature and below these processes are slowed down.

Addition of water to the oil phase leads at first (< 10% H₂O) to a complete incorporation of the water by the surfactant/oil mixture via molecular dissolution, forming a clear, slightly bluish inverse microemulsion (fig. 4.1 and 4.6). At higher water content the system becomes biphasic, containing the initial microemulsion in an upper phase (becoming more turbid with increasing water content), and a lower clear water excess phase. Around 50 wt% water content, a microemulsion-like single phase is observed that shows macroscopic phase separation after sev-

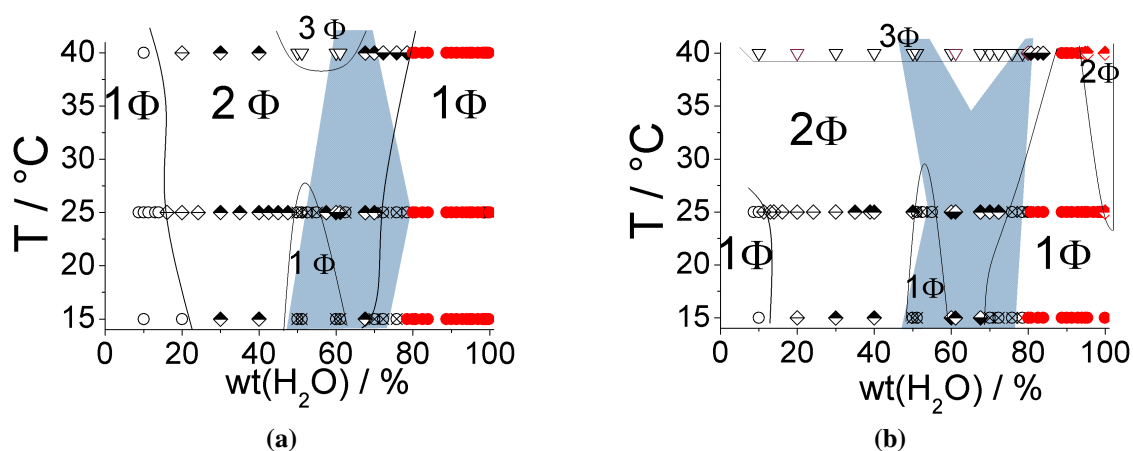


Figure 4.1: Phase behaviour of the oil/surfactant mixture as a function of water concentration, at various temperatures (15.0, 25.0, 40.0 ± 0.1 °C) taken after 2 (a) and 10 (b) days of preparation, shaded areas showed flow birefringence -in biphasic case: observed in upper phase (1Φ: ○ - clear, ⊗ - μE, ● - NE; 2Φ: ◇ - clear, ◆ - upper Φ, ◊ - lower Φ (more turbid); 3Φ: ▽)

eral weeks (which might be due to chemical degradation of the citrate surfactant).

As a rule the higher the water content the slower this process is up to a maximum amount of 60 wt% H₂O. The adjacent biphasic region at higher water content differs largely with respect to its visual appearance insofar as both phases appear bluish and are of similar turbidity (fig. 4.2) (measurements of the separated phases were only performed when adequate volumes were available, i.e. above ~25% of the total volume).

Generally the upper phases are more turbid than the lower phases, and they

become clearer with increasing water concentration. This happens until the phase inversion concentration (PIC) is reached (H₂O > 75%) and leads to single, slightly blue shining, milky nanoemulsions (NE). As indicated in fig. 4.2 further dilution to 90% H₂O enhances the turbidity strongly and can be correlated to the NE-evolution (see also section 4.1.2.2). Additional dilution leads to a clearing of the nanoemulsion due to the decreasing volume fraction of dispersed material. As already mentioned, before forming nanoemulsions, a more or less broad area of bluish microemulsions is passed in the H₂O-range of > 55 - 78.5 wt%, that shows flow birefringence. In that context it must be noted that this "1Φ NE" region is not a thermodynamically stable single phase region. After several months one will observe a macroscopic phase separation with an oil phase on top of the aqueous solution. This means that this system is an emulsion and due to its small size (see section 4.1.2) a nanoemulsion by definition. However, the structural evolution occurs rather slowly as shown in fig. A.5 and so apparently this nanoemulsion is kinetically very stable. This flow birefringence (shaded area in fig. 4.1) occurs in the single phases as well as in the upper phases of the biphasic samples and has either to be correlated to a non-spherical shape of the aggregates [39] or to the more likely presence of an L3-phase [32, 76, 130]. In general, it has been found that nanoemulsions are frequently formed by passing a bicontinuous microemulsion or a liquid crystalline lamellar phase [113] during the preparation process and this observation has in particular been detailed for the case of the PIT method [37, 45, 195]. It should further be mentioned that for nonionic surfactants also lamellar liquid crystals [169] and for ionic surfactants cubic liquid crystals [129] have been inferred to be relevant in order to yield robust nanoemulsions via the PIC-method (sometimes also referred as Emulsion Inversion Point method, EIP [49]; or Phase Inversion Composition

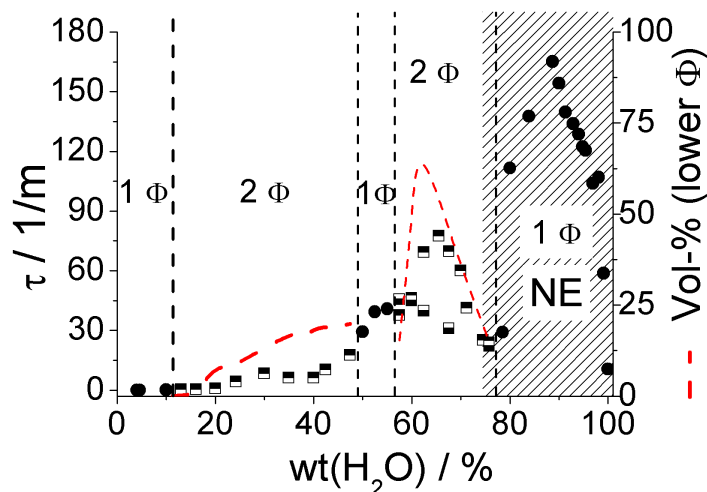


Figure 4.2: Turbidity coefficient τ at 626 nm of the composition-dependent UV-VIS measurements (dots) for O/S-mixtures as a function of water concentration and 25 ± 0.1 °C; and corresponding volume fraction (Vol-%) of the lower phases (dotted line) in the biphasic region (the shaded area is the nanoemulsion (NE))
1Φ: ●, 2Φ: ■ upper and ■ lower phase.

method, PIC [206]). All these structures have one characteristic in common in that they allow for a reversion of the sign of the curvature for the oil-water interfacial film. This phenomenon culminates in a complete overall structural inversion from having an oil-continuous system or vice-versa, which then leads to the formation of nanoemulsion droplets in the dispersed phase. Simultaneously the interfacial tension between oil and water passes through a minimum thereby enabling the formation of very small emulsion droplets [183].

The viscosity and conductivity measurements by Meyer et al. [108] of mixed solutions in the inhomogeneous region and our phase separated studies showed a similar behaviour when forming nanoemulsion by the PIC method compared to the PIT one [6, 43, 80]. In the case of PIT-nanoemulsions the formation process can be traced back to the change of solubility of polyoxyethylene-type surfactants (change of HLB value with temperature), whereas in case of PIC-nanoemulsions the relative amount of surfactant present in the water phase increases with dilution, thereby modifying the composition of the amphiphilic monolayer at the oil/water interface (eg. also section 4.5 to the PIC-mechanism).

Both methods take advantage of the extremely low interfacial tension (10^{-2} - 10^{-6} N/m [173]) at the phase inversion temperature [155, 158, 161] or phase inversion concentration [40, 66, 189, 200]. The value of the interfacial tension between the undiluted O/S-mixture and water as the continuous phase was measured to be 0.0175 mN/m by the spinning drop method (section 3.2.8). This value is rather low and would be typical for microemulsion forming systems [178]. However, in direct comparison, the first viscosity maximum at ≈ 52.5 wt%(H₂O) (fig. 4.3a) seems to indicate the transition of a droplet type to a bicontinuous microemulsion, as for classical microemulsions such a maximum of viscosity in the region of this structural transition is typically observed [56, 136]. The following biphasic area is caused by a morphological change

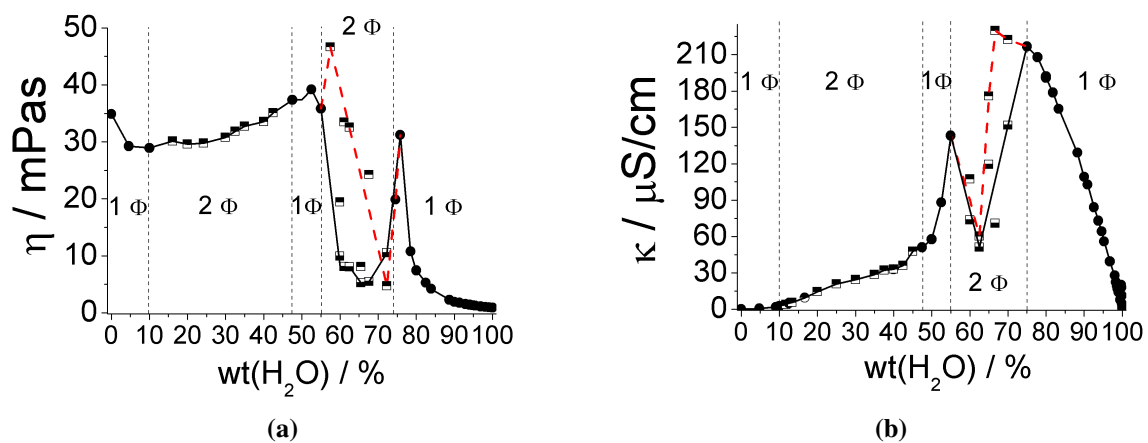


Figure 4.3: Dynamic viscosity η (a) and electric conductivity κ (b) measurements as a function of water concentration (TW+H₂O) at 25 ± 0.1 °C in respect to biphasic regions (for adequate volumes $> \sim 25$ Vol-%) - 1 Φ : ●, 2 Φ : □ upper and ▣ lower phase.

that can be due to the bicontinuous structure and is typically accompanied by a viscosity minimum [207]. In the region of the viscosity maximum the electrical conductivity (fig. 4.3b) passes through a pronounced maximum which peaks exactly at the point where the system becomes monophasic. Both observations indicate the presence of a bicontinuous structure of high connectivity at the phase boundary. The bicontinuous structure of the single-phase region around 50 wt%(H₂O) was further corroborated by cryo-TEM images, one example of which is shown in fig. 4.4.

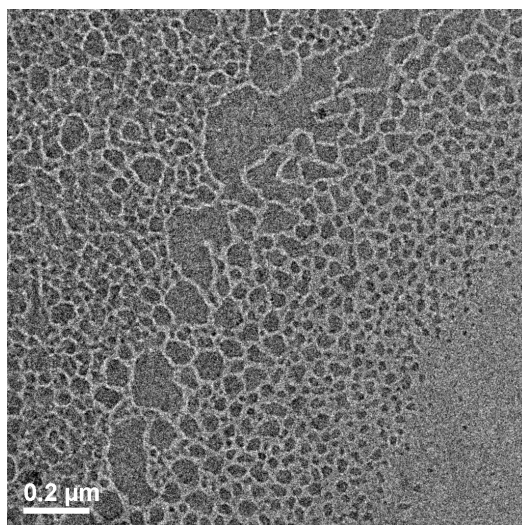


Figure 4.4: Cryo-TEM¹ image for a sample diluted to 50 wt% of water (TW+H₂O)

4.1.2 Structural Characterisation

After having studied the more general aspects of macroscopic phase behaviour during stepwise nanoemulsion formation, we were then interested in determining the mesoscopic structure of the respective samples in order to establish a correlation between structure and macroscopic phase behaviour. For this purpose we employed UV/Vis-spectroscopy, SANS, and cryo-TEM. Of course, our systems being metastable, one has to worry about their changes as a function of time. For the case of the nanoemulsion range we ascertained by long-time turbidity measurements (see fig. A.5) that no significant structural changes take place during our typical experimental time window of 2-5 days.

4.1.2.1. UV/Vis-Transmittance measurements of nanoemulsion region

Turbidity measurements have been performed for nanoemulsions with oil/water ratios of 80, 85, 90, 95 and 98% H₂O (fig. 4.5a). From the value of the turbidity τ we calculated the molecular weight Mw of the colloidal particles according to equation (3.5) [69] and converted this

¹cryo-TEM image by C.M. Marino (UD, USA)

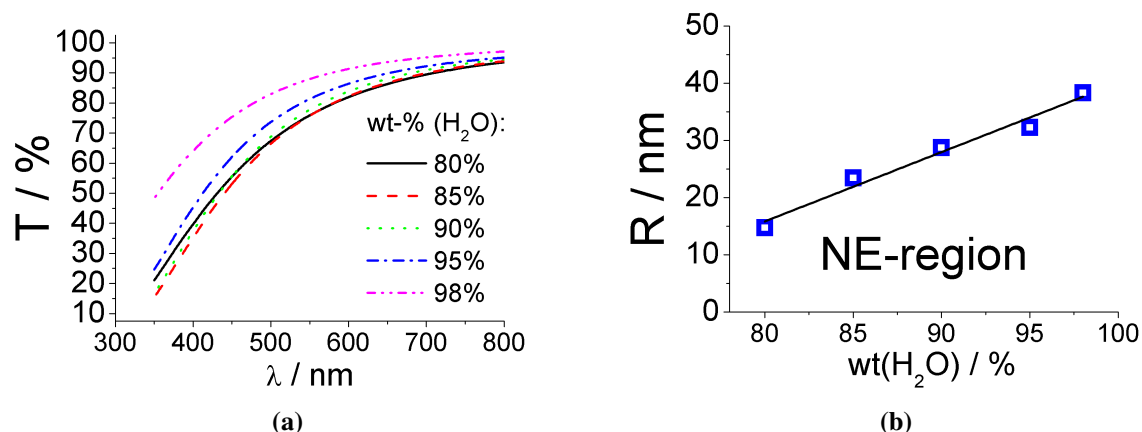


Figure 4.5: UV/Vis-transmittance spectra (a) and corresponding radii R (b) for oil/water solutions in the nanoemulsion region (> 75% H₂O) using 0.5 mm cells at 25.0 ± 0.1 °C - radii are averaged values of seven different wavelengths (350, 400, 500, 600, 626, 700, 800 nm)

value to obtain an approximate particle size R for spherical particles by equation (3.6). Calculations have been done for seven different wavelengths λ (350, 400, 500, 600, 626, 700, 800 nm), but we considered only transmission values above 80% and ascertained by comparing the values for different wavelengths that effects from multiple scattering were negligible (see also tab. A.6). The results show good agreement for all wavelengths and the mean of the turbidity τ has been used to calculate the molecular weights Mw and particle sizes R(Mw) of the oil droplets (fig. 4.5b), and the surfactant (S) head group area $a_h(S)$ (eq. (4.1)) - summarized in table 4.1. For the calculation of the surfactant head group area $a_h(S)$, c_S is the surfactant concentration.

$$a_h = \frac{3 \cdot c_g}{c_S \cdot N_{Av} \cdot \rho \cdot R(M_W)} \quad (4.1)$$

The typical size of the nanoemulsion droplets is bigger than 20 nm, whereas the required space of the surfactant head groups $a_h(S)$ is below 0.5 nm² (table 4.1). The particle size increases with water concentration, following a more or less linear relation (fig. 4.5b). This size increase with increasing dilution can be attributed to the fact that the relatively hydrophilic surfactant will become increasingly dissolved in the aqueous phase upon increasing dilution. Accordingly, the average particle size of emulsion droplets formed has to increase. As the scattering intensity is size dependent, one obtains a mass-average, i.e. in a broad distribution the bigger particles dominate the scattering. Of course, it must be stated here that these numbers have to be taken with a grain of salt, as in this analysis we completely neglect the fact that according to the proposed PIC mechanism a part of the oil/surfactant mixture should become dissolved into the water phase. Accordingly the real concentration c_g of dissolved aggregates should be smaller and therefore the radii and head group areas deduced have to be seen as lower and upper limits

| H ₂ O / % | Mw / 10 ⁷ g/mol | R(Mw) / nm | a _h / nm ² |
|----------------------|----------------------------|------------|----------------------------------|
| 80 | 0.76 | 14.7 | 0.804 |
| 85 | 3.08 | 23.4 | 0.505 |
| 90 | 5.66 | 28.7 | 0.412 |
| 95 | 8.05 | 32.2 | 0.367 |
| 98 | 13.5 | 38.3 | 0.309 |

Table 4.1: Average molecular weight Mw, particle radius R(Mw), and surfactant head group area a_h in the nanoemulsion region (> 75wt% H₂O) obtained by UV/Vis-transmittance measurements - calculated via eq. (3.6) & (4.1)

with respect to the real values. Therefore the rather low values deduced for a_h(S) are due to a reduction of the number of surfactant molecules at the interface of the nanoemulsion droplets, i.e., a lower value of c_S (as with increasing dilution increasing amounts of the surfactant are monomerically dissolved). For that reason one observes for the apparent a_h only values of 0.3-0.5 nm² while for surfactants with such head groups as in our case one would expect values of 0.4-0.6 nm² [144].

4.1.2.2. Small-Angle Neutron Scattering (SANS)

To observe the concentration dependent structural changes of the oil-water system in more detail SANS measurements were carried out, after storing the mixed samples for ten days at 25.0 ± 0.1 °C. The scattering curves for various water contents are depicted in fig. 4.6.

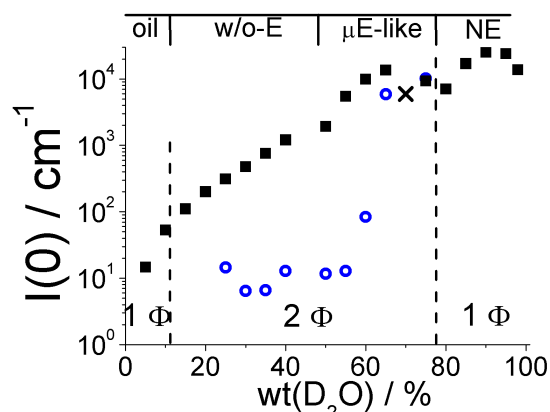


Figure 4.7: Initial intensities I(0) for different water conc. (values refer to H₂O) - after ten days of storage at 25.0 ± 0.1 °C. Phase separated measurements were performed only in case of having adequate volumes available. For the case of 70% D₂O it could not be avoided to measure a mixed sample, as phase separation could not be achieved ■ upper or single phase, ○ lower phase, × mixture

The intensity I(0) at q = 0 was extrapolated by the Guinier approximation and the obtained values (fig. 4.7) show a continuous increase of scattering intensity with increasing dilution until this effect levels off at high dilution (~ 80 wt% water). This demonstrates that the structural size increases with increasing dilution. It is interesting to note that for the biphasic systems the scattering intensity is always substantially lower for the lower, water-rich phase. The scattering of the upper phase is related very systematically to that of the single-phase regions, while the lower phase is mostly an excess water phase. Moreover, for the upper phase as well as for the single phase samples one observes a correlation peak (absent only for very low and very high water content), while the lower phase shows a much lower scattering intensity with a pronounced increase at low q that may arise from dispersed oil droplets (due to incomplete phase separation) that have not yet phase separated from the lower

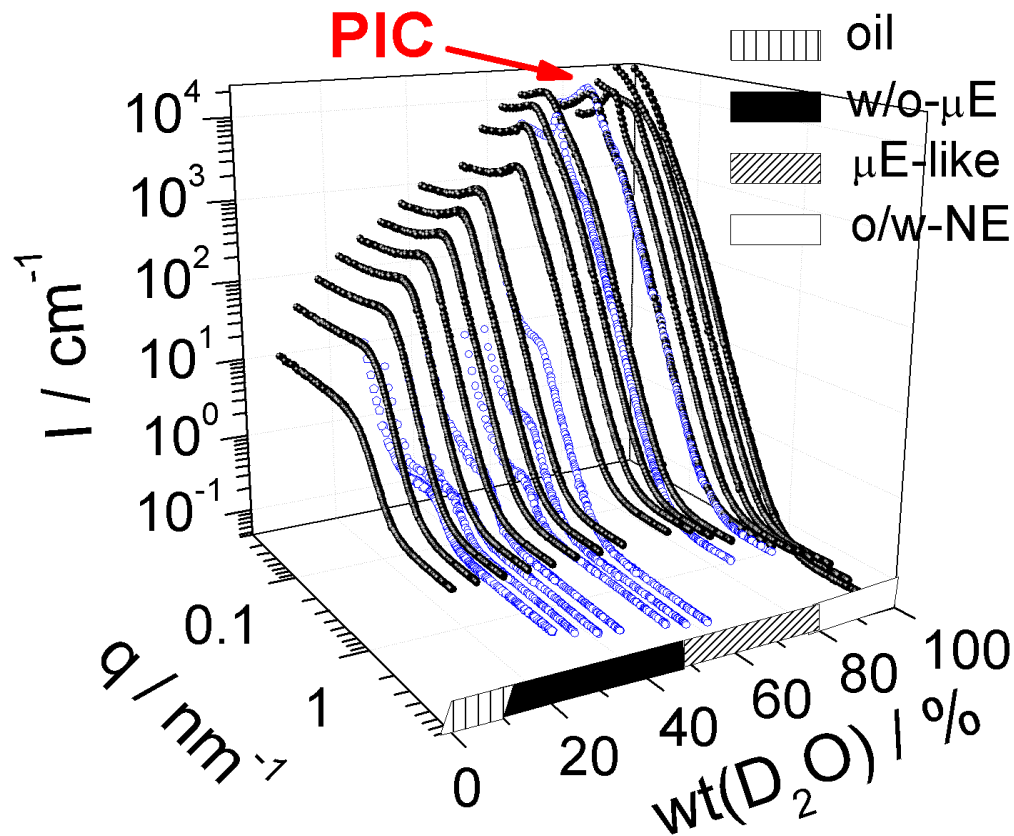


Figure 4.6: SANS-measurements of the oil-water system at different D_2O contents (water conc. refers to the equivalent concentration of H_2O) after ten days of storage at 25.0 ± 0.1 °C (surfactant/oil mixture about one year old). Measurements for phase separated samples were performed only in case of having adequate volumes available - ●: upper or single phase, ○: lower phase

phase (leading to q^{-4} Porod-scattering; fig. 4.8). In summary, this clearly demonstrates that in this 2-phase region the surfactant is primarily in the upper phase and forming a dense microemulsion there. Looking at fig. 4.7 it becomes obvious that, depending on the location in the phase diagram, different tendencies for the structural evolution are present. In the w/o-region (very low water concentration and upper phase) the water droplets become continuously bigger. The lower phase seems to contain small o/w- μE structures (see simulation 4.8b to lower phases of the scattering curves in the biphasic region 4.8a) that stay more or less constant in size before becoming much bigger at concentrations beyond 60% water. Beyond this point a sponge-like microemulsion is present as evidenced by the electrical conductivity (fig. 4.3b) and cryo-TEM (fig. 4.4). The scattering behaviour of the upper and lower phases coincide around the phase inversion concentration (PIC) (fig. 4.7).

A quantitative analysis of the scattering patterns was done using the Teubner-Strey model [186], which yields, as structural parameters, the domain size D_s (eq. (3.23)) and the correlation length ξ_i (eq. (3.24) -compare also TS-theory in section 3.2.13.2. All scattering curves could be described well with this empirical model and the deduced parameters are summarised in fig. 4.9 and tables A.7 and A.8. Ideally, for highly ordered systems (represented by the amphiphilicity

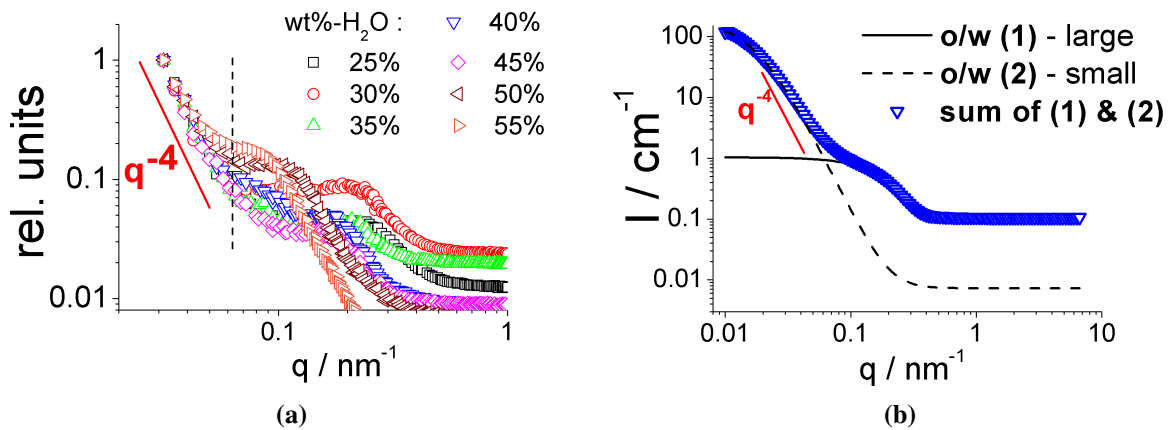


Figure 4.8: **a** Lower phases of scattering curves in the biphasic region (eg. fig. 4.6) have been normalised to a maximum intensity of 1 cm^{-1} respectively; **b** theoretical simulation (polydisperse Log-normal distributed spherical model) of a scattering curve consisting of two populations (large and small o/w droplets), observed q^{-4} dependence in Porod regime evidences assumptions of small o/w-droplets in the lower phase with bigger dispersed remainings of the upper one.

factor f_a (fig. 4.9b), the peak position describes the domain size (alternation of oil and water phases), and the peak width is connected with the correlation length. If the evolution of the domain size D_s (fig. 4.9a) is compared with a simple 3-dimensional dilution law (assuming to dilute particles of constant size for which a mean spacing D is given by eq. (4.2), where Φ is the volume fraction of the particles), a pronounced deviation appears shortly before the phase inversion, i.e., where the nanoemulsion is formed.

$$D \sim \frac{1}{\sqrt[3]{1 - \Phi}} \quad (4.2)$$

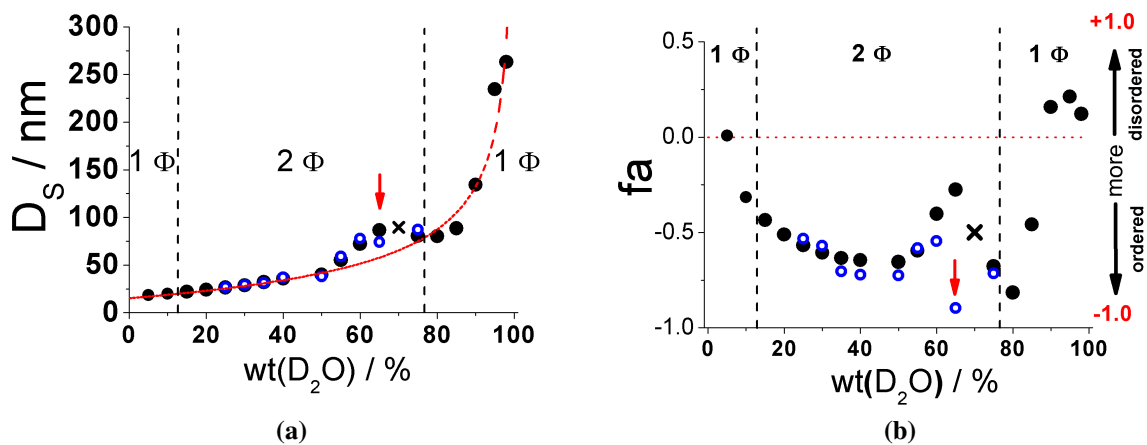


Figure 4.9: Periodic distance D_s compared to a - - - 3-dim. dilution law (eq. (4.2)) **(a)** and amphiphilicity factor f_a **(b)** of the Teubner-Strey model as obtained from SANS as a function of water concentration (values refer to H_2O conc.). Arrows indicate the occurrence of the more ordered phase. (● upper or single phase, ○ lower phase, × mixture).

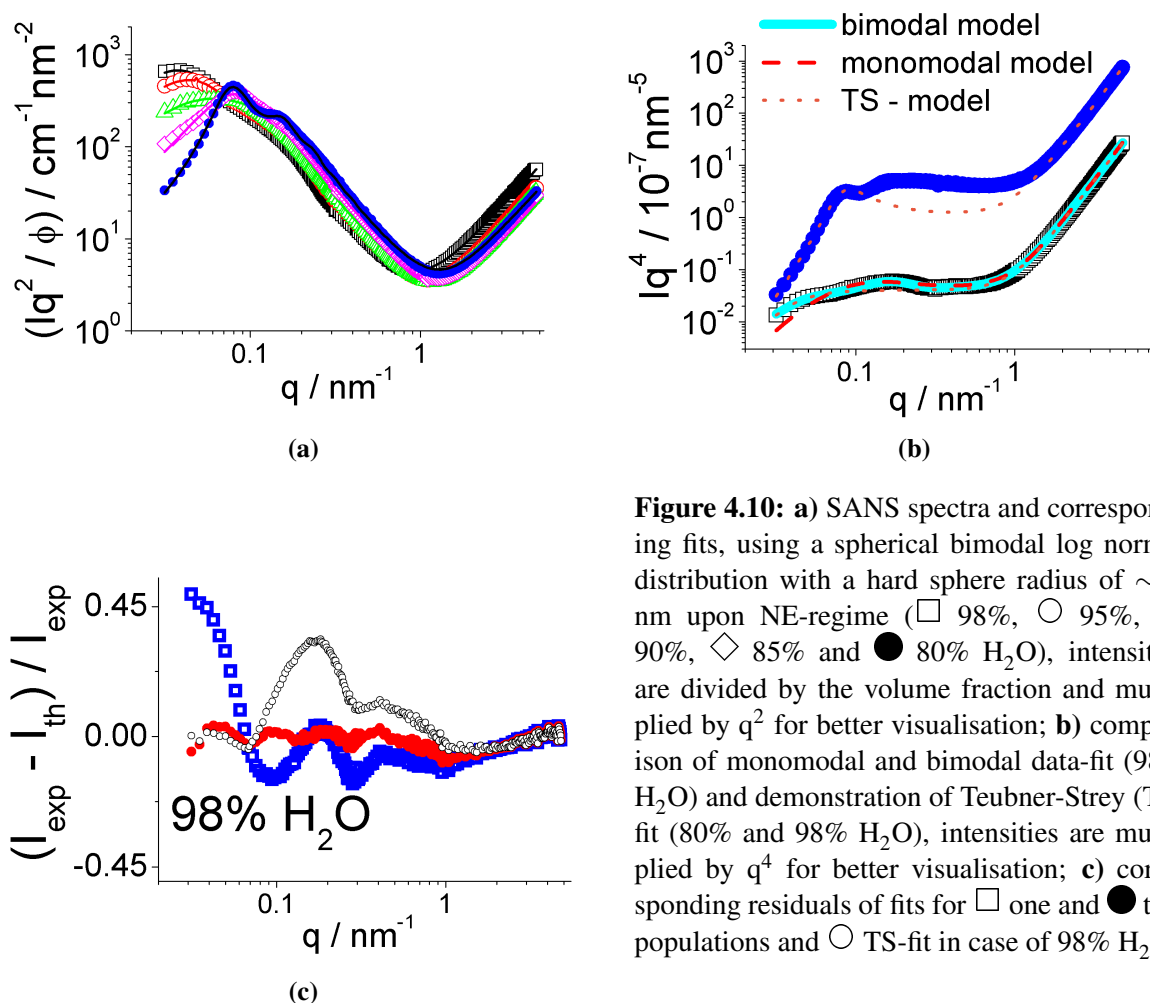


Figure 4.10: **a)** SANS spectra and corresponding fits, using a spherical bimodal log normal distribution with a hard sphere radius of ~ 39 nm upon NE-regime (\square 98%, \circ 95%, \triangle 90%, \diamond 85% and \bullet 80% H₂O), intensities are divided by the volume fraction and multiplied by q^2 for better visualisation; **b)** comparison of monomodal and bimodal data-fit (98% H₂O) and demonstration of Teubner-Strey (TS) fit (80% and 98% H₂O), intensities are multiplied by q^4 for better visualisation; **c)** corresponding residuals of fits for \square one and \bullet two populations and \circ TS-fit in case of 98% H₂O.

The deviations around 60-70 wt% (H₂O) (fig. 4.9a and 4.9b, particularly evident for the amphiphilicity factor f_a) correlate with the formation of a bicontinuous microemulsion of a high degree of ordering (fig. 4.9a). Going through a bicontinuous region might be required in order to induce the phase transition - shown also by the very distinct physical behaviour (fig. 4.3) in this region. The nanoemulsion formation then occurs by a phase inversion above 75% water concentration. Samples close to the phase boundary with around 75% water content vary sometimes in their appearance between single or biphasic behaviour, but the structure for the biphasic and monophasic cases are basically identical as seen from the SANS curves (fig. 4.6). In the range before phase inversion (60-75 wt% H₂O) the system shows the highest extent of ordering before further dilution increases disorder due to the growth of the nanoemulsion droplets, which was similarly observed by Gutiérrez et al. in the case of inversed nanoemulsions [132]. At this point it should be noted that the obtained parameters of the Teubner-Strey model (neglecting the q^{-4} dependence at small q) of the lower phases are very similar to those of the upper ones, despite the fact that the scattering intensities are largely different. The SANS spectra for the nanoemulsion range are shown in more detail in fig. 4.10a and they are divided by the volume fraction of the oil/surfactant mixture. By doing so one observes that this normalised scattering intensity increases with increasing dilution. Assuming that in this range nanoemulsion droplets are present, apparently their size increases; in agreement with the observations made by tur-

| wt(H ₂ O) | A | R _{1,Mw} | R _{1,N} | σ ₁ | R _{2,Mw} | R _{2,N} | σ ₂ | R _{1/2,Mw} (I0) | N ₁ / N ₂ |
|----------------------|------|-------------------|------------------|----------------|-------------------|------------------|----------------|--------------------------|---------------------------------|
| % | | nm | nm | | nm | nm | | nm | |
| 80 | 0.92 | 12.7 | 9.71 | 0.47 | 31.6 | 25.3 | 0.04 | 15.8 | 210 |
| 85 | 0.72 | 14.3 | 11.1 | 0.41 | 32.0 | 25.6 | 0.17 | 20.4 | 31.0 |
| 90 | 0.56 | 14.8 | 11.6 | 0.39 | 32.8 | 26.0 | 0.31 | 25.6 | 14.4 |
| 95 | 0.38 | 15.4 | 12.2 | 0.32 | 35.6 | 27.0 | 0.45 | 34.8 | 6.49 |
| 98 | 0.28 | 16.0 | 12.7 | 0.32 | 39.4 | 29.1 | 0.49 | 41.3 | 4.72 |

Table 4.2: Fit parameters amplitude A, mass- (Mw) and number-weighted (N) radii R and polydispersity indices σ_1 and σ_2 for populations 1 and 2, respectively - using a Log normal distributed spherical model for two populations; in addition mass weighted radius of both size distributions $R_{1/2,Mw}(I0)$ and ratio N_1 / N_2 of the number of droplets in population N_1 and N_2 . Exact SLDs and volume fractions are given in table 4.15 of section 4.5.1.3.

bidity measurements (fig. 4.5b). At low q one sees that with increasing concentration of the oil/surfactant mixture a repulsive structure factor becomes more prominent, and for higher concentrations a correlation peak is observed.

For the nanoemulsions the Teubner-Strey fits show clear deviations from the experimental data, as in the q -range above the scattering peak a distinct shoulder appears (fig. 4.10b/4.10c). This discrepancy is not surprising, as here droplet structures should be present, which are responsible for the appearance of such a shoulder and which are not well described by the Teubner-Strey model. Ideally it is applicable when bicontinuous structures are present.

Accordingly further data analysis for the nanoemulsion regime was performed, using monomodal and bimodal log-normal distributions of sphere models (eq. (3.26)- (3.29)). The pronounced superiority of the bimodal model is demonstrated in fig. 4.10c and fig. A.6, where the residuals of the monomodal and bimodal fits are directly compared. Accordingly in this nanoemulsion

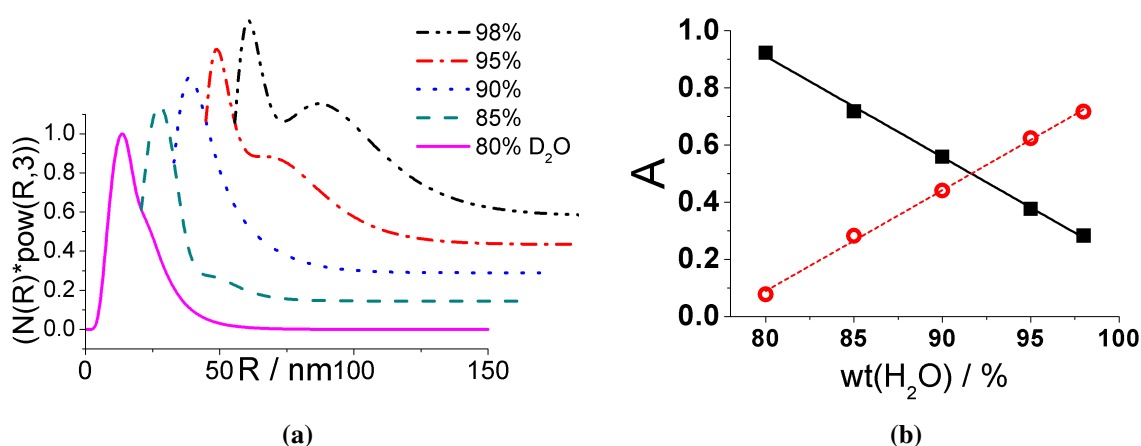


Figure 4.11: a) Standardised size distribution functions of scattering curves in the nanoemulsion region, using a bimodal log normal distributed spherical model; size distributions are depicted as number density N times the observed particle radius R to the power of three ($N(R) \cdot R^3$) vs. the radius R for a more pronounced visualisation of the two particle size evolutions with increasing water concentration; b) determined amplitude of SANS-fit (cp. tab. 4.2) for population \blacksquare R(1) and \circ population R(2).

a bimodal distribution of oil-in-water droplets is present. Close to the PIC concentration a description with the presence of just the smaller sized population is still feasible but the importance of the larger population becomes increasingly clear with increasing dilution (see amplitudes A in table 4.2). These tendencies of the bimodal distribution are best summarised by fig. 4.11a which shows the size distribution functions according to the bimodal fit of the SANS data. Generally we always observe two populations, one of the smaller sized distribution around $R_{1,Mw} \geq 14-16$ nm and a second somewhat bigger one with radii $R_{2,Mw} \geq 32-40$ nm. The average size increases due to a size increase of the individual populations (more pronounced for the larger population) and mostly due to increasing prominence of the larger population.

This increase can be explained by an increasing depletion of surfactant from the nanoemulsion interface due to the dilution. With less surfactant availability to stabilise nanoemulsion droplets, they have to grow in size. The increasing prominence of the larger size distribution is demonstrated in fig. 4.11b, which shows the relative content A (by mass) contained in the droplets of the smaller size distribution. It is interesting to note that there exists an almost perfectly linear dependence of A on the concentration of water contained in the mixture.

In fig. 4.12 we compare the sizes of the nanoemulsion droplets as derived from the various methods. The mean sizes of the smaller and larger population yield a lower and upper boundary for the mean particle size observed in the system. Directly after reaching the phase inversion concentration, population $R_{1,Mw}$ is dominant (see amplitudes A, in fig. 4.11b), while population $R_{2,Mw}$ might be negligible at this point. According to their proportion in the mixture we can then calculate from $I(0)$ the mass-averaged mean size \bar{R} , which is increasing much more strongly due to the shift of the proportion contained in the larger and smaller populations, respectively. It is very interesting to note that $R_{1/2,Mw}(I0)$ is in very good agreement with the radius obtained

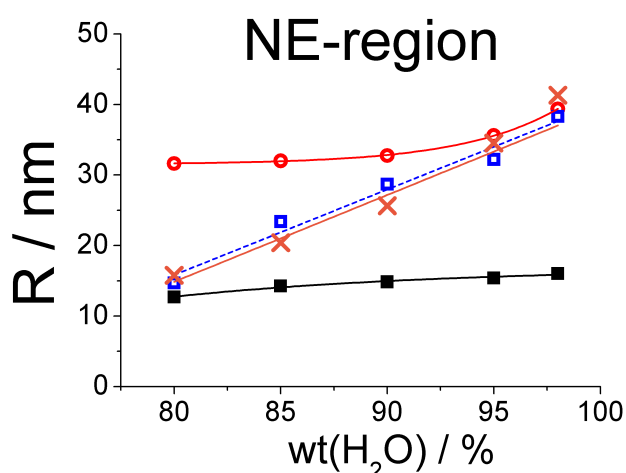


Figure 4.12: Initial intensities $I(0)$ for different water conc. (Comparison of the radii determined from turbidity and SANS via various methods (\square R_{avg} (turbidity), \blacksquare $R_{1,Mw}$ (SANS), \circ $R_{2,Mw}$ (SANS), \times R_{I0} (SANS)).

from the turbidity measurements (\square in fig. 4.12), which gives further credibility to the structural picture deduced here. Accordingly we have a very self-consistent picture of two nearby particle size distributions of around 14-16 and 30-40 nm in radius, which change their relative contribution with water concentration.

With the knowledge of the size distributions we could also calculate the relative ratios of the number of particles contained in size distributions 1 and 2, $N(1)/N(2)$, which is also given in table 4.2. These values as they can be directly compared to the analysis of the cryo-TEM images are discussed in the following.

4.1.2.3. Cryogenic Transmission Electron Microscopy (cryo-TEM)

In order to obtain complementary structural information, direct imaging of a nanoemulsion sample was done by means of cryo-TEM. The obtained images of o/w-mixture with 95% H₂O confirmed the strongly polydisperse character of this sample (cf. SANS-results tab. 4.2) and an example of these TEM images is given in fig. 4.13b. In order to obtain quantitative information regarding the size distribution, statistical evaluations of obtained images have been accomplished through Java-based image processing (ImageJ) [79]. From this analysis based on 312 analysed droplets using six different TEM images (fig. 4.13b being one example) a radii size distribution has been derived which is given in fig. 4.13a. This size distribution is distinctly bimodal and shows two well-defined peaks. In fig. 4.13a for comparison we also show the number weighted log-normal size distributions from the SANS data fit for the same sample. The position of the peaks coincides very well. However, the scattering experiment shows a significantly broader distribution of both populations. This might be due the fact that in scattering one sees an upper limit of the width of the size distribution, as there would be further effects like anisometry or fluctuations of the droplets that would look like polydispersity and which in our model will simply add onto the observed apparent polydispersity. However, in general the cryo-TEM results demonstrate in a convincing manner that the investigated nanoemulsions contain spherical droplets with a clearly bimodal size distribution. Both methods agree very well with respect to the number-averaged mean particle sizes to be located at ~ 12 and ~ 27 nm, respectively (eg. tab. 4.2). Even more impressive is the fact that the deduced ratio of the number of particles in the respective size distributions: $N(1)/N(2) \approx 6.5$ obtained from SANS is in excellent agreement with the cryo-TEM finding of $N(1)/N(2) = 6.6$ (fig. 4.13).

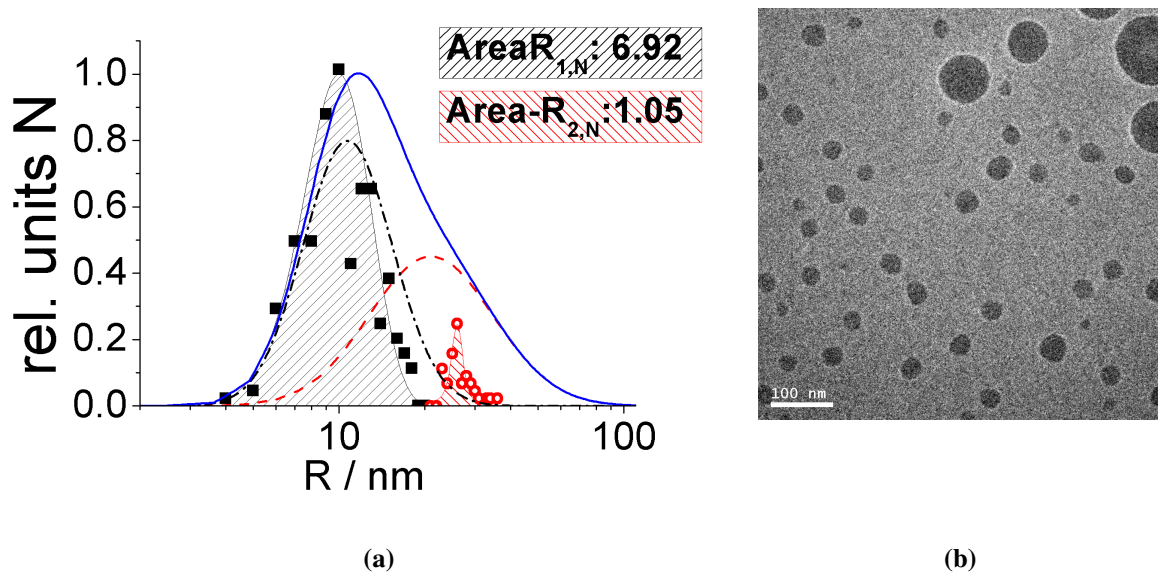


Figure 4.13: **a)** Normalised statistical evaluation of cryo-TEM images (**b)** -respectively), nanoemulsions formed at 95% H₂O (population \blacksquare $R_{1,N}$ and \circ $R_{2,N}$); compared with number weighted (tab. 4.2) normalised bimodal size distribution function (log normal) obtained from SANS-data fit ($-\cdot-\cdot-$ $R_{1,N}$, $-\cdot-\cdot-$ $R_{2,N}$, $—$ $R_{1/2,N}$).

4.1.3 Conclusion of PIC-method based nanoemulsion formation using commercially available oil/surfactant composition (Tego[®] Wipe DE)

An oil/surfactant/water system containing the oils diethylhexyl carbonate, phenoxyethanol, and a parabene mixture, and as surfactant polyglyceryl-4 laurate mixed with a small amount of anionic dilauryl citrate, spontaneously forms long-time stable nanoemulsions (phase separation only occurs after times longer than 6 months) by simply diluting the oil/surfactant mixture with water. The role of the dilauryl citrate is that of an electrostatic stabiliser, while the phenoxyethanol contained in the oil is a cosurfactant facilitating the high effective solubilisation capacity of the system. This process proceeds via the phase inversion concentration (PIC) mechanism, due to the presence of the relatively hydrophilic surfactant which becomes leached out from the emulsion droplets upon dilution.

Our observation of the phase behaviour shows that upon dilution with water this oil/surfactant system passes via an extended two-phase range to a homogeneous nanoemulsion phase that appears for a water content above 75%, which phase separates into an upper oil and a lower aqueous phase only after many months. At somewhat lower water content a bicontinuous structure is present, that shows a quite pronounced viscosity and conductivity maximum prior to the phase transition to the nanoemulsion phase. SANS measurements show a substantial increase in the degree of ordering while passing through the bicontinuous phase. This demonstrates that the generation of nanoemulsions is linked to the presence of a highly ordered phase in the vicinity in the phase diagram. Furthermore the very low interfacial tension of the oil/surfactant mixture explains the formation of a highly dispersed phase. Here it is interesting to note that from the interfacial tension value of 0.0175 mN/m one can estimate the droplet radius R via the relation [57, 141]:

$$\gamma \cdot R^2 = k \cdot T \quad (4.3)$$

to be about 15 nm, which is in excellent agreement with our further structural characterisation (especially for the smaller sized population observed). It should also be noted that this size estimate is one for the maximum size of microemulsion droplets formed at the boundary of emulsification failure. However, for some interesting reason this estimate also coincides rather well with the size of our nanoemulsion.

A detailed structural investigation of the nanoemulsion region by SANS and cryo-TEM at 95 wt% water content showed that it is composed of spherical droplets with a bimodal size distribution with average sizes of $R(1) \geq 10$ and $R(2) \geq 26$ nm. A concentration dependent SANS investigation shows that directly beyond the phase transition into the nanoemulsion region, i.e., at lowest dilution with water, this is dominated by the smaller o/w droplets. Generally both particle sizes are growing with increasing water concentration, but this growth is much more

pronounced for the larger sized population. The growth of the average particle size is in good agreement for the SANS and the turbidity data and one observes a roughly linear increase of size with the water content in the mixture. This growth is due to the fact that upon dilution the hydrophilic surfactant partitions increasingly into the aqueous phase and therefore less surfactant is available to cover the emulsion droplets, which consequently have to increase in size. With increasing water content the proportion of the smaller particles ($N(1)$) decreases in favour of the formation of the bigger droplets ($N(2)$). Using SANS and cryo-TEM imaging yields a reliable picture of this situation and both methods are in excellent agreement with respect to the relative amounts of particles present in the form of larger and smaller droplets. This bimodal size distribution might be the result of an initial Ostwald ripening of the system that becomes arrested in an early stage. Due to the rather high solubility of the oils contained one would expect a rather fast Ostwald ripening in our nanoemulsion but apparently this is effectively suppressed. The reason for this remarkable stability is not yet clear, but will be the focus of future studies. Our investigation demonstrates that the nanoemulsion studied here is in reality composed of a bimodal distribution of somewhat differently sized droplets with mean radii in the range of 15 or 30-40 nm, respectively. The smaller droplet size is consistent with the size expected for microemulsion droplets. This means that here one may have a situation where microemulsion droplets coexist with larger sized, metastable emulsion droplets. This is a new insight into the structural details of PIC nanoemulsions, which should be important for the future developments of these interesting systems. This knowledge will be important for the design of nanoemulsions and for their further applications.

4.2 Influence of Oil/Surfactant composition on Nanoemulsion-Structure and -Stability formed by the Phase Inversion Concentration (PIC) method

The spontaneous formation of nanoemulsions by low energy methods such as the Phase Inversion Temperature (PIT) or the Phase Inversion Concentration (PIC) method, also referred as Phase Inversion Composition [171,206], is a highly interesting phenomenon both from the fundamental point of colloid research but also due to its high potential for applications in cosmetic, pharmaceutical or agrochemical formulations. Accordingly the PIT [45,81,155,162,195] and, to a lesser extent, the PIC [113,172] method have been the subject of intense recent research activities. However, in particular the latter, which normally simply works by diluting an appropriate oil/surfactant mixture with water, is still rather poorly understood with respect to the requirements on the surfactant/oil mixture. This renders systematic approaches for finding appropriate PIC formulations rather difficult.

Often it is claimed that passing through a liquid crystalline phase, typically a lamellar phase, or the vicinity of it in the process of nanoemulsion formation is a necessary prerequisite for the spontaneous formation of stable nanoemulsions as it has been established for the PIT method [195]. This can be expected as by diluting one reverses the curvature of the system from a water-in-oil (W/O) to an oil-in-water (O/W) system. As this change occurs gradually it is necessary to pass a region in the phase diagram where the spontaneous curvature is zero and for a surfactant system with a sufficiently high bending stiffness, this then means the formation of a lamellar phase [68], while for lower bending rigidity the formation of bicontinuous microemulsions will be observed [86,93].

Such a behaviour has been reported for the hexadecane/potassium oleate-oleic acid- $C_{12}E_{10}$ system [170], where it also has been noticed that the droplet size is smaller when the liquid crystalline region is wide and extends to high water content. In contrast, for the case of oligo-isobutene ($n=6-8$) as oil and polyoxyethylene isostearic ester as surfactant a rather slow process of formation has been observed in which the droplets are formed only within about 60 s and reach their final size of 45-50 nm radius in about an hour [172]. In the latter case an evolution of the nanoemulsion via a multiple emulsion is claimed, which comes about due to the rapid change of spontaneous curvature due to the fast dilution.

Due to these largely different systems that are able to form nanoemulsions spontaneously via the PIC process, where also the process itself has been described to proceed quite differently from system to system, we decided to do a systematic investigation on a PIC oil/surfactant formulation based on polyglycerol-4 laurate (with a small amount of charged surfactant) as surfactant and diethylhexyl carbonate, phenoxyethanol and different parabens as oil. Such an oil/surfactant (O/S) composition is also commercially available (Tego[®] Wipe DE, Evonik Industries) [109] and has been investigated by us to some extent (cp. section 4.1). These investi-

gations had shown that in these nanoemulsions droplets with an average radius of about 25-35 nm are present, which are rather long-time stable. Furthermore in the phase diagram one finds upon dilution with water first a water-in-oil (W/O) microemulsion, and then passes through a biphasic region, which reaches its highest degree of ordering just prior to passing into the nanoemulsion region. It has also been noticed by us that the stability of these nanoemulsions depends largely on the presence of an anionic surfactant in this mixture and accordingly they are also sensitive to the addition of salt, which destabilize them, thereby leading to creaming.

However, so far it is rather unclear how the single structures of the oil/surfactant mixture affect structure and stability of the nanoemulsions formed. This interesting question therefore was addressed by us in this work, for which we employed the basic oil/surfactant model system studied before (eg. section 4.1) and varied systematically the surfactant and oil composition in it. From this variation we intend to learn which factors in the surfactant structure influence the nanoemulsion properties in which way. From this correlation we expect to gain a much better understanding of the requirements for forming PIC nanoemulsions, thereby obtaining a unified picture of these interesting systems that allows to prepare them in a much more systematic fashion as is possible so far.

Modification of PIC-Oil/Surfactant Concentrates

As for the studied model system a variation of the oil-to-surfactant (O/S) ratio, which is not discussed in the following work, affects the stability quite crucially (see section 4.3); our investigations were mainly done at constant oil-to-surfactant ratio (78/22). For this given O/S-ratio, our model system forms nanoemulsions via the PIC method by changing the interfacial composition during dilution, allows only the exchange of compounds in a narrow molecule range. However it should be noted that exchanged components of the oil/surfactant mixture that are not working for this certain O/S-ratio (78/22), might work for other ratios. Section 4.2.1 gives some perspectives how such O/S-mixtures may be achievable.

Here we want to give a short synopsis on the O/S-modifications we accomplished, using our model system that generally is based on the following ingredients: *oil*, *cosurfactant*² (*preservative mixture*), *nonionic surfactant* and *ionic surfactant* -eg. materials part section 3.1.1.2.

At variable O/S-ratio we exchanged:

- oil
- cosurfactant
- nonionic surfactant
- (eg. section 4.2.1)

At constant O/S-ratio (78/22) we exchanged:

- oil
- ionic surfactant
- nonionic surfactant
- (eg. section 4.2.2- 4.2.4)

²Accounts as oil phase for the given O/S-expressions.

4.2.1 O/S-Variation through concentrate modification

Oil. As shown by Meyer et al. [110] the main oil phase (2-ethylhexyl carbonate) of the oil/surfactant mixture is exchangeable, by more polar (C_{12-15} alkyl benzoate) or unpolar (isohexadecane) molecules (eg. tab. 4.3), when the necessary amount of cosurfactant (preservative mixture of phenoxy ethanol and parabens) is determined. This determination can be done by using the structural properties of the phases upon dilution pathway, prior to the PIC.

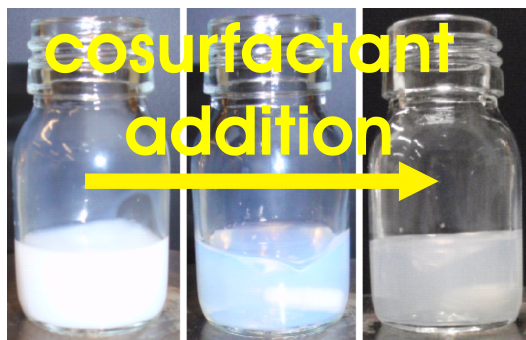


Figure 4.14: Determination of necessary amount of cosurfactant (phenoxy ethanol/paraben mixture) to form bicontinuous microemulsion structure (middle) while cosurfactant-addition to 1:1 mixture (left) of water and O/S-formulation (oil (eg. here: isohexadecane)/polyglycerol-4 laurate/ dilauryl citrate (75/24/1 wt-%); right excess of cosurfactant in O/S-mixture

Here, our model system (2-ethylhexyl carbonate/ phenoxy ethanol+parabens/polyglycerol-4 laurate/dilauryl citrate) forms blue shining bicontinuous microemulsion phases at water concentrations around 50 wt-%. Hence, a step-wise addition of cosurfactant to a 1:1 mixture of water and a new formulation (different oil/polyglycerol-4 laurate/ dilauryl citrate), while keeping the initial oil/surfactant-ratios of this new formulation constant, leads to a clearing in solution until the expected bicontinuous microemulsion is reached at the transitional point, under continuous stirring 4.14. From the used amount of cosurfactant, to obtain this bicontinuous microemulsion phase, the new O/S-ratio can easily be recalculated and used to formulate nanoemulsion

qualified concentrates. Upon dilution the exact PIC depends on the detailed composition and the formation process. The amount of cosurfactant therefore has to be balanced with respect to the PIC-formation process, monolayer at the oil/water interface upon dilution. Thereby polar

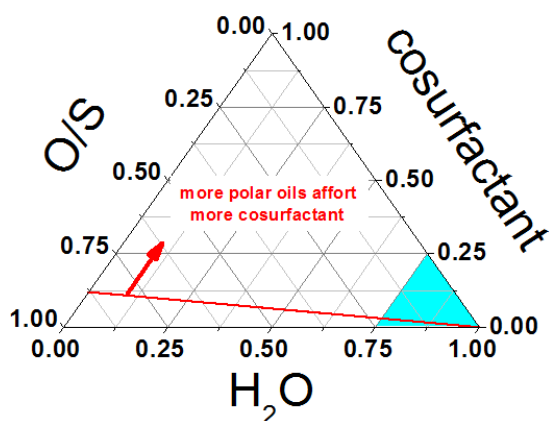


Figure 4.15: Scheme of ternary PIC phase diagram, showing the rise of dilution line when using more polar oils to higher cosurfactant ratios; shaded area in water rich region shows possible domains of NE appearances for qualified O/S-mixtures

| oil | γ mN/cm | V_m 10^{-22} cm^3 | G J/cm^3 |
|----------------------------|-------------------|----------------------------------|----------------------|
| isohexadecane | 0.243 | 4.74 | 31.2 |
| 2-ethylhexyl carbonate | 0.270 | 5.32 | 33.3 |
| 2-octyl carbonate | 0.287 | 5.33 | 35.4 |
| octyloctanoate | 0.281 | 4.95 | 35.6 |
| C_{12-15} alkyl benzoate | 0.316 | 6.24 | 37.0 |
| 2-n-butyl carbonate | 0.264 | 3.14 | 38.8 |
| 2-ethyl carbonate | 0.256 | 2.01 | 43.6 |
| H_2O | 0.728 | 0.30 | 234 |
| cosurfactant | | | |
| tetradecane | 0.268 | 4.32 | 35.5 |
| K300 | 0.426 | 2.51 | 67.5 |

Table 4.3: Gordon parameter G for quantification of molecule polarities; calculated from the solvent surface tension γ (measured at ILL) and its molar volume V_m (compare section 3.2.7.2). The higher the Gordon parameter the more polar and thus water soluble is the molecule.

oils require more and unpolar oils less cosurfactant (eg. fig. 4.15).

Cosurfactant. Similar determinations for PIC-qualified oil/surfactant mixtures might be applicable while which assumes a modification of the composition of the amphiphilic using different cosurfactants, provided their properties are facilitating the high effective solubilisation capacity of the system and thus enable the nanoemulsion formation [16] or nonionic surfactant.

For the given O/S-ratio 78/22 we could exchange the preservative mixture of the model system (Euxyl[®] K300) with tetradecane, to form a homogenous oil/surfactant concentrate that generates bluish white nanoemulsions at high dilution ratios (95-98 wt-% H₂O) of \approx 50-60 nm. Nevertheless, this system does not pass blue shining bicontinuous microemulsion like phases upon dilution and hence complicates the formation of PIC-suited O/S-mixtures.

Nonionic surfactant. Despite intense trials to exchange the nonionic surfactant (polyglycerol-4 laurate) of our model system for the given O/S-ratio (78/22), no alternatives have been found. This could be seen in the formation of non-homogenous O/S-mixtures, where oil and surfactant were not miscible.

The determination of other usable O/S-ratios, as described above, failed because of two different reasons. Either the initial O/S-mixture without cosurfactant was not homogenous before dilution ($HLB(\text{surfactant}) \geq 10$), or the addition of cosurfactant to a 1:1 mixture of water and O/S-concentrate did not pass through a bluish microemulsion phase. Thus, there was no indication for the right amount of cosurfactant to form nanoemulsions. Surfactants chosen for the replacement were selected due to their hydrophilic-lipophilic properties and structural likeness to the model one. Detailed information about the surfactants employed and their properties are given in section A.1.2.2.

4.2.2 Variation of the nonionic surfactant at constant O/S-ratio (78/22)

To exchange the main surfactant phase (polyglycerol-4 laurate) that accounts with a mass fraction of \sim 21wt-% in the O/S-mixture, extensive replacement studies were done that stayed ineffective in terms of forming homogenous concentrates and accordingly nanoemulsions. Surfactants have been chosen due to their hydrophilic-lipophilic properties. The hydrophilic head group thereby based on glycerol units of different lengths (2, 3, 4 and 10). The hydrophobic tail varied in chain length and structure (linear (laurate, caprate, oleate), branched (isostearate), non-saturated (oleate) and saturated (caprate, oleate, isostearate) molecules). Table A.3 in the appendix is summarising all tested surfactants and their physical properties that might influence a successful (homogenous) oil/surfactant-mixture for other ratios.

Main result of the surfactant variation was the finding that the nonionic surfactant polyglycerol-4 laurate can not be trivially replaced.

4.2.3 Variation of the ionic surfactant at constant O/S-ratio (78/22)

As apparently the electrostatic conditions in the surfactant/oil mixture play a key role in the stability of formed nanoemulsions, we first studied the effect of having different types of ionic surfactants present in this formulation at constant O/S-ratio (78/22). Furthermore the influence of the charge concentration of the formed nanoemulsions was analysed by increasing the charged surfactant concentration in the total surfactant admixture stepwise. Some relevant characteristics of the charged surfactants in use are summarised in table 3.4.

4.2.3.1 Phase behaviour and stability

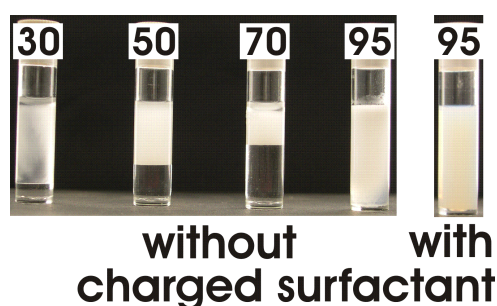


Figure 4.16: *left:* o/w mixtures with 30/ 50 / 70 and 95% water concentration for DEHC/K300/P4L (66/12/22 wt-%) system, missing the charged surfactant, which is essential to form meta stable nanoemulsions at very high dilution ratios (95% H₂O) - *right:* ~ 0.9 wt-% addition of dilauryl citrate as charged surfactant to initial O/S-mixture.

So far we observed that the presence of a charged surfactant is essential to achieve a nanoemulsion, as in its absence it is impossible to emulsify the oil phase into the aqueous one (fig. 4.16). Our reference system contains - beside 2-ethylhexyl carbonate, a preservative mixture (of phenoxy ethanol + parabens) and polyglycerol-4 laurate - dilauryl citrate as ionic surfactant. For this system we already did comprehensive structural studies (see section 4.1). In this investigation, we now employ singly (AOT; di-oleic acidyl isopropylester dimethylammonium methosulfate) and doubly charged (sulfonated castor oil, Na-salt; disodium laureth sulfosuccinate) surfactants. However, even if a nanoemulsion (NE) is not formed without a charged surfactant in the oil/surfactant concentrate, only a small amount (~0.9 wt-%) of it is necessary to enable the NE-formation for qualified mixtures. Concerning our studies on differently charged surfactants, we always used to formulate our O/S-concentrates in weight percent. As the surfactants employed differ structurally and thus by their molecular weight, they also exhibit different charge concentrations. Structures of the charged surfactants employed are given in table A.4, whereas table 4.4 summarises some of their molecule characteristics and gives the concentration of the charged surfactants with respect to their mass fraction (~ 0.9wt-%) and molecular weight. Generally, the higher the molecular weight the lower the surfactant concentration in the formulation. Surfactants with multiple charges multiply their charge density correspondingly. Hence the singly charged surfactant dilauryl citrate (DC) of the model system is embedded by the lower (esterquat (EQ)) and higher (AOT) concentrated formulations. The doubly charged surfactants raise the effective charge concentration by a factor of two and exhibit therefore concentrations double (disodium laureth sulfo succinate (SS)) or greater than double (sulfonated castor oil (SCO)) compared to the model one.

| charged surfactant | abbr. | Mw g/mol | z(S) | anionic | cationic | c mM | HLB |
|--|-------|----------|------|--|------------------------|------|-----|
| dilauryl citrate | DC | 528.8 | -1 | citrate: $R_3C_2O_2^-$ | proton: H^+ | 16.6 | 5 |
| Di-Oleic Acidyl Isopropylester Dimethylammonium Methosulfate | EQ | 773.6 | +1 | methosulfate: $MeSO_3^-$ | R_4N^+ | 11.4 | 23 |
| Dioctyl Sodium sulfosuccinate | AOT | 444.3 | -1 | sulfonate: RSO_3^- | sodium ion: Na^+ | 19.8 | 15 |
| Sulfonated castor oil, Na-salt | SCO | 422.2 | -2 | sulfonate: RSO_3^- , carboxylate: RCO_2^- | sodium ion: $2Na^+$ | 20.8 | 25 |
| Disodium Laureth Sulfosuccinate | SS | 542.2 | -2 | sulfonate: RSO_3^- , carboxylate: RCO_2^- | sodium ion: $2Na^+$ | 16.2 | 35 |

Table 4.4: Charged surfactants employed for O/S-concentrates, containing 2-ethylhexyl carbonate/phenoxy ethanol + parabens/polyglycerol-4 laurate/charged surfactant (66/12/21.1/~0.9 wt-%); their abbreviation (abbr.), molecular weight Mw, effective charge z(S) of the dissolved surfactant molecule, functional groups possessing the charge of the surfactant molecule and counter charge (cat- and anionic), surfactant concentration c based on its mass fraction in the O/S mixture g(S-charged)/kg(O/S-mixture) and the hydrophilic lipophilic balance HLB-value. Critical micellar concentration (cmc) of charged surfactants are given in table 3.4 of the material section 3.1.1.2.

Figure 4.17 gives the phase behaviour upon dilution for the three single charged surfactants (dilauryl citrate (DC), AOT and di-oleic acidyl isopropylester dimethylammonium methosulfate (EQ)) respectively, and visualises their structural influence time- and temperature-dependently. Whether some general tendencies upon nanoemulsion formation are similar for each surfactant; like the passing through a more or less extended region of flow birefringence (shaded areas in fig. 4.17a-c) and the quite certain occurrence of the nanoemulsion phase at higher dilution ratios (> 75% wt%-H₂O); the way upon dilution is quite strongly influenced by the type of charged surfactant (~ 0.9 wt-%) given in the O/S-mixture.

However, temperature seems to play an important role in terms of stabilisation. Higher temperatures lead to a stronger destabilisation of the single phases formed than lower ones. This effect gets more compensated for higher surfactant concentrations and thus charge contribution. Contrary, the state of phases is only little affected by time. Therefore the following descriptions are given for temperatures at ≈ 25°C and two to three days. At this point, it should be additionally noted, that samples formulated with AOT tend to a greater change of physical properties by

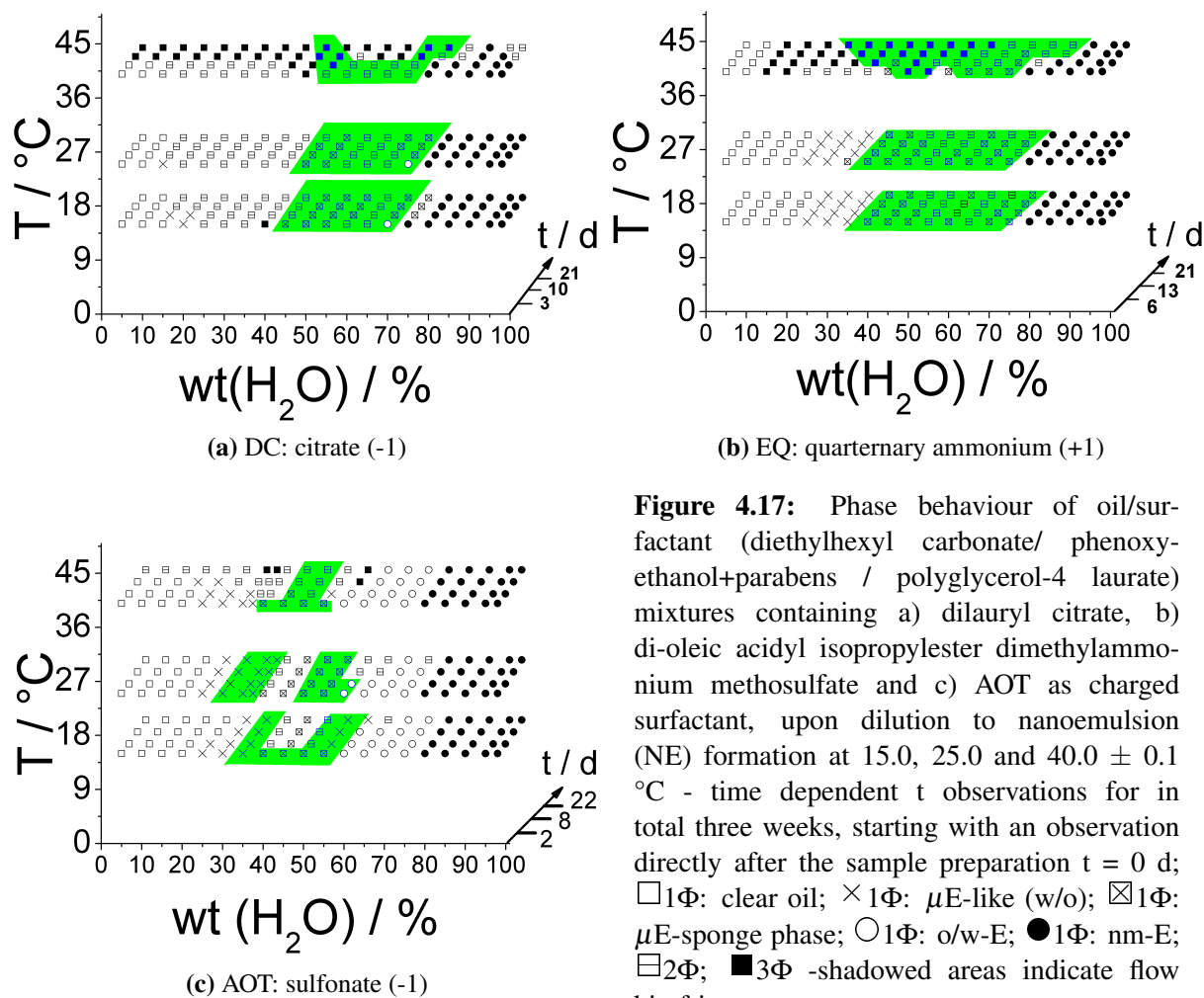


Figure 4.17: Phase behaviour of oil/surfactant (diethylhexyl carbonate/ phenoxy-ethanol+parabens / polyglycerol-4 laurate) mixtures containing a) dilauryl citrate, b) di-oleic acidyl isopropylester dimethylammonium methosulfate and c) AOT as charged surfactant, upon dilution to nanoemulsion (NE) formation at 15.0, 25.0 and 40.0 ± 0.1 °C - time dependent t observations for in total three weeks, starting with an observation directly after the sample preparation $t = 0$ d; \square 1 Φ : clear oil; \times 1 Φ : μ E-like (w/o); \boxtimes 1 Φ : μ E-sponge phase; \circ 1 Φ : o/w-E; \bullet 1 Φ : nm-E; \square 2 Φ ; \blacksquare 3 Φ -shadowed areas indicate flow birefringence

time than the other surfactants. This is according to its chemical degradation by bacteria. Trials to suppress this degradation are given in the appendix section A.3.2.

During the dilution process all compositions start with a complete incorporation of the water into the organic phase (symbol \square in fig. 4.17), at 25°C, respectively, thereby forming a w/o microemulsion which covers the broadest region for the mixtures with the highest HLB-value (EQ and AOT -eg. tab. 3.4). As the oil/surfactant formulations differ only for the type of charged surfactant and hence its concentration, one can assume that a certain amount of water is bound to these surfactant molecules. The molecules hydrophilicity (and thus solubility [97]) is represented by their HLB value (eg. tab. 1.1 and 4.4) and shows that formulations with the EQ bind more water molecules due to its greater hydrophilicity (HLB(EQ) = 23) than the model system (HLB(DC) = 5), while simultaneously exhibiting a lower concentration than the DC-formulation.

Almost all anionic- and cationic surfactants are highly water soluble and hence exhibit a high HLB-value. Contrary it is the case for the anionically charged surfactant dilauryl citrate used in

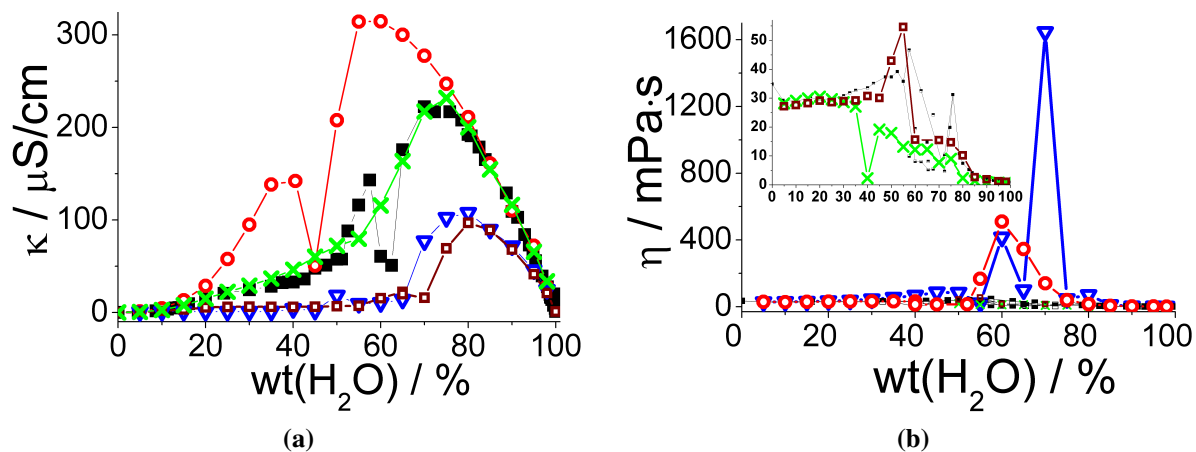


Figure 4.18: a) Conductivity κ and b) viscosity data η for oil/water-dilutions of oil/surfactant formulations (2-ethylhexyl carbonate/phenoxy ethanol + parabens/polyglycerol-4 laurate/charged surfactant (66/12/21.1/0.9 wt-%)) with different charged surfactants (■ DC, ▽ EQ, ○ AOT, □ SCO, × SS) at $25.0 \pm 0.1^\circ\text{C}$ and homogenised samples.

our model system (Tego[®] Wipe DE). However, it should be mentioned that o/w-nanoemulsions are finally formed in both cases for either anionically or cationically charged surfactants at water concentrations >75 wt% nevertheless. Even if the nanoemulsion emulsification is not influenced, the hydrophilic-lipophilic properties of the charged surfactant affect all observed structures before the PIC is reached. After passing the region of water incorporation, one observes independent of the surfactant concentration but dependent on its hydrophilicity, either a broad domain of single (\uparrow HLB) or biphasic (\downarrow HLB) arrangements ($T \leq 25^\circ\text{C}$), that stays more or less with time, respectively to the observed time range. Nevertheless, all systems are passing at least once a biphasic region upon dilution (fig. 4.17), which marks the structural transition to bicontinuous structures and correlates also with the first conductivity and viscosity maximum observed (fig. 4.18 -data given herein can be found in the tables 4.17-A.11 of the appendix).

A comparison of the physical properties (HLB-value, concentration), upon dilution pathway does not show any significant tendencies. Especially not if multiple charged surfactants are also considered.

Similar results are given for nanoemulsion stabilities, as examined by UV/Vis transmittance spectroscopy 4.19a to calculate an overall droplet radius 4.19b of the formed nanoemulsions using equation (3.3)- (3.6).

Except for AOT, all charged surfactants in use form nanoemulsions of more or less the same mean radius ($R \approx 33/34$ nm) that lies slightly higher than those of our model system containing dilauryl citrate ($R(\text{DC}) \approx 32$ nm). They appear likewise meta-stable for a quite long time-range and did not lead for the given dilution ratio (95wt-% H_2O) to a macroscopic phase separation during observation time (~ 40 days).

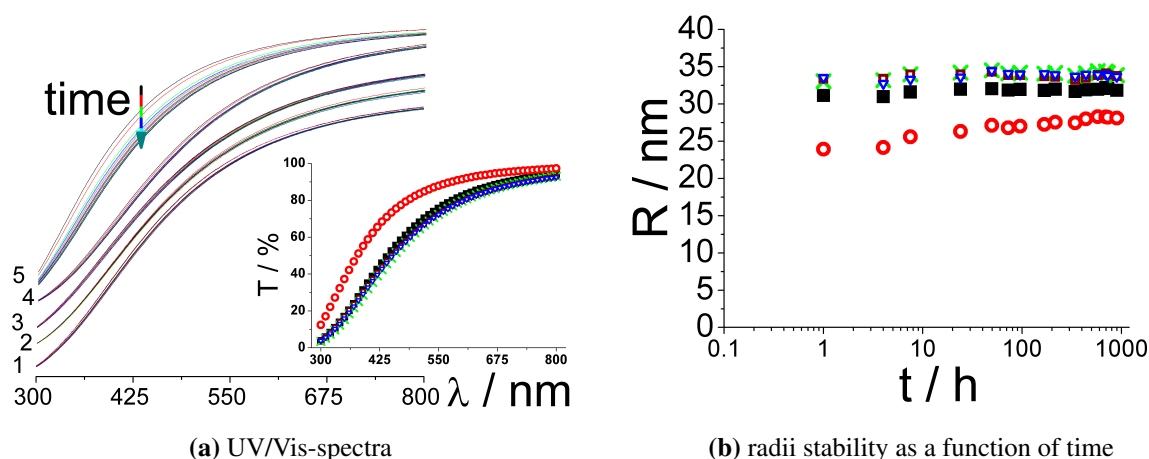


Figure 4.19: **a)** UV/Vis transmittance T spectra ($\lambda = 300 - 800$ nm) taken of o/w dilutions (5:95) for O/S-formulations containing 2-ethylhexyl carbonate/phenoxy ethanol + parabens/polyglycerol-4 laurate/charged surfactant (66/12/21.1/0.9). Charged surfactants in use are 1: \blacksquare DC, 2: ∇ EQ, 3: \square SCO, 4: \times SS, 5: \circ AOT. Transmittance T was observed over a period of about 40 days, keeping the samples horizontally stored at $25.0 \pm 0.1^\circ\text{C}$ in 0.5 mm cells. For a better distinction the main plot shows the evolution of the wavelength-dependent transmittance T in arbitrary units for the individual nanoemulsions with time. The Inset in **a)** points out the correlation of the relative transmittances for the different formulations directly after dilution ($t = 0$). **b)** Evolution of radii R with time t .

However, AOT influences the finally formed nanoemulsions in other directions. Besides forming initially o/w droplets of 24 nm radius, it tends to a slightly faster destabilisation with time which might also originate from the chemical degradation by bacteria (eg. section A.3.2). Nevertheless, no distinct indications have been found, why exactly this molecule forms smaller particle sizes than the others while comparing their physical properties.

It is quite well known that AOT facilitates the formation of thermodynamically stable microemulsions which are smaller (5-10 nm) than nano- and macroemulsions (eg. tab. 1.2). However, concerning the AOT properties a lot of studies have already been carried out by *Eastoe et al.* to determine what is so special about it [119–122].

Nevertheless, this should not be in our concern but if one considers a coexistence of microemulsion droplets beside metastable nanoemulsion ones, like we concluded in section 4.1, one may assume that this balance is somewhat moved further in direction microemulsion during the initial dilution process. We also observed a more bluish/translucent tint for the nanoemulsions formed by AOT than for the others. At this point one should refer again to the small portion of AOT ($\sim 0.9\text{wt-\%}$), given in the O/S-formulation, that causes this behaviour.

It is normally assumed that coalescence and Ostwald-ripening [14] are the major destabilisation processes of nanoemulsions [183, 189]. If coalescence is the driving force for the instabilities, the change of droplet size with time will follow equation (4.4)

$$\frac{1}{r^2} = \frac{1}{r_0^2} - \left(\frac{8\pi}{3}\right) \cdot \omega t \quad (4.4)$$

where r is the average droplet radius after a certain time t , r_0 the radius at time zero ($t = 0$) and ω the frequency of rupture per unit of surface of the interfacial film. A proper deduction of the given relation can be found elsewhere [31].

The Lifshitz-Slezov and Wagner (LSW) theory [96, 196] yields a size increase due to Ostwald ripening according to eq. (4.6) and is derived from the difference in solubility between small and large droplets due to their different chemical potential ($\Delta \mu = \mu_r - \mu_\infty \approx \frac{2\gamma V_m}{r}$) given by the Kelvin eq. (4.5) and as a result of the difference in Laplace pressure $p = 2\gamma / r_{spherical}$ (difference between inside and outside the droplet).

$$C(r) = C(\infty) \cdot \exp\left(\frac{2\gamma V_m}{rRT}\right) \quad (4.5)$$

Where $C(r)$ is the solubility of the oil dispersed in an emulsion droplet of size r , $C(\infty)$ the solubility of the bulk phase (the solubility of an infinitely large droplet), r the droplet radius, γ the interfacial tension, V_m the molar volume of the oil phase, R the gas constant and T the temperature.

$$r^3 = \frac{8}{9} \left[\frac{c(\infty)\gamma V_m D}{\rho RT} \right] \cdot t \quad (4.6)$$

D is the diffusion coefficient of the oil and ρ its density [131, 132]. Equation (4.4) predicts in case of coalescence (for the inverse squared radius (R^{-2}) versus time) and equation (4.6) in case of Ostwald-ripening (for the cubic radius versus time t) a linear dependency. The data for both are given in table 4.5. Neither of the predictions showed a linear behaviour (eg. fig. 4.20),

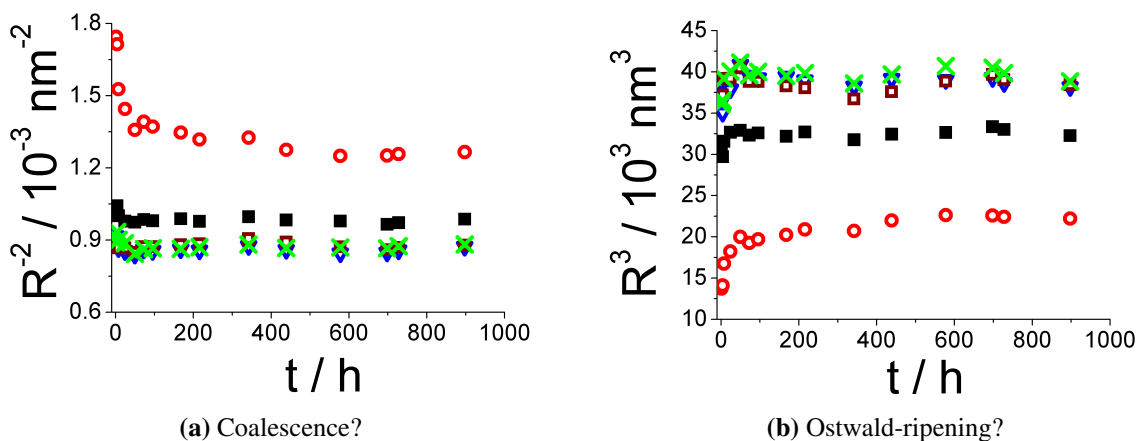


Figure 4.20: Verification of nanoemulsion kinetics for either **a)** coalescence, if linear dependency of inverse square radius R^{-2} vs. time t or **b)** Ostwald-ripening, if linear dependency of cubic radius R^3 vs. time t ; for o/w-nanoemulsions (5:95) using O/S-formulations of 2-ethylhexyl carbonate/phenoxy ethanol + parabens/polyglycerol-4 laurate/ charged surfactant (66/12/21.1/0.9). Charged surfactants in use are ■ DC, ▽ EQ, ○ AOT, □ SCO, × SS. Radii evolution of nanoemulsions were observed for a time range t (~ 40 days) with UV/Vis transmittance spectroscopy.

| t / h | DC | | | AOT | | | EQ | | | SCO | | | SS | | |
|-------|------|-------------------------------|-------------------------|------|-------------------------------|-------------------------|------|-------------------------------|-------------------------|------|-------------------------------|-------------------------|------|-------------------------------|-------------------------|
| | R | R^{-2} | R^3 |
| | nm | 10^{-3} nm^{-2} | 10^3 nm^3 | nm | 10^{-3} nm^{-2} | 10^3 nm^3 | nm | 10^{-4} nm^{-2} | 10^3 nm^3 | nm | 10^{-4} nm^{-2} | 10^3 nm^3 | nm | 10^{-4} nm^{-2} | 10^3 nm^3 |
| 1 | 31.1 | 1.03 | 30.2 | 23.9 | 1.75 | 13.7 | 33.5 | 9.16 | 37.6 | 33.4 | 8.97 | 37.2 | 33.0 | 8.91 | 36.1 |
| 4 | 31.0 | 1.04 | 29.7 | 24.2 | 1.71 | 14.1 | 32.7 | 9.08 | 35.1 | 33.4 | 8.98 | 37.2 | 33.2 | 9.34 | 36.6 |
| 8 | 31.6 | 1.00 | 31.6 | 25.6 | 1.53 | 16.8 | 33.3 | 8.67 | 37.0 | 34.0 | 8.67 | 39.2 | 34.0 | 9.01 | 39.2 |
| 24 | 32.0 | 0.978 | 32.7 | 26.3 | 1.44 | 18.2 | 33.6 | 8.54 | 37.9 | 34.0 | 8.66 | 39.2 | 34.2 | 8.87 | 40.0 |
| 50 | 32.0 | 0.974 | 32.9 | 27.1 | 1.36 | 20.0 | 34.4 | 8.39 | 40.9 | 34.3 | 8.48 | 40.5 | 34.5 | 8.43 | 41.1 |
| 73 | 31.9 | 0.985 | 32.3 | 26.8 | 1.39 | 19.3 | 34.1 | 8.61 | 39.5 | 33.9 | 8.72 | 38.8 | 34.1 | 8.62 | 39.6 |
| 96 | 31.9 | 0.980 | 32.6 | 27.0 | 1.37 | 19.7 | 34.0 | 8.55 | 39.2 | 33.9 | 8.72 | 38.8 | 34.2 | 8.66 | 40.0 |
| 168 | 31.8 | 0.988 | 32.2 | 27.3 | 1.35 | 20.2 | 34.0 | 8.62 | 39.4 | 33.7 | 8.80 | 38.3 | 34.1 | 8.63 | 39.5 |
| 216 | 32.0 | 0.978 | 32.7 | 27.5 | 1.32 | 20.9 | 33.9 | 8.57 | 39.0 | 33.6 | 8.84 | 38.1 | 34.2 | 8.70 | 39.9 |
| 342 | 31.7 | 0.997 | 31.8 | 27.5 | 1.33 | 20.7 | 33.7 | 8.75 | 38.2 | 33.2 | 9.05 | 36.7 | 33.8 | 8.81 | 38.6 |
| 439 | 31.9 | 0.983 | 32.4 | 28.0 | 1.27 | 22.0 | 34.0 | 8.60 | 39.2 | 33.5 | 8.91 | 37.6 | 34.1 | 8.67 | 39.7 |
| 578 | 32.0 | 0.979 | 32.7 | 28.3 | 1.25 | 22.6 | 33.9 | 8.45 | 39.0 | 33.9 | 8.71 | 38.9 | 34.4 | 8.69 | 40.7 |
| 698 | 32.2 | 0.965 | 33.4 | 28.3 | 1.25 | 22.6 | 34.0 | 8.48 | 39.3 | 34.1 | 8.60 | 39.7 | 34.3 | 8.66 | 40.5 |
| 728 | 32.1 | 0.972 | 33.0 | 28.2 | 1.26 | 22.4 | 33.8 | 8.57 | 38.7 | 33.9 | 8.69 | 39.0 | 34.2 | 8.75 | 39.8 |
| 898 | 31.8 | 0.987 | 32.3 | 28.1 | 1.27 | 22.2 | 33.7 | 8.72 | 38.2 | 33.7 | 8.78 | 38.4 | 33.9 | 8.82 | 38.8 |

Table 4.5: Mean radii R , inverse square radii R^{-2} and cubic radii R^3 obtained via UV/Vis measurements for o/w-nanoemulsions (5:95) using O/S-formulations of 2-ethylhexyl carbonate/phenoxy ethanol + parabens/polyglycerol-4 laurate/ charged surfactant (66/12/21.1/0.9). Charged surfactants in use are diluaryl citrate (DC), AOT, 2-methylammonium Methosulfate (EQ), sulfonated castor oil, Na-salt (SCO) and 2-sodium laureth sulfosuccinate (SS). Radii evolution of nanoemulsions were observed for a time range t (~ 40 days).

hence more complex processes are taking place that cause the meta-stability for this type of nanoemulsion [8].

The following part renders another interesting observation by SANS concerning the nanoemulsion stability of formed emulsions based on our model system Tego[®] Wipe DE, before getting a more detailed insight into the nanoemulsion formation by using differently charged surfactants.

4.2.3.2 Small-Angle Neutron Scattering (SANS)

Stability. SANS-measurements were also employed to study the stability of nanoemulsions time dependently (eg. fig. 4.21a). Thereby we observed, contrary to the light studies (horizontally storage of samples -eg. fig. 4.19), a decrease of the mean particle size (eg. fig. 4.21b). This can be traced back to the migration of bigger dispersed particles by buoyancy forces to the top of the sample. As the bigger particles, due to their density difference, are lighter than the smaller ones and the continuous phase, they disappear time dependently from the cross-sectional area of the neutron beam and cause a decreasing scattering intensity I due to the loss of larger particles (eg. fig. 4.21c). The great density difference of the emulsified particles occurs due to their different o/s-ratio, whereas the smaller oil droplets contain more of the non-ionic surfactant polyglycerol-4 laurate ($\rho(\text{P4L}) = 1.0944 \text{ g/cm}^3$) and the bigger droplets more of the oil component 2-ethylhexyl carbonate ($\rho(\text{DEHC}) = 0.8925 \text{ g/cm}^3$).

Whether this creaming (particles remain separated) is accompanied by other destabilisation processes is rather unclear. Nevertheless, this process should be far too slow to overlap processes like coalescence or Ostwald-ripening, which we could already exclude as major breakdown processes by our light experiments (UV/Vis-transmittance: eg. 4.2.3).

Structures. A structural evolution upon dilution pathway is schematically depicted in figure 4.22 using cationic Rewoquat CR 3099 respectively in the oil/surfactant mixture. The esterquat was chosen due to its charge properties, as detailed structural analysis of the phases prior nanoemulsion (NE) region, using anionically dilauryl citrate, have been already described in section 4.1.2.2. A comparison of the structural evolution upon dilution pathway with the anionic model system (see fig. 4.6) shows great similarities. The main differences can be seen in a greater tendency to form biphasic phases prior to the PIC for the dilauryl citrate system and a stronger particle correlation for the esterquat system, given by the early occurrence of the structure peak (eg. fig. 4.22 at 20wt-% H_2O). This stronger correlation does not go with the surfactant concentration, as the esterquat concentration ($c(\text{EQ}) = 11.4 \text{ mM}$) is smaller than the dilauryl citrate one ($c(\text{DC}) = 16.6 \text{ mM}$).

However, it is important to mention again that all systems are passing through a biphasic region very close to the phase inversion point, whose exact water concentration ($75 \leq \text{PIC} < 85 \text{ wt-\% H}_2\text{O}$) depends mainly on the detailed O/S-composition. Thereby, no systematic correlation of the physical properties (HLB, cmc, concentration...) and the phase inversion concentration

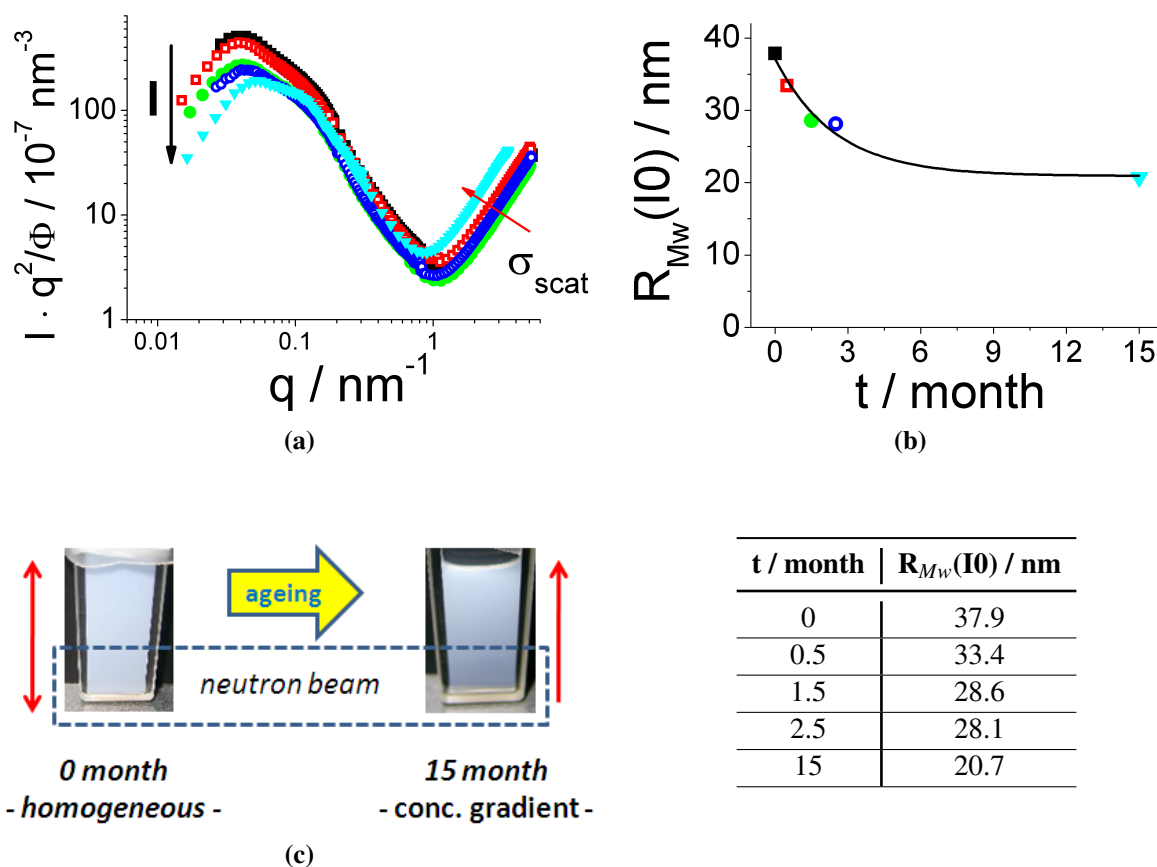


Figure 4.21: SANS curves taken of o/w dilution (5:95) for O/S-mixture of our model system (Tego[®] Wipe DE) containing 2-ethylhexyl carbonate/phenoxy ethanol + parabens/polyglycerol-4 laurate/di-lauryl citrate (66/12/21.1/0.9). Scattering intensities I were observed over a duration of 15 months, keeping the samples vertically stored at $25.0 \pm 0.1^\circ\text{C}$ in 1 mm cells. **a)** Plot of obtained scattering intensities times the square of the scattering vector q divided by the given volume fraction Φ versus the scattering vector q for a more pronounced distinction. **b)** Obtained mass weighted radii $R_{Mw}(I0)$ via Guinier approximation for extrapolations to zero angle intensity. **c)** Observation of nanoemulsion creaming and emerging of a gradiental concentration coefficient of small (bottom) to large (top) droplets after 15 months.

were observed. Figure 4.24a shows SANS of samples close to the nanoemulsion phase boundary and depicts quite nicely the strong influence of the charged surfactants in use ($< 1\text{wt}\%$ in O/S-mixture!) on the PIC-dilution mechanism. As upon dilution a certain amount of the cosurfactant is leached out into the aqueous phase, this ratio seems to be dependent on the solubility (HLB-value) of the charged surfactant and is directly linked to the intensity of the incoherent background. Furthermore there is a formation of highly ordered phases prior to the PIC. The specification of this characteristic does not correlate with the concentration but differs in its occurrence with the type of charged surfactant in use. In case of the esterquat two distinct structure peaks, at $q_1 = 0.1174 \text{ nm}^{-1}$ and $q_2 = 0.2332 \text{ nm}^{-1}$, were visible (eg. fig. 4.23a) for the scattering curve of the lower phase at 60wt-% (H_2O). If the second order reflection is observed at twice the wave vector of the first order one ($q_2/q_1 \approx \sqrt{4} = 2$), one can assume a long-range ordered

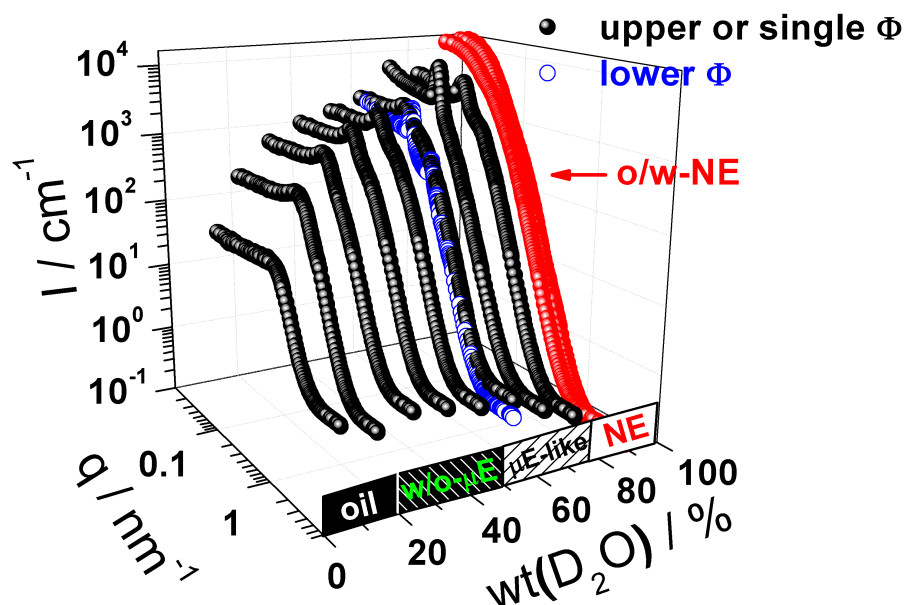


Figure 4.22: 3-dimensional plot of the phase behaviour upon dilution pathway for oil/surfactant mixture (DEHC/K300/P4L/EQ (66/12/21.1/~0.9wt-%)) with D₂O (water conc. refers to the equivalent concentration of H₂O) at 25.0 ± 0.1°C using Rewoquat CR3099 (EQ) as cationically charged surfactant. Measurements have been done after ten days of storage at 25.0°C - ●: upper or single phase, ○: lower phase.

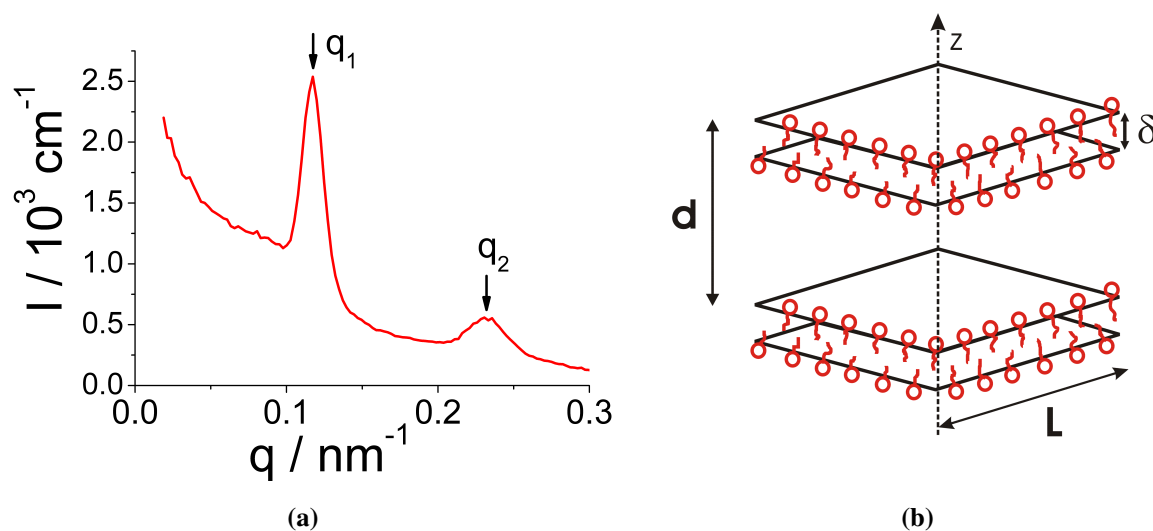


Figure 4.23: **a)** SANS-Intensity profile of lower phase at 60wt-% H₂O for dilution of oil/surfactant mixture DEHC/K300/P4L/EQ (66/12/21.1/0.9), showing two distinct Bragg peaks in a distance of $q_2/q_1 \approx 2$ that assumes well ordered lamellar structure; **b)** Geometrical model of lyotropic lamellar L_α phase taken from reference [117]; the planar surfactant bilayer has a thickness δ and is stacked along z-direction with a periodicity of $d (= 2 \pi / q_1 \approx 54 \text{ nm})$

lamellar phase (L_α) [117] that is described by a periodic stack with a periodicity $d = 2 \pi / q_1$ (≈ 54 nm) and membrane thickness δ . A knowledge about the surfactant volume fraction Φ_S ($= 0.094$, P4L in 60% H_2O sample) yields $q_1 = 2 \pi \cdot \Phi_S / \delta$ or vice versa a membrane thickness of $\delta_{P4L} = 5.2$ nm. A comparison of periodicity and membrane thickness with the surfactant dimensions given in figure 3.1c and the volumetric ratio oil/water 4:6 shows that small oil-layers are entrapped by the lipophilic surfactant tail, and that the stack distance is mainly defined by the employed amount of water. This fact becomes more evident when the membrane thickness ($\delta_{P4L, lipophilic} = 2.3$ nm) is calculated due to the lipophilic part of the surfactant molecule only ($\Phi_{P4L, lipophilic} = 0.042$, lipophilic part of P4L in 60% H_2O sample) and compared with doubly the length (layer-equivalent) of the lipophilic surfactant part (approx. ~ 2.4 nm).

The corresponding SANS curves of the formed nanoemulsions for the various surfactants are compared and given in figure 4.24. A model dependent data-treatment of the scattering curves

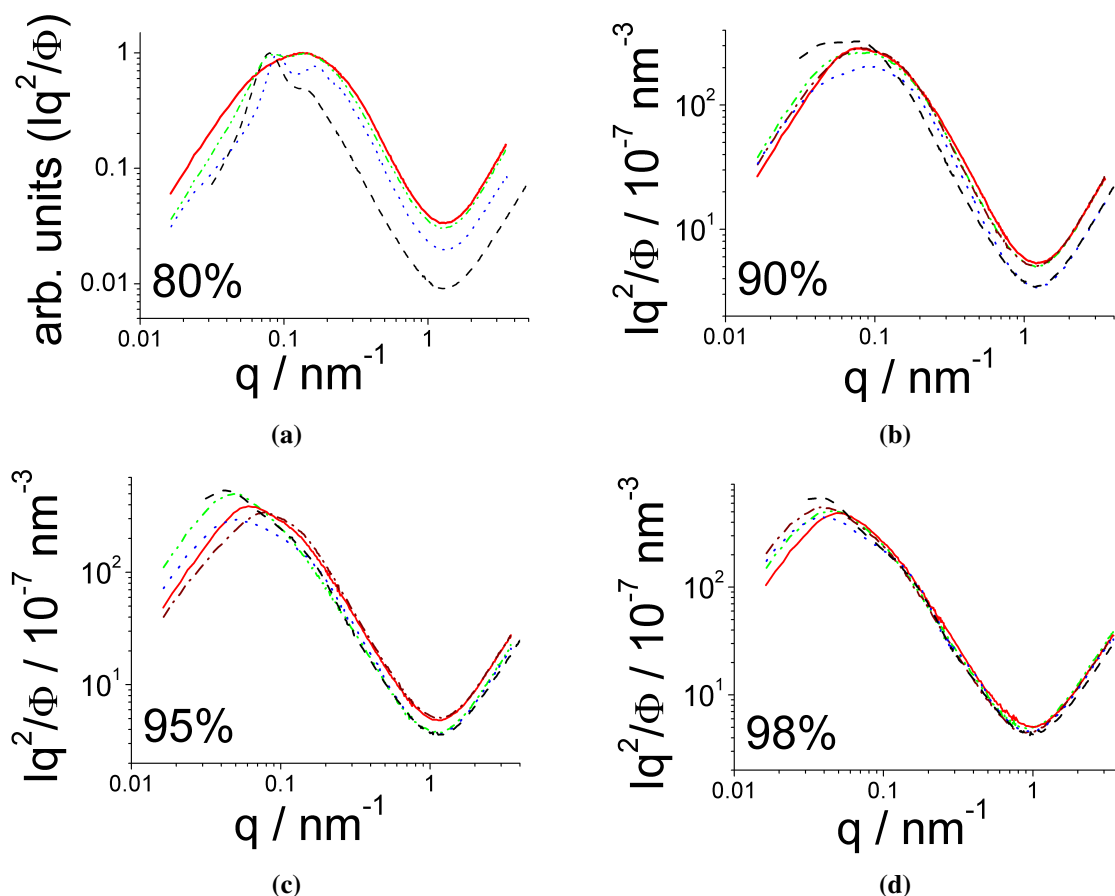


Figure 4.24: SANS-scattering curves in the nanoemulsion region of oil/water dilutions at 80, 90, 95 and 98% (H_2O respectively) for oil/surfactant mixtures (DEHC/K300/P4L/charged surfactant 66/12/21.1/0.9 wt-%) using differently charged surfactants (- - DC, ··· EQ, — AOT, - - - SCO, ····· SS). Intensities I are given times the square of the wavefactor q and divided by the emulsified volume fraction of the oil/surfactant mixture ($I \cdot q^2 / \Phi$) for a better comparison. Normalisation (in arbitrary units) of the curves given in graph a), to draw further systematic conclusions on the phases close to the PIC ≤ 80 wt-% H_2O .

was applied, using a log-normal distributed spherical model given in section 4.1.2.2. Depending on the used surfactant the finally formed nanoemulsions (> 80 wt-% (H₂O)) differ slightly in their average particle size and polydispersity (fig. 4.25 and table A.12), but are in general quite similar (as obtained by fitting the experimental data by means of eq. (3.29) and section (A.8.1)). They all show a pronounced trend for increasing particle size with increasing dilution (see fig. 4.25). This growth in particle size is easily explained by the fact that the surfactant is rather hydrophilic and therefore becomes increasingly dissolved into the aqueous phase upon dilution. By doing so the total surface available at the amphiphilic interface becomes smaller and therefore the droplets have to grow in size. The greater deviation at lower concentrations (80wt-% H₂O) arises from the change of phase inversion concentration (PIC) with the precise formulation. At this point it appears that the nanoemulsion formation is more preferable at a lower water content if the HLB-value is rather low (eg. shaded area of fig. 4.25).

However, for the nanoemulsions themselves, neither the concentration nor the HLB-value of the charged surfactants seem to indicate the sizing exclusively.

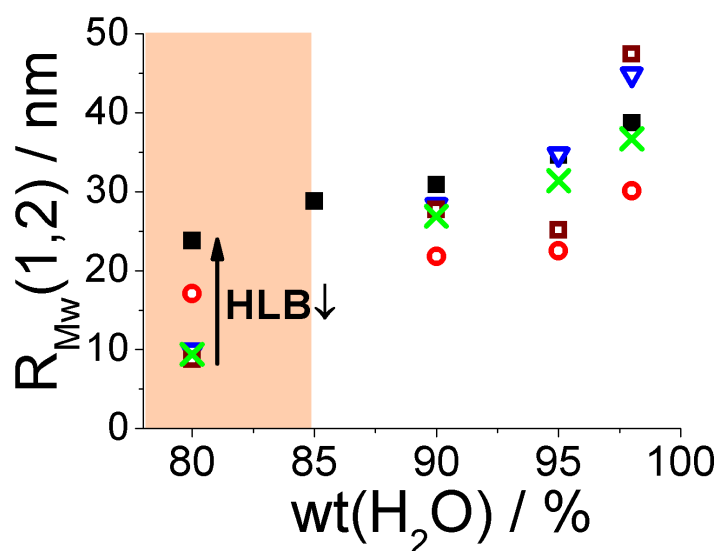


Figure 4.25: Mean mass weighted radius $R_{1/2,Mw}$ of nanoemulsions formed by dilution (H₂O-wt%) of different oil/surfactant formulations containing DEHC/K300/P4L/charged surfactant (66/12/21.1/0.9) using ■ DC, ▽ EQ, ○ AOT, □ SCO, × SS as charged surfactants. Radii were obtained from SANS-data treatment using a bimodal log-normal distributed spherical model. Beginning of nanoemulsion formation unclear in shaded area.

Charge. As the existence of an ionically charged surfactant is a crucial precondition for the nanoemulsion formation we were interested to see how strongly the nanoemulsion structures are influenced by reducing or increasing the given charge ratio (0.88wt-%) while keeping all other ratios constant, as in our model system Tego[®] Wipe DE (eg. tab. 3.2). We therefore varied the amount of charged surfactant from 0.2 - 2wt-% for the oil/surfactant-mixture. As charged surfactant we choose 2-sodium laureth sulfosuccinate, as it possess a similar molecular weight

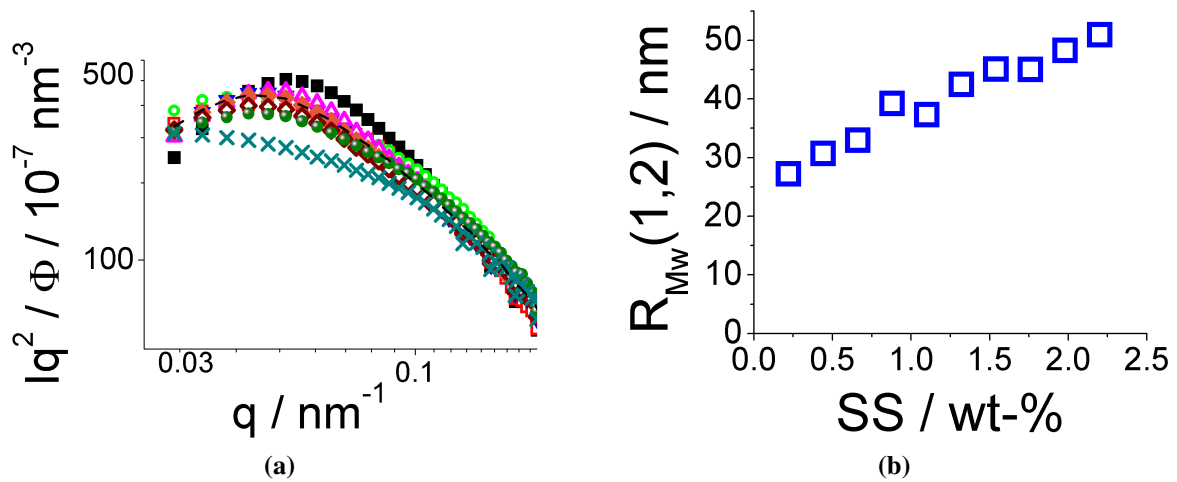


Figure 4.26: **a)** SANS-curves at low q -range for NEs at 95wt-% (H_2O) formed from oil/surfactant mixtures containing DEHC/K300/P4L/SS (66.6/12.1/21.3 + SS) varying the SS-concentration (■ 0.22, □ 0.44, ○ 0.66, - - - 0.88, ▼ 1.10, △ 1.32, ◆ 1.54, ◇ 1.76, ● 1.98, × 2.20 wt-%). A plot over the full q -range can be found in fig. of the A.8 appendix. **b)** Corresponding mean mass weighted radius $R_{1/2,Mw}$ obtained by SANS-data treatment with a bimodal log-normal distributed model.

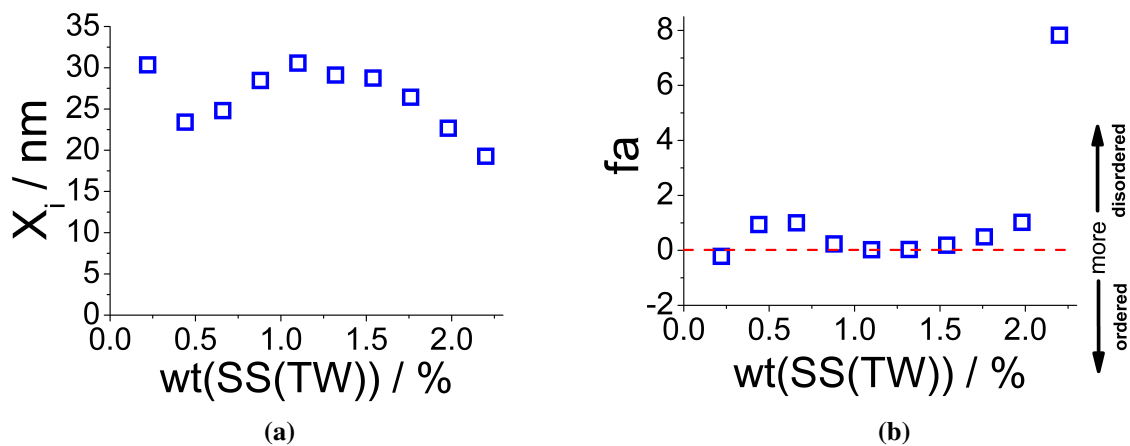


Figure 4.27: **a)** Correlation length X_i and **b)** amphiphilicity factor fa of Teubner-Strey model analysis; obtained from SANS-spectra of nanoemulsions prepared from O/S-mixtures based on DEHC/K300/P4L (66.7/12.1/21.2wt-%) and variable SS-concentration (0.22-2.2wt-%). O/S-mixtures were diluted with 95wt-% water.

and hence concentration like the singly anionically charged surfactant dilauryl citrate of the model system. However, as the sulfosuccinate is doubly charged one can anticipate greater structural changes while increasing slightly its portion in the O/S-mixture. SANS-studies, taken directly after sample preparation, did not show large differences at high q (eg. fig. A.8) of the formed nanoemulsions at 95-wt% water. Pronounced differences are seen at low scattering vector which are mostly due to the correlation peak that interestingly shifts to smaller q -vectors and gets less prominent with increasing charge. This behaviour corresponds to the formation of bigger aggregates and goes along with an electrostatically destabilisation of the nanoemulsion droplets, seen in figure 4.26b by the volume averaged mass weighted radii (compare eq. (A.3)) that we obtained by fitting a bimodal lognormal distributed spherical model (eg. section 3.2.13) to the SANS scattering curves (fig. 4.26a). Similar to our model system Tego[®] Wipe DE the SANS-data was better described by a bimodal than a monomodal model (residuals are not shown). The individual fit parameters are given in table 4.6 and visualised in figure 4.28. They show that the average growing of nanoemulsion droplets can be mainly attributed to the second (bigger) size distribution. It increases strongly in size (R_2), while being less polydisperse (σ_2) and less bulky (A) with increasing charge concentration. The smaller droplets contrary decrease only slightly in size (R_1) while becoming strongly polydisperse (σ_1) and being more bulky ($1-A$). It is obvious that whether a variation of the charged surfactant does not influence the initial NE-formation significantly, it accounts intensely for its (de)stabilisation (e.g. figure 4.27). The metastable state of a nanoemulsion is thereby mainly driven by the added SS-concentration (eg. fig. 4.75 in section 4.6.1). Teubner-Strey analysis (parameters are given in table A.13

| SS | A | $R_{1,Mw}$ | $R_{1,N}$ | σ_1 | $R_{2,Mw}$ | $R_{2,N}$ | σ_2 | $R_{1/2,Mw}$ (I0) |
|------|------|------------|-----------|------------|------------|-----------|------------|-------------------|
| wt-% | | nm | nm | | nm | nm | | nm |
| 0.22 | 0.12 | 24.7 | 19.7 | 0.26 | 27.5 | 20.6 | 0.52 | 27.2 |
| 0.44 | 0.24 | 21.1 | 16.9 | 0.22 | 31.6 | 24.4 | 0.46 | 30.7 |
| 0.66 | 0.34 | 19.1 | 15.3 | 0.28 | 34.2 | 26.2 | 0.48 | 33.0 |
| 0.88 | 0.40 | 18.3 | 14.5 | 0.38 | 40.5 | 32.0 | 0.37 | 39.2 |
| 1.10 | 0.37 | 16.0 | 13.1 | 0.44 | 38.2 | 31.5 | 0.36 | 37.3 |
| 1.32 | 0.50 | 16.1 | 13.0 | 0.54 | 43.7 | 37.4 | 0.25 | 42.5 |
| 1.54 | 0.55 | 15.6 | 12.3 | 0.61 | 46.3 | 40.4 | 0.24 | 45.1 |
| 1.76 | 0.57 | 14.8 | 11.9 | 0.62 | 46.2 | 41.0 | 0.25 | 45.0 |
| 1.98 | 0.67 | 15.1 | 11.8 | 0.68 | 49.8 | 44.8 | 0.23 | 48.3 |
| 2.20 | 0.68 | 14.2 | 11.6 | 0.65 | 52.3 | 47.4 | 0.28 | 50.9 |

Table 4.6: Following fit parameters belong to the SANS-curves of oil/surfactant mixtures containing DEHC/K300/P4L/SS (66.6/12.1/21.3 + SS) and varying the disodium laureth sulfosuccinate (SS) concentration (0.22, 0.44, 0.66, 0.88, 1.10, 1.32, 1.54, 1.76, 1.98 and 2.20 wt-%). The fit parameters are amplitude A , mass- (Mw) and number-weighted (N) radii R and polydispersity indices σ_1 and σ_2 for populations 1 and 2, respectively - using a Log-normal distributed spherical model for two populations; in addition mass weighted radius of both size distributions $R_{1/2,Mw}$ (I0). The contrast in scattering length density of solvent and particles ΔSLD was kept constant to $6.06 \cdot 10^{-6} \text{Å}^{-2}$ and the volume fraction Φ to 0.03.

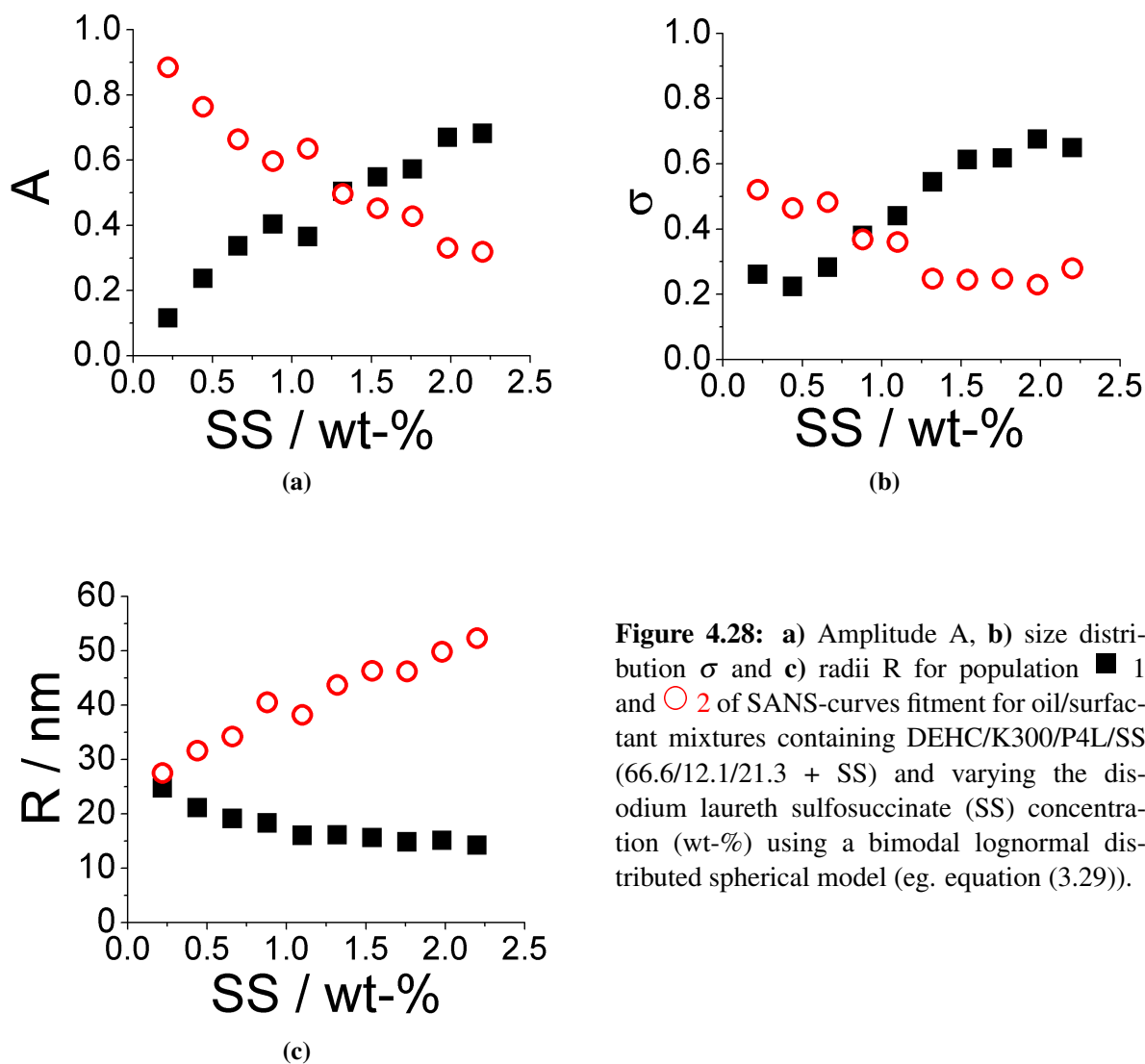


Figure 4.28: a) Amplitude A, b) size distribution σ and c) radii R for population \blacksquare 1 and \circ 2 of SANS-curves fitment for oil/surfactant mixtures containing DEHC/K300/P4L/SS (66.6/12.1/21.3 + SS) and varying the disodium laureth sulfosuccinate (SS) concentration (wt-%) using a bimodal lognormal distributed spherical model (eg. equation (3.29)).

in the appendix) of the obtained SANS-curves are illustrating this, as the correlation lengths ξ of the aggregates tend to an increase with increasing SS-concentration. Simultaneously the system gets more ordered, seen by the amphiphilicity factor f_a . However, after reaching an optimal charge balance (approx. 1 wt-% in the O/S-mixture) at which the particles are maximally separated and ordered, a further charge addition causes a decrease of correlation length and leads as well to more disordered systems. This continues until the particles converge due to the employed charge and break down while forming bigger aggregates (> 2 wt-%).

4.2.4 Variation of the oil component at constant O/S-ratio (78/22)

After having studied the electrostatic stabilisation and general influence of the charged surfactants on the finally formed nanoemulsions, we now want to investigate the effect that the type of oil has on the ability to form nanoemulsions at constant O/S-ratio (78/22). For this purpose we compared 2-ethylhexyl carbonate, 2-octyl carbonate and octyl octanoate that are basically esters with a C8-chain.

It might be noted in that context that we also investigated similar systems with dibutyl or di-

ethyl carbonate, but for both cases the formation of nanoemulsions was not achieved due to their higher polarities or rather high water solubilities (eg. Gordon parameters of different oils in table 4.3) and hence disability to form homogenous nanoemulsion qualified oil/surfactant-concentrates. In general, the homologous structures of the carbonate showed that an increase in aliphatic chain length facilitates the formation of a homogenous concentrate due to its increasing lipophilicity (eg. table 3.3).

4.2.4.1 Phase behaviour and stability

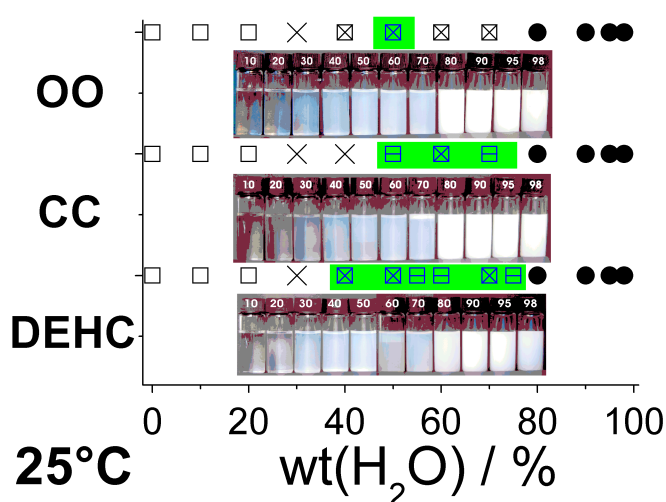


Figure 4.29: Comparison of the phase behaviour upon dilution pathway after 16 days of sample storage at $25.0 \pm ^\circ\text{C}$ for oil/surfactant (O/S) mixtures (oil/phenoxyethanol+parabenes/ polyglycerol-4 laurate/Rewoquat CR 3099) at constant O/S ratio (78/22) using different oil phases (2-ethylhexyl carbonate (DEHC), 2-octylcarbonate (CC) and octyloctanoate (OO)). □1Φ: clear oil; ×1Φ: μE -like (w/o); ⊠1Φ: μE -sponge phase; ○1Φ: grows o/w-E; ●1Φ: nm-E; □2Φ; ■3Φ -shadowed areas indicate flow birefringence

As the main oil component contributes with the highest mass ratio (66 wt-%) in the O/S-mixture, one may expect a considerable effect on the nanoemulsion properties. In the following the phase behaviour and stabilities are given for O/S-concentrates upon dilution pathway and in the nanoemulsion region. The O/S-compositions contain as oils (2-ethylhexyl carbonate (DEHC), 2-octyl carbonate (CC) or octyl octanoate (OO) (66wt-%)), the preservative mixture Euxyl K300 (phenoxy ethanol and parabens (in total 12wt-%)), polyglycerol-4 laurate (P4L) 21.1wt-% and the esterquat (EQ) Rewoquat CR 3099 as cationically charged surfactant ($\sim 0.9\text{wt}\%$). The EQ was chosen due to its charge characteristics; exhibiting an overall positive charge while forming nanoemulsions quite similar to our model system that contrary possesses an overall singly negative charge.

The phase behaviour (fig. 4.29) shows that the extent of the 2-phase region decreases in the order DEHC - CC - OO, while at the same time the size of the formed droplets increases in that order. A possible explanation of this behaviour could be that in this order the cosurfactant (amphiphilic) character of the oil decreases - and therefore it is less likely located in the amphiphilic interface.

Nevertheless, the structural evolution and the occurrence of nanoemulsions at a certain water concentration are quite similar and resemble therefore to the previous surfactant studies. This impression continues also for the analysis of nanoemulsion stabilities, where the radii increase slightly with time (eg. fig. 4.30a) but do neither show coalescence nor Ostwald ripening (eg. fig. 4.30b).

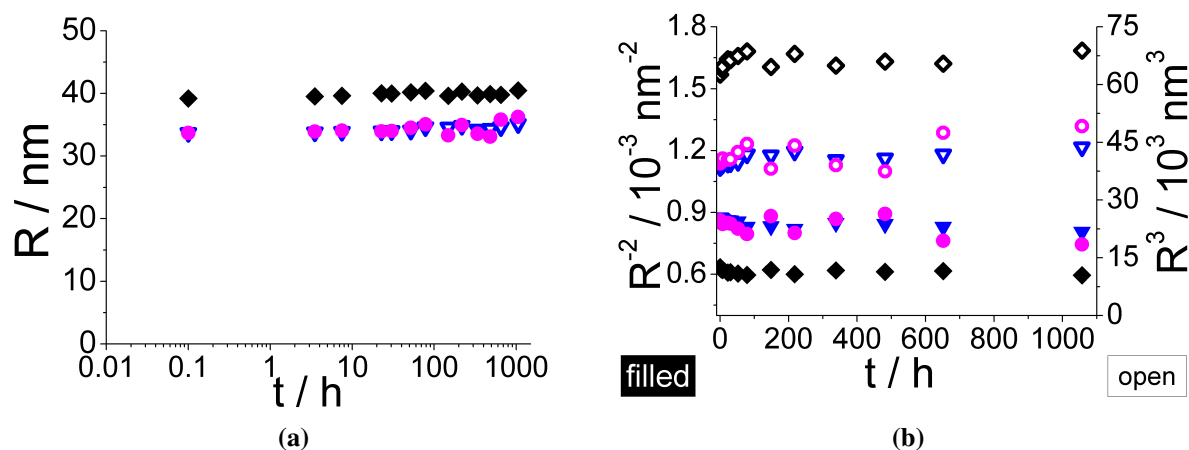


Figure 4.30: **a)** Radii R evolution with time t , from measured UV/Vis transmittance spectra of o/w nanoemulsions (5:95) in 1 mm cells at 25.0 ± 0.1 °C, accounting a whole spectra ($\lambda = 300 - 800$ nm) and proving according to eq. (3.3) its validity ($T_0 = 100\%$). Studied O/S-mixtures contained oil/K300/P4L/EQ (66/12/21.1/0.9) with different oil phases (∇ DEHC, \bullet CC, \blacklozenge OO). Radii evolution of nanoemulsions were observed for a time range t (~ 40 days). **b)** Verification of nanoemulsion breakdown by either coalescence (*left ordinate*), if linear dependency of inverse square radius R^{-2} vs. time t or Ostwald-ripening (*right ordinate*), if linear dependency of cubic radius R^3 vs. time t .

4.2.4.2 Small-Angle Neutron Scattering (SANS)

For a more detailed structural insight into the effect of the different oils on the nanoemulsion structure, SANS experiments were performed. The obtained scattering curves show very

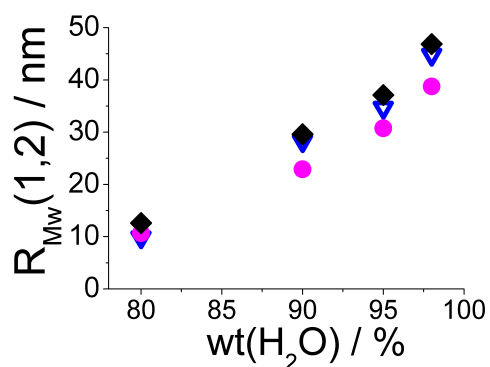


Figure 4.31: Mean mass weighted radius $R_{1/2,Mw}$ of nanoemulsions formed by dilution (H_2O -wt%) of different oil/surfactant formulations containing oil/K300/P4L/EQ (66/12/21.1/0.9 wt-%) using different oil components (∇ DEHC, \bullet CC, \blacklozenge OO). Radii were obtained from SANS-data treatment using a bimodal log-normal distributed spherical model.

similar scattering pattern (eg. fig. 4.32) at high dilution ratios ($> 80\%$ H_2O). Here the intensities increase only slightly at low q from 2-octyl carbonate over 2-ethyl hexyl carbonate to the octyl octanoate. This means that exchanging the main oil component with oils of similar polarity (eg. tab. 4.3) and molecular structure (eg. tab. A.2) yields droplets in quite comparable size ranges (eg. fig. 4.31 and fit data in tab. A.14).

Altogether a replacement of the main oil compound in the oil/surfactant mixture affects the final particle size less strongly than seen for the differently charged surfactants in respect to their effectively used mass fractions. This is not surprising as it just shows that this oil is not surface active and rather insoluble in the aqueous phase, therefore it just delivers the volume for the interior of the nanoemulsion droplets and accordingly has no effect on the particle size. Interesting differences are seen for the 80% sample, i.e. just upon entering the

NE regime. Here apparently no simple droplet structure is present but one sees highly ordered systems, where the extent of ordering is most pronounced for the DEHC and less so for the OO and CC. This can be seen by the occurrence of a more or less pronounced double-peak (degree of ordering) in figure 4.32a whose separation in q shows a ratio of 1:2 that typically lamellar structures are showing (see also fig. 4.23).

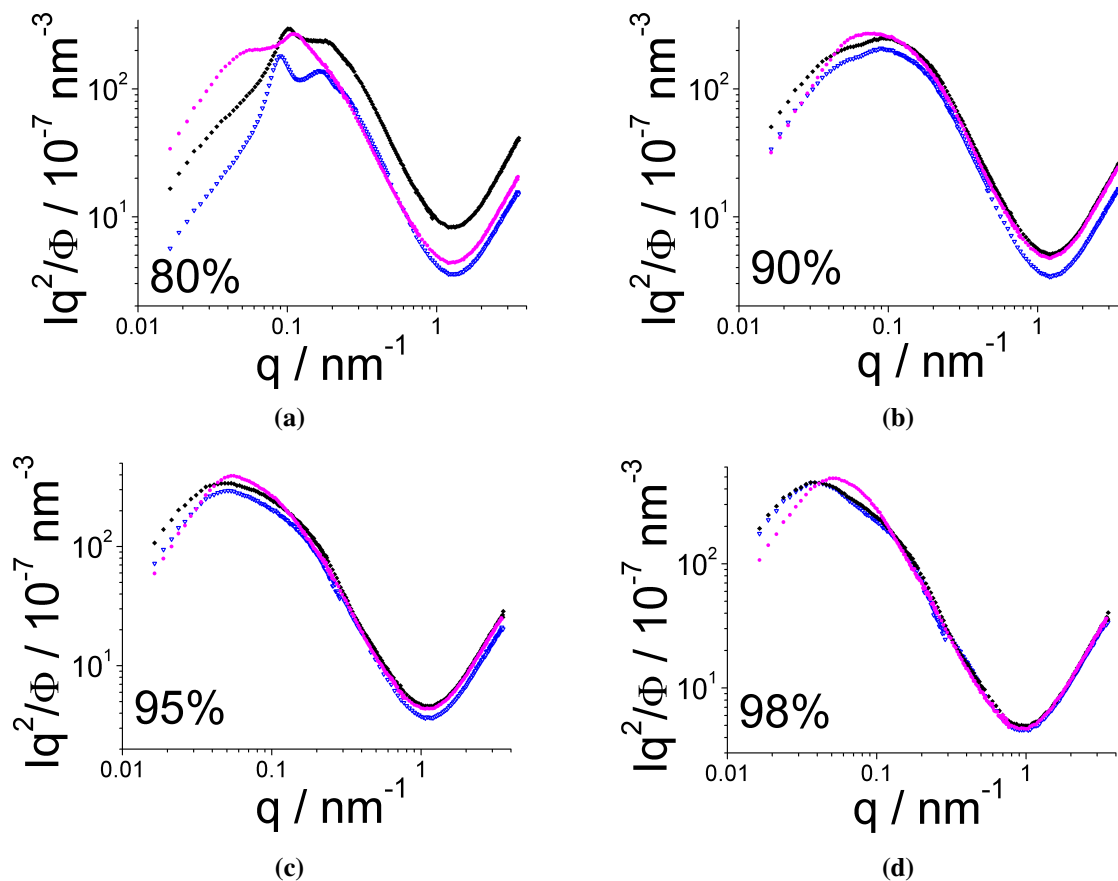


Figure 4.32: SANS-scattering curves in the nanoemulsion region of oil/water dilutions at 80, 90, 95 and 98% (H₂O respectively) for oil/surfactant mixtures oil/K300/P4L/EQ (66/12/21.1/0.9 wt-%) using different oil components (∇ DEHC, \bullet CC, \blacklozenge OO). Intensities I are given times the square of the wavefactor q and divided by the emulsified volume fraction of the oil/surfactant mixture ($I \cdot q^2 / \Phi$) due to better comparison reasons.

4.2.5 Conclusion of components influence, used in the O/S-mixture, on PIC nanoemulsion formation and -stability

The influence of nanoemulsions and their stability formed by the phase inversion concentration (PIC) method was investigated. For this purpose we employed a model system based on the commercially available O/S-mixture Tego[®] Wipe DE that is known to be suited to form nanoemulsions by the PIC-method. The O/S-mixture, composed of 78wt-% oil plus cosurfactant³ (preservative mixture) and 22wt-% nonionic surfactant plus ionic surfactant, was modified at variable and constant O/S-ratio.

Modifications at variable O/S-ratio were done exchanging the oil, cosurfactant and nonionic surfactant component of the model system by a systematic determination of the right proportions to ensure a nanoemulsion formation at high dilution ratios. In doing so, we figured out that the exact PIC depends on the detailed O/S-composition and the formation process. Thereby especially the amount of the preservative mixture has to be balanced with respect to the remaining ingredients, whereas studies showed that polar oils require more and unpolar oils less cosurfactant. Generally the increase of the oils aliphatic chain length ($\#C \geq 8$) facilitates the formation of a homogenous concentrate due to its increasing lipophilicity.

For a better comparability of the formed nanoemulsion systems modifications at constant O/S-ratio (78/22) were done by exchanging the oil, nonionic- and ionic surfactant component of the model system. Both, modifications at variable and constant O/S-ratios revealed a narrow molecule range for forming PIC-suitable O/S-mixtures with this system. As for example no homogenous concentrates could be formulated despite intensive replacement studies for using different nonionic surfactants of the glyceride type.

However, from the concentrates modification studies at constant O/S-ratio we learned that the system is very sensitive to the employed charges. Electro static conditions seem to play a major role for the nanoemulsions stabilisation, as in their absence it is impossible to emulsify the oil phase into the aqueous one. Systematic variations of the charged surfactant component revealed a strong affection, in respect to the employed fraction (1wt-%), of the physical properties (viscosity, conductivity) for the phases formed upon dilution to the PIC that do not correlate with the surfactants properties (concentration, HLB-value, charge). Nevertheless, some general tendencies are evident like the passing of a more or less extended region of flow birefringence (ordered region) and the quite certain occurrence of the nanoemulsion phase at higher dilution ratios, no matter if cat- or anionically surfactants are used. Moreover the PIC-position, the structure of the resulting nanoemulsions and their stability stays relatively unaffected (at standard conditions), unless higher temperatures ($> 25^{\circ}\text{C}$) are employed. This effect gets more compensated with increasing charged surfactant concentrations. Although greater charge concentrations (≈ 2

³Accounts as oil phase for the given O/S-expressions.

mM) may cause nanoemulsions destabilisation due to a decrease of the correlation length (mean distance of aggregates) that lead to a reversible creaming.

With respect to the effectively employed mass fractions the exchange of the ionic surfactant component ($\sim 1\text{wt-}\%$) in the O/S-mixture affects the final particle size more strongly (deviation of mean particle size $\Delta R \approx 12\text{ nm}$) as if the main oil phase ($66\text{wt-}\%$) is replaced (deviation of mean particle size $\Delta R \approx 7\text{ nm}$). The structural evolution and the occurrence of nanoemulsions at a certain water concentration resemble with the ionic surfactant studies and do not show any considerable effects on the nanoemulsion properties. This is not surprising as the oils are not surface active and therefore rather insoluble in the aqueous phase. They just deliver the volume for the interior of the nanoemulsion droplets, which should not have any effect on the particle size.

As nanoemulsions are metastable systems their aggregates grow with time. This size evolution proceeds for the different O/S-mixtures almost identical slowly (gradiental creaming in several month) and does not show significantly clear evidences of pure coalescence- or Ostwald ripening driven breakdown processes. From our observations we could derive that buoyancy forces may have a considerably contribution in the particle creaming but should be far too slow in overlapping other breakdown processes. Hence, more complex breakdown dynamics might be present that cause this unique long-term metastability of this system.

However, we might have found an explanation for this extraordinary stability behaviour while employing the well known AOT as charged surfactant that normally facilitates the formation of thermodynamically stable microemulsions. If one considers a coexistence of microemulsion droplets beside metastable nanoemulsion ones, one may assume that the balance gets somewhat displaced in direction microemulsion during the initial dilution process when AOT is employed. And indeed the formulated nanoemulsions for this system appeared substantially smaller (mean size $\sim 25\text{ nm}$ instead of $\sim 35\text{ nm}$) than for the others.

4.3 Variation of O/S-ratio at fixed water concentration of a PIC-formed NE

The nanoemulsion systems we are studying are based on the phase inversion concentration PIC method, where just a certain amount of water has to be given to an oil-surfactant-mixture that favours the formation of long-time metastable nanoemulsions due to a change in curvature upon dilution. For our investigations we used an O/S-composition formulated of diethylhexyl carbonate (DEHC), Euxyl K300 (K300), polyglycerol-4 laurate (P4L) and disodium laureth sulfosuccinate (SS).

The ingredients have been chosen due to the composition of our commercial available model system Tego Wipe DE (eg. tab. 3.2), replacing only the anionic surfactant dilauryl citrate (DC), which was not purely available, by an alternative (SS) that parallels its physical properties most likely (eg. results in section 4.2.3).

In the following studies the term oil corresponds to a homogenous mixture of DEHC and K300 ($\sim 85/15$); just as for the term surfactant a homogenous mixture of P4L and SS ($\sim 96/4$) is meant. In order to elucidate the role of the O/S-ratio on the ability to form nanoemulsions we studied such a variation at a fixed dilution ratio (95wt-% water). According to the PIC-mechanism nanoemulsions are only formed at high di-

lution ratios ($> 75\%$ H_2O) and hence therefore restricted to a small corner of the ternary phase diagram based on oil/surfactant/water (eg. fig. 4.15). Detailed studies on the phase behaviour in this region showed a quite narrow domain in which the nanoemulsions are formed (eg. section 4.2). This is also depicted in figure 4.33 which represents a zoom in on a ternary phase diagram at high dilution ratios ($> 75\%$ H_2O) of the O/S-mixtures. The line given at 95wt-% water is the cut through the ternary phase diagram taken in our experiments.

O/S-mixtures starting from homogenous oil and surfactant stock solutions (as well as proper mixtures of the individual compounds) caused a phase separation for O/S-ratios with a surfactant concentration $S < 10\text{wt}\%$ and $65 < S < 95\text{wt}\%$. Due to the surfactant properties of polyglycerol-4 laurate the O/S-mixtures become more viscous with increasing surfactant con-

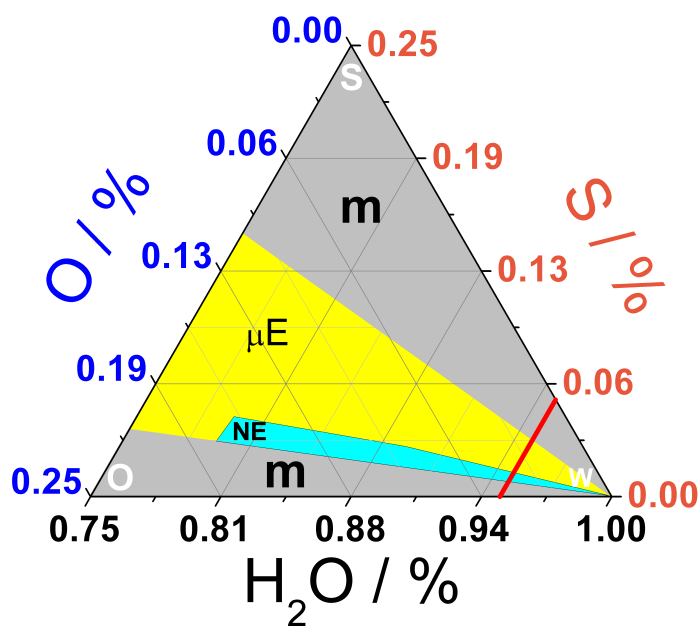


Figure 4.33: Zoom in of a ternary phase diagram based on oil (O) / surfactant (S) /water (W). Studied O/S-mixture is based on DEHC/K300 as oil (85/15) and P4L/SS as surfactant phase (96/4). O/S-dilutions form nanoemulsions (NE), microemulsions (μE) and multiple phase regions (m, 2Φ). Red dilution line at 95wt-% water (right corner) illustrates a cut through the phase diagram for the samples studied in more detail in this section.

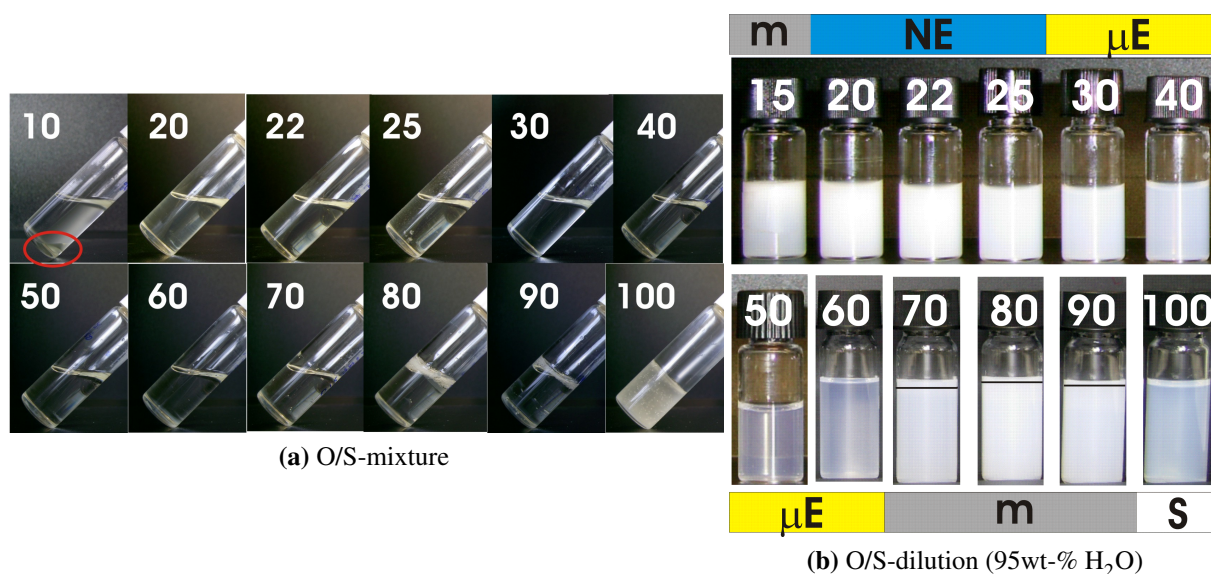


Figure 4.34: **a)** O/S-mixtures for the system DEHC/K300/P4L/SS; varying the O/S-ratio with DEHC/K300 as oil (85/15) and P4L/SS as surfactant phase (96/4). Given numbers are indicating the surfactant concentration (s:10, 20, 30... 100wt-%). Tilted positions should visualise the O/S-mixtures viscosity that increases strongly at ~ 60 -70wt-% surfactant. Red circle marks inhomogeneity at 10wt-% surfactant that stayed also after heat-treatment (70 °C). Influence of heat homogenised O/S-mixtures for surfactant concentrations $65 < S < 95$ wt-%. **b)** Dilution of O/S-mixtures at constant dilution ratio (95wt-% H₂O) forming nanoemulsions (NE), microemulsions (μ E) and multiple phases (m: 2Φ - line marks phase boundary) dependent on the position in the phase diagram (eg. fig. 4.33).

centration (eg. fig. 4.34a). As already mentioned and visible in figure 4.34b, we are passing through different phases at constant dilution ratio (95wt-% H₂O) when the O/S-ratio is varied. At very low surfactant concentrations ($S < 10\%$) biphasic systems are formed while trying to form a homogenous O/S-concentrate (eg. fig. 4.34a). Heating (70 °C) did not change this behaviour. As the way of formulation does not change the final structure for such systems, direct dilutions of the ingredients net weight have been done, resulting in unstable macroemulsions. At higher surfactant concentration nanoemulsions are formed within a narrow concentration range ($20 < NE < 25$ wt-% S of O/S-mixtures), until subsequently a microemulsion region is reached when more surfactant is employed. It is reasonable that with increasing surfactant content and less oil one continuously reaches a microemulsion phase that for the pure surfactant turns into a micellar solution. From this point of view it is more astonishing that at higher surfactant concentrations ($S > 60\%$, eg. fig. 4.34b) another biphasic region is observed that has a strong greyish appearance, as that amount of surfactant is insufficient to stabilise the microemulsion. Only at $S > 95$ wt-% a more bluish single-phased surfactant solution is formed again.

Conductivity measurements on macroscopically homogenous mixtures for this system directly after preparation (eg. figure 4.35), show a linear dependence with increasing surfactant concentration until ~ 55 wt-%, which is related to the employed charge of the anionic surfactant fraction (red line in fig. 4.35). This tendency continues for the nano- and microemulsion region (NE and μ E), and breaks primary shortly before reaching the homogenised multiphase region

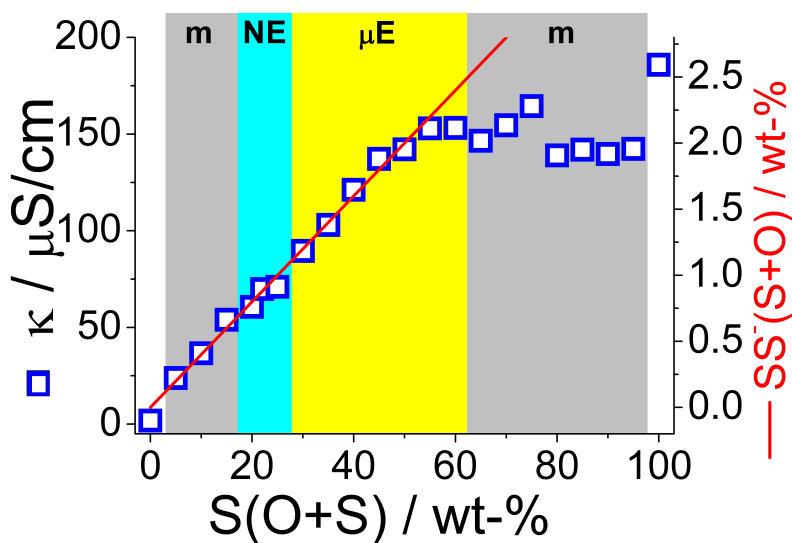


Figure 4.35: Conductivity for oil-surfactant (O/S) variation at constant dilution (95wt-% H₂O) at $25.0 \pm 0.1^\circ\text{C}$. The different regions of the phase diagram are nanoemulsion (NE), microemulsion (μE) and biphasic domains (m). Biphasic samples were measured prior to macroscopic phase separation. Linear line (red) visualises the theoretical volume fraction of charged surfactant component (SS) in the O/S-mixture (DEHC/K300/P4L/SS).

(m) at high surfactant ratios ($S(S+O) \geq 60\text{wt}\%$). Hence, the structures formed in this region might be mainly composed of surfactant-assemblies.

4.3.1 SANS-analysis

In consideration to this unordinary structural behaviour, we did more detailed analysis on the formed structures by SANS measurements. Figure 4.37 depicts SANS curves of the O/S-variation at 95wt-% water. First model free analysis on the particle sizes were done by Guiniers approximation (eq. (3.17)), assuming that always spherical aggregates are formed upon O/S-dilution and extrapolating the SANS scattering curves to zero angle intensity $I(q=0)$. The mass weighted apparent radii obtained are given in figure 4.36 and show different tendencies dependent on the given structures (inset shows number weighted radius of gyration). Table A.4.1 in the appendix summarises the model free Guinier-analysis. As expected, the particles formed in the nanoemulsion region possess the greatest size that with increasing surfactant concentra-

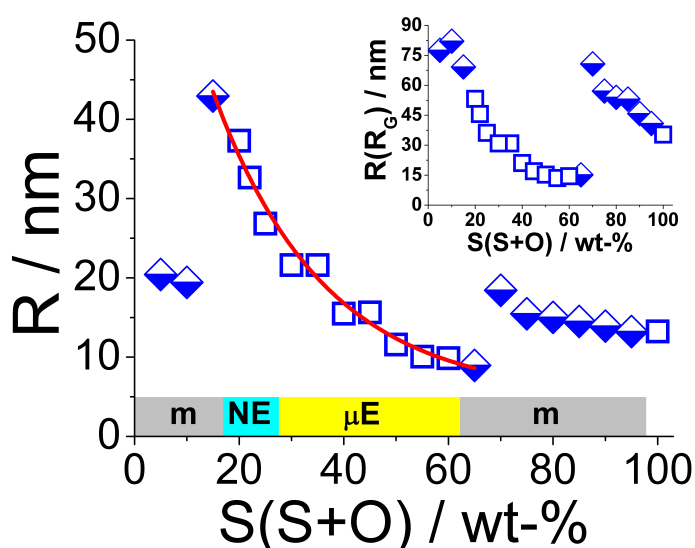


Figure 4.36: Obtained mass weighted radii $R_{Mw}(I_0)$ via Guinier approximation for extrapolations to zero angle intensity $I(q = 0)$ of SANS curves given in fig. 4.37. Oil phase contained DEHC+K300, surfactant phase P4L+SS. O/S-mixtures were diluted to 95wt-% water. For biphasic samples only \blacklozenge lower phase gave adequate volumes for SANS measurements. Inset shows number weighted radii obtained by the radius of gyration $R(R_G)$.

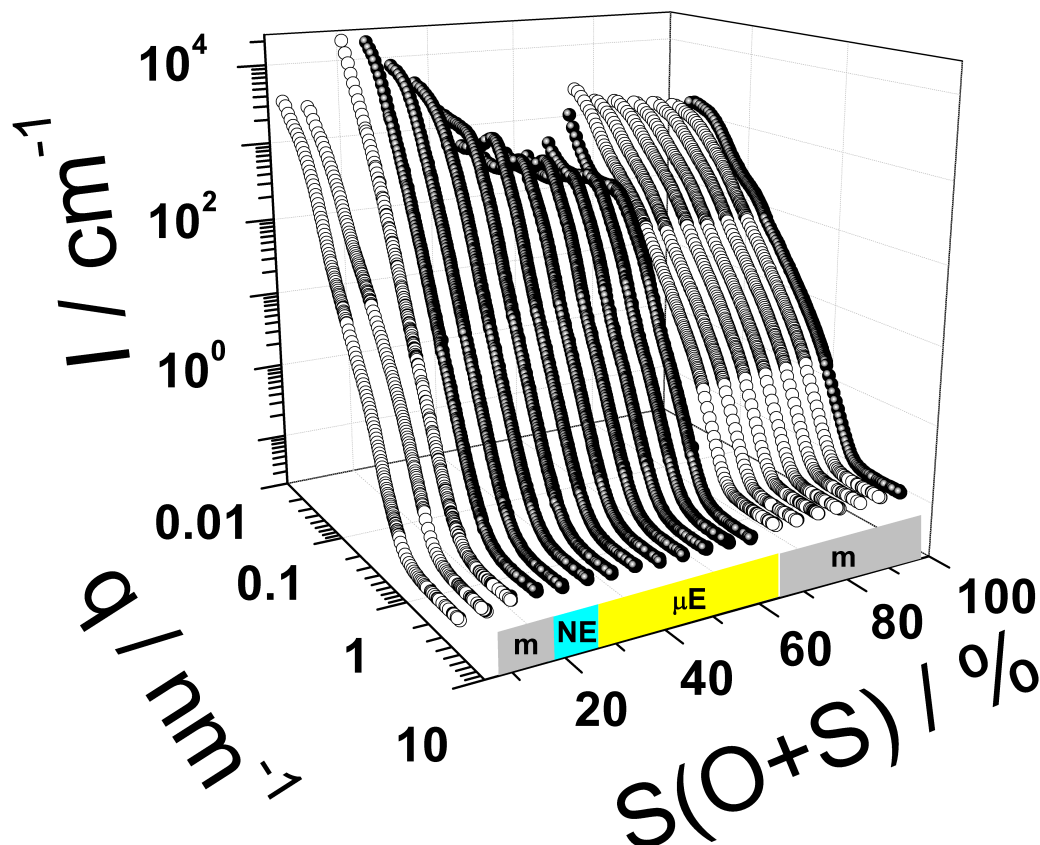


Figure 4.37: SANS-measurements of diluted O/S-mixtures that bases on DEHC/K300 as oil (85/15) and P4L/SS as surfactant phase (96/4). Dilution ratio was kept constant at 95wt-% D₂O (water concentration refers to equivalent concentration of H₂O). Cut through the phase digram crosses domains of nanoemulsions (NE), microemulsions (μ E) and biphasic regions (m). At 100% surfactant a micellar phase is formed. In case of biphasic regions only lower phases \circ have been measured, as for the upper ones no adequate volume was available.

tion decreases due to a formation of stable microemulsion droplets. However, this decrease is interrupted once the surfactant-rich biphasic region is reached and holds until the pure single surfactant dilution. Following we will discuss and map the structures that form for the different O/S-ratios.

4.3.1.1 O/S-ratio: $0 < S \leq 15$ wt-% surfactant S

For surfactant concentrations $S \leq 15$ wt-% instable o/w-emulsions are formed, whose surfactant phase is not sufficient to stabilise the dispersed oil phase in the aqueous media. Subsequently, some oil moves to the samples top, which gave insufficient volumes for SANS-measurement. However, the appearance of the SANS-curves for the individual samples follows an almost q^{-4} -scattering for high q -values and passes to a more general scattering with a slope of q^{-3} for the mid and low q -range, implying a great polydispersity for the dispersed oil droplets due to a lack of surfactant. Thereby the q^{-4} -dependence becomes more and the q^{-3} -dependence less pronounced while approaching the nanoemulsion region (eg. fig. 4.38). For the polydispersi-

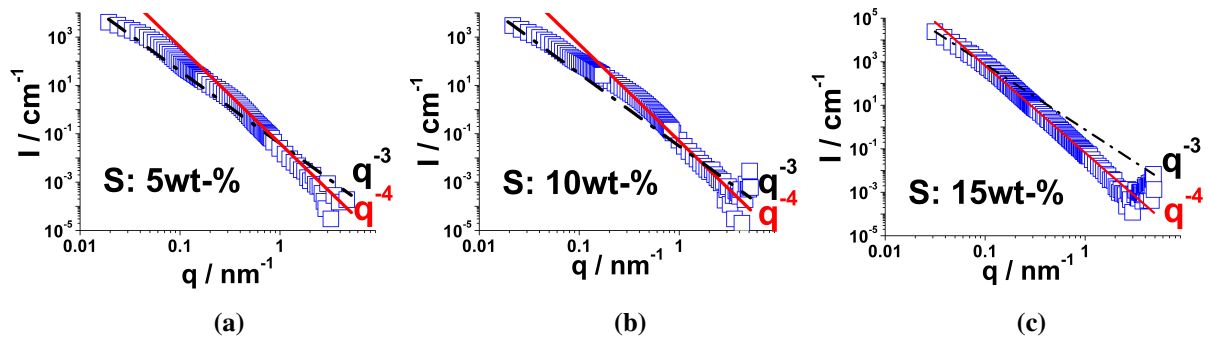


Figure 4.38: Dependence of scattering vector q for SANS-scattering curves of o/w-emulsions. O/S-mixtures that were diluted to 95wt-% water contained **a)** 5, **b)** 10 and **c)** 15wt-% surfactant S. — q^{-4} is an indication of spherical scattering. - - q^{-3} can be understood as the factor of polydispersity in this case.

ties compare also radii divergencies between Guinier approximated mass weighted radii and number weighted radii obtained by the radius of gyration (fig. 4.36 in the current section and table A.15 of the appendix) for low surfactant concentrations.

4.3.1.2 O/S-ratio: $15 < S \leq 65$ wt-% surfactant S

For surfactant concentrations $15 < S \leq 65$ wt-% the dispersed oil phase can be sufficiently stabilised by the employed surfactant. This leads to metastable nanoemulsions in a narrow surfactant concentration range ($15 < S < 30$ wt-%) exhibiting mean particle sizes of 25 - 35 nm. With increasing surfactant concentration the particle size is decreasing exponentially as a function of $S/(S+O)$ (eg. single exponential fit of fig. 4.36) and causes a continuous transition to blue looking stable microemulsion phases ($30 < S < 65$ wt-%) of approximately 10 nm. Simultaneously the mean particle size is decreasing before suddenly a leap to slightly bigger aggregates occurs. However, so far we always used a lognormal bimodal distributed spherical model for

| S(O/S) | Φ_1 | σ_1 | $R_{N,1}$ nm | Φ_2 | σ_2 | $R_{N,2}$ nm | S(O+S) wt-% | Φ | σ | R_N nm |
|--------|----------|------------|-----------------|----------|------------|-----------------|----------------|--------|----------|-------------|
| 20 | 0.012 | 0.54 | 9.16 | 0.023 | 0.34 | 32.8 | 30 | 0.034 | 0.47 | 10.3 |
| 22 | 0.015 | 0.51 | 10.3 | 0.020 | 0.31 | 31.8 | 35 | 0.033 | 0.49 | 9.94 |
| 25 | 0.015 | 0.51 | 9.40 | 0.018 | 0.27 | 29.0 | 40 | 0.032 | 0.51 | 9.08 |
| | | | | | | | 45 | 0.028 | 0.54 | 6.61 |
| | | | | | | | 50 | 0.032 | 0.53 | 6.64 |
| | | | | | | | 55 | 0.030 | 0.54 | 5.69 |
| | | | | | | | 60 | 0.030 | 0.67 | 3.31 |
| | | | | | | | 65 | 0.028 | 0.71 | 2.53 |

Table 4.7: *left:* SANS-fit parameters of bimodal lognormal distributed spherical model for systems in nanoemulsion region (volume fraction Φ , polydispersity σ and number weighted droplet radius R of population 1 and 2), *right:* SANS-fit parameters of monomodal lognormal distributed spherical model for systems in microemulsion region.

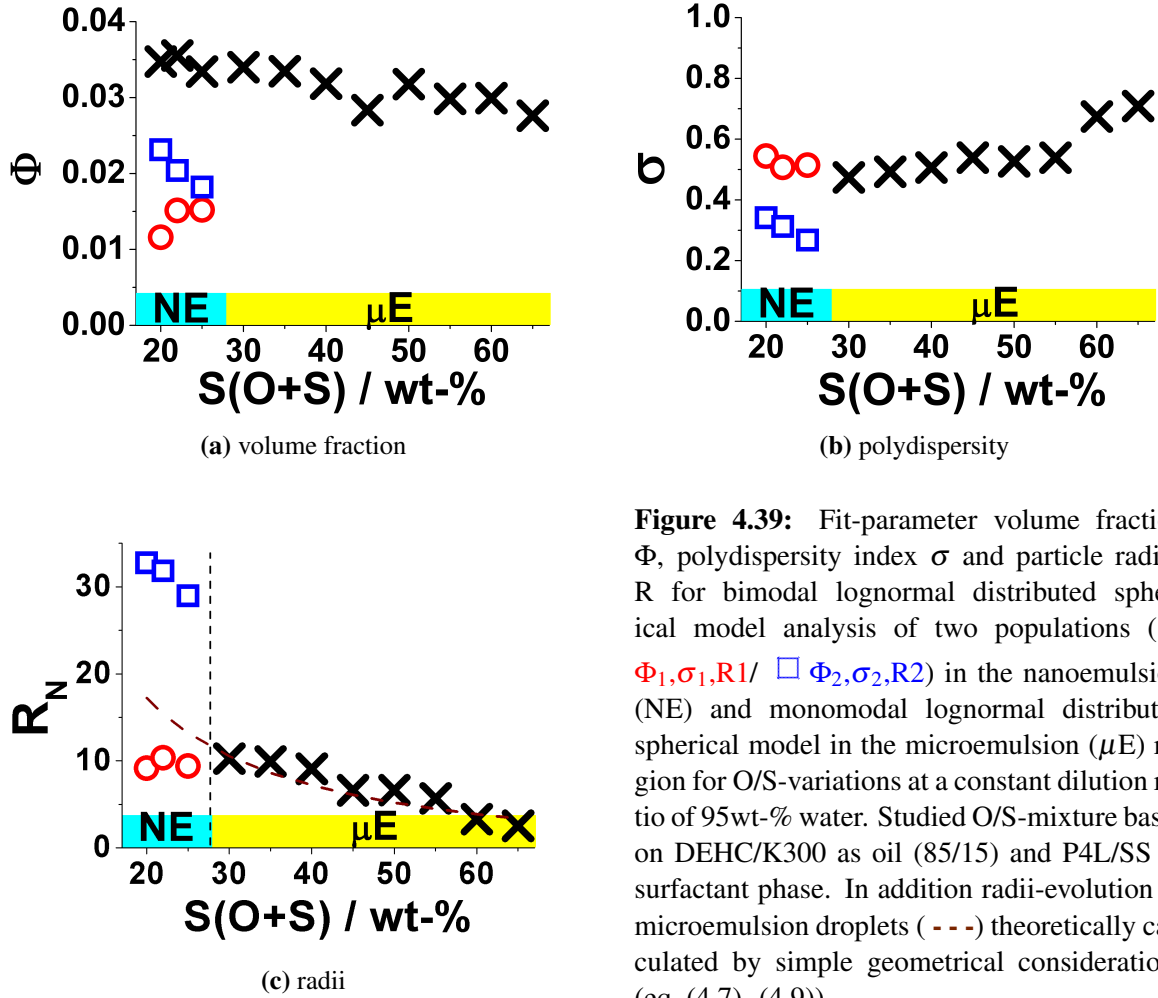


Figure 4.39: Fit-parameter volume fraction Φ , polydispersity index σ and particle radius R for bimodal lognormal distributed spherical model analysis of two populations (\circ Φ_1, σ_1, R_1 / \square Φ_2, σ_2, R_2) in the nanoemulsion (NE) and monomodal lognormal distributed spherical model in the microemulsion (μE) region for O/S-variations at a constant dilution ratio of 95wt-% water. Studied O/S-mixture bases on DEHC/K300 as oil (85/15) and P4L/SS as surfactant phase. In addition radii-evolution of microemulsion droplets (---) theoretically calculated by simple geometrical considerations (eq. (4.7)- (4.9)).

the structure analysis of the PIC-formed nanoemulsions (eg. section 4.1.2.2f.). For the stable microemulsions this model is not anymore applicable (the volume fraction of the second size distribution turns negative) and thus needs to be reduced to a single size distribution (eg. section 3.2.13.3). Table 4.7 summarises the fit parameters of both models (bi- and mono-modal) applied either on the scattering curves given by the nano- or microemulsions. The individual fit parameters are visualised in figure 4.39.

It is obvious that the smaller sized population of the bimodal nanoemulsion droplets $R_{N,1}$ changes more or less continuously into the single sized microemulsion phase. A theoretical radius of microemulsions can be estimated by a geometrical approximation according to the corresponding total volume $V_{\mu E}$ of a sphere (eq. (4.7)) and its total droplet-area $A_{\mu E}$ (eq. (4.8)) [203].

$$V_{\mu E} = \frac{4}{3} \cdot \pi R^3 = n_s \cdot v_s + n_o \cdot v_o \quad (4.7)$$

$$A_{\mu E} = 4 \cdot \pi R^2 = n_s \cdot a_h \quad (4.8)$$

$$V/A = \frac{R_{\mu E}}{3} = \frac{v_s}{a_h} + \frac{n_o v_o}{n_s a_h} \quad (4.9)$$

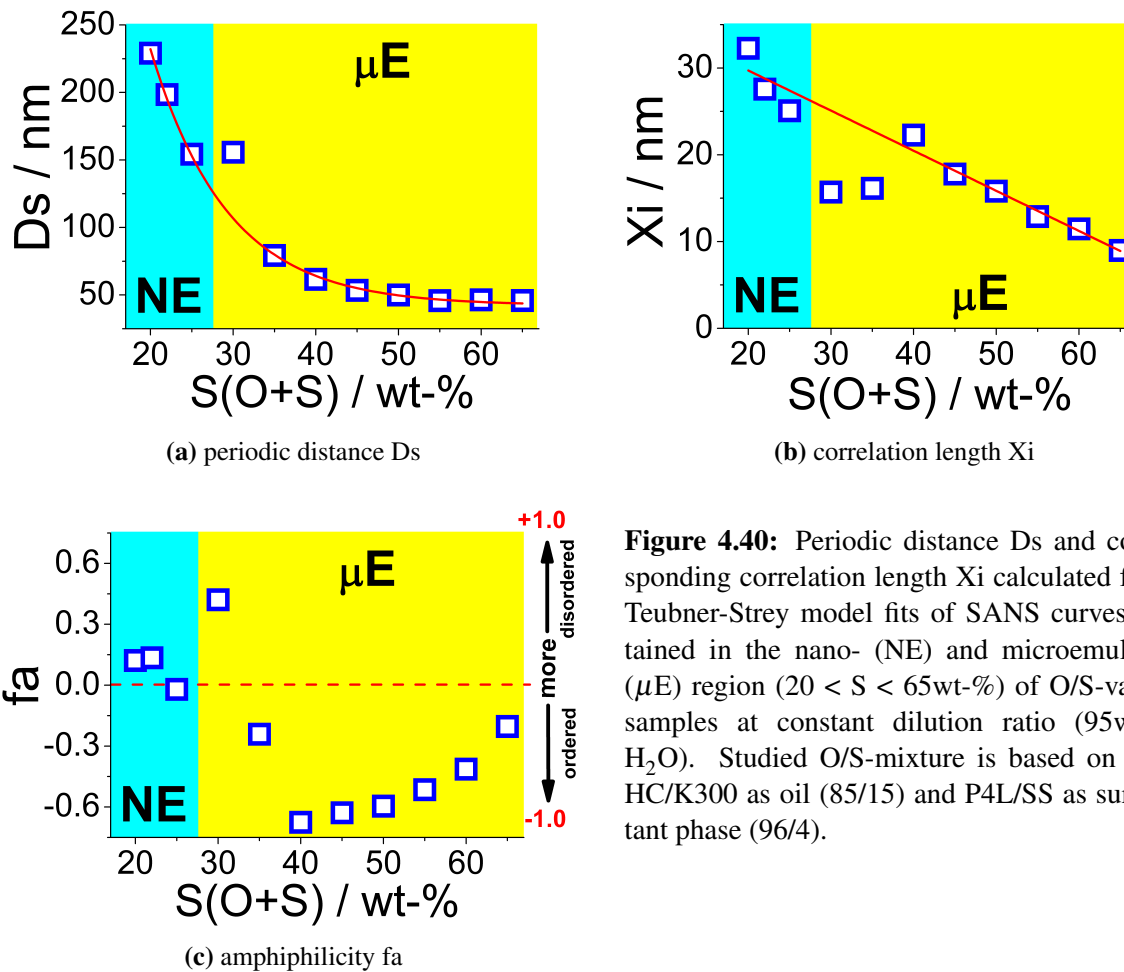


Figure 4.40: Periodic distance D_s and corresponding correlation length X_i calculated from Teubner-Strey model fits of SANS curves obtained in the nano- (NE) and microemulsion (μE) region ($20 < S < 65 \text{ wt-}\%$) of O/S-varied samples at constant dilution ratio (95wt-% H_2O). Studied O/S-mixture is based on DEHC/K300 as oil (85/15) and P4L/SS as surfactant phase (96/4).

With n_s and n_o are the number of either surfactant (s) or oil (o) molecules given in an aggregate. v_s and v_o are the volume of the hydrophobic part of the surfactant molecule and the volume of the oil per aggregate. a_h is the surfactant head group area.

The experimentally observed radii evolution by changing the O/S-composition in the microemulsion region ($30 < S \leq 65 \text{ wt-}\%$) is in good agreement with the theory one would expect for simple microemulsion phases (e.g figure 4.39c). This result supports our assumption on PIC-formulated nanoemulsions (eg. conclusion of section 4.1) for the coexistence of larger sized, metastable emulsion droplets that go along with stable microemulsion droplets due to a lack of stabilising surfactant.

For the sake of completeness Teubner-Strey analysis (eg. section 3.2.13.2) revealed a single exponential decay for the periodic distance D_s of oil and water regions with increasing surfactant concentration. Simultaneously the correlation length X_i (interparticle distance) decreases almost linearly with the decrease of particle size (compare fig. 4.39c and 4.40b), which is more pronounced for high surfactant concentrations. In fact close to the nano-/microemulsion transition ($\approx 30 \text{ wt-}\% S(S+O)$) large deviations of the linear trend occur due to a rearrangement of the systems properties. This can also be seen in the amphiphilicity data that describes the degree of ordering in the system. The order of bimodally distributed nanoemulsions is more or less constant and shows a strong dislocation at the transition point of nano- to microemulsions. This dislocation gets reversed with higher surfactant concentrations; until a microemulsion system

of maximal order ($f_a \sim -0.7$) is reached at a surfactant concentration of 40wt-%. Subsequently and somehow surprisingly, the system disorders anew. The following section might explain this progression. However, the obtained Teubner Strey parameters for the nano- and microemulsion SANS-data of the O/S-variation are given in table A.16 of the appendix. The most meaningful Teubner Strey criteria (periodicity, correlation length and amphiphilicity) are visualised in figure 4.40.

4.3.1.3 O/S-ratio: $65 < S \leq 100$ wt-% surfactant S

During our investigations on the O/S-variation of oil-surfactant mixtures based on DEHC/K300 as oil (85/15) and P4L/SS as surfactant phase (96/4), we observed an irregular phase behaviour for high surfactant ratios $S(S+O) > 65$ wt-% at constant dilution ratio (95wt-% water). After passing from nano- to microemulsion phases with increasing surfactant concentration, we expected a continuous change to oil solubilising micellar solutions that finally remain only micelles in case of the pure surfactant ($S = 100$ wt-%). In contrast the system causes biphasic samples over a broad concentration range ($65 < S \leq 95$ wt-% surfactant S).

A similar inverse behaviour was observed by *Hoffmann et al.* [77] for the solubilisation of some aromatic hydrocarbons (benzene, toluene, cyclohexane), which is due to a rod-sphere transition upon solubilisation. Their studies revealed the formation of a coacervate phase due to a condensation of rodlike micelles⁴, when a certain concentration of solubilised hydrocarbon phase was crossed. Then the single-phase solution of solubilised hydrocarbon separates into two phases one was in a denser and the other in a more diluted state, before sufficient oil is present to transform the rodlike micelles into globular microemulsion droplets.

However, for the given case biphasic structures are formed in which the lower phases are much more voluminous than for the upper ones (eg. fig. 4.34b). SANS-measurements for the lower phases were accomplished to get a more detailed insight into the present structures (eg. fig. 4.37). As for the presented system DEHC/K300/P4L/SS no sufficient volumes of the upper phases were available we exchanged the anionically charged surfactant component disodium laureth sulfosuccinate SS by the cationically charged esterquat EQ, which provides adequate volumes in the biphasic region. From our PIC studies we already experienced that no significant structural changes occur in the nanoemulsion region while exchanging this component (eg. section 4.2.3). A direct comparison of the structures formed for a surfactant concentration of 80wt-% revealed indeed no considerable differences (eg. fig. 4.41a) for the lower phases. Only slight divergences appeared due to the different charge properties (eg. charged surfactant properties in table 3.4). As the variation of the charged surfactant should not be the scope of this section, no further analysis were done concerning the charge influence. However, as the EQ-system provides sufficient volumes for the upper phases, SANS measurements on both

⁴Rod structures would reveal a q^{-1} -dependence for the SANS curves.

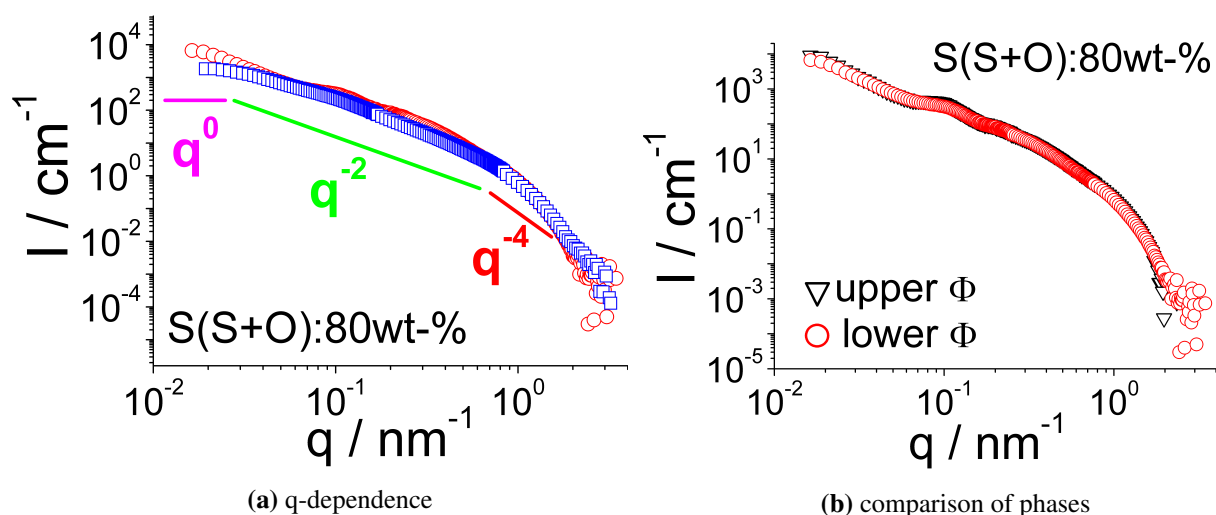


Figure 4.41: **a)** Comparison of the lower phase (Φ) for O/S-mixtures ($S(S+O) = 80\text{wt-}\%$) containing \square DEHC/K300/P4L/SS and \circ DEHC/K300/P4L/EQ (17/3/76.8/3.2 wt-% -respectively O/S 20/80) that were diluted to 95wt-% water; in addition indication of q^n -dependence of the measured scattering curves for the individual q -ranges. **b)** Comparison of the \circ lower and ∇ upper phase (Φ) at a surfactant concentration of 80wt-% of the O/S-mixture DEHC/K300/P4L/EQ (17/3/76.8/3.2 wt-%).

phases at a surfactant concentration of 80wt-% revealed no great structural differences (eg. figure 4.41b). The structures formed for the lower phases in the biphasic region of the SS-system remain almost constant with increasing surfactant concentration (eg. fig. 4.37). Interpretations of the given SANS-data for these phases revealed a predominantly q^{-2} -dependence that can go a long with the formation of planar lamellar structures as given in the form of vesicles. The instantaneous decrease of electric conductivity we observed while entering the biphasic region might suggest such a formation due to the entrapment of ions within the vesicles. Within more detailed model analysis for the given structures it emerged

progressively that no vesicles are formed. A literature search on the vesicle-formation possibility of the main surfactant component polyglycerol-4 laurate (P4L) confirmed this result (eg. reference [102]). Thereby *Manosroi et. al.* determined the vesicle formation by maltose cross formation under light polarization after entrapping water-soluble fluorescence marker calcein into the vesicles formed by various non-ionic surfactants. However, as we deal with the mixture of two surfactants polyglycerol-4 laurate (96wt-%) and charged 2-sodium laureth sulfosuccinate (4wt-%), further analysis were necessary to confirm this result. The transition of the q -dependence from spherical scattering (q^{-4}), via lamellar (q^{-2}) to finally longitudinal q^{-1} or spherical micellar scattering q^0 (eg figure 4.41a) suggested an elongated, cylindrical structure for the formed aggregates. Detailed model analysis of the SANS-scattering curves refer to disk-like micellar structures. As it was not completely evident to distinguish between a disk-like or vesicular scattering from the SANS-pattern, we calculated their theoretical scattering intensities for all aggregates I_0 in case of a 100wt-% surfactant solution. Assuming a disk- or vesicle-radius R of approximately 32 nm (given from model-fits -eg. fig. 4.42), a layer- or

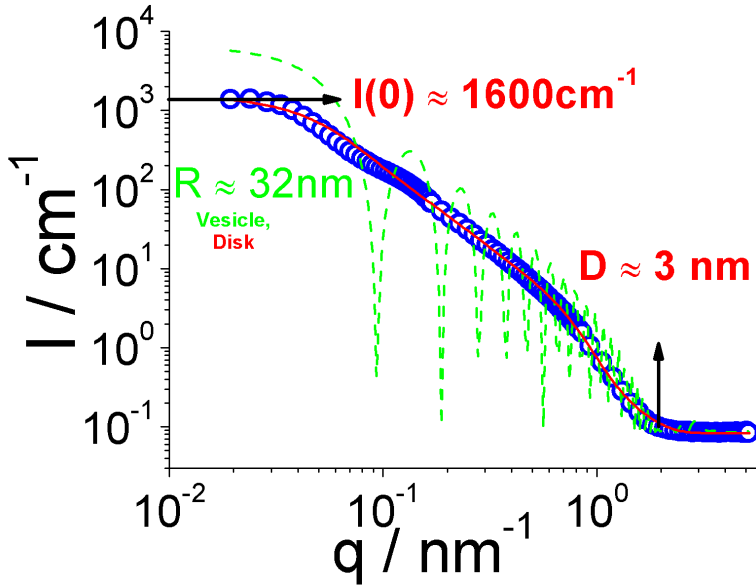


Figure 4.42: Distinction of surfactant structure using monomodal — disk- and - - vesicle model exemplarily for SANS-scattering curve of \circ 100wt-% surfactant S in O/S-variation. O/S-mixture, containing DEHC/K300 (85/15) as oil and P4L/SS (96/4) as surfactant phase, was diluted with water to 95wt-% (D_2O -respecting the density difference to H_2O). The layer/shell-thickness D is given at high q to $2\pi/q_{layer/shell} \approx 3$ nm. The experimental Guinier approximated scattering intensity extrapolated to zero angle scattering $I(0)$ was determined to ~ 1450 cm^{-1} .

shell-thickness D of 3 nm, all surfactant to be contained in the guessed structure with a volume fraction Φ of 0.046 and a corresponding scattering length density SLD difference of the layer or shell to the solvent (D_2O) of $5.81 \cdot 10^{-4} \text{ nm}^{-2}$. In case of monodisperse particle scattering the intensity of a disk I_{disk} or a vesicle $I_{vesicle}$ is given by:

$$I(0) = N^1 \cdot V_p \cdot \Delta SLD^2 \quad (4.10)$$

$$I_{disk} = \Phi \cdot \pi R^2 D \cdot \Delta SLD^2 \quad (4.11)$$

$$I_{vesicle} = \Phi \cdot \frac{4}{3} \pi \left(R^3 - (R - D)^3 \right) \cdot \Delta SLD^2 \quad (4.12)$$

with N^1 being the number density of the particles, V_p the particles' volume and ΔSLD the scattering length density difference of aggregates and matrix (eg. section 3.2.13). R is the disk- or vesicle-radius, D its layer- or shell-thickness. A short source code for the calculations in Igor Pro 6.12A is given in section A.4.3 of the appendix. The calculations revealed a theoretical scattering intensity of $I(0) = 1500 \text{ cm}^{-1}$ in case of disks and $I(0) = 5500 \text{ cm}^{-1}$ for vesicles. In consideration to the assumptions we made, the disk-model fits the experimental data ($I(0) = 1600 \text{ cm}^{-1}$, fig. 4.42) very good.

Due to the imprecise knowledge about the exact distribution-ratios for the surfactant and oil-phase incorporated into either the upper or the lower phase in the biphasic region, we assumed to have only the surfactant (volume fractions are given in table A.5 of the appendix) dissolved in the lower phases and the oil lying on its top. Hence the scattering length density of the aggregates used for the model fits was calculated due to the given P4L/SS-ratio (96/4) to $5.81 \cdot 10^{-4} \text{ nm}^{-2}$. It was kept constant during the data-set analysis of the different O/S-ratios.

Fits for the lower phases (fig. 4.43) of the SANS-data curves with a polydisperse disk model

| S(S+O) wt-% | R nm | σ | D nm | Φ | I_{Bkg} cm^{-1} |
|----------------|---------|----------|---------|--------|-------------------------------|
| 70 | 37.7 | 0.3 | 2.91 | 0.032 | 0.086 |
| 75 | 35.9 | 0.3 | 2.60 | 0.034 | 0.082 |
| 80 | 35.2 | 0.3 | 2.57 | 0.037 | 0.085 |
| 85 | 34.7 | 0.3 | 2.28 | 0.039 | 0.082 |
| 90 | 34.5 | 0.3 | 2.27 | 0.041 | 0.085 |
| 95 | 34.0 | 0.3 | 2.13 | 0.044 | 0.085 |
| 100 | 32.8 | 0.3 | 1.95 | 0.046 | 0.083 |

Table 4.8: Fit parameter for lognormal distributed disk-model (eg. section 3.2.13.4), obtained from SANS-data fit for samples of O/S-variation at constant dilution ratio (95wt-% D_2O , respecting the density difference to H_2O) and surfactant concentrations $S \geq 70\text{wt}\%$ of O/S-mixtures containing DEHC/K300 (85/15) as oil and P4L/SS (96/4) as surfactant phase.

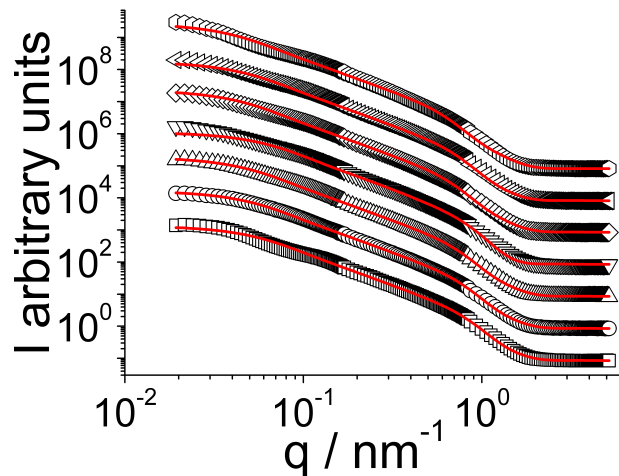
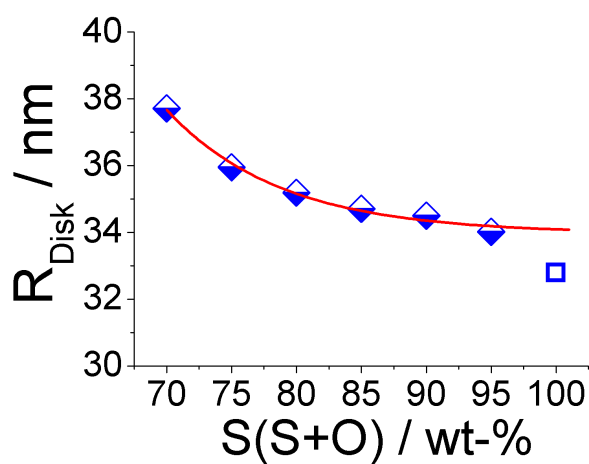
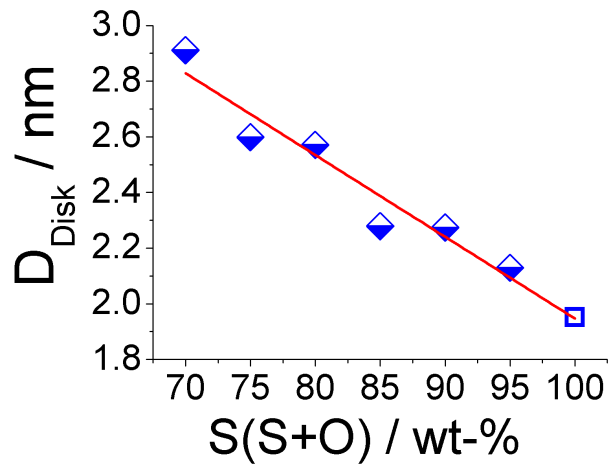


Figure 4.43: Experimental data (lower phases of $< 100\%$ S(S+O)) and lognormal distributed disk-model fits for samples of O/S-variation containing $\circ 70$, $\triangleleft 75$, $\diamond 80$, $\nabla 85$, $\triangle 90$, $\circ 95$ and $\square 100\text{wt}\%$ surfactant S in O/S-mixture (O: DEHC/K300, S: P4L/SS) that were diluted to 95wt-% water (D_2O , respecting the density difference to H_2O).



(a) Disk-radius R



(b) Disk-layer thickness D

Figure 4.44: Visualisation of disk-radii R_{disk} and disk-layer D_{Disk} evolution with increasing surfactant concentration for SANS-data fits with a lognormal distributed disk-model for samples of O/S-variation at constant dilution ratio (95wt-% D_2O , respecting the density difference to H_2O) and surfactant concentrations $S \geq 70\text{wt}\%$ of O/S-mixtures containing DEHC/K300 (85/15) as oil and P4L/SS (96/4) as surfactant phase. Data of lower phases: \blacklozenge and single phase: \square (see also section 4.3 and 4.3.1).

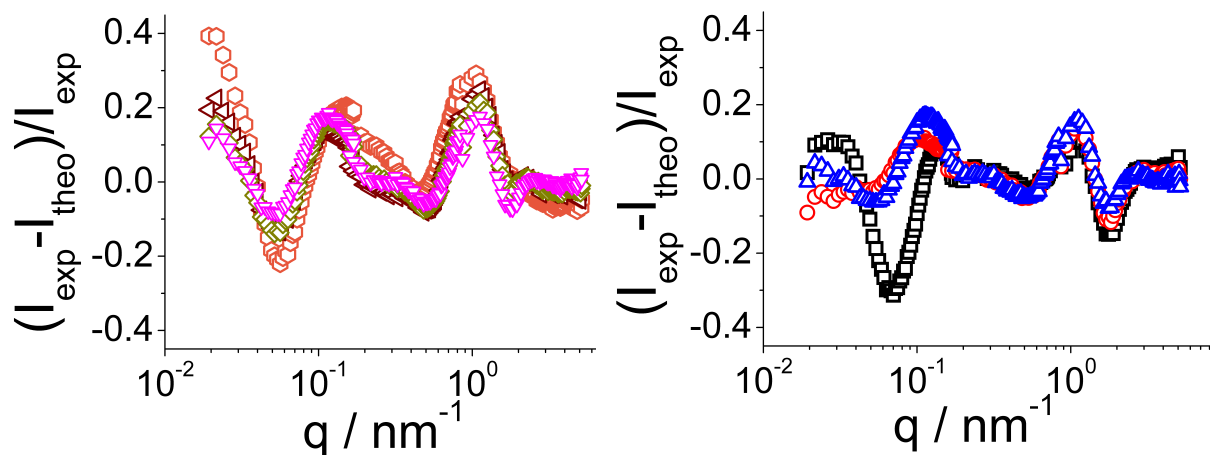


Figure 4.45: Residue of SANS-data fits (lognormal distributed disk-model) for samples of O/S-variation containing \circ 70, \triangleleft 75, \diamond 80, ∇ 85, \triangle 90, \circ 95 and \square 100wt-% surfactant S in O/S-mixture (O: DEHC/K300, S: P4L/SS) that were diluted to 95wt-% water (D_2O , respecting the density difference to H_2O).

(eg. section 3.2.13.4) showed tendencies of an almost exponential decrease of the disk radius and a linear decrease of its layer thickness with increasing surfactant concentration (fig. 4.44). This means that the obtained radii can be seen as lower limits, due to our initial assumptions, as some oil gets solubilised into the disk-like structures. This solubilisation decreases with decreasing oil content at larger surfactant concentrations. The polydispersity of the aggregates stays almost constant at $\sigma \approx 0.3$ for all O/S-ratios. The surfactant dependent disk-radius and layer-thickness evolution is plotted in figure 4.44. Further parameters of the employed poly-disperse disk-model are listed in table 4.8. Calculations of the fit-residua in respect to the measured SANS-data showed some deviations when singly a disk-model is employed. This deviation gets more pronounced for samples close to the phase boundary (eg. 70 and 100wt-% S(S+O)). The addition of a simple micellar model beside the disks (not shown) did not really improve the goodness-of-fit. For such systems it is imaginable to find a mixture of diverse surfactant-structures (spherical micelles, cylinders, bilayers, vesicles... [50]) dependent on different factors (eg. packing parameter of surfactant) [21]. Hence, the observed disk-structure of the surfactant mixture might go along with less bulky mixed surfactant structures.

4.3.2 Conclusion of O/S-variation at constant dilution ratio (95wt-% water) for O: DEHC/K300 (85/15) and S: P4L/SS (96/4).

As nanoemulsions (NE) by the PIC-process are formed at high dilution ratios (> 75wt-% water) of a NE-suited O/S-concentrate, we varied its O/S-ratio to study the finally formed phases at constant dilution ratio. For this purpose we used a model system based on diethylhexyl carbonate (DEHC) and Euxyl K300 (K300) as oil (85/15), and polyglycerol-4 laurate (P4L) and disodium laureth sulfosuccinate (SS) as surfactant phase (96/4). Detailed studies on the phase behaviour upon concentrate-dilution revealed a very narrow domain of the phase diagram in which nanoemulsions are allowed to form. However, O/S-concentrates were formed for various O/S-ratios between 0 and 100% surfactant and subsequently diluted with water to 95wt-% (H₂O). For surfactant concentrations $S < 10\%$ and $65 < S < 95\%$ no homogenous O/S-mixtures could be achieved, whereas for the latter one heating (70 °C) led to a homogenisation. A dilution of the O/S-concentrates revealed the formation of different phases dependent on the surfactant concentration. At low surfactant concentrations ($S \leq 15\%$) instable o/w-emulsions are formed, whose surfactant phase is not sufficient to stabilise the dispersed oil phase in the aqueous media and hence causes a phase separation. For surfactant concentrations $15 < S < 30\%$ bimodal nanoemulsions with a mean radius of 25 - 35 nm are formed due to a better stabilisation of the dispersed oil phase. The particle size decreases exponentially with increasing surfactant concentration and passes continuously to smaller sized stable microemulsion structures ($30 \leq S < 70\%$). The studies confirmed our assumption for the structural composition of nanoemulsions, where we assumed that larger sized, metastable emulsion droplets coexist with stable microemulsion droplets due to a lack of stabilising surfactant. Contrary than expected, the microemulsion phase does not change continuously to smaller sized oil solubilising micellar solutions with increasing surfactant concentration. In fact the linear decrease of the microemulsion particle-size is interrupted once a surfactant-rich biphasic region is reached ($65 < S \leq 95\%$) and holds until the pure surfactant solution ($S = 100\%$). The biphasic samples did not show big structural differences for the lower and upper phases and might differ only in a denser or more diluted state of oil-solubilised (mainly in the upper phases) disk-like structures the pure surfactant mixture (P4L/SS (96/4)) forms. Likewise, the formed structures for the different O/S-ratios in the biphasic region and for the pure surfactant solution remain almost constant. An exponential decrease of the disk radius and a linear decrease of its layer thickness were observed with increasing surfactant concentration due to a decreased solubilisation of the diminishing oil phase.

4.4 Time-resolved studies on PIC nanoemulsions

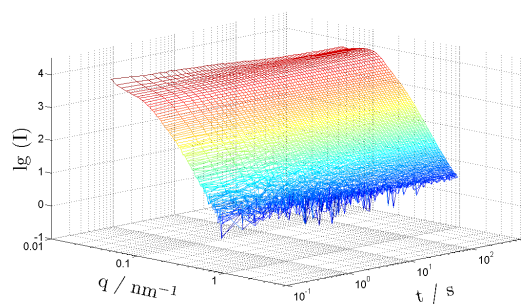
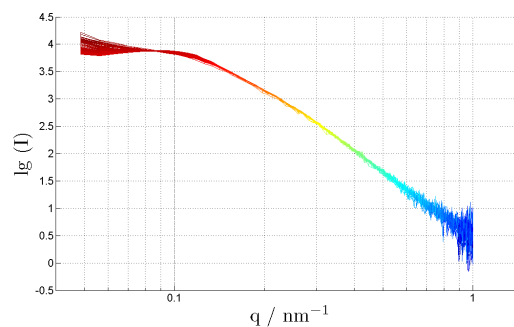
Nanoemulsions formed by low-energy methods are highly interesting systems for dispersing oil phases finely in an aqueous environment. Under given conditions they can be obtained simply by diluting an appropriate oil/surfactant mixture with water. Whether a nano- or microemulsion is formed depends thereby mainly on the dilution ratio, with nanoemulsions typically formed at high dilution ratios. As such generated nanoemulsions are metastable their structure is necessarily controlled by their formation process. Therefore detailed structural knowledge of this formation process is a central aspect for its understanding.

4.4.1 PIC-formation kinetics

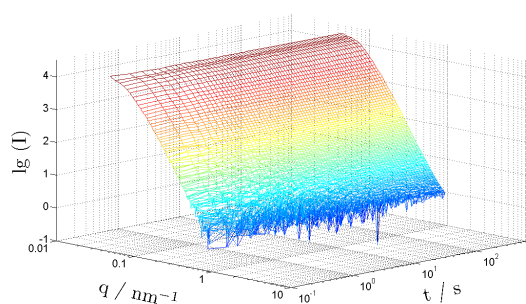
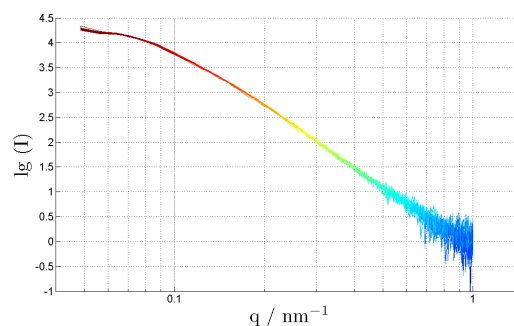
The key factor for emulsion formation has been attributed to the kinetics of the emulsification process. In addition the change in the natural curvature of the surfactant during the emulsification process may play a major role in achieving emulsions with small droplet sizes [182]. Furthermore their metastability is linked to the interdroplet exchange dynamics of the droplets. Accordingly we studied the nanoemulsion kinetics by following their formation process and interdroplet exchange dynamics by time-resolved stopped flow experiments (eg. section 3.2.12) coupled with turbidity and scattering (SAXS/SANS) detection.

Stopped flow turbidity measurements of PIC formed NE

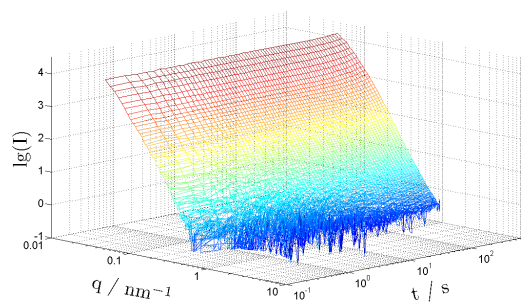
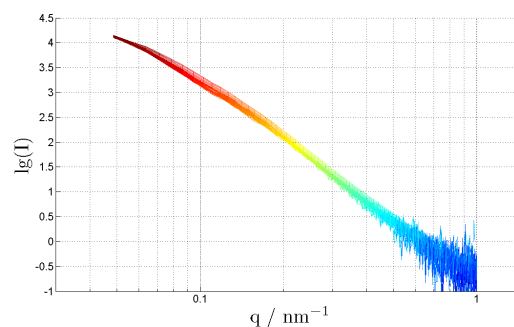
Our model system Tego[®] Wipe DE (exact oil-surfactant mixture is given in section 3.1.1.1) forms long time metastable nanoemulsions at high dilution ratios (> 75% H₂O). From long-term turbidity measurements (eg. fig. A.5 in the appendix) we did not observe significant structural changes even for rather long times (~ 40 days). In contrast a slight decrease in turbidity can be correlated to aging processes and creaming (see also section 4.2.3ff.). Stopped-flow SANS experiments approved this observation and showed likewise no significant structural changes within a time-range of 100 ms < t₀ < 10 min. Fig. 4.46 is showing this for oil-water dilutions of 50, 83 and 95% water, respectively. With stopped flow turbidity measurements we could observe within approx. 100 ms a very quick evolution of the solutions mixture before a more or less metastable state is reached (> 10 s) by a smooth transition (eg. fig. 4.47). Hence, the fast process has to be correlated to the nanoemulsion formation. In the transitional state, during the NE-formation and its metastability, the curves are not exactly delimitable and therefore no exact formation-times of the nanoemulsions at the different dilution ratios can be stated. In section 4.1 we learned that dependent on the exact dilution ratio the droplets differ in their mean size. Thereby we found the greater the dilution ratio the greater also the droplets, which must have also an influence on the given formation kinetics. However, the general curve progression of the nanoemulsion phases implies a shortening of the formation times with higher dilution ratios (eg. white arrow in fig. 4.47).

(a) 50% H₂O time series (10 min)

(b) X-Z - view of 4.46a

(c) 83% H₂O time series (10 min)

(d) X-Z - view of 4.46c

(e) 95% H₂O time series (10 min)

(f) X-Z - view of 4.46e

Figure 4.46: Time series of nanoemulsions formed by our model system Tego[®] Wipe DE and water (50wt-% (a/b), 83wt-% (b/c) and 95wt-% (e/f), nanoemulsion formation was initiated by stopped-flow mixing and the structural evolution detected via SANS at D22 (ILL) in a 1 mm quartz cell at 25°C for approx. 10min.

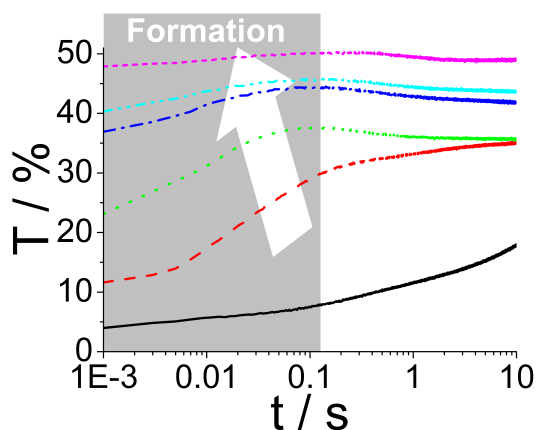


Figure 4.47: Stopped flow turbidity measurements (TUB) of nanoemulsions formed by our model system Tego[®] Wipe DE and water (— 50, - - - 83, ··· 90, - · - · 95, - - - - 96.5, - - - - 98), nanoemulsion formation was initiated by stopped-flow mixing and the structural evolution detected in transmission mode at 626 nm in a 1.5 mm suprasil cell at 25°C for 10 s.

As the required exposure time for a 2d-SAXS pattern with good statistics (3%) can be less than a 1 ms for a strongly scattering sample ($I_{\Omega} \approx 1.6 \cdot 10^{-3}$ sterad⁻¹) [118], the nanoemulsion formation at different dilution ratios was also studied via stopped flow SAXS measurements within the first 100 ms. This was done by varying the starting time of consecutive series by 5 ms and hence covering the whole time range of interest (2.3⁵ - 100 ms). Water-oil mixtures showed with increasing dilution ratio that the final structures observed (o/w-droplets, in NE-region (> 75wt-% H₂O)), appear more similar to the initial ones, as also seen in SANS (fig. 4.46) for the longer time behaviour. However, in more detail a systematic structural change from the initial to the final state was monitored that, similarly to the SF-light experiments, showed a shortening of

the formation times with increasing dilution ratio (eg. fig. 4.50). Hence, the greater the leap to high dilution ratios the greater the driving force of nanoemulsion formation. This might be also supported through the greater extraction of surfactant in the aqueous phase, the growing

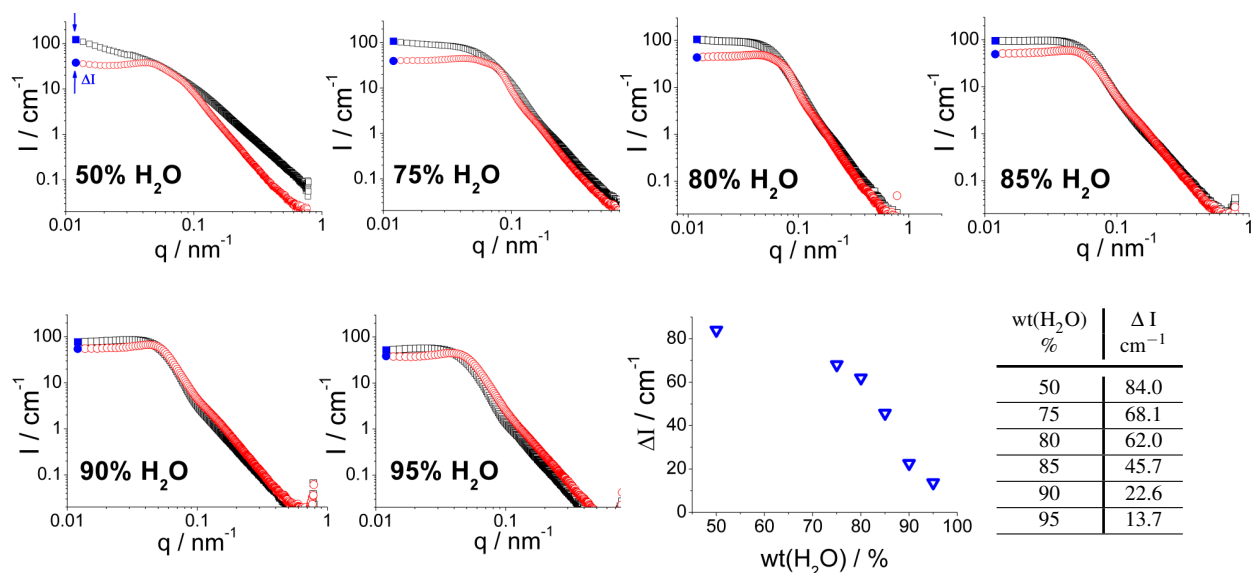


Figure 4.48: SAXS curves of structures measured at earliest (□ 2.3 ms, SF-SAXS dead time) and equilibration-state (○ ≈ 100 ms) while mixing O/S composition Tego[®] Wipe DE with water at different dilution ratios (50, 75, 80, 85, 90, 95 wt-% H₂O) using a stopped flow apparatus. Additional visualisation of the intensity differences $\nabla \Delta I = I_{\text{earliest}} - I_{\text{equilibr.}}$ between earliest measured and equilibration state structures given at a scattering vector $q = 0.012 \text{ nm}^{-1}$ and marked with closed symbols (■, ●).

⁵SF-SAXS dead-time: 2.3 ms, compare section 3.2.12

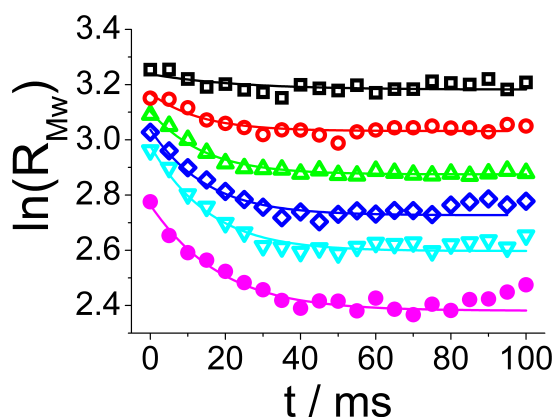
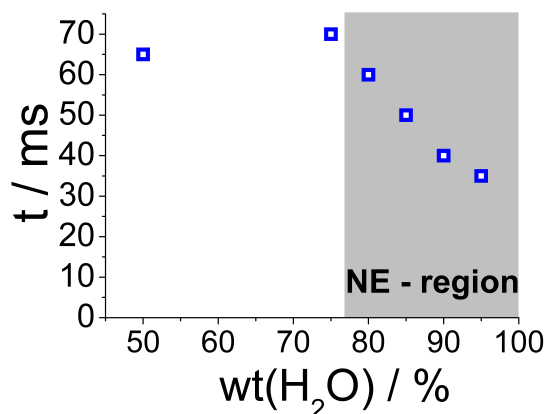


Figure 4.49: Time resolved studies on structural evolution for dilutions of O/S-mixture Tego[®] Wipe DE with water at different dilution ratios (●50, ▽75, ◇80, △85, ○90 and □95wt-% H₂O). Mass weighted effective mean radii R_{Mw} were obtained via Guinier approximation to zero angle intensity ($I(q = 0)$), assuming the whole O/S-mixture given in the structures and hence a scattering length density difference aggregates to solvent for x-ray of $\Delta \text{SLD}(\text{TW})_{\text{SAXS}} = 0.369 \cdot 10^{-6} \text{ \AA}^{-2}$. For a better visualisation of the rapid nanoemulsion formation process at dilution ratios $> 75\text{wt-\% H}_2\text{O}$ a plot of the radii logarithm versus the passing time was chosen.

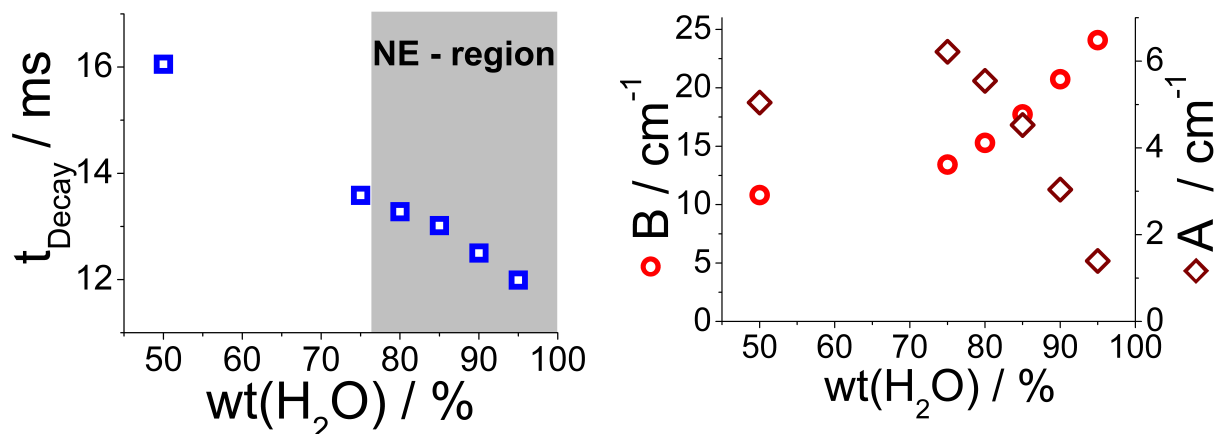


| wt(H ₂ O) / % | 50 | 75 | 80 | 85 | 90 | 95 |
|--------------------------|----|----|----|----|----|----|
| t / ms | 65 | 70 | 60 | 50 | 40 | 35 |

Figure 4.50: Times t required to form structures upon dilution of O/S mixture Tego[®] Wipe DE, before breakdown processes are taking place. Values have been obtained by fast kinetic stopped flow SAXS measurements within 100 ms, registering the point of no further structural changes. In nanoemulsion region, phase transition proceeds faster with increasing dilution ratio.

of mean particle size and thus the decrease of bending with increasing dilution ratio.

Nevertheless, the rapid phase transition from an initial w/o-emulsion to an o/w-nanoemulsion does structurally not show significant changes of the x-ray scattering patterns (eg. fig. 4.48). Model free analysis of the SAXS-curves using Guinier's approximation extrapolating the intensities to zero angle scattering $I(0)$ show a slight decrease of the mean particle size upon phase transition (eg. fig. 4.49), while assuming the whole O/S mixture in the dispersed phase and hence a scattering length density difference between aggregates and solvent of $\Delta \text{SLD}(\text{TW})_{\text{SAXS}} = 0.369 \cdot 10^{-6} \text{ \AA}^{-2}$. Fitting the size evolution with a single exponential decay function shows a decrease of the nanoemulsion formation time with increasing dilution ratio. Detailed fit parameters to the aggregates evolution (eg. fig. 4.49) are given in the table of figure 4.51. The logarithm of the aggregates size evolution (eg. fig. 4.49) should show the termination of the nanoemulsion formation given by the change from linear to constant curve behaviour ($> 75\text{wt-\% H}_2\text{O}$). Time differences between faster Guinier approximated size evolution (fig. 4.49) and direct registration of no further structural change of SAXS scattering patterns in a time series (eg. fig. 4.50), might be related to our assumptions of overall contained volume fraction and hence scattering length density. As for the PIC mechanism a relatively hydrophilic surfactant in the initial O/S-mixture is required, that becomes more and more leached out upon dilution and



| wt-% (H ₂ O) | B | A | t_{Decay} ms |
|----------------------------|------|------|-------------------|
| 50 | 2.38 | 1.62 | 16.1 |
| 75 | 2.60 | 1.83 | 13.6 |
| 80 | 2.73 | 1.71 | 13.3 |
| 85 | 2.87 | 1.51 | 13.0 |
| 90 | 3.03 | 1.11 | 12.5 |
| 95 | 3.18 | 0.33 | 11.9 |

Figure 4.51: Fit parameter amplitude A , offset B and decay constant t_{Decay} of a single exponential decay function ($y = B + A \cdot \exp(-t/t_{Decay})$) used to model formation dynamics of nanoemulsions. Corresponding fit-curves and data points are given in fig. 4.49.

thus changes the theoretical volume fraction and scattering length density.

In general we observe a very fast formation process (< 60 ms) that becomes faster with increasing dilution ratio. Here we want to point out that due to the azimuthally averaged one-dimensional scattering pattern one completely neglects slight anisotropic effects that occur during the formation kinetics. Figure 4.52 visualise the anisotropic evolution within the formation process in time (horizontal patterns) and for the different dilution ratios (vertical patterns) of the O/S-mixture. At a dilution ratio of 50-wt% water one finds a distinct shear-induced anisotropy that appears instantaneously after admixing oil and water, and may indicate an intermediate formation of a liquid crystal phase or a sponge microemulsion oriented due to the shear. The anisotropy (directional expansion of scattering) increases within the next 15 ms before it diminishes again slowly until more or less 60 ms after initiation. A similar but less pronounced behavior can be seen in the nanoemulsion region (> 75 wt-% H₂O). However, different to the formation of liquid crystalline structures we start from an isotropic scattering sample that passes through an anisotropic region to form finally isotropically scattering nanoemulsion structures within 60 ms. Similar to our previous SF-light and -SAXS analysis we thereby observe faster formation kinetics with increasing dilution ratio and hence a faster passing of the anisotropic phase. At dilution ratios of 90 and 95wt-% water, the passing of the liquid crystal phase, cannot be sufficiently resolved (< 5 ms) anymore. In summary most interesting is certainly the fact that the formation of the nanoemulsion droplets is an enormously fast process with a characteristic formation time of 10-20 ms.

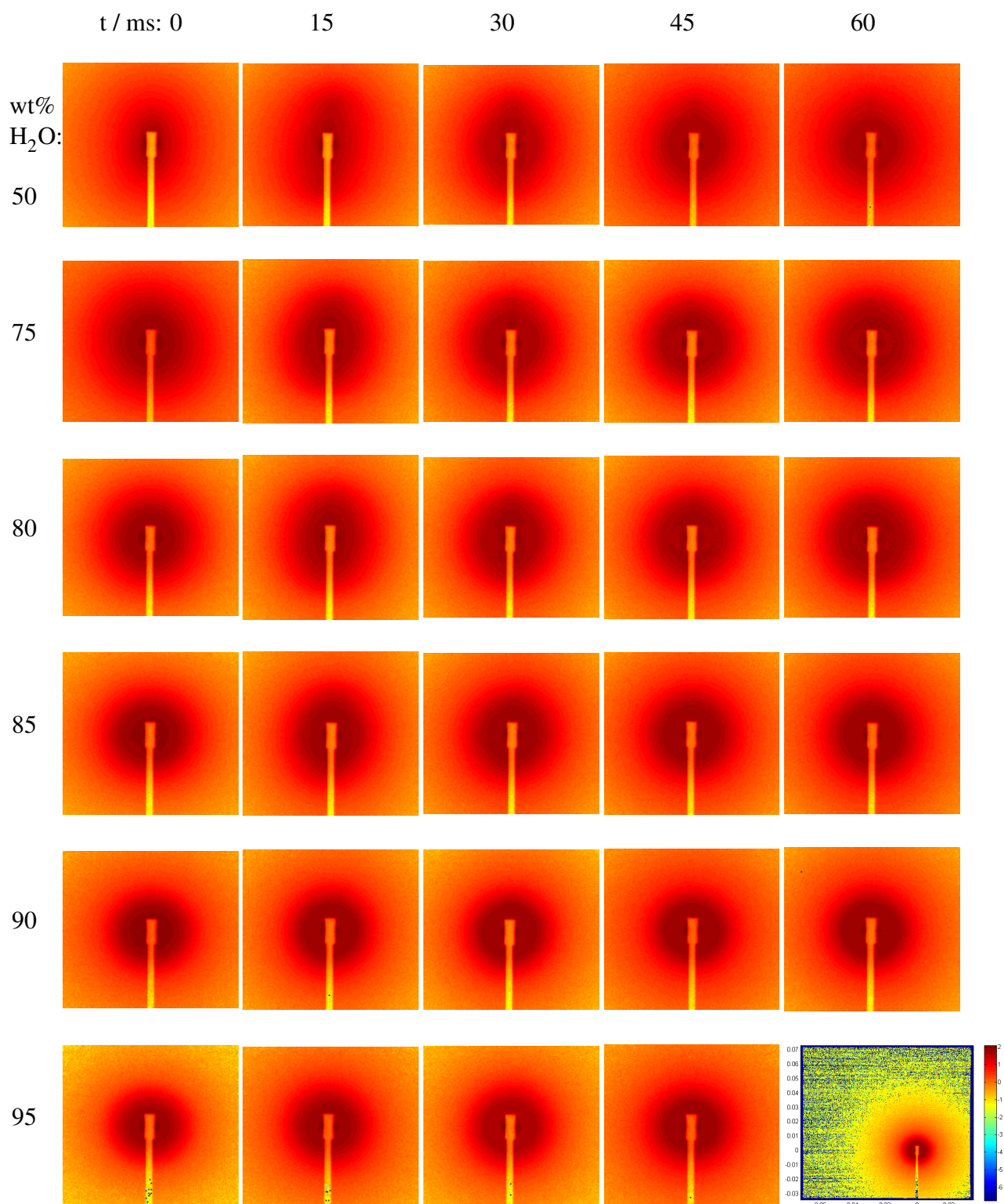


Figure 4.52: SAXS 2D-patterns of sample scattering within the first 60 ms of formation (horizontal images) for six different dilution ratios (vertical images: 50, 75, 80, 85, 90 and 95wt-% H₂O). Formation was initiated by rapid stopped flow mixing of O/S model system Tego[®] Wipe DE and water at 25.0 ± 0.1 °C. Displayed patterns show a cutout (x: -0.02 - 0.02; y: -0.02 - 0.02) of the whole detected SAXS 2D-pattern - eg. image 95wt-% H₂O at 60 ms respectively (color scale indicates the scattering intensity).

4.4.2 Nanoemulsion interdroplet exchange dynamics

In section 4.4.1 we studied the fast formation process of nanoemulsions by the PIC-process and found that metastable nanoemulsions are formed within less than 60 ms if a high amount of water ($> 75\text{wt-}\%$) is added to an O/S-mixture. Despite their metastability, nanoemulsions can persist for many weeks, months or years depending on the applied surfactant that inhibits common breakdown processes like coalescence or Ostwald ripening.

However, it is still rather poorly understood how the compositional ingredients, emulsification method and hence energy input during emulsion-formation define their (interdroplet) dynamical behavior during equilibration and hence their life time.

The exchange of lipophilic materials inside emulsion droplets that are separated by an aqueous medium is an important property for understanding the dynamics of nanoemulsion droplets. Furthermore the interdroplet exchange dynamics are also important for a better understanding of the ingredients partitioning between dispersed and continuous phase [106], and thereby is also relevant for aging of nanoemulsions and their applications.

For the following analysis of the nanoemulsion interdroplet exchange dynamics we used the contrast sensitivity of neutron experiments. We therefore formulated O/S-mixtures consisting of either fully hydrogenated (h-) or fully deuterated (d-) main oil component diethylhexyl carbonate (DEHC 66wt-% of O/S-mixture) and un-deuterated preservative mixture Euxyl K300 (12wt-%), nonionic surfactant polyglycerol-4 laurate ($\sim 21.1\text{wt-}\%$) and anionic surfactant AOT ($\sim 0.9\text{wt-}\%$). Detailed information about molecules properties are given in section 3.1.1 and information on d_{34} -DEHC preparation are given in section A.1.2.5 of the appendix.

The exchange dynamics of identically prepared nanoemulsions, which differ only in containing hydrogenated or deuterated oil, was studied at different dilution ratios (90, 95, 98, 99 and 99.5wt-% H_2O). This was done in order to investigate the concentration effect on the interdroplet dynamics, as that should allow distinguishing between the different exchange mechanisms like Ostwald ripening or coalescence. We therefore prepared one-to-one mixtures of the deuterated and hydrogenated nanoemulsion in a stopped flow apparatus and followed the exchange dynamics of the mixture time dependently via SANS for ~ 30 min.

As for an ideal neutron experiment a contrast with maximum intensity is necessary that simultaneously visualise a maximum change in scattering behaviour from the initial (unexchanged) to the final (equilibrated) state, solvent contrast simulations have been done prior to the experiment in order to optimise the required experimental parameters.

The Matlab-Simulations on time-dependent interdroplet exchange dynamics assumed an ideal core-shell-scattering model with a fixed mean radius of 10 nm and an estimated shell thickness for the lipophilic tail of the nonionic surfactant P4L of 1.3 nm (eg. molecular structure of P4L in figure 3.1c). Bimodality and polydispersity of nanoemulsions were neglected.

Two limiting pathways (eg. fig. 4.53), for reaching the equilibrated state (hydrogenated and deuterated oil are balanced in the nanoemulsion mixture) while starting from two populations that are separated by their contrast, are imaginable. Either one assumes a closer move together of the two nanoemulsion populations (via molecular diffusion) or

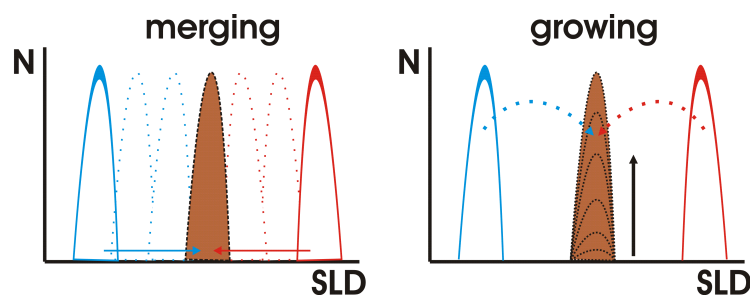


Figure 4.53: Fusion of hydrogenated and deuterated nanoemulsion (with different contrasts) to a common equilibrated state. Two mechanisms are imaginable *left*: merging of both populations or *right*: growing of a third population in the expense of the two initial ones.

a third (contrast averaged) population is built up out of the two initial ones directly (association-dissociation mechanism; coalescence). Simulations for both cases varied just slightly in scattering curve steepness at the mid- q range and hence did not show any great impact on the final scattering curves. Therefore, the simulation used for our stopped flow nanoemulsion exchange dynamics SANS-experiment to estimate a proper contrast is given in section A.5.1 of the appendix and is based on the assumption of the merging of two populations. Preliminary SANS-contrast variation measurements of nanoemulsions diluted with 95wt-% water ($\text{H}_2\text{O}/\text{D}_2\text{O}$ -mixture) allowed us to determine the matching point of the dispersed aggregates that presumably hold mainly the main deuterated oil component (d_{34} -DEHC) and polyglycerol-4 laurate in respect to

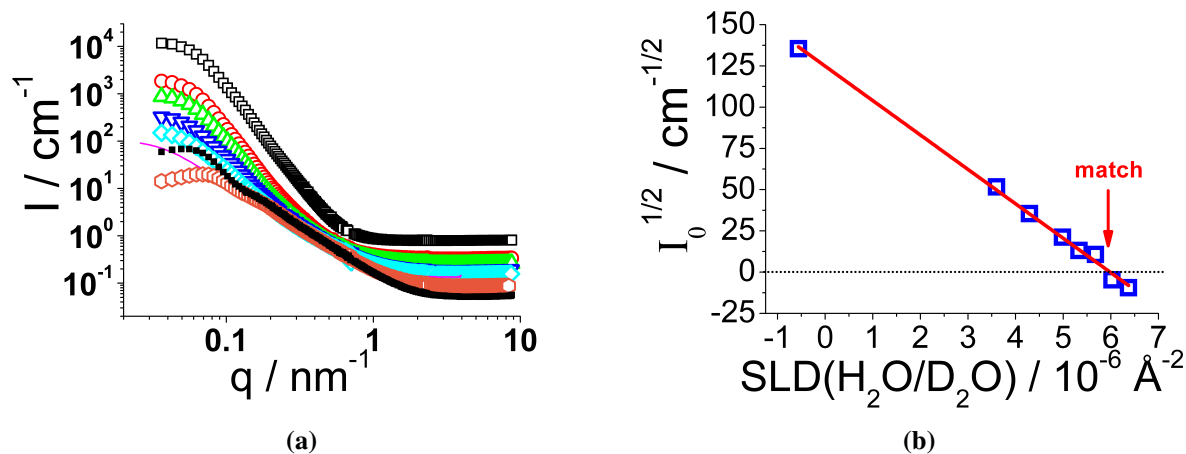


Figure 4.54: **a)** Contrast variation of O/S-mixture diluted with 95wt-% water ($\text{H}_2\text{O}/\text{D}_2\text{O}$) at 25.0 ± 0.1 °C. O/S-mixture consisted of d_{34} -DEHC/K300/P4L/AOT. Contrast of aqueous phase was changed by different $\text{H}_2\text{O}/\text{D}_2\text{O}$ -ratios (■ 0, ○ 5, — 10, ◇ 15, ▽ 20, △ 30, ○ 40, □ 100% H_2O). Density difference for deuterated components was taken into account during sample preparation.

b) Determination of the scattering length density SLD the dispersed aggregates possess. The matching point of the aggregates with the solvent is marked as interception point with the abscissa for a plot of the square root of Guinier approximated intensities $\sqrt{I_0}$ of the scattering curves in fig. 4.54a versus the scattering length density of the solvent mixture ($\text{SLD}(\text{H}_2\text{O}/\text{D}_2\text{O})$).

the PIC-mechanism (assumption, eg. for more details on composition section 4.5). The matching point of the deuterated aggregates was determined to be $6.11 \cdot 10^{-6} \text{ \AA}^{-2}$, as the interception point of the abscissa for the square root of Guinier approximated intensities $\sqrt{I_0}$ of the measured scattering curves (extrapolated to zero angle q scattering) and the scattering length density of the solvent mixture $\text{SLD}(\text{H}_2\text{O}/\text{D}_2\text{O})$ -eg. fig. 4.54. The general assumption that the aggregates are only formed out of the main oil (DEHC) and surfactant (P4L) components, lead to an O/S-ratio of 90.7% DEHC and 9.3% P4L for a nanoemulsion dilution ratio of 95wt-% water whose initial O/S-mixture is based on DEHC/K300/P4L/AOT (66/12/21.1/0.9 wt-%). Consequently the matching point for the aggregates in the non-deuterated nanoemulsions could be estimated to $0.102 \cdot 10^{-6} \text{ \AA}^{-2}$.

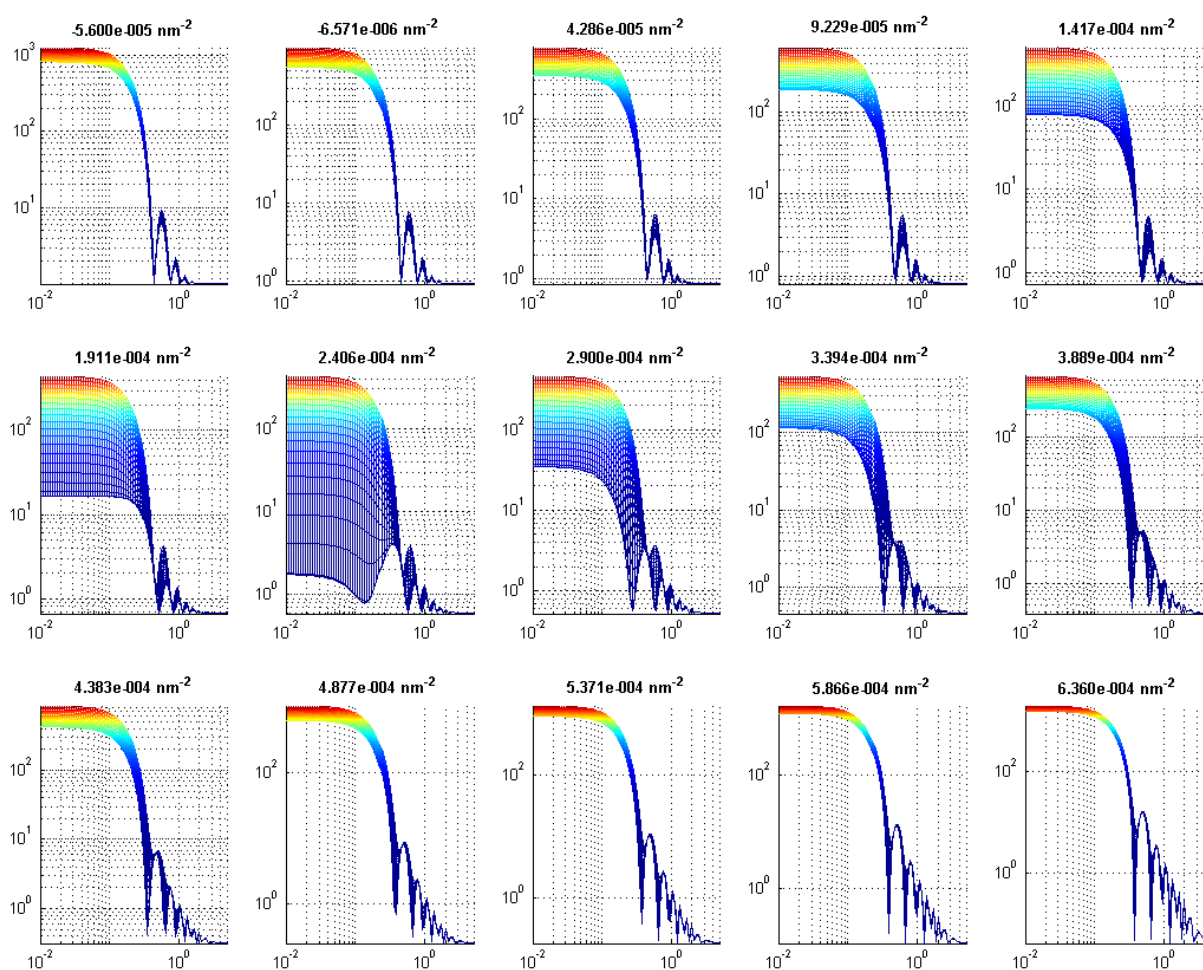


Figure 4.55: Simulation of scattering evolution with time for interdroplet exchange between two nanoemulsions of different contrasts and at 15 different contrast conditions ($\text{H}_2\text{O}/\text{D}_2\text{O}$ -mixtures between pure H_2O ($-0.56 \cdot 10^{-6} \text{ \AA}^{-2}$) and pure D_2O ($6.36 \cdot 10^{-6} \text{ \AA}^{-2}$) solvent contrast). Assuming a mean particle size of the droplets of 10 nm ($\text{SLD}(\text{h-NE}) = 0.10 \cdot 10^{-6} \text{ \AA}^{-2}$; $\text{SLD}(\text{d-NE}) = 6.11 \cdot 10^{-6} \text{ \AA}^{-2}$) that are surrounded by a surfactant shell of 1.3 nm ($0.51 \cdot 10^{-6} \text{ \AA}^{-2}$) for a 95wt-% diluted O/S-mixture of (DEHC/K300/P4L/AOT 66/12/21.1/0.9). Plots are given in x-z-view (intensity I in cm^{-1} , scattering vector q in nm^{-1}) to visualise the maximum change in scattering properly.

Hence, an equivalent mixture of identically prepared nanoemulsions with different contrast properties results in a common contrast of $3.11 \cdot 10^{-6} \text{ \AA}^{-2}$ for the equilibrated nanoemulsion droplets. Accomplished simulations of the interdroplet exchange dynamics using the obtained contrasts to predict a maximal change of the scattering curves (during contrast equilibration) at a simultaneously reasonable scattering intensity showed that the ideal contrast conditions would be slightly lower than the contrast of the matching point. The contrast conditions with a maximum change while passing zero intensity scattering (eg. fig. 4.55 at $\sim 2.4 \cdot 10^{-6} \text{ \AA}^{-2}$) are not favored due to temporal resolution problems within the stopped flow experiment for low scattering. As with increasing dilution more surfactant gets leached out while the relative amount of oil and hence mean droplet particle size increases, our simulations showed a shifting of the ideal contrast to slightly higher values.

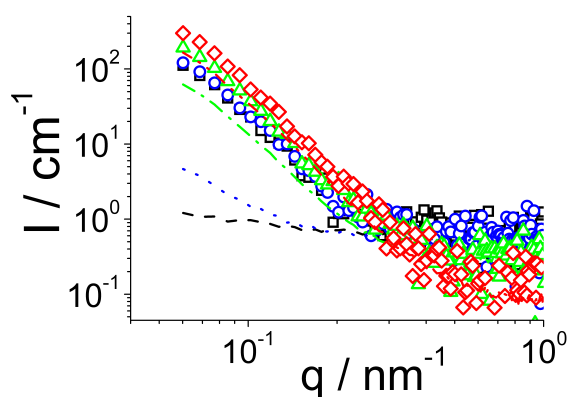


Figure 4.56: Determination of optimal contrast to observe interdroplet exchange dynamics until equilibrium state for two equivalent nanoemulsions of different core contrasts via time resolved stopped flow SANS. Nanoemulsions are diluted with 99.5wt-% water ($\text{H}_2\text{O}/\text{D}_2\text{O}$) of different contrasts (\square - - - 50, \circ . . . 60, \triangle - - - 80, \diamond - - - 100% D_2O - symbols mark initial and lines mark state after approx. ten minutes).

ous solvent mixture ($\text{H}_2\text{O}/\text{D}_2\text{O}$). This becomes more evident during equilibration than for the initial states. Simultaneously the relative change (ΔI) of the scattering curves becomes less pronounced (coverage of order of magnitudes). We finally chose a contrast of $3.5 \cdot 10^{-6} \text{ \AA}^{-2}$ that corresponds to a $\text{H}_2\text{O}/\text{D}_2\text{O}$ -ratio of 40:60. Figure 4.57a visualizes a time resolved stopped flow SANS experiment, following the interdroplet exchange dynamics of two identically prepared nanoemulsions of different contrasts at a dilution ratio of 90wt-% water ($\text{H}_2\text{O}/\text{D}_2\text{O}$) respectively. The dynamics of equally mixed nanoemulsions have been followed via SANS for approx. 30 minutes at five different dilution ratios (99.5, 99, 98,95 and 90wt-% water). Their time-dependent evolution of the contrast equilibration is depicted in figure 4.57b and shows an exponential decaying function that equilibrates within ten minutes. Data analysis revealed

Before proceeding with our time resolved stopped flow SANS experiments that concern the interdroplet exchange dynamics of nanoemulsions at different dilution ratios obtained by the PIC method, we ascertained experimentally our contrast simulations (eg. fig. 4.56) for four different contrasts (50/60/80/100% D_2O) at a dilution ratio of 99.5wt-% water ($\text{H}_2\text{O}/\text{D}_2\text{O}$). The dilution ratio for this purpose was chosen such as to work most efficiently with the limited amount of deuterated oil component.

However, these preliminary experiments already show that the contrast mixture of the equivalently prepared nanoemulsions starts initially at high intensities and drops down with equilibration. Whereas the scattering intensity rises with increasing fraction of deuterium oxide in the aqueous

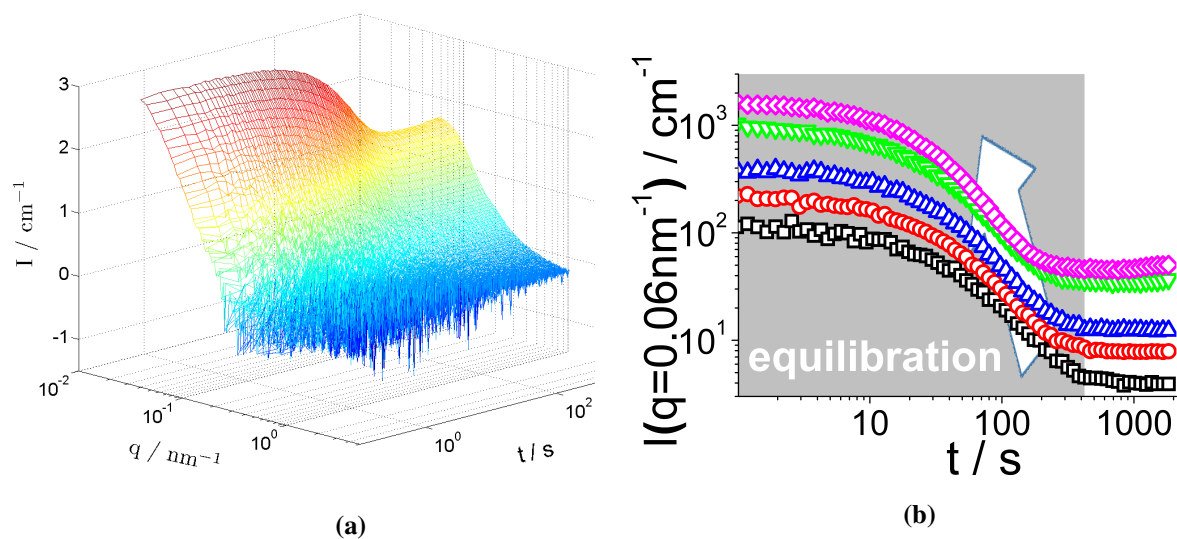


Figure 4.57: **a)** Time resolved stopped flow SANS measurements at $25.0 \pm 0.1^\circ\text{C}$, following the interdroplet exchange dynamics (for approx. 30 min) of two identically prepared nanoemulsions (d_{34}/h_{34} -DEHC/K300/P4L/AOT (66/12/21.1/ ~ 0.9 wt-% - in case of deuterated oil, accounting for the density difference to the hydrogenated one)) of different contrasts at a dilution ratio of 90wt-% ($\text{H}_2\text{O}/\text{D}_2\text{O}$ 40/60) respectively. **b)** General equilibration dynamics for the nanoemulsion droplet exchange processes at different dilution ratios (\square 99.5, \circ 99, \triangle 98, ∇ 95 and \diamond 90% water $\text{H}_2\text{O}/\text{D}_2\text{O}$). Curves are plotted as measured scattering intensity I at $q = 0.06 \text{ nm}^{-1}$ versus the time t . Equilibration slows down with increasing water concentration (eg. white arrow in plot).

at least two simultaneously running processes that might be attributed to coalescence and Ostwald ripening processes, as no one of both really dominates the metastable properties of the nanoemulsions. This was seen due to the nonlinear growing properties (coalescence: R^{-2} , Ostwald-ripening: R^3) of the particles diameter with time in section 4.2. Calculations, concerning an average time τ (saddle point of curve) for the particles to equilibrate at the different dilution ratios, have been done by integrating the experimental decay function and dividing its

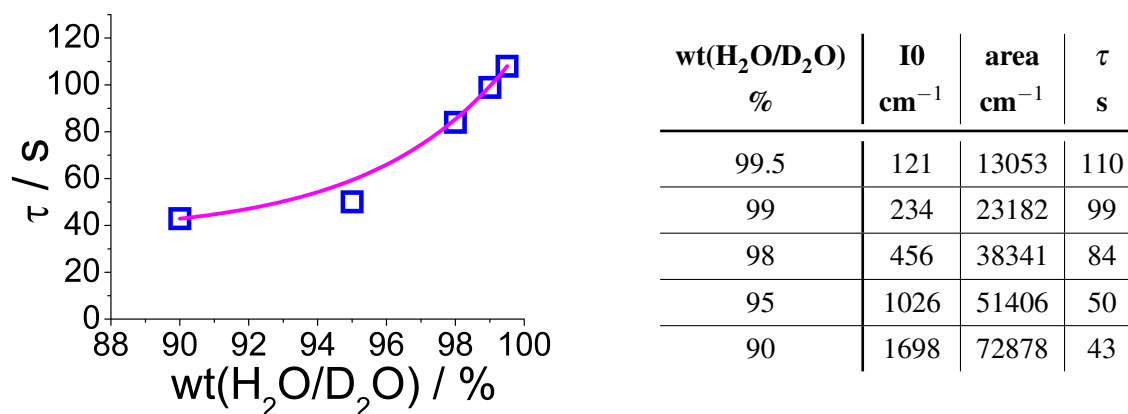


Figure 4.58: Average relaxation times τ of interdroplet exchange dynamics of nanoemulsions at different dilution ratios (99.5, 99, 98, 95 and 90wt-% water ($\text{H}_2\text{O}/\text{D}_2\text{O}$)). Calculations correspond to figure 4.57b. τ was obtained as integral (area) of time dependent intensity-evolution divided by the primary intensity given at time zero $I(t=0)$ - eg. eq. (4.13).

area by the initial intensity ($I(t = 0)$). Thereby the decay slows down with increasing dilution ratio (eg. white arrow in fig. 4.57b) due to the greater interdroplet distances (eg. figure and table in 4.58).

$$area = \int_{t=0}^{\infty} I_0 \cdot \exp(-kt) dt \approx \frac{I_0}{k} = I_0 \cdot \tau \quad (4.13)$$

However, analysis on the concentration dependent time evolution revealed an almost first-order interdroplet exchange dynamic and hence indicates a molecular diffusion process among the nanoemulsion droplets. This is seen by the linear dependency of the concentrates natural logarithm versus the time (eg. figure 4.59b) and was observed for other emulsion systems likewise [105, 106]. From the linear plot, $dc/dt = -k \cdot c$, we obtained a rate constant of $k = 0.04 \text{ s}^{-1}$ that depends on such factors as the temperature, surfactant type and -concentration, and ionic strength. *McClements et al.* demonstrated that the rate of oil exchange between emulsion droplets depends linearly on the surfactant concentration [105]. Thus these rates might be manipulable by varying the main surfactant component of the PIC O/S-starting formulation.

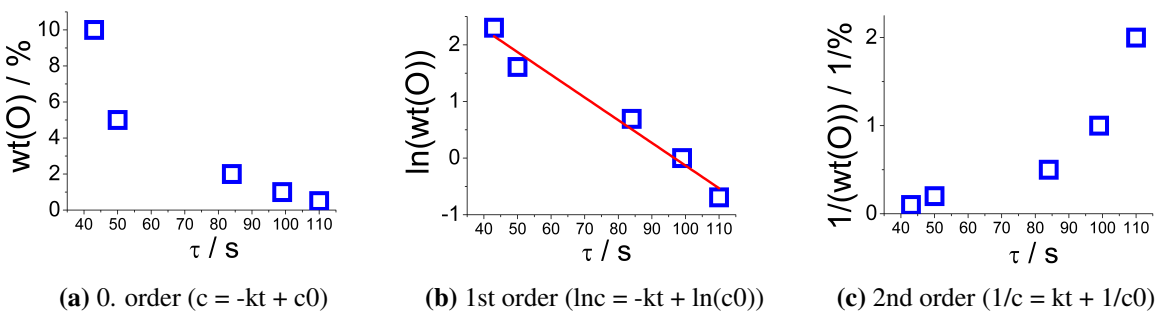


Figure 4.59: Plots of reaction rate laws for zero-order, first-order and second-order reactions, in respect to the obtained relaxation times τ at the different dilution ratios (o/w: **0.5/99.5**, **1/99**, **2/98**, **5/95** and **10/90**) with stopped flow SANS-measurements (eg. fig. 4.57b and 4.58). k being the reaction rate constant and c_0 the initial concentration of a substance at time $t = 0$. Linear fit of 1st-order reaction revealed a rate constant of $k = 0.04 \text{ s}^{-1}$ and an offset of $\ln(c_0) = 3.87$.

4.4.2.1 Nanoemulsion interdroplet exchange dynamics - Additives

In the following we are going to study the influence of nanoemulsion additives on the interdroplet exchange dynamics by the stopped flow SANS-technique. The model system contained either hydrogenated or deuterated (h_{34} or d_{34})-DEHC/K300/P4L/AOT (66/12/21.1/ ~ 0.9 wt-%), with additional AOT to a collective weight fraction of 0.9, 2 and 5wt-% (AOT) or triblock copolymer Pluronic L31 of 0, 1 and 5wt-% (L31). Subsequently the O/S-mixtures were diluted with 98wt-% water ($\text{H}_2\text{O}/\text{D}_2\text{O}$ -mixture 40/60). The time dependent contrast equilibration, caused by the jointly exchange of nanoemulsion droplets, was followed after a stopped flow initiated one-to-one mixing of the hydrogenated and deuterated nanoemulsions. The evolution of their scattering patterns looks similar to the untreated ones (eg. fig. 4.60 respectively)

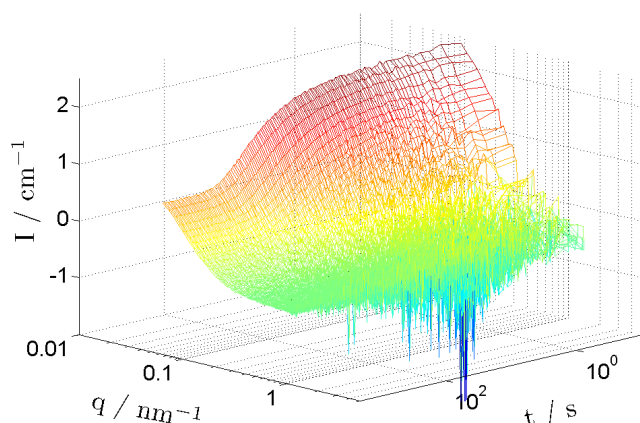


Figure 4.60: Stopped flow SANS measurements of interdroplet exchange dynamics among nanoemulsion droplets at a dilution ratio of 98wt-% water ($\text{H}_2\text{O}/\text{D}_2\text{O}$ -mixture 40/60), using the contrast sensitivity of neutron experiments while mixing equally prepared nanoemulsions of hydrogenated and deuterated contrast at same portions. O/S-concentrates based on (h_{34} or d_{34} - respecting the density difference)-DEHC/K300/P4L/AOT (66/12/21.1/ \sim 0.9).

over, this shortening implies a linear increase of the oil exchange rate with the surfactant concentration due to a better solubilisation of the hydrophobic solutes into the aqueous phase by the additional surfactant which may aid the oil transport. Similar findings were already stated elsewhere for nonionic surfactants [100, 105, 115]. However, as this might be the most likely mechanism concerning the interdroplet exchange of emulsion droplets, we also would like to point out that preliminary studies (zeta potential and cryo-TEM micrographs)

and shows an exponential decaying function likewise. The individual time-dependent SANS measurements for the additives can be found in the appendix (eg. fig. A.9).

From the SANS scattering pattern, at a scattering vector of $q = 0.06\text{nm}^{-1}$ we plotted the time-dependent intensity evolution given by the equilibration dynamics of the droplets exchange process. The profiles for the different AOT- and polymer-concentrations are given in figure 4.61. Calculations on the average decay times τ , using equation (4.13), revealed a very minute shortening of the time constant for the oil exchange when a greater extent of AOT is applied (eg. figure 4.62). More-

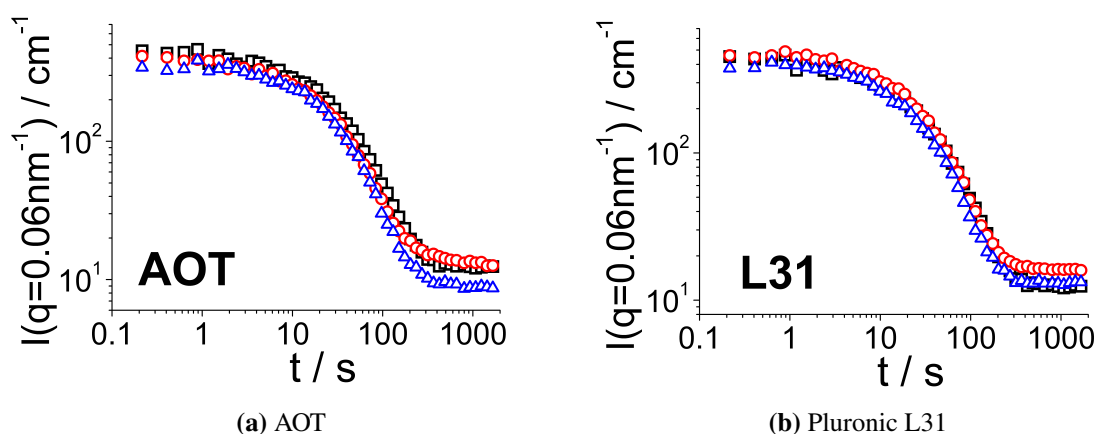


Figure 4.61: Equilibration dynamics of 1:1-mixtures of hydrogenated and deuterated nanoemulsions at a dilution ratio of 98wt-% water ($\text{H}_2\text{O}/\text{D}_2\text{O}$ -mixture 40/60). To the initial O/S-mixture based on (h_{34} or d_{34})-DEHC/K300/P4L/AOT (66/12/21.1/ \sim 0.9) was added either further AOT to a collective weight fraction of $\square \sim 0.9$, $\circ 2$ or $\triangle 5\text{wt}\%$; or with triblock copolymer Pluronic L31 to $\square 0$, $\circ 1$ or $\triangle 5\text{wt}\%$. Curves are plotted as measured scattering intensity I at $q = 0.06\text{nm}^{-1}$ versus the time t .

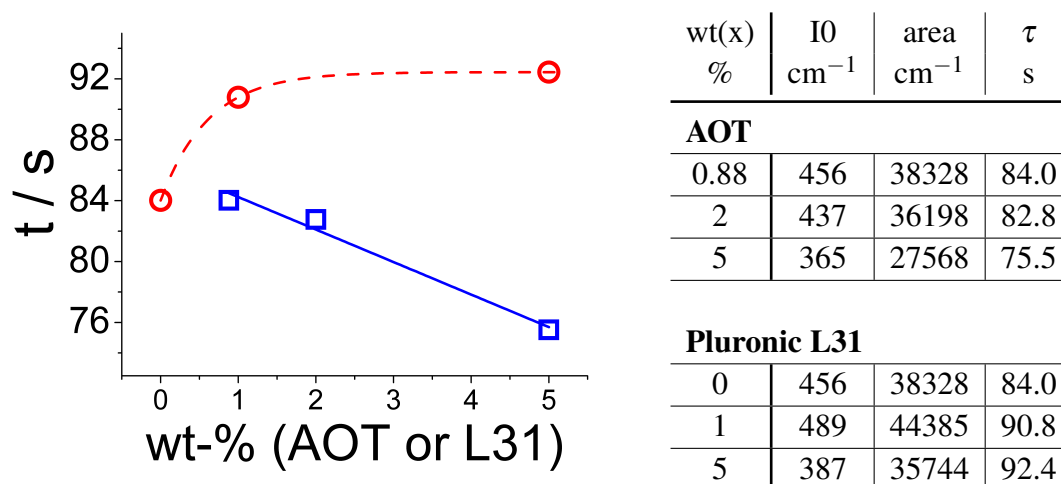


Figure 4.62: Average relaxation times τ of interdroplet exchange dynamics of nanoemulsions at a dilution ratio of 98wt-% water (H_2O/D_2O -mixture 40/60). O/S-mixtures (h_{34} or d_{34})-DEHC/K300/P4L/AOT (66/12/21.1/ \sim 0.9) for exchange studies were either spiked with additional \square AOT to a collective weight fraction of 0.9, 2 and 5wt-%; or with triblock copolymer \circ Pluronic L31 of 0, 1 and 5wt-%. Calculations correspond to figure 4.61. τ was obtained as integral (area) of time dependent intensity-evolution divided by the primary intensity given at time zero $I(t=0)$ - eg. eq. (4.13).

on the charge influence of nanoemulsions showed a decrease of the interparticle distance with increasing charge (eg. section 4.2.3.2-*charge* and 4.6.1.2). Subsequently the interdroplet distance a solute has to pass and thus the diffusion-time required for an exchange shortens likewise.

In case of the added nonionic triblock copolymer Pluronic L31, we observed a slowing down of the equilibration dynamics with increasing polymer content (eg. fig. 4.62). Differently to the charged surfactant no linear dependence of the relaxation times with the employed polymer concentration were observed. This is not surprising as the polyol indeed exhibits surface active properties but shows a quite high critical micelle concentration of 650 ppm [150]. Hence, for the employed polymer concentrations no micelles are formed that incorporate the hydrophobic molecules for an enhanced oil solubility or interdroplet migration respectively.

However, on the molecular level, surfactant molecules exist in dynamic equilibrium between a number of different environments: at the oil-water interface, as micelles, or as individual molecules in solution [105]. From the molecular structure of the amphiphilic triblock copolymer (PEO-PPO-PEO) it might be most likely beside a micellisation that the PEO end-blocks (\sim 1nm) are selectively soluble in the aqueous phase, whereas the PPO-midblock only dissolves in the oily environment. Thus, the polymer addition leads to an integration of the building blocks into the oil-water-interface, while single surfactants are displaced. Due to the non-micellisation and steric hindrance at the o/w-interface, the nanoemulsion interdroplet exchange is slowed down.

4.4.3 Conclusion of nanoemulsion dynamics: PIC-formation and inter-droplet exchange.

Nanoemulsions were formed by the simple dilution procedure of a PIC-suited O/S-mixture (Tego[®] Wipe DE) at high dilution ratios of water (> 75wt-%). The structural evolution for long ($100 \text{ ms} < t < 40 \text{ d}$) and short ($0 < t < 100 \text{ ms}$) time-ranges was followed by different techniques (turbidity, stopped flow light/SANS/SAXS). In doing so, we noted for the long times no great structural changes. The processes followed although appeared very slow and might be related to the metastable properties (breakdown processes like coalescence and Ostwald-ripening) of nanoemulsions. Due to their metastability, the nanoemulsions final structure is necessarily controlled by their formation process.

Time resolved measurements on their formation dynamics revealed within approximately 70 ms a very fast kinetic of the structural inversion and nanoemulsion formation, before a smooth transition to the metastable state is reached. Dependent on the exact dilution ratio, the time required for the structural inversion shortens and the mean particle size upon phase transition decreases less strongly with increasing water concentration. Simultaneously, an equalization of the initial and final structures occurs that suggest a greater driving force for the nanoemulsion formation at higher dilution ratios. This effect is explainable by the greater extraction of the surfactant phase into the aqueous media upon dilution, as it causes a growing of the mean particle size and likewise the decrease of the droplets bending. However, 2D-SAXS pattern upon phase transition with time revealed a fast shear-induced anisotropic scattering (directional expansion of scattering) within the first 15 ms while passing through a liquid crystal phase prior the nanoemulsion formation. This is an important precondition to facilitate the PIC-caused phase inversion. Thereby, the passing of the anisotropic phases proceeds faster with increasing dilution ratio and goes along with the general formation dynamics seen.

Furthermore we studied the interdroplet exchange dynamics among nanoemulsion droplets for different dilution ratios ($\geq 90\text{wt-\%}$ water ($\text{H}_2\text{O}/\text{D}_2\text{O}$ 40/60)) using the contrast sensitivity of neutron experiments (SANS), while mixing identically prepared hydrogenated and deuterated nanoemulsions equally in a stopped flow apparatus. The observed contrast equilibration during the oil exchange process started initially at high intensities and dropped down by an exponential decay with characteristic times in the minute range that showed at least two simultaneously running processes. With increasing dilution ratio an increase of the equilibration-time was revealed due to the greater interdroplet distances. Nevertheless, from the data analysis we could not clearly identify which processes are causing the metastability of nanoemulsions.

Analysis on the concentration dependent time evolution demonstrated that the rate of oil exchange between nanoemulsion droplets depends linearly (1st order kinetic) on the surfactant concentration. This favours molecular diffusion processes for the oil-exchange dynamics which might be manipulable by varying the main surfactant component of the PIC O/S-starting for-

mulation. In summary, it is very interesting to note that the oil exchange occurs in the minute range, while aging processes take months and are apparently not directly related to this oil exchange.

However, investigations on the influence of nanoemulsion additives on the droplet exchange dynamics at constant dilution ratio (98wt-% water ($\text{H}_2\text{O}/\text{D}_2\text{O}$ 40/60)) using either additional AOT or nonionic triblock copolymer Pluronic L31 had only little effect on the time constant and revealed a time-shortening for the oil-exchange dynamics by AOT and a slowing down of the equilibration dynamics by the polymer. Apparently there is no electrostatic stabilisation and only a rather small steric stabilisation due to the added amphiphile. In case of AOT a better solubilisation of the hydrophobic solute is reached through micellization that shows (likewise to the change of dilution ratio) a linear increase of the oil exchange rate with increasing surfactant concentration. An additional shortening of the interparticle distance the additionally employed charge might support the faster diffusion process and hence equilibration. In case of the polymer no micelles are formed due to its high cmc (650 ppm). Moreover, the polymer addition leads to an integration of the building blocks (PEO-PPO-PEO) into the oil-water-interface, while single surfactants are displaced. This leads to a sterical hindrance of the oil-exchange process and a prolongation of the equilibration-time.

Hence, from these investigations one can conclude that breakdown processes are either more stimulated or temporally delayed with the right choice of additive. This is, of course, a relevant finding for reactions in such nanoemulsions or for encapsulation reactions with them.

4.5 The Phase-Inversion-Concentration (PIC) Mechanism of nanoemulsion formation

After having studied the compositional requirements for forming nanoemulsions in the type of system chosen by us, we were now interested in obtaining more insight into the compositional changes occurring during the dilution process. In this respect we are particularly interested in the change of the composition within the formed nanoemulsion droplets as that allows for a more detailed understanding of the mechanism involved. In order to obtain such information we performed NMR, refractive index, and SANS experiments as a function of the degree of dilution.

4.5.1 Experimental and theoretical studies on the PIC-mechanism

In the previous sections we described the formation and structures of slightly charged nanoemulsions obtained by the phase inversion concentration (PIC) method quite explicitly. Within this section we address its mechanism upon dilution of the oil/surfactant mixture; as so far only little information on this topic has been obtained.

4.5.1.1 Nuclear Magnetic Resonance (NMR) measurements

Nevertheless, the general acceptance of a change in surfactant curvature due to a modification of the oil/surfactant composition upon dilution was a starting point for our investigations. Consequentially, we first followed the presumed compositional change of the O/S-mixture upon dilution by NMR measurements. NMR spectra provide information about the chemical environment of the spinning hydrogen nucleus, and can be used to deduce the atomic bonding patterns in the molecule. For our studies we diluted our PIC-qualified O/S-mixture (diethylhexyl carbonate / phenoxy ethanol + parabene mixture (Euxyl[®] K300) / polyglycerol-4 laurate / AOT (66/12/21.1/~0.9%)) with deuterium oxide (D₂O) taking into account the density difference to water (H₂O). AOT was chosen as charged surfactant (eg. ¹H-NMR reference spectrum of AOT in fig. A.11e of the appendix). However, according to its low fraction (~ 0.9 wt-%) employed in the O/S-mixture, we do not expect to find strong resonance-signals of electron-nucleus interactions for this molecule with atoms in its vicinity (the surfactant itself and other ingredients of the O/S-mixture) in the NMR spectra.

The obtained spectra for O/S-dilutions (30, 60, 75, 90, 95% H₂O) are given in fig. 4.63. The chemical shift for peaks of the O/S-ingredients is indicated in respect to the composition of the mixture. Reference spectra for more detailed information about single components and their chemical shifts are given in the NMR-spectra A.11 of the pure components in the appendix.

The signals between 0-2 ppm are mainly attributed to the carbonate DEHC (main oil component, 66wt-% of O/S-mixture) and does not change much in terms of peak position (fig. 4.63 and fig. 4.64a). The decrease in intensity is caused due to the decreasing concentration of the initial

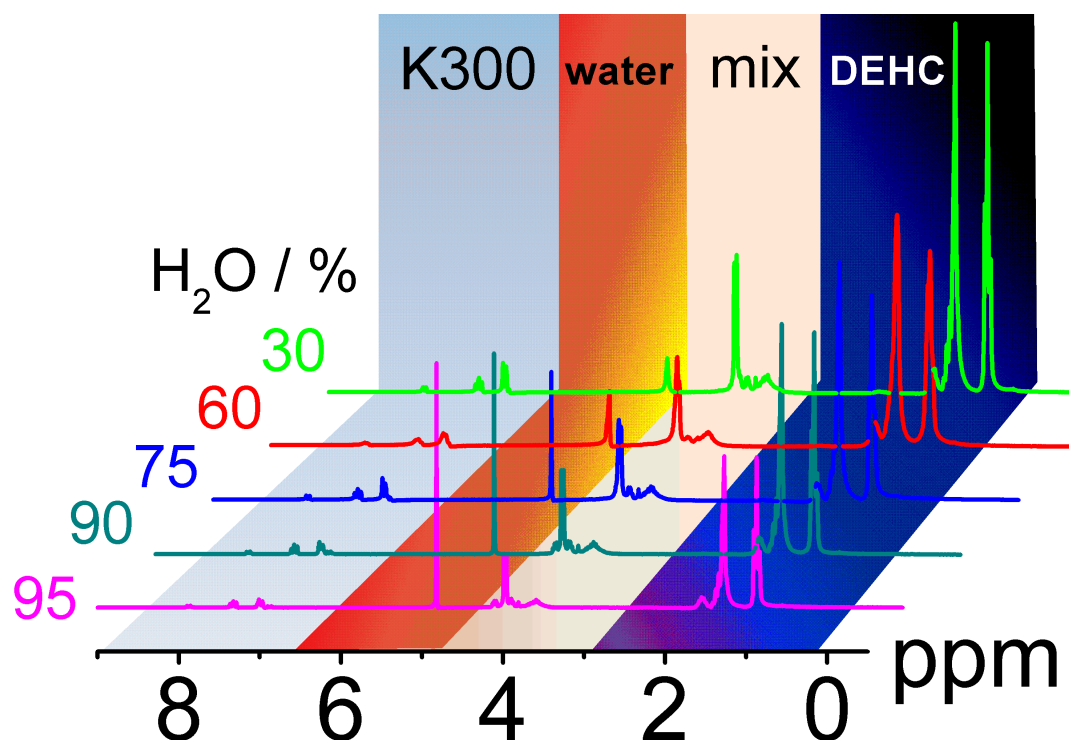


Figure 4.63: ^1H -NMR (200 MHz) of diluted oil/surfactant mixture upon dilution pathway while forming nanoemulsions at concentrations $> 75\%$ H_2O ; peak indication is specified for the compound of oil/surfactant mixture (diethylhexyl carbonate (DEHC) / Euxyl[®] K300 (parabens + phenoxy ethanol mixture) / polyglycerol-4 laurate (P4L) / AOT) with the highest influence at given chemical shift (for an overall comparison of each single compound to the given PIC-spectra see NMR-reference spectra A.11 in the appendix).

O/S-mixture upon dilution. Detailed information about signal position and intensities are given in table A.18 of the appendix. The singlet-peak around 4.82 ppm is given by the water signal ($\text{HDO}/\text{H}_2\text{O}$) due to an exchange of deuterium with the hydroxyl groups of the O/S-mixture. According to a systematic increase of water concentration one would expect a linear increase of the intensity likewise. In fact that is exactly what we observe (inset fig. 4.64c) at higher dilution ratios, as for lower concentrations the water gets first bound to the protonatable hydroxyl groups of the compounds (eg. reference spectra fig. A.11 in appendix).

The NMR-spectra between 2-4 ppm (eg. fig. 4.64b) are due to nuclear magnetic resonances of various components of the O/S-mixture. The main peak (~ 4 ppm, doublet) is due to the preservative mixture and the broad smeared ones by the hydrophilic head-group of the main surfactant polyglycerol-4 laurate (3.5 - 3.9 ppm). The reason for the slight shift (0.2%) in up-field direction can be seen in a dissolution of the preservative mixture (K300 $\sim 12\text{wt}\%$ of O/S-mixture) upon dilution whose chemical shift for the ether neighbored carbon atoms appear at similar resonance frequencies. The dissolution of the preservative mixture (K300) becomes more apparent if one considers the strong chemical shift (2%) downfield for the resonances given around 6-8 ppm that belong only to the parabens and the phenoxy ethanol. one can calculate an approximate fraction that remains in oil phase upon dilution. The chemical shift

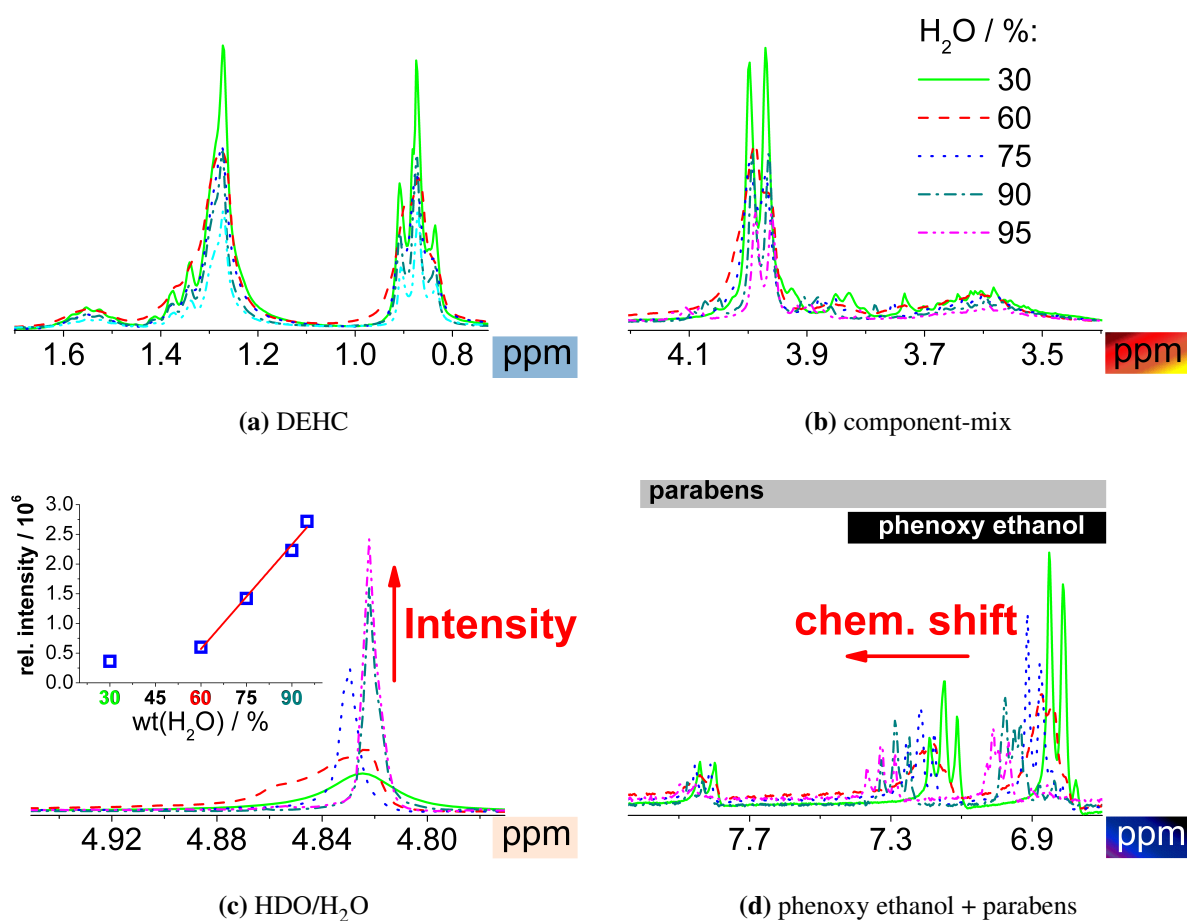


Figure 4.64: The graphs **a - d** show different parts along the chemical shift of the $^1\text{H-NMR}$ spectrum given in figure 4.63. They are more detailed analysis of $^1\text{H-NMR}$ (200 MHz) spectra for oil/surfactant mixtures (diethylhexyl carbonate / phenoxy ethanol + parabene mixture / polyglycerol-4 laurate / AOT) diluted upon emulsification pathway (— 30, - - - 60, . . . 75, - - - - 90 and - - - - - 95 wt-% H_2O) to form nanoemulsions at concentrations $> 75\%$ H_2O . Grey and black bars in fig. 4.64d are distinguishing between common NMR resonances caused by phenoxy ethanol and parabens, and references by parabens only.

downfield with increasing water concentration is describable by a single exponential growing function. If there is a linear dependence of the diluted preservative mixture in the water phase with the drift of the chemical shift, we can assume that the offset of the exponential function gives the chemical shift when all preservative mixture is contained in the oil phase and calculate an approximate fraction of the individual preservative components given in either the oil or water phase respectively. From our reference spectra we obtain the corresponding value for its fully dilution in water. Table 4.10 summarises these calculations and gives the overall fraction of the preservative mixture remaining in the oil phase upon dilution. Thereby a further distinction is possible, whereas the doublet-signal refers (~ 7.8 ppm) to the parabens only and the two triplet-signals (7.2 and 6.9 ppm) are due to the parabens and the phenoxy ethanol. It is obvious that the triplet signals have a larger chemical shift downfield ($\Delta\text{ppm} \approx 0.18$ ppm) than the doublet one ($\Delta\text{ppm} \approx 0.07$ ppm) -fig. 4.64d. This is due to the additional dissolution of

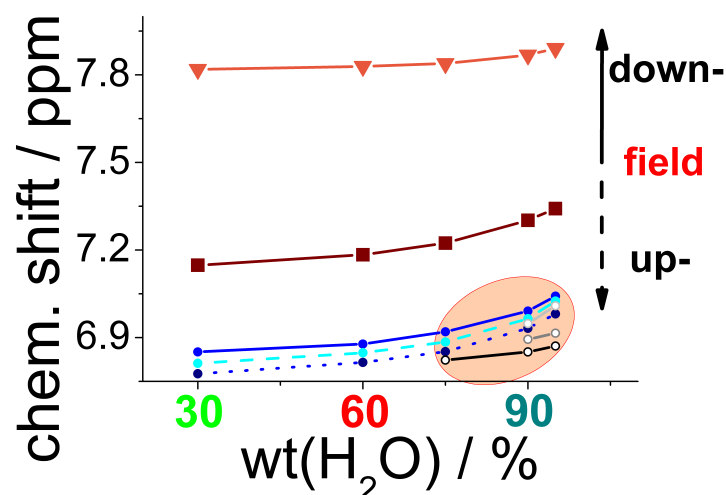


Figure 4.65: Shift of NMR-signal more down-field with increasing water concentration due to a dissolution of the preservative mixture (phenoxy ethanol/parabens 72/28) in the aqueous phase; shift appears stronger for triplet signals (7.2 (shift of main peak) and 6.9 ppm (evolution from triplet- to multiplet-state at higher concentrations; shaded circle)) given by the parabens + the phenoxy ethanol, than for the doublet one (7.8 ppm (average of the doublet)), that belongs to the less available and less soluble parabens only.

larger amounts of phenoxy ethanol beside the parabenes into the aqueous phase (ratio phenoxy ethanol/parabens in the O/S-mixture 72/28). The different solubility properties of the parabens and the phenoxyethanol become more pronounced at higher dilution ratios in the nanoemulsion region. Here, the individual solubilities of the paraben mixture lead to a splitting of the initial triplet state at ~ 6.9 ppm to a multiplet (eg. fig. 4.64d and shaded area in fig. 4.65). However, all ingredients of the preservative mixture seem to be accounted to get leached out upon dilution (change of chemical shift down-field, eg. fig. 4.65) due to their relatively high hydrophilicity (eg. tab. 4.13).

From the change of chemical shift caused by the preservative mixture (K300) one can calculate the approximate fractions given in either oil or water phase while diluting the O/S-concentrate Tego[®]Wipe DE (mixture of DEHC/K300/P4L/DC (66/12/21.1/0.9wt-%)) with water. The

| K300 component | peak type | fully dissolved | |
|----------------|-----------|-----------------|---------------------|
| | | in oil | in H ₂ O |
| PB | db | 7.83 | 7.95 |
| | | 7.81 | 7.91 |
| PhOH | tp | 7.07 | 7.43 |
| | | 6.74 | 7.10 |

Table 4.9: Signal positions (δ) for two paraben (PB) doublet- (db) and phenoxy ethanol (PhOH) triplet- (tp) peaks, when the preservative mixture (K300 consists of 72% PhOH and 28% PB) is either totally dissolved in the pure oil (offset y_0 of single exponential fit-function in 4.65) or pure water (NMR-signal directly measured for water saturated with K300-solution) phase.

| H ₂ O wt-% | in oil | | in H ₂ O | |
|--------------------------|--------|------|---------------------|------|
| | PhOH | PB | PhOH | PB |
| 0 | 1 | 1 | 0 | 0 |
| 30 | 0.96 | 0.99 | 0.04 | 0.01 |
| 60 | 0.91 | 0.99 | 0.09 | 0.01 |
| 75 | 0.71 | 0.81 | 0.29 | 0.19 |
| 90 | 0.41 | 0.54 | 0.59 | 0.46 |
| 95 | 0.24 | 0.36 | 0.76 | 0.64 |
| 100 | 0 | 0 | 1 | 1 |

Table 4.10

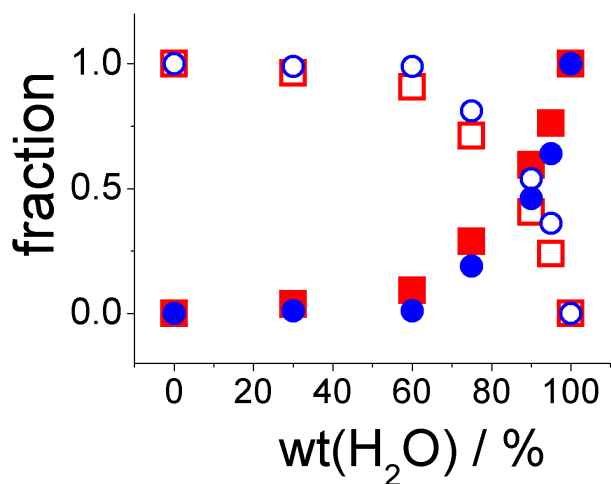


Figure 4.66

Table left: Tabulation and **Figure right:** Visualization of calculated fractions of phenoxyethanol (□ ■ PhOH) and parabens (○ ● PB) given in either oil (*open symbols*) or water phase (*closed symbols*) while diluting the O/S-concentrate Tego[®]Wipe DE (mixture of DE-HC/K300/P4L/DC (66/12/21.1/0.9wt-%)) upon dilution with water (0, 30, 60, 75, 90, 95 and 100wt-% H₂O). Calculations were derived from NMR-spectra (fig. 4.63 and 4.64d) due to the chemical shift of the preservative mixture Euxyl[®]K300 which consists undiluted of 72% phenoxyethanol and 28% diverse parabens. The chemical shift correlates systematically with the percentage of cosurfactant and allows the deduction of the individual components fraction given in oil or water phase due to the knowledge about the signal position when the cosurfactant is totally dissolved either in the pure oil or pure water phase.

chemical shift downfield is describable by a single exponential growing function ($y = A1 \cdot \exp(-x/t1) + y0$) with increasing water concentration (see exponential dependence in fig. 4.65). The function's offset y_0 gives the individual peak position of the preservative mixture components that are totally dissolved in the oil phase. The individual peak positions (chemical shift δ) given in the NMR-spectra upon dilution (for $x = 30, 60, 75, 90$ and 95 wt-% water (H₂O)) are listed in table A.18 of the appendix.

Due to the knowledge about the signal position when the preservative mixture is totally dissolved either in the pure oil (ordinate-offset of single exponential growing function in fig. 4.65) or pure water phase (NMR-signal directly measured for water saturated with K300-solution), one can deduce its percentage for the individual phases upon dilution of the O/S-concentrate. For our calculations we assumed a linear dependence for the dilution of the preservative mixture with the drift of the chemical shift. Table 4.10 lists the calculated fractions of phenoxy ethanol (PhOH) and the diverse parabens (PB) in water and oil phase upon dilution of the oil/surfactant concentrate. Both fractions of the preservative mixture (K300), phenoxy ethanol and the diverse parabense, are getting leached (*open symbols* in figure 4.66) out from the oil phase with increasing water concentration. For low and middle dilution ratios (H₂O < 60wt-%) only little of the preservative mixture (~1%, in respect to the O/S-mixture) gets dissolved into the aqueous phase. This dissolution of the cosurfactant is sufficient to lower the interfacial tension substantially prior the phase inversion concentration and enables the formation of bicontinuous

microemulsion-like structures with a zero mean surface curvature. Such structures are prerequisites for the formation of nanoemulsions.

At higher dilution ratios $\geq 75\%$ H₂O more and more of the preservative mixture diffuses into the aqueous phase and facilitates the high effective solubilisation capacity of the NE-system.

The distribution of a given solute in bulk phases can be described also by the Nernst partition law. It declares that the concentration-ratio for some solute species in two bulk phases in contact is constant for a sufficiently diluted system [36]:

$$K_N = \frac{[c(\text{solute})]_{aq}}{[c(\text{solute})]_{oil}} \quad (4.14)$$

The value of the constant K_N depends on the temperature and is called Nernst partition coefficient. The equation is only valid if the concentrations are not too large and if the observed species (solute) does not change its form in any of the two phases (oil or water). In case of molecule association or dissociation it describes the equilibration of both phases, but only when the same form is present - concentrations of all remaining forms must be calculated by taking into account all the other equilibria [107]. We applied this simple approximation to the phenoxy ethanol and paraben fraction. A plot of function $f(c(\text{solute})_{oil}) = c(\text{solute})_{aq}$ results thereby in a proportional dependence with an interception point at the graph-origin. Its slope

| H ₂ O wt-% | c(PhOH) | | c(PB) | |
|--------------------------|----------------|-----------------------------|----------------|-----------------------------|
| | in oil g/mL | in H ₂ O g/mL | in oil g/mL | in H ₂ O g/mL |
| 0 | 11.6 | 0.0 | 29.8 | 0.0 |
| 30 | 12.0 | 132 | 30.1 | 1191 |
| 60 | 12.8 | 187 | 30.1 | 4168 |
| 75 | 16.3 | 120 | 36.7 | 472 |
| 90 | 28.5 | 175 | 55.2 | 581 |
| 95 | 48.4 | 289 | 82.5 | 885 |

Table 4.11

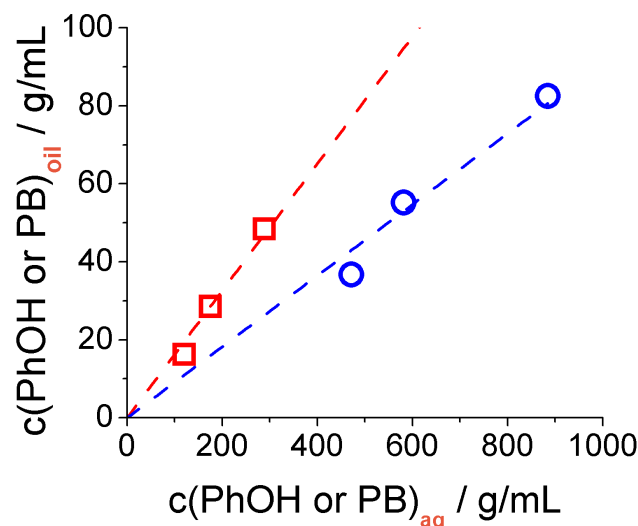


Figure 4.67

Table left: Tabulation and **Figure right:** Visualization of calculated concentrations of phenoxyethanol (\square PhOH) and parabens (\circ PB) given in either oil or water phase while diluting the O/S-concentrate Tego[®] Wipe DE (mixture of DEHC/K300/P4L/DC (66/12/21.1/0.9wt-%)) upon dilution with water (0, 30, 60, 75, 90 and 95 wt-% H₂O). In addition figure 4.67 illustrates the Nernst partition law (equation (4.14)), which states that the concentration-ratio for some solute species (here: PhOH and PB) in two bulk phases in contact (here oil and water) is constant for a sufficiently diluted system (H₂O > 60wt-%). The slope of the first order law gives the Nernst partition coefficient K_N for phenoxyethanol $K_N(\text{PhOH}) \approx 0.16$ and the diverse parabens $K_N(\text{PB}) \approx 0.09$.

constitutes the Nernst partition coefficient for phenoxy ethanol $\square K_N (\text{PhOH}) = 0.16$ and the parabens $\circ K_N (\text{PB}) = 0.09$. Table 4.11 summarises the individual concentrations of phenoxy ethanol and parabens in either oil or water phase, according to the fractions we determined by the NMR-measurements (compare table 4.10). Figure 4.67 plots the Nernst partition law for phenoxy ethanol and parabens, showing a steeper slope (Nernst partition coefficient) for phenoxy ethanol than for the parabens. Visualised values for this plot were taken only for high dilution ratios ($\geq 75\%$ H_2O), as otherwise the Nernst partition law is not valid anymore and also does not give a linear dependency (see also values $< 75\%$ H_2O in table 4.67).

4.5.1.2 Refractive index contrast matching

As a consequence of our NMR-studies on the effect of dilution we had to learn more about the detailed mixture given in our nanoemulsion oil droplets at water concentrations $> 75\%$ H_2O . Here, refractivity measurements have been the means of choice as their employment, while using refractive index matching substances like glycerol or sugars (glucose, galactose - refractivities of water/index matching substance are given in table A.17), in combination with turbidity measurements allow to draw more refined conclusions.

For that we added different mass fractions of glycerol (1, 5, 10, 15, 20, 30 and 50%) to beforehand formed nanoemulsions at different water ratios (80, 85, 90, 95, 98% H_2O). Glycerol was chosen, as its miscibility covers a greater range than dissolved sugar ($\leq 10\text{wt}\%$) and hence lowers the absolute difference of the interception point (± 0.0010). However, fig. 4.68 shows a contrast match for the different sugars and glycerol for a nanoemulsion of 95% water respectively. The interception point with the abscissa marks the refractive index of the dispersed aggregates in the given solvent. Detailed values of refractivities $n^{25^\circ\text{C}}$ and turbidities τ for the other dilution ratios are given in table A.19 of the appendix. The contrast evolution of the dispersed aggregates in the nanoemulsion region ($> 75\text{wt}\%$ (H_2O))) are listed in table 4.12 and shown in fig. 4.69. A slight increase of the matching point with increasing water concentration is visible. A comparison of the obtained refractivities by the dispersed aggregates with the one of the initial nanoemulsion O/S-mixture of our model system ($n^{25^\circ\text{C}} (\text{TW}) = 1.4535$) shows a great discrepancy. This is not astonishing due to the loss of preservative mixture (phenoxy ethanol and div. parabens) upon dilution pathway, we already observed during our NMR-experiments and which is expectable due to their solubility properties. Refractivities $n^{25^\circ\text{C}}$ and water solubility tendencies (eg. Hildebrand parameter δ) of the individual components employed in our model system Tego[®] Wipe DE (TW) are listed in table 4.13.

However, at this point it is interesting to note that the given refractivities of the dispersed aggregates possess lower values than the refractivities of the individual components that are assumed to remain in the nanoemulsion droplets (eg. NMR-observations in section 4.5.1.1 and table 4.13). From this fact we can derive that the main surface active agent polyglycerol-4 laurate (eg. molecular structure in fig. 3.1c) does not exist molecularly dissolved in the oil phase according to its high refraction index that would have led to refractivities of the dispersed aggre-

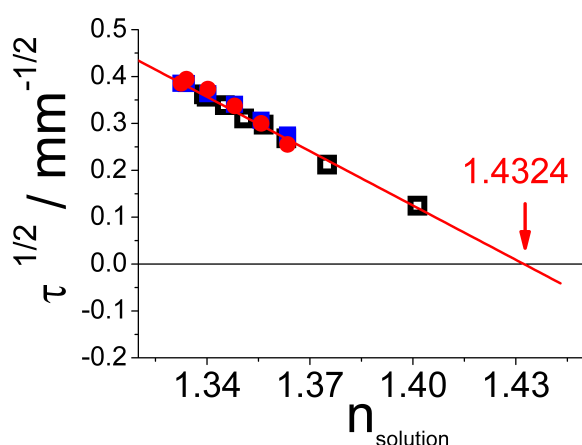


Figure 4.68: Square root of turbidity τ , determined by UV/Vis-transmittance measurements (eg. appendix fig. A.10), of oil/water nanoemulsions (5:95) based on our model system Tego[®] Wipe DE spiked with refractive index influencing substances (glycerol (0,1,5,10,15,20,30,50%), glucose and galactose (0,1,5,10,15,20%)) versus the concentration dependent refractivity of the solvent mixtures \square H₂O/glycerol, \bullet H₂O/glucose and \blacksquare H₂O/galactose. Interception point with the abscissa marks the refractivity of the dispersed aggregates.

| H ₂ O | $n^{25^\circ\text{C}}$ -match | x(DEHC) | x(undecane) |
|------------------|-------------------------------|---------|-------------|
| 80 | 1.4306 | 70.8 | 29.2 |
| 85 | 1.4311 | 73.6 | 26.4 |
| 90 | 1.4322 | 79.0 | 21.0 |
| 95 | 1.4324 | 80.0 | 20.0 |
| 98 | 1.4323 | 79.5 | 20.5 |

Table 4.12: Refractivities at $25.0 \pm 0.1^\circ\text{C}$ in matched case (eg. interception point of abscissa in graph 4.68) of nanoemulsion droplets at different dilution ratios (80,85,90,95 and 98% H₂O) and concluded oil/surfactant composition of the dispersed nanoemulsion mixture; given by the main oil component (2-ethylhexyl carbonate (DEHC)) and the lipophilic part (undecane) of the main surfactant polyglycerol-4 laurate (P4L).

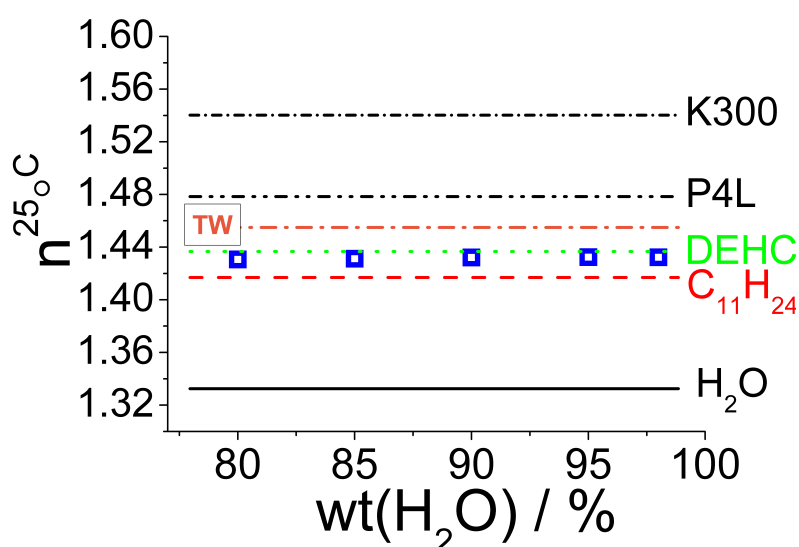


Figure 4.69: \square Refractivities (eg. tab. 4.12) of the dispersed aggregates at different dilution ratios in the nanoemulsion region ($> 75\%$ H₂O). Different types of lines are indicating the refractive index of the individual components contained in our model system Tego[®] Wipe DE (DEHC/K300/P4L/DC - 66/12/21.1/0.9). Reference refractivity of water and additional one of undecane (lipophilic part of P4L-surfactant) are complemented.

| component | wt-% in TW | $\rho^{25^\circ\text{C}}$ g/cm ³ | $n^{25^\circ\text{C}}$ | $\text{H}_2\text{O}_{\text{solub.}}$ mg/L | V_m mL/g | ΔH_{vap} kJ/mol | δ (J/cm ³) ^{1/2} |
|---------------------------------|---------------|--|------------------------|--|---------------|-----------------------------------|---|
| TW | | 0.954 | 1.4535 | | | | |
| DEHC | 66 | 0.893 | 1.4362 | 2.8 | 321 | 64.2 | 13.9 |
| K300 | 12 | 1.122 | 1.5400 | 5000 | 128 | | >20 |
| phenoxy ethanol | (8.6) | 1.11 | 1.5373 | 20 000 | 124 | 54.8 | 20.5 |
| div. parabens (avrg. values) | (3.4) | >1.1 | >1.5 | >1700 | 136 | 61.2 | 20.8 |
| P4L | 21.1 | 1.094 | 1.4759 | 4.8 | 454 | 91.7 | 14 |
| DC | ~0.9 | 1.011 | >1.441* | <252 100* | 523 | 139 | 16.2 |

| | | | | | | | |
|------------------|--|-------|--------|-----------|------|--------|------|
| tetraglycerol | | 1.280 | 1.4825 | >100000** | 205 | >100** | > 95 |
| undecane | | 0.746 | 1.4170 | | 212 | 40.1 | 13.3 |
| glycerol | | 1.260 | 1.473 | 100000 | 73.1 | 71.9 | 30.8 |
| H ₂ O | | 0.997 | 1.3325 | | | | |

Table 4.13: Densities $\rho^{25^\circ\text{C}}$, refractivities $n^{25^\circ\text{C}}$, water solubility $\text{H}_2\text{O}_{\text{solub.}}$, molar volume V_m , heat of vaporization ΔH_{vap} and Hildebrand parameter δ (eg. section 3.2.7.2) at $25.0 \pm 0.1^\circ\text{C}$ for individual components of the oil/surfactant formulation Tego[®] Wipe DE (TW - 2-ethyl hexyl carbonate (DEHC), Euxyl K300 (phenoxyethanol + diverse parabens), polyglycerol-4 laurate (P4L) and dilauryl citrate (DC)); *values of diethyl citrate and **glycerol, due to a lack of availability of pure dilauryl citrate and tetraglycerol respectively.

gates much bigger than the one of the main oil phase 2-ethylhexyl carbonate ($n^{25^\circ\text{C}}$ (DEHC) = 1.4362). Furthermore its lipophilic headgroup (tetraglycerol), whose refractivity is just slightly higher than those of the monoglycerol, gets masked out due to the dissolution of the water miscible substances (preservative mixture) of the initial O/S-mixture that possess greater refractivities and therefore rise the common refractivity level for the solvent mixture. As a result of this, the observed refractivities of the dispersed aggregates are mainly given by the surfactants lipophilic tail (undecane) and the oil diethylhexyl carbonate.

Consequently we are enabled to calculate an approximately O/S-ratio for the individual dilution ratios. Table 4.12 summarises the given fractions (x) of either diethylhexyl carbonate (DEHC) or polyglycerol-4 laurate (lipophilic part of P4L: undecane). Our calculations revealed that the hydrophilic surfactant gets progressively dissolved into the aqueous phase with increasing water concentration and therefore is less available to cover the emulsion droplets and results in a particle growing.

However, it should be mentioned again that the calculations give only approximated values of the individual O/S-fractions, as the proper contrast conditions are not completely clear in respect to the multi-component system. This becomes more obvious if we also consider the NMR-results showing a remaining fraction of approximately < 6wt-% for the preservative mixture (initially 12wt-% of the O/S-mixture) in the nanoemulsion droplets (tab. 4.10).

4.5.1.3 Small-Angle Neutron Scattering (SANS)

With refractivity and NMR measurements we could ascertain that a larger amount of the O/S-mixture gets dissolved into the aqueous phase upon dilution to form nanoemulsions. We observed an almost fully transfer from the dispersed (oil) to the continuous phase (water) for the preservative mixture and a fractional transfer for the hydrophilic surfactant. The surfactant is positioned at the oil water interface of the aggregates and not molecularly dissolved in the oil phase (known from the refractivity measurements eg. section 4.5.1.2).

As neutrons are quite sensitive to the isotopic composition of the observed sample, we could draw some further conclusions on the nanoemulsion droplets formed at different water ratios. During our SANS-data analysis of the model system Tego[®] Wipe De in the nanoemulsion region ($> 75\%$ H₂O; eg. fig. 4.10a), which was already investigated quite intensively by us (eg. section 4.1), we experienced, similar to the refractivity and NMR measurements, that the actual volume fraction, to fit the data properly, needed to be smaller than the theoretically expected one. However, due to the change of O/S-composition given in the dispersed aggregates, an adjustment of the used scattering length density (SLD) was necessary that again influences the volume fraction Φ of the aggregates (eg. eq. (3.14)). At this point it should be mentioned that an adjustment of the employed SLD for the aggregates does not have any impact on the model, particle sizes and distributions we referred to in section 4.1.

| H ₂ O wt-% | Φ theo. | Φ actual |
|--------------------------|-----------------|------------------|
| 80 | 0.208 | 0.168 |
| 85 | 0.156 | 0.117 |
| 90 | 0.105 | 0.074 |
| 95 | 0.052 | 0.042 |
| 98 | 0.021 | 0.017 |

Table 4.14: Comparison of theoretical and actual volume fraction Φ , given in the nanoemulsion droplets upon dilution (H₂O). Actual volume fraction was ascertained by contrast SANS-measurements.

Contrast Variation - Verification of O/S-composition in aggregates

Small-angle Neutron scattering contrast variations of the solvent (H₂O/D₂O-ratio), while using nanoemulsions based on our model system Tego[®] Wipe DE at different dilution ratios (taking into account the density difference of deuterium oxide $\rho(\text{D}_2\text{O}) \approx 1.1 \text{ g/cm}^3$), should help us to ascertain our refractivity results in terms of the determined O/S-ratio hold by the emulsified oil-droplets. As a consequence of this, we also aimed to achieve a proper scattering length density SLD and hence volume fraction Φ of the dispersed aggregates for further detailed SANS-data analysis. The scattering curves of a contrast variation for a nanoemulsion at 95wt-% are given in fig. 4.70a. They show a decrease of scattering intensity with increasing the hydrogenated part of the solvent mixture (H₂O/D₂O); starting at full contrast (100% D₂O) and maximum intensity for the observed nanoemulsion (95% water).

In case of a contrast match, which describes the situation in which the solvent mixture exhibits exactly the same contrast conditions like the dispersed oil droplets, the scattering curve

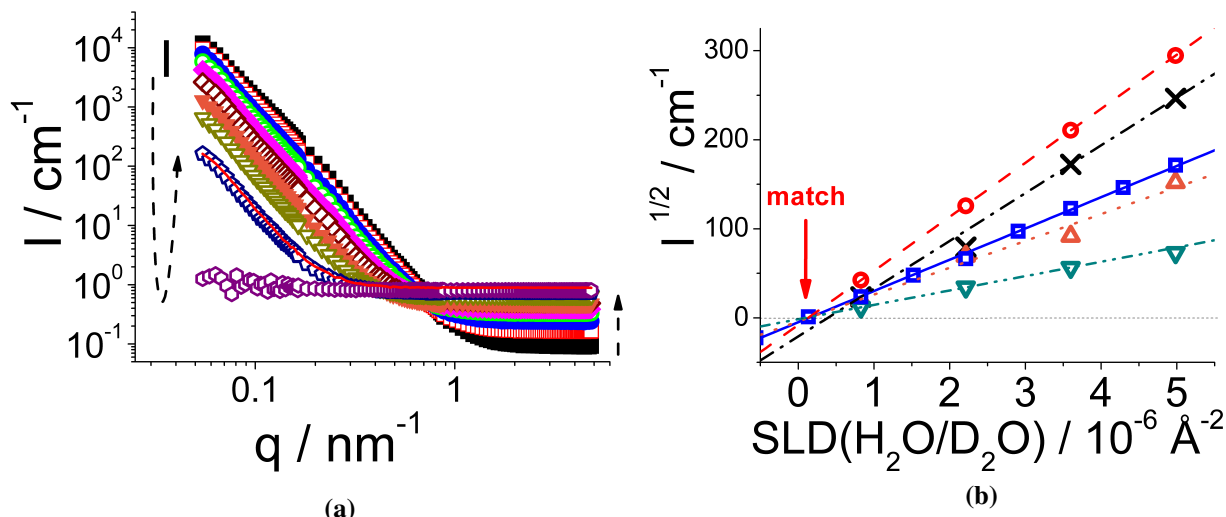


Figure 4.70: a) Contrast variation of a nanoemulsion, based on our model system Tego[®] Wipe DE at a dilution ratio of 95wt-% water. Contrast of aqueous phase was changed by different H₂O/D₂O-ratios (■0, □10, ●20, ○30, ◆40, ◇50, ▼60, ▽70, ◇80, ○90 and — 100% H₂O), while accounting for the density difference of deuterium oxide.

b) Determination of SLD the oil droplets possess in the nanoemulsion region (x 80, ○ 85, △ 90, □ 95, ▽ 98wt-% H₂O). The matching point of the aggregates with the solvent is marked as interception point with the abscissa. Plot shows the square root of Guinier approximated intensities $\sqrt{I_0}$ for the SANS curves of the individual contrast variations versus the scattering length density of the solvent mixture (SLD(H₂O/D₂O)).

passes through zero-intensity scattering. Hence, the aggregates scattering length density can be determined. In figure 4.70b the aggregates matching point is marked as interception point with the abscissa for a plot of the square root of Guinier approximated intensities to $q = 0$: $\sqrt{I_{(q=0)}}$ of the scattering curves (eg. 4.70a for 95wt-% H₂O, respectively) versus the scattering length density of the solvent mixture (SLD(H₂O/D₂O)). In case of interparticle interferences (80 and 85wt-% H₂O) a hard sphere structure factor was taken into account (fig. 4.71) and the corresponding scattering curve of a sphere used for the Guinier approximation due to equa-

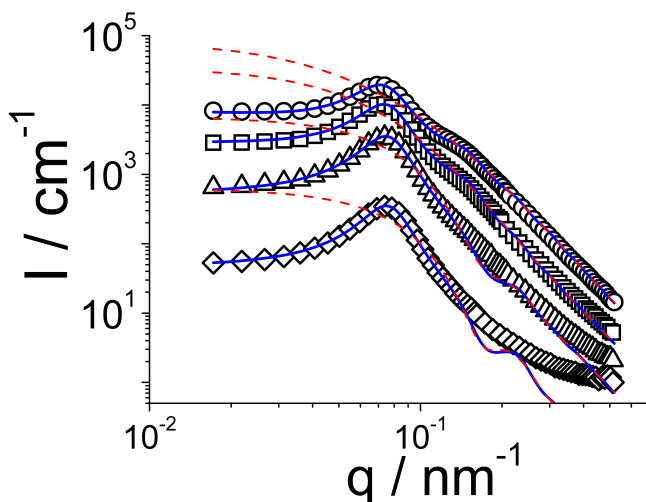


Figure 4.71: Contrast variation for TW-sample diluted with 80% (H₂O/D₂O) at four different contrasts (○20, ◇40, △60 and ◇80wt-% H₂O, respecting the density difference to H₂O). In addition fits of polydisperse sphere model taking a structure factor into account — and its pure spherical scattering without structure factor - - - to obtain reliable initial scattering intensities for Guiniers' approximation in contrast match analysis.

tion (3.30). The different aggregates SLDs, given by the interception points in plot 4.70b, are listed in table 4.15. Figure 4.70b visualises the evolution of the aggregates SLD upon dilution of the nanoemulsion droplets. Similar to the refractivity trends we observe a slight increase of the SLD with increasing water concentration before the contrast decreases again at high dilution ratios. Our comparisons of the refractivity and SANS contrast evolution show a large discrepancy at 80wt-% water. Correlations with the contrasts seen for the individual compounds (refractivities in table 4.13 and SLDs in table 4.16) revealed for the SANS observations a full contrast of the main surfactant polyglycerol-4 laurate. This is different to the refractivity measurements, where we observed just the hydrophobic chain (undecane) of the surfactant P4L, and therefore is not really conclusive to us as refractivity and SANS contrast variations should lead to the same observations. From the matching points we calculated the individual volume fractions of the preservative mixture and the main surfactant phase, assuming that all oil is accounted to form nanoemulsion droplets. In respect to the SLD-deviations ($\sim 25\%$, tab. 4.15) we could only qualify that both the preservative mixture and the surfactant are dissolving progressively into the aqueous phase with increasing water concentration. As for the contrast studies for the dilution of TW with 95wt-% water eight different solvent contrasts were measured, we used the volume fraction, deduced from its matching point, to derive an approximately fraction of the preservative mixture remaining in the oil phase upon dilution. This was done due to the fact that only four different solvent contrasts were performable for the other four dilution ratios (80, 85, 90 and 98wt-% water) and hence less uncertainties are present for the determination of the matching point at 95wt-% water. However, from the volume fraction $\Phi_{actual,95}$ (tab. 4.15) at a dilution of the O/S-mixture at 95wt-% water, its matching point for the aggregates $SLD_{Agg,95}$ (tab. 4.15) and the individual scattering length densities of the pure compounds (DEHC, K300 and P4L in tab. 4.16) we calculated an approximately fraction of the preservative mixture of 3wt-% and

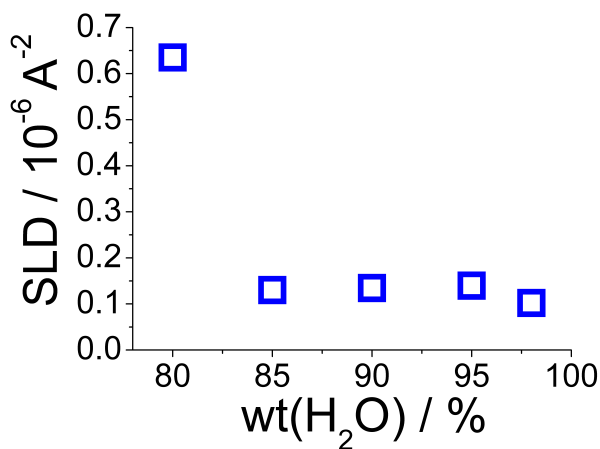


Figure 4.72: SLD at the matching point in nanoemulsions upon dilution.

| H ₂ O % | SLD_{Agg} 10^{-6} \AA^{-2} | ΔSLD_{Agg} 10^{-6} \AA^{-2} | Φ theo. | Φ actual |
|-----------------------|---|--|-----------------|------------------|
| 80 | 0.5336 | 0.1818 | 0.208 | 0.168 |
| 85 | 0.1303 | 0.0077 | 0.156 | 0.117 |
| 90 | 0.1346 | 0.3726 | 0.105 | 0.074 |
| 95 | 0.1397 | 0.0397 | 0.052 | 0.042 |
| 98 | 0.1022 | 0.0256 | 0.021 | 0.017 |

Table 4.15: Scattering length densities SLD_{Agg} . (and its error ΔSLD_{Agg} .) of nanoemulsion droplets given for different dilution ratios (H₂O/D₂O) using our model system Tego[®] Wipe DE. In respect to the given SLDs, resulting volume fractions Φ_{actual} of the aggregates and theoretical ones Φ_{theo} . for comparison reasons. Hence, this table is an extension of the fit parameters given in table 4.2 of section 4.1.2.2.

for the surfactant of $\sim 17\text{wt-}\%$ according to equation (3.14) and in respect to whole initially employed O/S-mixture (DEHC/K300/P4L/DC (66/12/21.1/ $\sim 0.9\text{wt-}\%$), see also tab. A.21 in the appendix). These results go along with our NMR- and refractivity observations.

However, with the obtained scattering length densities for the individual dilution ratios we could adjust the volume fractions achieved by the model analysis (section 4.1.2.2). According to equation (3.29) the particle sizes and distributions remain constant, we already obtained from the model fits of the aggregates, forming in the nanoemulsion region upon dilution. The volume fractions that we derived from our contrast match experiments are given in table 4.15.

From the number weighted average particle size $\langle R \rangle_{Mw}$ of the two populations formed in the nanoemulsion region (see section 4.1.2.2) and the volume fraction obtained by the contrast variations we deduced the surfactant volume fraction that stabilises the emulsion droplets. The radius of both populations was averaged by the first four moments of a Log-normal distribution function (section A.8.1) and corrected (corr.) for the surfactant's head group (eq. 4.15).

$$\langle R \rangle_{Mw,corr.} = \sqrt[3]{1-A} \cdot \langle R \rangle_{Mw} \quad (4.15)$$

$$\text{with } A = \frac{V_{HG}}{V_{total}} \quad (4.16)$$

With V_{HG} being the volume of a surfactant head group and $V_{total} = 4/3 \cdot \langle R \rangle_{Mw}^3$ the volume of a droplet.

The surfactant head group area of polyglycerol-4 laurate P4L a_h was determined by surface tension measurements to $a_h(\text{P4L}) = 0.604 \text{ nm}^2$. The Gibb's adsorption isotherm for its determination is given in figure A.6.6 of the appendix. A percentage fraction of the surfactant hold at the droplets interface $x(\text{P4L})_{oil,\Phi}$ in respect to the the volume fraction of the dispersed phase Φ is given by the number of surfactant molecules at the interface of the total volume $^1N_{As}$, the

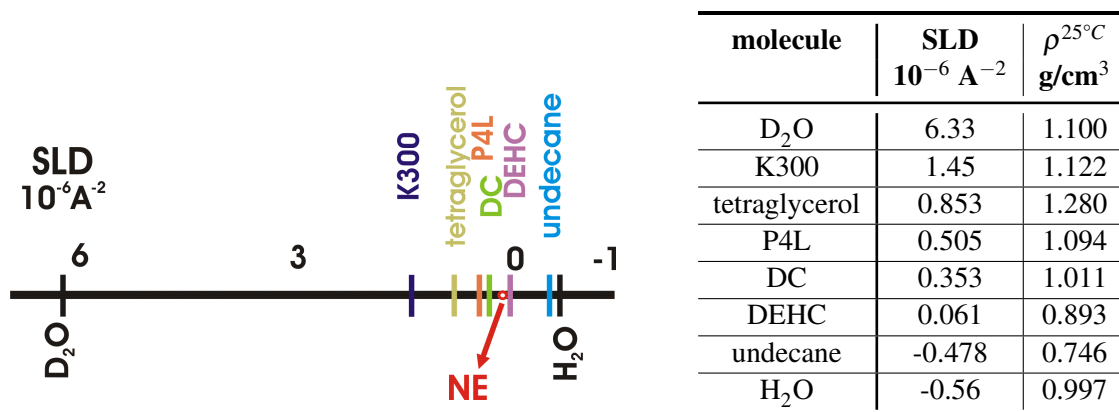


Table 4.16: Scattering length densities (SLD) number ray and list with corresponding densities ρ at 25°C for components hold in the nanoemulsion (NE) mixtures.

| H ₂ O % | $\langle R \rangle_{Mw,corr.}$ nm | Φ | ${}^1N_{As}$ $10^{-3}/\text{nm}^3$ | $x(\text{P4L})_{oil,\Phi}$ % | $x(\text{P4L})_{oil,P4L-total}$ % | $\Phi(\text{P4L})_{oil}$ | $\Phi(\text{P4L})_{H_2O}$ |
|-----------------------|--------------------------------------|--------|---------------------------------------|---------------------------------|--------------------------------------|--------------------------|---------------------------|
| 80 | 23.0 | 0.168 | 12.1 | 5.41 | 20.7 | 0.00910 | 0.03479 |
| 85 | 28.0 | 0.117 | 6.89 | 4.45 | 15.8 | 0.00520 | 0.02765 |
| 90 | 30.1 | 0.074 | 4.07 | 4.14 | 13.8 | 0.00307 | 0.01914 |
| 95 | 33.9 | 0.042 | 2.03 | 3.69 | 13.9 | 0.00153 | 0.00948 |
| 98 | 38.0 | 0.017 | 0.72 | 3.29 | 12.4 | 0.00054 | 0.00382 |

Table 4.17: Determination of surfactant volume fraction in oil $\Phi(\text{P4L})_{oil}$ and water phase $\Phi(\text{P4L})_{H_2O}$ of nanoemulsions ($\geq 80\text{wt-}\%$ water). Additional parameters mean mass weighted radius of both populations including surfactant head group correction $\langle R \rangle_{Mw,corr.}$, actual volume fraction Φ obtained from contrast variation, number of surfactant molecules at the interface of the total volume ${}^1N_{As}$ and resulting percentage fraction of the surfactant hold at the droplets interface $x(\text{P4L})_{oil,\Phi}$ and corresponding fraction $x(\text{P4L})_{oil,P4L-total}$ in respect to the initially employed volume fraction of the surfactant (eg. tab. A.21 for individual volume fractions of O/S-mixture).

molar volume of a single surfactant molecule $V_m = 0.745 \text{ nm}^3$ and the O/S-volume fraction in the dispersed phase (eq. (4.17)). Thereby the number of surfactant molecules at the interface of the total volume ${}^1N_{As}$ can be obtained by the specific surface area $As = \Phi / \langle R \rangle_{Mw,corr.}^3$ and the surfactant head group area a_h (eq. (4.18)).

$$x(\text{P4L})_{oil,\Phi} = \frac{{}^1N_{As} \cdot V_m}{\Phi} \quad (4.17)$$

$$\text{with } {}^1N_{As} = \frac{As}{a_h} \quad (4.18)$$

Table A.21 summarises some important parameters for these calculations and lists the surfactant volume fraction hold by the dispersed emulsion droplets $\Phi(\text{P4L})_{oil}$. The volume fraction decreases with dilution due to a progressive dissolution of the hydrophilic surfactant into the aqueous phase (fig. 4.73).

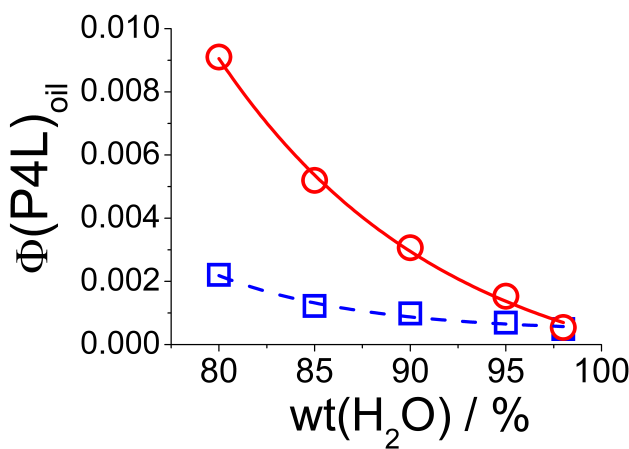


Figure 4.73: Theoretical \square and experimental \circ volume fraction $\Phi(\text{P4L})_{oil}$ of the surfactant P4L employed in the nanoemulsion droplets upon dilution of TW with water in the NE-region ($H_2O \geq 80\%$). Individual values are given in tabel 4.18.

The surfactant fraction transferred from the oil droplets into the aqueous phase causes thus a growing of the mean particle size, while a constant oil fraction is remaining. A simple geometrical estimation of the theoretical surfactant volume fraction $\Phi = L^3 / \langle R \rangle_{Mw,corr.}^3$ using the surfactant molecule length L of $\sim 3 \text{ nm}$ (fig. 3.1c) and the surfactant corrected mean mass weighted radius of both populations $\langle R \rangle_{Mw,corr.}$ showed that the mean

| | exp. | theo. | exp. | theo. | exp./theo | exp./theo |
|--------------------------|--------------------------------------|-------------------|-------------------|--------------------------------------|--------------------------------------|-------------------|
| H ₂ O wt-% | $\langle R \rangle_{Mw,corr.}$ nm | $\Phi(P4L)_{oil}$ | $\Phi(P4L)_{oil}$ | $\langle R \rangle_{Mw,corr.}$ nm | $\langle R \rangle_{Mw,corr.}$ nm | $\Phi(P4L)_{oil}$ |
| 80 | 23.0 | 0.0022 | 0.0091 | 14.4 | 1.60 | 4.14 |
| 85 | 28.0 | 0.0012 | 0.0052 | 17.3 | 1.62 | 4.33 |
| 90 | 30.1 | 0.0010 | 0.0031 | 20.6 | 1.46 | 3.10 |
| 95 | 33.9 | 0.0007 | 0.0015 | 26.0 | 1.30 | 2.14 |
| 98 | 38.0 | 0.0005 | 0.0005 | 36.8 | 1.03 | 1.00 |

Table 4.18: Comparison of theoretical (theo.) and experimental (exp.) evolution for mean NE-radii $\langle R \rangle_{Mw,corr.}$ and surfactant (P4L) volume fraction employed in the NE-droplets ($\Phi(P4L)_{oil} = L^3 / \langle R \rangle_{Mw,corr.}^3$) upon dilution of Tego[®] Wipe DE concentrate with water (H₂O). For theoretical calculations we assumed a surfactant molecule length of $L(P4L) \approx 3$ nm. In addition ratios of exp./theo. values of mean particle radius $\langle R \rangle_{Mw,corr.}$ and surfactant volume fraction employed in the oil droplets $\Phi(P4L)_{oil}$.

radius of the bimodal system has to be somewhat smaller, than the model fits with a bi-lognormal distributed spherical model revealed. A comparison of theoretical and experimental evolution of the mean NE-radius and the surfactant volume fraction employed in the NE-droplets upon dilution is given in figurefig. 4.73 (or respectively tab.fig. 4.18). As we are quite certain about the obtained particle sizes in our bimodal system we studied by different methods (UV-Vis, SANS, cryo-TEM -eg. section 4.1.2), the observed discrepancy might be related to the exact polydispersity of the individual population. The connection of radius and polydispersity for a singly sized distribution function is described in equation (3.27) and becomes more complex for the bimodal case. Moreover, the polidispersities are influencing the value of the mean particle size strongly, calculated by the first four moments of the lognormal size distribution (section A.8.1).

However, our studies show that due to the surfactant hydrophilicity, and its transfer from the oil/water-interface of a nanoemulsion droplet into the aqueous phase, the mean particle size of the emulsion droplets have to increase with increasing water concentration.

4.5.2 Conclusion on PIC-nanoemulsion mechanism.

The formation of nanoemulsions formed by the low-energy phase inversion concentration (PIC) method is based on the change of interfacial composition during the dilution of an appropriate O/S-mixture. We studied the PIC-mechanism as a function of the degree of dilution and followed the compositional change occurring during the dilution process for our model system Tego[®] Wipe DE by means of NMR, refractive index and SANS-experiments.

SANS-model fits on the formed nanoemulsions at dilution ratios $\geq 80\text{wt-}\%$ (H_2O) revealed a general deficit of $\sim 25\text{wt-}\%$ for the actual measured volume fraction to the theoretical initially employed fraction of O/S-mixture to form the nanoemulsions. Due to contrast variations, we could deduce the aggregates exact contrast (scattering length density) and thus achieve the volume fraction of the dispersed phase in the nanoemulsion region by refitting the SANS-data. The loss of volume fraction upon dilution goes along with the finding that we observe an almost complete transfer from the dispersed (oil) to the continuous phase (water) for the preservative mixture (the cosurfactant) and a fractional transfer for the hydrophilic surfactant, while the oil fraction remains constant. The partial extraction of surfactant from the oil droplets causes a growing of the mean particle size with increasing dilution ratio. In summary, the contrast variation in SANS is the most powerful of the methods employed in order to deduce information about the composition of the emulsion droplets as a function of dilution.

4.6 Encapsulation of nanoemulsion droplets formed by the phase inversion concentration method.

Emulsion droplets have been employed frequently as templates to form microcapsules [5, 38, 163] or just a shell around them in order to modify and control their release and take up properties. Of course, as emulsion droplets can vary in size from 50 nm to several μm such shell-like particles are similarly flexible in size and depending on a given application, different size ranges are interesting. However, in general small sizes, as offered by nanoemulsions, are appealing as they allow a very fine distribution of such capsules or shell-modified nanoparticles.

In that context the functionalisation of nanoemulsions that are simply formed by the PIC-dilution process is quite appealing in terms of energy effort, being very benign (thereby allowing to incorporate sensitive active agents, such as biomolecules or drugs), formation dynamics (< 100 ms - eg. section 4.4.1) and structural characteristics (particle size < 100 nm).

In particular we are interested in the encapsulation of nanoemulsion droplets, which is achievable in different ways [25,30,163,180], using surfactant/polyelectrolyte and interpolyelectrolyte complexes (IPEC⁶) or polymerisation reactions.

The investigations described in the following section, concern various encapsulation attempts of PIC-formed nanoemulsion droplets using attractive electrostatic interaction-forces for the assembly process.

As an alternative the formation of a polymeric shell by an interfacial polycondensation reaction using oil-soluble monomer toluene 2,4-diisocyanate (TDI) with water-soluble monomer and crosslinker diethylentriamine (DETA) [176] was contemplated but not further pursued, as the diisocyanate reacts also non-selectively with hydroxyl groups and hence as well with the surfactant/co-surfactant components in our initial O/S-concentrate. However, for completeness some kinetic studies on this topic are given in the appendix (compare section A.7.1).

4.6.1 Encapsulation of PIC-formed nanoemulsion droplets using electrostatic interactions of charged surfactants and the protein lysozyme

The initial idea of our studies was to employ oppositely charged surfactants and polyelectrolytes, where one of the components will be contained in the oily nanoemulsion starting formulation and the second one in the water used for the concentrates-dilution. We expected that their attractive forces lead to a surfactant/polyelectrolyte shell that surrounds the hydrophobic nanoemulsion droplets. Figure 4.74 demonstrates schematically the idea of the encapsulation of nanoemulsions formed by the PIC-process.

⁶Polymers act as polyelectrolytes dependent on the pH.

Almost all ionic and amphoteric surfactants are water soluble. Contrary, mainly non-ionic, some anionic and only rarely cationic surfactants are oil-soluble.

As polyelectrolytes are primarily soluble in aqueous media, we either formulated our O/S-mixtures analogous to our model system Tego[®] Wipe DE (exact compositions are given in section 3.1.1.1) with an anionic surfactant by just replacing the not purely available dilauryl citrate or adding another surfactant to it. As the latter already supplies everything to ensure a successful nanoemulsion formation by a simple dilution procedure we commonly used this possibility to work on the encapsulation of the nanoemulsion droplets. In particular, we employed the protein lysozyme as biopolyelectrolyte due to its biorelevance and the fact that such bio-hybrid nanoemulsions are an interesting novel type of nanostructured material.

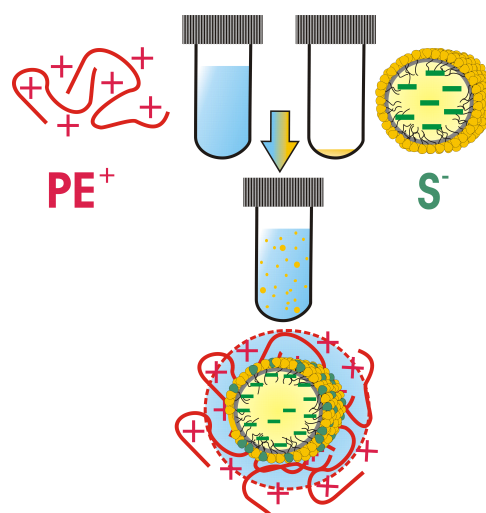


Figure 4.74: Scheme of nanoemulsion encapsulation using oppositely charged surfactants and polyelectrolytes inside the oil and water phase. Nanoemulsion formation is initiated at very high dilution ratios via the PIC-process.

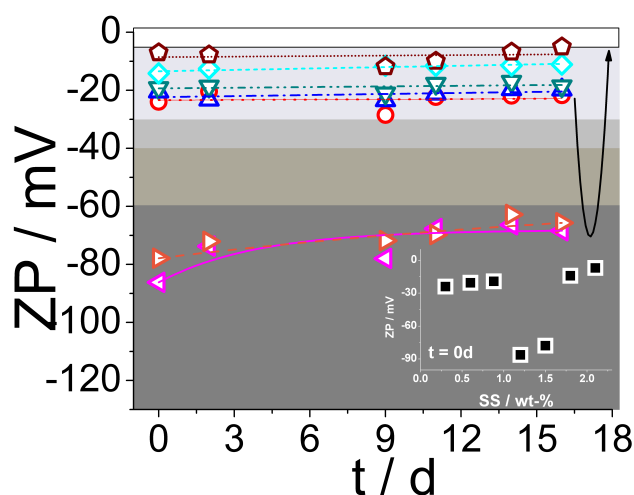


Figure 4.75: Zeta potential ZP time dependently measured for PIC-formed nanoemulsions (95wt-% H₂O) at eight different concentrations (○--- 0.3, △--- 0.6, ▽--- 0.9, ◀--- 1.2, ▶--- 1.5, ◇--- 1.8 and ◻--- 2.1wt-% SS) of the anionic surfactant 2-sodium laureth sulfosuccinate (SS) in the O/S-mixture DEHC/K300/P4L (66.6/12.1/21.3). Insert illustrates concentration dependent stability directly after PIC-nanoemulsion formation (0 days). Different plot-shading grades the level of stability by the zeta potential: more than ±60 (excellent), ±60 to ±40 (good), ±40 to ±30 (moderate), ±30 to ±10 (incipient stability) and 0 to ±5 (rapid coagulation or flocculation).

As a first step and in order to get an insight into the interaction and binding properties we analysed nanoemulsion stabilities by zeta potential measurements, dependent on the amount of anionic surfactant employed in the initial O/S-mixture and diluted with bidistilled water. We therefore formulated O/S-mixtures analogous to our model system Tego[®] Wipe DE containing diethylhexyl carbonate, the preservative mixture Euxyl[®] K300 and polyglycerol-4 laurate (66.6/12.1/21.3). The anionic surfactant concentration of the added 2-sodium laureth sulfosuccinate (SS) was varied between 0.3 to 2.1wt-%. Due to comparison reasons it should be noted that the O/S-model system contains ~ 0.9wt-% of anionic dilauryl citrate. SS was chosen to replace the anionic surfactant component dilauryl citrate in the O/S-mixture due to

its similar physical properties while forming metastable nanoemulsion systems (eg. section 4.2.3.1). Figure 4.75 shows the nanoemulsion stability for the different charged surfactant concentrations followed for about two weeks. A general addition of charged surfactant does not ensure the formation of long-time metastable nanoemulsions in general. This is depicted by the SS-concentration-dependent zeta-potential, illustrated in the inset of figure 4.75 directly after the nanoemulsion formation (0 days). Thereby neither a very high, nor a very low SS-concentration favours electrostatically very stable nanoemulsions ($ZP \geq -60$ mV). The optimal concentration range ($0.9 < [SS]_{O/S} < 1.8$ wt-%) seems to be quite narrow and tend to a slight degradation within the first days. It is interesting to note that the SS-concentration ($wt(SS) \approx 0.9\%$) we generally employ in the O/S-mixture to form meta-stable nanoemulsions gives just zeta potentials of incipient stabilities and might have been adjusted to obtain higher stabilities. However section 4.2.3.1 showed good nanoemulsion stabilities with time at ~ 0.9 wt-% for the SS as charged surfactant in the O/S-mixture.

When a counter charge is employed, the stability behaviour of the nanoemulsion solutions changes dependent on the used concentrations and the charge ratio z . For our encapsulation studies we varied the additive concentration of the 2-sodium laureth sulfosuccinate in the Tego[®] Wipe DE mixture and employed cationic lysozyme as counter charge in the aqueous phase. At a constant SS-concentration of 1wt-% in the O/S-mixture we arranged a charge ratio z of cationic

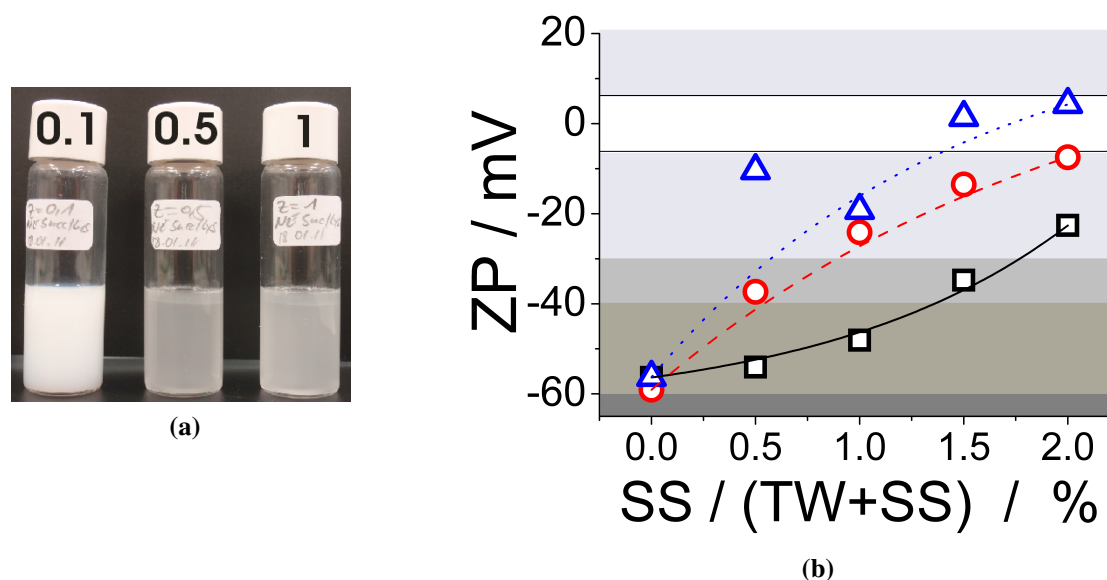


Figure 4.76: **a)** Photographs of samples formed by the PIC-process at 95wt-% water. 1wt-% 2-sodium laureth sulfosuccinate was added to the O/S-mixture based on our model system Tego[®] Wipe DE (DEHC/K300/P4L/DC 66/12/21.1/0.9) and diluted with an aqueous solution of lysozyme of proper concentrations to obtain charge ratios of $z[\text{lys}^+/\text{SS}^-] = 0.1, 0.5$ and 1 . **b)** Zeta potential measurements of encapsulated nanoemulsions formed by our model system Tego[®] Wipe DE containing different SS-concentrations and finally diluted with an aqueous solution of lysozyme of proper concentrations to obtain charge ratios of $z[\text{lys}^+/\text{SS}^-] = \square 0.1, \circ 0.2$ and $\triangle 0.3$. As the exact charge of lysozyme is pH-dependent, pH-measurements have been done for these three series (see appendix fig. A.15).

protein to anionic surfactant of 0.1, 0.5 and 1. Image 4.76a shows that already at charge ratios of $z \geq 0.5$ a strong destabilisation of the nanoemulsions occurs which leads to phase separation and a greyish colour of the solutions. If this already can be attributed to the encapsulation of the nanoemulsion droplets or if it is caused by aggregation and other breakdown processes need to be checked by other techniques (SANS, cryo-TEM).

Zeta potential measurements (eg. fig. 4.76b) at very low charge ratios ($z[\text{lys}^+/\text{SS}^-] = 0.1, 0.2, 0.3$) revealed a compensation of the nanoemulsion destabilisation properties when the anionic surfactant concentration in the initial O/S-mixture is varied (compare figures 4.75 and 4.76b). This clearly proves that the lysozyme becomes attached to the nanoemulsion droplets, thereby increasing its zeta-potential. Accordingly it is the key experiment for showing that hybrid lysozyme/nanoemulsion particles are formed. To find a good compromise in terms of working conditions (masses to be weighted) and nanoemulsion stability we decided for our subsequent encapsulation attempts to stick to a SS-concentration of 1wt-% in the O/S-mixture and hence work at low charge ratios ($z \leq 0.5$).

As it is not trivial to determine a successful encapsulation of nanoemulsion droplets, SANS-measurements and cryo-TEM micrographs have been employed to analyse the outcome of the encapsulation experiment.

4.6.1.1 SANS-studies on encapsulated PIC-formed nanoemulsion droplets

Static SANS-measurements have been done at two different charge ratios ($z[\text{lys}^+/\text{SS}^-] = 0.1$ and 0.5) for the encapsulation attempts of nanoemulsions formed by the PIC-process. The given charges correspond to the ratio of the dissolved cationic lysozyme in the aqueous phase of the nanoemulsions and the anionic surfactant component employed in the O/S-mixture. In case of $z = 0.5$, the coagulates of the emulsion breakdown from the samples top have been collected to analyse. Figure 4.77 shows SANS curves of nanoemulsions formed with the help of our model system at high dilution ratios (95wt-% H_2O) via the PIC-mechanism for different lysozyme content.

A comparison of the scattering curves for the two encapsulation attempts with

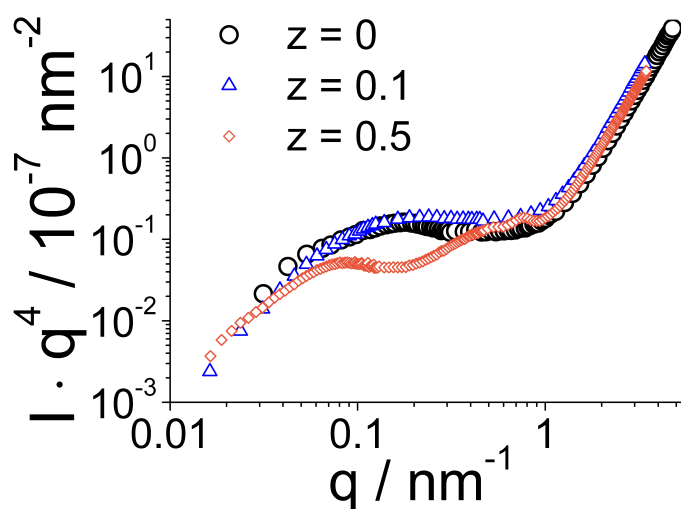


Figure 4.77: SANS intensity for encapsulation attempts of nanoemulsion droplets formed by the PIC-process. Encapsulation is initiated by counter charged surfactant/lysozyme interactions using 1wt-% of SS in the O/S-concentrate and appropriate lysozyme concentrations in the aqueous phase. O/S-mixture was diluted with lysozyme dilution to 95wt-% (H_2O (lysozyme)). Two different charge ratios $z[\text{lys}^+/\text{SS}^- = 0.1$ and 0.5] have been employed. $z = 0.1$ to check the structures for the stable and $z = 0.5$ to check the coagulates structure for the unstable conditions.

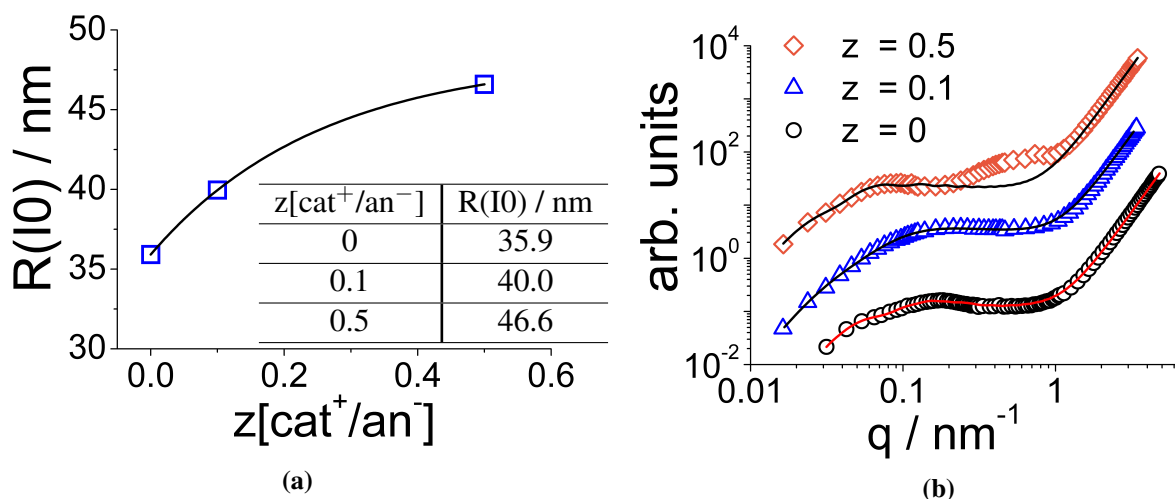


Figure 4.78: **a)** Radii of encapsulation attempts (compare SANS curves in absolute scale in fig. 4.77), obtained via Guinier approximation to zero angle intensity ($I(q=0)$), assuming all O/S-mixture contained in the nanoemulsion droplets. **b)** Structural analyses of SANS curves using a bimodal lognormal distributed spherical model for \square non-encapsulated and encapsulated nanoemulsion droplets using surfactant/lysozyme complexes (charge ratio of $z[\text{Lys}^+/\text{SS}^-] = 0.1$ \triangle and 0.5 \diamond). Straight lines show individual curve fits. Residuals are given in figure A.16 of the appendix.

the reference one revealed different structural changes. As a general trend the formed structures become bigger with the employed charge ratio while assuming the presence of spherical particles (eg. Guinier approximated radii to zero angle scattering in fig. 4.78a). This might be due to a growing of the surfactant/lysozyme complex that surrounds the nanoemulsion droplets after formation. As the surfactant/lysozyme complexes should not change the main structure of the PIC-formed nanoemulsion droplets one would expect similar to the untreated nanoemulsions a bimodal lognormal distributed spherical model for their encapsulation (eg. section 4.1.2.2), that just exhibits bigger droplet diameters. However, structurally a big discrepancy is evident for the scattering behaviour between pure nanoemulsions and encapsulated ones at a charge ratio of 0.5 (eg. fig. 4.77). Model analyses using a bimodal lognormal distributed spherical model could not fit the obtained scattering curves of the encapsulation attempts properly (eg. fig. 4.78b). Nor the addition of a theoretical shell in the model analyses led to reasonable results (fits are not shown). Figure 4.78b visualises the best fits that could be obtained while maxing

| z [Lys ⁺ /SS ⁻] | A | $R_{1,N}$ nm | σ_1 | $R_{2,N}$ nm | σ_2 | bkg cm ⁻¹ |
|---|------|-----------------|------------|-----------------|------------|-------------------------|
| 0 | 0.38 | 12.2 | 0.32 | 27 | 0.45 | 0.07 |
| 0.1 | 0.75 | 5.0 | 1.00 | 25.3 | 1.00 | 0.11 |
| 0.5 | 0.66 | 15 | 0.83 | 38.8 | 0.81 | 0.08 |

Table 4.19: Fit parameters amplitude A (volume fraction of scattering material that is in species with radius R_1), number-weighted (N) radii R and polydispersity indices σ_1 and σ_2 for population 1 and 2, respectively - using a Log normal distributed spherical model for two populations. Corresponding SANS-curves of the nanoemulsion encapsulation attempts at different charge ratio z are given in plot 4.77, curve fits in plot 4.78b and residuals in plot A.16 of the appendix.

out the fit parameters reasonably (eg. table 4.19). At a charge ratio of $z = 0.5$ it is quite obvious from the shape of the SANS curve that we observe bigger aggregates that are not involved in the nanoemulsion encapsulation process beside possibly encapsulated ones. So coagulation of single components clearly occurs at too high charge ratios.

However, for low charge ratios the measured structure can be fitted for a bimodal system with low divergences to the data-points. Despite that, the obtained radii and especially the corresponding polydispersities ($\sigma_1 = \sigma_2 = 1.0$) indicate strong interferences of the initial bimodal nanoemulsion system that normally possesses particle sizes of about $R_{N,1} \approx 10$ nm and $R_{N,2} \approx 30$ nm. At this point one has to realise that the interior structure of the nanoemulsion encapsulation attempts is not fully explainable with SANS analyses only.

4.6.1.2 Cryo-TEM studies on encapsulated PIC-formed nanoemulsion droplets

The System: 2-sodium laureth sulfosuccinate/lysozyme

For aqueous soft colloidal particles transmission electron microscopy on cryo-genic prepared samples is a powerful tool for structure determination. Accordingly for the encapsulation of nanoemulsion droplets cryo-TEM images have been done. Pure non-encapsulated nanoemulsions formed by the PIC-method possess two close neighbored particle size distributions whose exact mean diameter depends mainly on the degree of dilution. This was shown by us using SANS-model analyses (eg. section 4.1.2.2) and complementary cryo-TEM micrographs (eg. fig. 4.13b) on nanoemulsions formed by our model system Tego[®] Wipe DE that was diluted with 95wt-% water. For our encapsulation attempts of such simply formed nanoemulsions, we prepared the O/S-mixture with 1wt-% of anionic surfactant 2-sodium laureth sulfosuccinate and diluted it likewise (95wt-% water) with an aqueous solution of lysozyme in proper concentrations

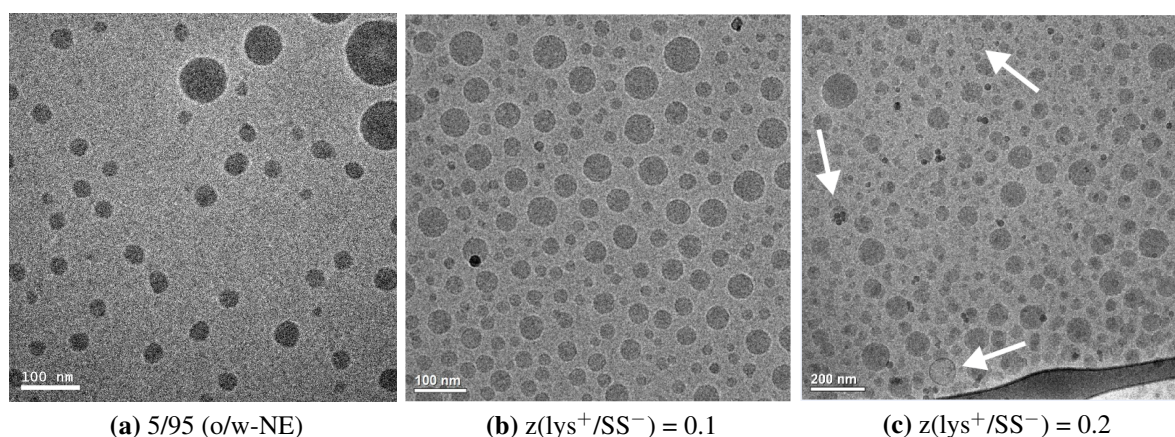


Figure 4.79: Freeze fracture cryo-transmission electron microscopy on nanoemulsions prepared via the PIC-formation process, by **a)** diluting the O/S-mixture of our model system (Tego[®] Wipe DE) with water to 95wt-% H₂O, or **b-c)** encapsulation attempts of O/S-mixtures with 1wt-% of SS and diluted with an aqueous solution of lysozyme (95wt-% water) in proper concentrations to reach final charge ratios of $z[\text{lys}^+/\text{SS}^-] = 0.1$ **b)** and 0.2 **c)**. White arrows mark hollow-sphere like structures (shell of approx. 4.8nm).

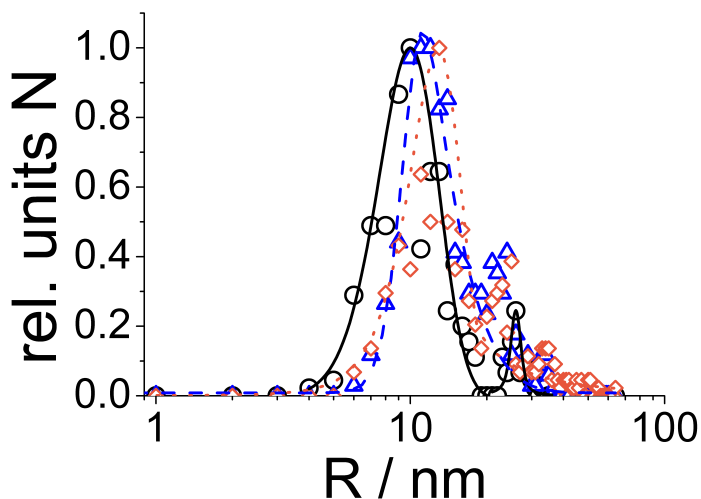
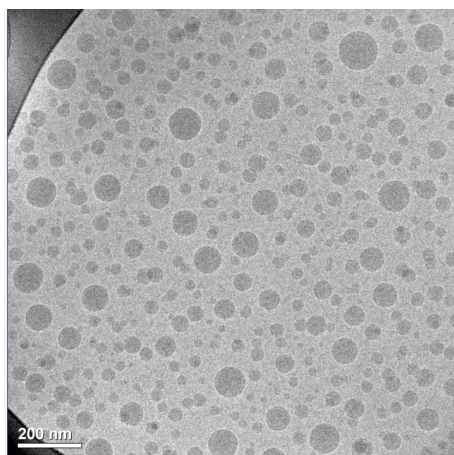


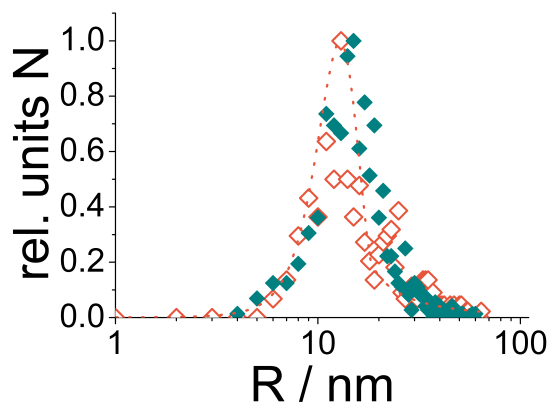
Figure 4.80: Normalised statistical evaluation of cryo-TEM images given in fig. 4.79. Studied nanoemulsion systems are prepared via the PIC-formation process, by diluting the O/S-mixture of our model system (Tego[®] Wipe DE) with water to 95wt-% H₂O ($z = 0$, \square), or encapsulation attempts of O/S-mixtures contained 1wt-% of SS and diluted with an aqueous solution of lysozyme (95wt-% water) in proper concentrations to reach final charge ratios of $z[\text{lys}^+/\text{SS}^-] = 0.1$, \triangle and 0.2 , \diamond .

primary tendencies of particle-agglomeration for the observed system. As this behaviour already occurs for a charge ratio of 0.2 , we clearly can confirm the agglomeration at even higher charge ratios, we observed with SANS at $z[\text{lys}^+/\text{SS}^-] = 0.5$ respectively (eg. section 4.6.1.1). More

to reach final charge ratios of $z[\text{lys}^+/\text{SS}^-] = 0.1$ and 0.2 . The cryo-TEM pattern for the encapsulation attempts of nanoemulsions formed by the PIC-dilution process, show a decrease of the interdroplet distance ξ (mean distance of aggregates) between the single particles with increasing charge ratio z . This result was already approachable by former SANS-data analyses concerning the employed concentration of the charged surfactant in the O/S-mixture (see figure 4.27 in section 4.2.3.2-charge). Nevertheless, due to comparison reasons Teubner Strey parameters of the SANS-data fits are subsequently given in table A.22 of the appendix. Moreover, the cryo-TEM image for a charge ratio of 0.2 shows primary tendencies of particle-agglomeration for the observed system.



(a) 0.5wt-% SS⁻ in TW



(b) Comparison 0.5 vs. 1.0wt-% SS⁻ in TW

Figure 4.81: **a)** Freeze fracture cryo-transmission electron microscopy on nanoemulsions prepared via the PIC-formation process, by diluting the O/S-mixture of our model system (Tego[®] Wipe DE) with \blacklozenge 0.5wt-% of SS and diluted with an aqueous solution of lysozyme (95wt-% water) in a proper concentration to reach a final charge ratio of $z(\text{lys}^+/\text{SS}^-) = 0.2$. **b)** Statistical comparison to an equivalent nanoemulsion system where the O/S-mixture contained \blacklozenge 1.0wt-% of SS and a lysozyme-solution added to reach the same charge ratio -eg. cryo-TEM fig. 4.79c respectively.

detailed analyses of the obtained cryo-TEM micrographs, using the statistical evaluation software ImageJ program [79], revealed a slight increase of the mean particle size and the particles polydispersity. This is not astonishing as we expect a slight increase of the particle-diameter when the surfactant-lysozyme complex is formed. At the same time the bimodal character of the observed nanoemulsions gets more and more lost while a broad smearing of the second (greater) size distribution appears (eg. fig. 4.80). However, from the cryo-TEM images it is not clearly evident if an encapsulation of the nanoemulsion droplets took place. At this point we would like to point out that the surface of the nanoemulsion droplets appear more structured (coarse like) with increasing charge ratio, and that from time to time one observes hollow-sphere like structures (shell thickness ~ 4.8 nm) at mainly higher charge ratios (eg. white arrows in fig. 4.79c). These hollow spheres do not appear for the same charge ratio (lys^+/SS^-) when the anionic surfactant phase was chosen too low in the O/S-mixture, in respect to obtain more stabilised nanoemulsions (eg. section of zeta potential measurements 4.6.1). Figure 4.81a shows such a case for 0.5wt-% SS in the O/S-mixture respectively. A comparison of the encapsulation attempts for the same charge ratio (0.2) but different relative amounts of charged components do not show significant structural differences while analysing their cryo-TEM micrographs statistically (eg. fig. 4.81b).

The System: 1,2-diacyl-sn-glycerol-3-phospho-L-serine sodium salt/lysozyme

As during the dilution a certain part of the anionic surfactant will be leached out from the initial O/S mixture, it is important to make the anionic surfactant as hydrophobic as possible. We therefore replaced the anionic surfactant SS by anionically charged phospholipid 1,2-diacyl-sn-glycerol-3-phospho-L-serine sodium salt (PGL) to ensure a strong lipophilicity of the anionic surfactant and retain it more likely in the oil phase of the nanoemulsion.

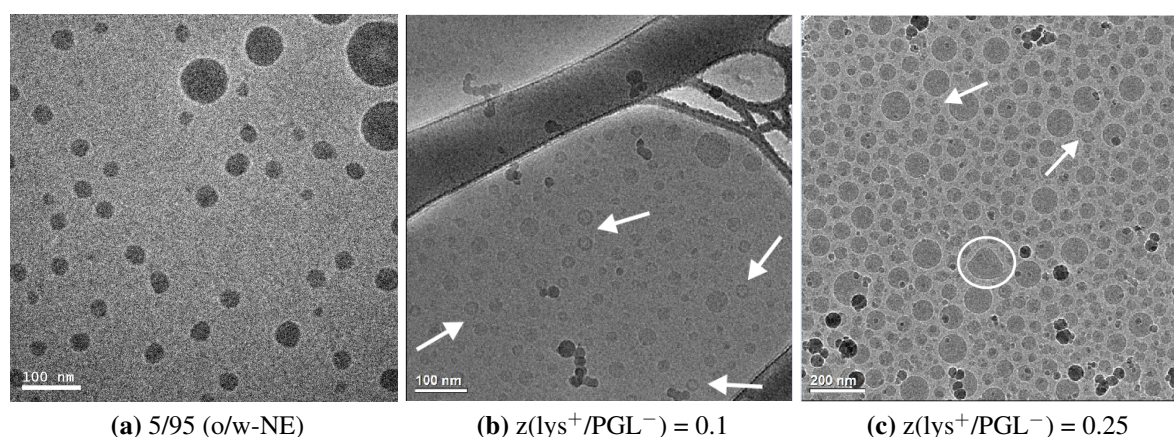


Figure 4.82: Freeze fracture cryo-transmission electron microscopy on nanoemulsions prepared via the PIC-formation process, by **a**) diluting the O/S-mixture of our model system (Tego[®] Wipe DE) with water to 95wt-% (H_2O), or **b-c**) encapsulation attempts of O/S-mixtures that contained 1wt-% of PGL and were diluted with an aqueous solution of lysozyme (95wt-% water) in proper concentrations to reach final charge ratios of $z[\text{lys}^+/\text{PGL}^-] = 0.1$ **b**) and 0.25 **c**). White arrows mark hollow-sphere like structures (shell of approx. 5 nm). White circle depicts non-spherical particle.

Encapsulation attempts of nanoemulsions formed by such a system are shown in the cryo-TEM micrographs of figure 4.82b and 4.82c for charge ratios of $z = 0.1$ and 0.25 respectively. Likewise to the SS/lys-complexation the interdroplet distance decreases with increasing charge ratio and one observes hollow-sphere like structures (shell thickness ~ 5.0 nm) that are more frequent for lower charge ratios than for greater ones. At $z = 0.5$ one observes them mainly for very small particles occasionally. At the same time bigger particles are surrounded numerously by smaller droplets that sometimes assemble to bigger clusters. Nevertheless, the droplets surface appears

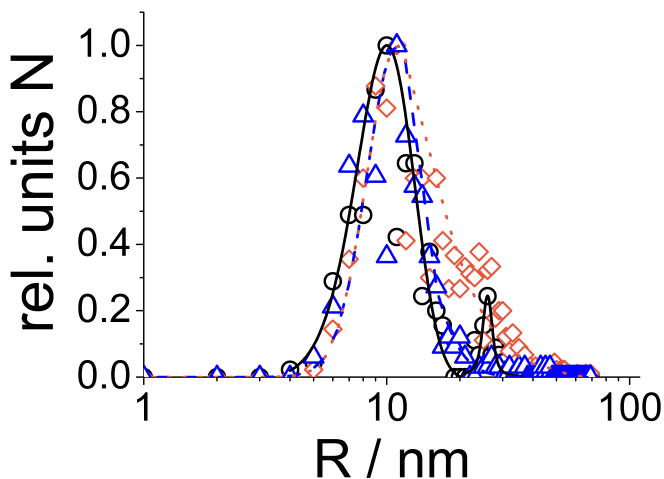


Figure 4.83: Normalised statistical evaluation of cryo-TEM images given in fig. 4.82. Studied nanoemulsion systems are prepared via the PIC-formation process, by diluting the O/S-mixture of our model system (Tego[®] Wipe DE) with purified deionized water of 95wt-% ($z = 0$, \square), or encapsulation attempts of O/S-mixtures that contained 1wt-% of PGL and were diluted with an aqueous solution of lysozyme (95wt-% water) in proper concentrations to reach final charge ratios of $z[\text{lys}^+/\text{PGL}^-] = 0.1$, \triangle and 0.25 , \diamond .

more structured (coarse like) with increasing charge ratio and loses its spherical shape at high charge ratio (eg. white circle in fig. 4.82c). A comparison on the droplet statistics reveals as well a slight increase of the main particle size while the second size distribution smears out and broadens the overall size distribution (eg. fig. 4.83). Similar to the SS system it is not clear how the encapsulation process proceeds structurally despite the fact that the zeta-potential measurements clearly demonstrate a strong interaction between the lysozyme and the nanoemulsion droplets.

4.6.2 Conclusion of PIC-NE encapsulation attempts by electrostatic assembly.

The encapsulation of nanoemulsion droplets formed by the low energy phase inversion concentration (PIC) process was investigated. The droplets-encapsulation should be achieved by a charge induced complexation of oppositely charged surfactant/protein (SS^-/lys^+) and phospholipid/protein (PGL^-/lys^+) components at the oil/water interface of the nanoemulsion droplets. For this purpose the O/S-mixture of our model system Tego Wipe DE contained 1wt-% of the anionic component and added aqueous lysozyme solutions of proper concentrations to reach the desired charge ratios ($0 < z[cat^+/an^-] < 1$). The amount of anionic component contained in the oil phase was chosen to 1wt-% due to preliminary zeta-potential measurements of nanoemulsion-stabilities that revealed a maximum stability in that range of content of ionic surfactant. A compensation of the destabilisation-effect can be achieved for low charge ratios ($0 < z[cat^+/an^-] < 0.3$) when a counter charge is employed. Hence, our nanoemulsion encapsulation attempts where mainly proceed inside this range of charge ratio.

However, SANS and complementary cryo-TEM measurements of the encapsulation attempts showed an increase of the mean particle size with increasing charge ratio. Beside this, the SANS-data analyses showed a disappearance of the bimodal character of the formed nanoemulsions with increasing charge ratio. Simultaneously the size distribution broadens substantially, while the structures become more complex due to the formation of agglomerates. This could also be approved via cryo-TEM measurements that showed a smearing of the second greater size distribution and hence broadening of overall polydispersity. Due to a shortening of the interdroplet distance with the charge ratio (revealed by SANS correlation length studies and mean distance measurements of aggregates in cryo-TEM micrographs), the particles tend to converge, and form bigger clusters ($z > 0.3$ breakdown of nanoemulsion occurs). At low charge ratios ($z < 0.3$) hollow-sphere like structures are observable with a shell thickness of approximately 4.8-5.0 nm (i.e., a bit more than the size of a lysozyme molecule) that are more frequent for the system with a greater lipophilicity of the anionic component contained in the oil phase (o(PGL)/w(lys)). Slightly lower or higher charge ratios, as well as lower concentrations of the anionic component in the O/S-mixture ($[an^-]_{O/S} < 1wt\%$) leads to a disappearance of them. Nevertheless, the droplets surface appears more structured (coarse like) with increasing charge ratio and loses spherical shape irregularly at high charge ratios. Hence, it is not clearly evident if the nanoemulsion droplets could be successfully encapsulated using electrostatic interaction forces.

However, the achieved results to encapsulate nanoemulsion droplets that are formed by the PIC-method procure interesting insights into the charge sensitivity of the system, the components required for the complexation and the nanoemulsion influence (structure, stability).

Chapter 5

Summary

Nanoemulsions, which are structurally located between thermodynamically stable microemulsions (< 10nm) and kinetically stable macroemulsions (> 200nm), became quite popular in the last years due to their relatively high stability and as they allow to disperse materials very finely. Such metastable nanoemulsions can be formed, in a size range of 10-200 nm, by different high- or low-energy methods and lend themselves to versatile purposes in industry. Especially nanoemulsions formed by low-energy methods are particularly attractive, due to the mild conditions of preparation (important for the incorporation of sensitive compounds), but also only poorly understood yet with respect to the surfactant composition required and the structural pathway of formation. However, such knowledge is the key for applying such systems in a more versatile way.

For the work in this thesis we were particular interested in the Phase-Inversion-Concentration (PIC) method in which nanoemulsions are formed at a certain oil/water-ratio due to the change of interfacial composition during the dilution of an appropriate oil/surfactant (O/S) mixture.

Our work is based on a commercial formulation (Tego[®] Wipe DE) - containing the oils, diethylhexyl carbonate, phenoxy ethanol, and a parabene mixture, and as surfactants polyglyceryl-4 laurate mixed with a small amount of anionic dilauryl citrate (66/8.6/3.4/21.1/~0.9wt-%)- that we modified in a systematic fashion with respect to the composition of the surfactant and oil components. These modifications of our model system revealed quite restrictive conditions for type and amount of various employed ingredients, whose individual volume fractions need to be balanced with respect to the remaining components to favour a successful formation of metastable nanoemulsions. Nevertheless, we could draw some conclusions on the systems requirements, and establish an approach to determine individual fractions to formulate appropriate O/S-mixtures. Here, the role of the charged surfactant is that of an electrostatic stabiliser that is essential for the nanoemulsion formation, where its type of charge (cat- or anionic) does not influence the final structure. The preservative mixture (Euxyl[®] K300: mixture of phenoxy ethanol + parabens (72/28wt-%)) in the oil phase acts as a cosurfactant and thus facilitates the high effective solubilisation capacity of the system; the oil needs to be rather insoluble in the

aqueous phase and should contain preferably a long aliphatic chain ($\#C\text{-atoms} \geq 8$) that allows the system to form homogenous O/S-concentrates. The choice of an appropriate main surfactant phase is the most delicate one as it has to be relatively hydrophilic, due to the PIC-mechanism, and exhibit a high compatibility with the other ingredients.

Whether a nano- or microemulsion is formed depends mainly on the dilution ratio, with nanoemulsions typically forming at larger water concentrations, as by dilution the amount of surfactant available for aggregate stabilisation becomes smaller, which leads to increasingly larger particles and once the maximum size for a microemulsion is exceeded a nanoemulsion is formed. In order to obtain a more general understanding of the criteria required for the formation of nanoemulsions by the PIC method, we studied the structural progression upon dilution, and the structure and stability of the finally formed nanoemulsion droplets by a combination of physico-chemical characterisation methods like conductivity, viscosity, density, UV/Vis-transmittance and zeta-potential measurements. Additional small-angle neutron and x-ray scattering (SANS/SAXS) experiments, and some complementary cryo-TEM micrographs led to a more refined structural understanding. For our model system and its modifications, where we substituted the ionic surfactant and/or the oil, the phase behaviour upon dilution with water showed an analogous phase sequence, forming metastable nanoemulsions that possess a bimodal size distribution of almost same particle sizes for water concentrations $> 75\text{wt-\%}$, where this bimodality is a surprising and novel finding. Nevertheless, the exact details of the PIC process and the way taken to form these nanoemulsions are influenced by the detailed O/S-composition but show significant correlations among each other. For instance the passing of bicontinuous structures that show a quite pronounced viscosity and conductivity maximum prior to the phase transition. Furthermore SANS measurements revealed a substantial increase in the degree of ordering while passing through these bicontinuous phases. This demonstrates that the generation of nanoemulsions is linked to the presence of a well ordered phase in its vicinity.

As nanoemulsions are metastable systems their structure is necessarily controlled by their formation process. Therefore detailed structural knowledge of this formation process is a central aspect for its understanding. The formation-dynamics of nanoemulsions formed by direct dilution of an appropriate O/S-mixture was followed by time-resolved stopped flow experiments coupled with turbidity and scattering (SAXS/SANS) detection, and revealed an enormously fast formation process of the nanoemulsion droplets within approximately 10-20 ms. We observed a fastening of the inversion process with a simultaneous increase of the mean particle size by increasing the water concentration. The latter observations are due to a dilution of the hydrophilic surfactant that partitions increasingly into the aqueous phase with increasing amount of water and therefore is less available to cover the emulsion droplets and results in a particle growth. A study of the initial stage of the fast structural evolution was not possible due to the exper-

imental dead time (2.3 ms) of the stopped-flow experiment, as apparently a larger part of the structural transformation process that occurs upon dilution has already taken place by that time. But our results show that the formation dynamics are comparable with those of spontaneously formed stable microemulsions and shall provide a rationale for a generalised concept for choice of O/S-mixtures that are appropriate for the PIC process. Additionally, 2D-SAXS pattern of the structures obtained for dilutions into the microemulsion range revealed a fast shear-induced anisotropic scattering while passing through a liquid crystal or sponge microemulsion (oriented to the shear) phase, which is an important precondition to facilitate the PIC-caused phase inversion. Static observations of the phase behaviour upon dilution revealed always the passing of more or less broad regions of flow birefringence likewise. To get a better insight in the compositional changes occurring during the dilution process and the structures formed; NMR, refractive index and contrast SANS experiments were accomplished. In doing so, we observed upon dilution an almost complete transfer from the dispersed (oil) to the continuous phase (water) for the preservative mixture (the cosurfactant) and a fractional transfer for the hydrophilic surfactant. The preservative mixture based mainly on phenoxy ethanol apparently allows, by reducing substantially the interfacial tension, for the formation of bicontinuous microemulsion-like phases with a zero mean surface curvature and thus consequently initialises the phase inversion for the nanoemulsion formation. The progressive dissolution of the hydrophilic surfactant into the aqueous phase triggers the formation of nanoemulsions with their unique properties (eg. particle size, metastability, lower amount of surfactant necessary than for microemulsions). In addition the surfactant has to stabilise subsequently the formed nanoemulsion. This ability depends much on its molecular architecture, where, however, the detailed role for this stabilisation mechanism is still only very poorly understood.

As nanoemulsions are metastable systems their aggregates grow with time. This size evolution proceeds for the different O/S-mixtures almost identically slow (phase separation only occurs after times longer than 6 months) and does not show significant clear evidence for a pure coalescence- or Ostwald-ripening driven breakdown process. In contrast, studies on the interdroplet exchange dynamics among nanoemulsion droplets showed an exponential decay of the equilibration process with characteristic times in the minute range (approx. 10 min), i.e., the oil exchange is much faster than the aging. These equilibration times extend with increasing dilution ratio due to the larger interdroplet distances can be modified by further additives.

In summary, it is very interesting to note that the oil exchange occurs in the minute range, while aging processes take months and are apparently not directly related to this oil exchange.

Our studies revealed complex nanoemulsion-dynamics that cause the uncommon long-term metastability of the employed systems. This extraordinary stability can be correlated with the bimodal structure of the formed nanoemulsions, as confirmed by SANS and cryo-TEM. This bimodal size distribution might be the result of an initial Ostwald ripening that becomes arrested in an early stage and derives from the coexistence of stable microemulsion droplets with

larger sized, metastable emulsion droplets. O/S-variations at constant dilution ratio verified this assumption by a continuous transition from bimodally distributed metastable nanoemulsions to monomodally distributed stable microemulsions when somewhat more surfactant is employed. This is a completely new insight into the structural details of PIC nanoemulsions, which should be important for the future developments of these interesting systems. This knowledge will be important for the rational design of nanoemulsions and for their further applications.

Another very interesting aspect is the functionalisation of such formulated nanoemulsions in order to obtain modified and functionalised nanoemulsion droplets that can be used to incorporate hydrophobic active substances. Thereby they may be employed as carrier systems in drug delivery or nanocontainers for the control of more complex chemical reactions. In our investigations the encapsulation was pursued by attractive electrostatic forces for the assembly process; using oppositely charged surfactant/protein (SS^-/lys^+) and phospholipid/protein (PGL^-/lys^+) components dissolved in the oil and water phase prior O/S-dilution, respectively. Cryo-TEM and SANS measurements of these samples revealed a strong dependence of stability for the formed aggregates on the employed charge ratio $z = [cat^+/an^-]$. For ratios $z > 0.3$ they become instable, forming non-spherical particles and agglomerates. For charge ratios $z < 0.3$ hollow-sphere like structures could be observed and the droplets interface appeared more structured and faceted, suggesting a partial nanoemulsion encapsulation. However, the achieved results to encapsulate nanoemulsion droplets that are formed by the PIC-method provide interesting insights into the charge sensitivity of the system, the components required for the complexation and the nanoemulsion influence (structure, stability). They should allow to further enhancements of such functionalised nanoemulsion systems formed by the PIC-method.

In general, the results of this work allow for a more general understanding of the requirements on the molecular composition for forming nanoemulsions by means of the PIC process. Its formation always requires the formation of a well-ordered phase at intermediate dilution and a high hydrophilicity of the surfactant and cosurfactant. In contrast, the aging is not related to the oil exchange dynamics which occurs on a much faster time scale. Finally it could also be shown that functionalisation and encapsulation of such nanoemulsions is possible (for instance with a protein), which allows for the formation of more complex and versatile nanoemulsion based formulations. All these findings enhance our understanding of the fascinating nanoemulsion systems, in particular with respect to their low-energy formation, substantially, thereby opening the ways for further future developments and applications.

Appendix A

A.1 Further details to chemicals in use

A.1.1 Composition of Euxyl[®] K300

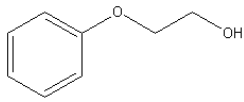
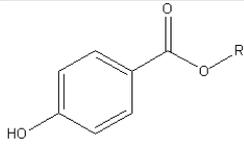
| name | structure | Σ -formula | $\rho^{25^\circ\text{C}}$ g/cm ³ | wt % | SLD 10 ⁻⁶ Å ⁻² |
|----------------|---|--|--|---------|---|
| phenoxyethanol |  | C ₈ H ₁₀ O ₂ | 1.11 | 72 | 1.32 |
| paraben: |  | | | | |
| methyl- | R = CH ₃ | C ₈ H ₈ O ₃ | 1.21 | 16 | 1.95 |
| butyl- | R = C ₄ H ₉ | C ₁₁ H ₁₄ O ₃ | 1.28 | 4 | 1.51 |
| ethyl- | R = C ₂ H ₅ | C ₉ H ₁₀ O ₃ | 1.17 | 4 | 1.69 |
| propyl- | R = C ₃ H ₇ | C ₁₀ H ₁₂ O ₃ | 1.13 | 2 | 1.47 |
| isobutyl- | R = CH ₂ CH(CH ₃) ₂ | C ₁₁ H ₁₄ O ₃ | 1.11 | 2 | 1.31 |

Table A.1: Sum formula, densities ρ , weight fraction wt-% and scattering length densities SLD for the individual components of the preservative mixture Euxyl[®] K300

A.1.2 Structures of Exchange studies

A.1.2.1 Oil-Exchange

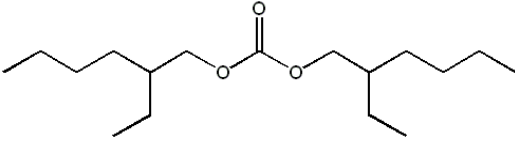
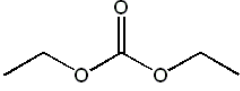
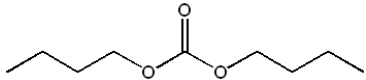
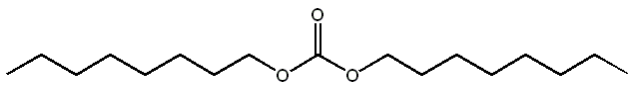
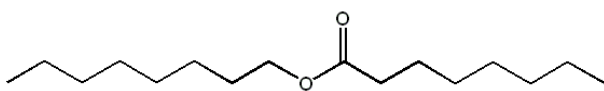
| compound (oil) | commercial name | structure |
|------------------------|------------------|---|
| 2-ethylhexyl carbonate | Tegosoft® DEC |  |
| 2-ethyl carbonate | |  |
| 2-n-butyl carbonate | |  |
| 2-octyl carbonate | Cetiol CC |  |
| octyl-octanoate | |  |

Table A.2: Molecular structures of used compounds in oil-exchange studies (oil/phenoxyethanol+paraben-mixture/polyglycerol-4 laurate/Rewoquat CR 3099 (66/12/ 21.1/0.9 (wt%)))

A.1.2.2 Surfactant-Exchange (non-ionic)

Surfactants have been chosen due to their hydrophilic-lipophilic properties. The hydrophilic head group thereby based on glycerol units of different lengths (2,3,4 and 10). The hydrophobic tail varied in chain length and structure (linear (laurate, caprate, oleat), branched (isostearate), non-saturated (oleate) and saturated (caprate, oleat, isostearate) molecules). Surfactants with same structural name but different commercial name differ in their grade of esterification and hence surfactant properties (HLB-value).

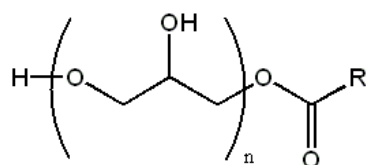


Figure A.1: Basic structure of different polyglycerol surfactants with n glycerol units and aliphatic tail R

In fact Hydriol PGO, PGMO.4 and PGHO.4 are products of an esterification, synthesised by a thermal condensation process of polyglycerol-4 and olein. The esterification ratio of polyglyc-

| compound (surfactant) | commercial name | Σ -formula | $\rho^{25^\circ\text{C}}$ g/cm ³ | cmc mM | n | R | HLB |
|----------------------------|--------------------------------|---|---|--------|----|---------------------------------|-----|
| polyglycerol-4 laurate | Tego [®] Care PL4 | C ₂₄ H ₄₈ O ₁₀ | 1.094 | 4-5 | 4 | C ₁₁ H ₂₃ | 13 |
| polyglycerol-4 caprate | Hydriol [®] PGCL4 | C ₂₂ H ₄₄ O ₁₀ | 1.178 | 0.43 | 4 | C ₉ H ₁₉ | 15 |
| polyglycerol-4 oleat | Hydriol [®] PGO | C ₃₀ H ₅₈ O ₁₀ | 0.954 | 0.23 | 4 | C ₁₇ H ₃₃ | 3 |
| polyglycerol-4 oleat | Hydriol [®] PGMO.4 | C ₃₀ H ₅₈ O ₁₀ | 1.027 | 4.02 | 4 | C ₁₇ H ₃₃ | 8 |
| polyglycerol-4 oleat | Hydriol [®] PGHO.4 | C ₃₀ H ₅₈ O ₁₀ | 1.123 | 1.07 | 4 | C ₁₇ H ₃₃ | 13 |
| polyglycerol-4 isostearate | Hydriol [®] PGI | C ₃₀ H ₆₀ O ₁₀ | 0.956 | 0.03 | 4 | C ₁₇ H ₃₅ | 3 |
| polyglycerol-2 Caprate | Hydriol [®] PGC2 | C ₁₆ H ₃₂ O ₆ | 1.046 | 0.51 | 2 | C ₉ H ₁₉ | 9 |
| polyglycerol-3 Caprate | Hydriol [®] PGC3 | C ₁₉ H ₃₈ O ₈ | 1.105 | 0.46 | 3 | C ₉ H ₁₉ | 14 |
| polyglycerol-10 laurate | SY-Glyster [®] ML-750 | C ₄₂ H ₈₄ O ₂₂ | 1.162 | 0.06 | 10 | C ₁₁ H ₂₃ | 15 |

Table A.3: Surfactants in use, based on glycerol units (n) and aliphatic tail (R) (eg. fig. A.1), to form homogenous oil/surfactant (O/S) nanoemulsion (NE) qualified mixtures, their commercial name, sum-formula, density ρ , critical micelle concentration cmc, hydrophilic-lipophilic balance (HLB) value; (O/S-composition: 2-ethylhexyl carbonate/phenoxyethanol+paraben-mixture/surfactant/Rewoquat CR 3099 (66/12/21.1/0.9(wt%)))

erol to fatty acid increases from Hydriol PGO via Hydriol PGMO.4 to Hydriol PGHO.4. Therefore Hydriol PGHO.4 exhibits the greatest amount of mono-ester proportion among those.

A.1.2.3 Surfactant-Exchange (cat- and anionically charged)

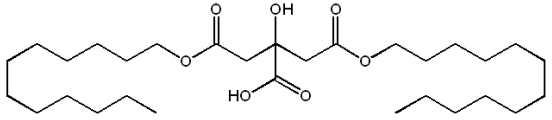
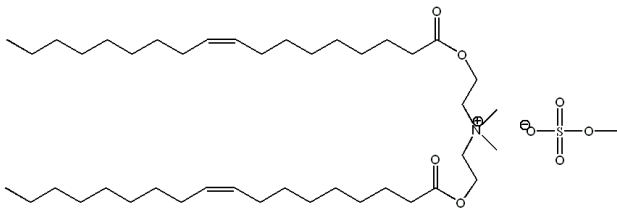
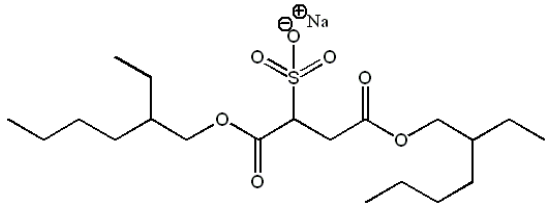
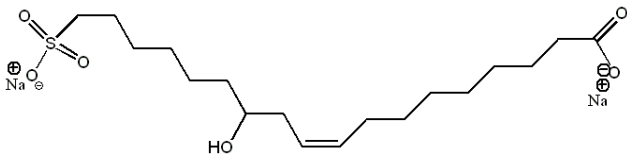
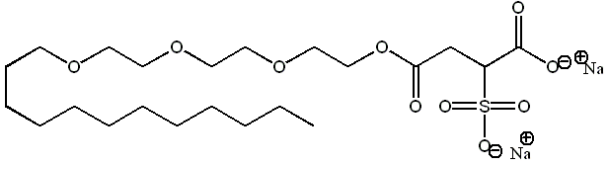
| compound (oil) | commercial name | structure |
|--|-----------------------|--|
| 2-lauryl citrate | |  |
| 2-oleic acidyl isopropylester 2-methylammonium Methosulfat | Rewoquat® CR 3099 |  |
| 2-octyl sodium sulfosuccinate | AOT |  |
| sulfonated castor oil, Na salt | Hydriosul® HRN 100 |  |
| 2-sodium laureth sulfosuccinate | Rewopol® SB FA 30 |  |

Table A.4: Molecular structures of charged surfactants in use (2-ethylhexyl carbonate/phe-noxyethanol+ paraben-mixture/polyglycerol-4 laurate/charged surfactant (66/12/21.1/0.9 (wt%)))

A.1.2.4 O/S-variation: Composition

The O/S-ratio was varied for 100/0, 95/5, 90/10... to 0/100. The O/S-mixtures employed based on 2-ethylhexyl carbonate (DEHC) and Euxyl[®] K300 (K300) as oil (O), and polyglycerol-4 laurate (P4L) and 2-sodium laureth sulfosuccinate (SS) or Rewoquat CR3099 (EQ) as surfactant (S) phase.

| | | O | | S | | O | | S | |
|--------|--------|--------|-----------|------|------|---------|---------|---------|---------|
| O % | S % | DEHC | K300 % | P4L | SS | DEHC | K300 | P4L | SS |
| | | Φ | | | | | | | |
| 100 | 0 | 85.0 | 15.0 | 0.00 | 0.00 | 0.03910 | 0.00690 | 0.00000 | 0.00000 |
| 95 | 5 | 80.8 | 14.3 | 4.80 | 0.20 | 0.03714 | 0.00656 | 0.00221 | 0.00009 |
| 90 | 10 | 76.5 | 13.5 | 9.60 | 0.40 | 0.03519 | 0.00621 | 0.00442 | 0.00018 |
| 85 | 15 | 72.3 | 12.8 | 14.4 | 0.60 | 0.03324 | 0.00587 | 0.00662 | 0.00028 |
| 80 | 20 | 68.0 | 12.0 | 19.2 | 0.80 | 0.03128 | 0.00552 | 0.00883 | 0.00037 |
| 75 | 25 | 63.8 | 11.3 | 24.0 | 1.00 | 0.02933 | 0.00517 | 0.01104 | 0.00046 |
| 70 | 30 | 59.5 | 10.5 | 28.8 | 1.20 | 0.02737 | 0.00483 | 0.01325 | 0.00055 |
| 65 | 35 | 55.3 | 9.75 | 33.6 | 1.40 | 0.02542 | 0.00449 | 0.01546 | 0.00064 |
| 60 | 40 | 51.0 | 9.00 | 38.4 | 1.60 | 0.02346 | 0.00414 | 0.01766 | 0.00074 |
| 55 | 45 | 46.8 | 8.25 | 43.2 | 1.80 | 0.02151 | 0.00380 | 0.01987 | 0.00083 |
| 50 | 50 | 42.5 | 7.50 | 48.0 | 2.00 | 0.01955 | 0.00345 | 0.02208 | 0.00092 |
| 45 | 55 | 38.3 | 6.75 | 52.8 | 2.20 | 0.01760 | 0.00311 | 0.02429 | 0.00101 |
| 40 | 60 | 34.0 | 6.00 | 57.6 | 2.40 | 0.01564 | 0.00276 | 0.02650 | 0.00110 |
| 35 | 65 | 29.8 | 5.25 | 62.4 | 2.60 | 0.01368 | 0.00242 | 0.02870 | 0.00120 |
| 30 | 70 | 25.5 | 4.50 | 67.2 | 2.80 | 0.01173 | 0.00207 | 0.03091 | 0.00129 |
| 25 | 75 | 21.3 | 3.75 | 72.0 | 3.00 | 0.00978 | 0.00173 | 0.03312 | 0.00138 |
| 20 | 80 | 17.0 | 3.00 | 76.8 | 3.20 | 0.00782 | 0.00138 | 0.03533 | 0.00147 |
| 15 | 85 | 12.8 | 2.25 | 81.6 | 3.40 | 0.00587 | 0.00103 | 0.03754 | 0.00156 |
| 10 | 90 | 8.50 | 1.50 | 86.4 | 3.60 | 0.00391 | 0.00069 | 0.03974 | 0.00166 |
| 5 | 95 | 4.25 | 0.75 | 91.2 | 3.80 | 0.00196 | 0.00035 | 0.04195 | 0.00175 |
| 0 | 100 | 0.00 | 0.00 | 96.0 | 4.00 | 0.00000 | 0.00000 | 0.04416 | 0.00184 |

Table A.5: Individual percentage and volume fraction Φ composition of O/S-mixtures based on DEHC/K300 (85/15) as oil and P4L/SS (alternative P4L/EQ - 96/4) as surfactant phase.

A.1.2.5 Synthesis of d_{34} -diethylhexyl carbonate (d-DEHC)

As the formed nanoemulsions are essentially made of the main oil component 2-ethylhexyl carbonate (DEHC), given with a weight fraction of 66wt-% in our nanoemulsion qualified O/S-model system (Tego[®] Wipe DE), we were interested in getting more detailed information out of the nanoemulsion structure while using the contrast sensibility of neutron experiments. Therefore we tried to synthesis the fully deuterated 2-ethylhexyl carbonate (d_{34} -DEHC).

This can be done with different starting materials that mainly manage to obtain the carbonate from 2-ethylhexanol by diverse reaction mechanism [54, 75, 85, 99]. Beside different synthesis routes [94], the deuterated alcohol ($C_8D_{17}OH$) can be most promisingly synthesised in high yields by direct deuteration of ethyl hexanoic acid using D_2O and a Pt catalyst. Due to the need of quite high sophisticated equipment to proceed this synthesis, we purchased the deuterated alcohol from Prof. R.K. Thomas (Oxford University). Its conversion to the fully deuterated d_{34} -carbonate was ensured with high yields by a phosgenation reaction. Synthesis procedure was proceed as follow:

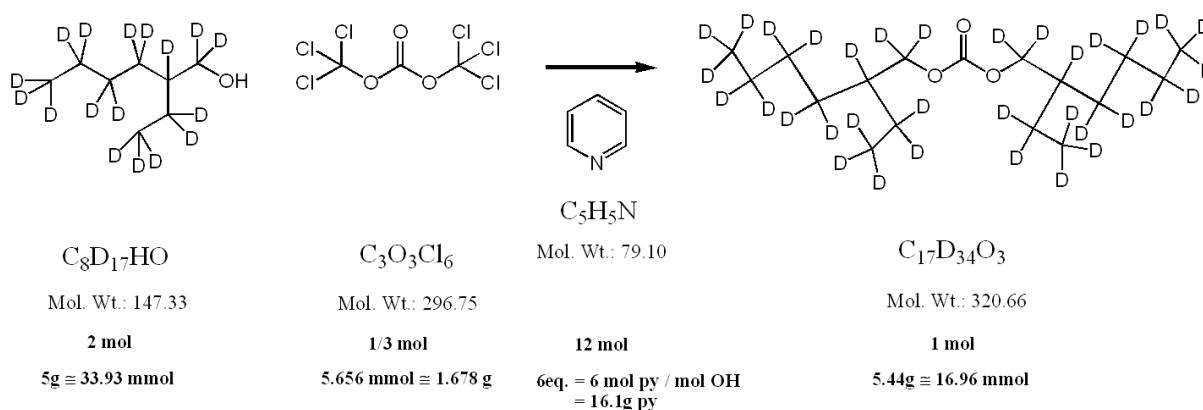


Figure A.2: Synthesis plan of fully deuterated 2-ethylhexyl carbonate ($C_{17}D_{34}O_3$) starting from deuterated 2-ethylhexanol $C_8D_{17}OH$ and triphosgene $C_3Cl_6O_3$. Relevant literature can be found elsewhere [17, 19, 33, 99].

Reaction. Full flask of d_{17} -2-Ethylhexanol was weighted and its content given in a 250 mL Schlenk flask with a septum, before back gauging it: 5.001g of educt. Furthermore 16.4 mL of pyridine¹ (py) were added to the deuterated alcohol, using a 20 mL syringe and N_2 -counter flow. With a second 20 mL syringe 45 mL of dry methylene chloride (DMC) were added likewise.

1.678g of triphosgene (already removed from freezer long time before use, to avoid condensation of water!) was weighted quickly into a Schlenk tube and second 20 mL syringe used to add 20 mL of dry methylene chloride. Using the DMC-syringe (250 mm - hollow needle!), in DMC dissolved triphosgene was given to the alcohol-pyridine-solution drop wise while continuous steering and cooling in a water bath (tap water temperature).

¹Activation of triphosgene using triphenylphosphine (PPh_3) as base did not work out!

Formation of a thick, crystalline white precipitate of $\text{py} \cdot \text{HCl}$ occurred after 10 min. Mixture was stirred over night at room temperature.

Reprocess. Complete approach was transferred into a 250 mL separating funnel. Addition of approx. 70 mL of water; addition of bromphenol blue (transition point at 3-4.6 from blue/violet to yellow) for pyridine-detection; addition of HCl drop wise (extract 15 mL concentrated HCl in a small beaker and pipetting from it) and mixing. After addition of approx. 10 mL HCl phase separation occurs. Transfer of DMC-phase in a flask (that obviously extracted the bromphenol blue!). Addition of 20 mL DMC to the remaining upper aqueous phase and shaking, before combining the DMC phase with the main organic one while dropping the aqueous one. All organic phases were transferred into the separating funnel and covered with fresh bidistilled water which turns blue again, due to the leftover of pyridine! Pyridine gets extracted by a drop wise addition of concentrated HCl which leads to a phase separation. Addition of a saturated bicarbonate solution extracts bromphenol blue from DMC phase. Aqueous solution is wasted. Washing with saturated solution of sodium chloride and redo extraction using fresh DMC. Aqueous phase is wasted again. DMC phase is tried with Na_2SO_4 and evaporated at 65°C (water bath) and 700 mbar. Leftovers of DMC are evaporated at 700 mbar. Residuum of 6.0g was distilled at $150\text{-}160^\circ\text{C}$ in full vacuum without controller using a Kugelrohr-distillation. Yield approx. 4.71g (87%) after transferring it into a transport vessel.

Analytic. Completion of reaction was proofed using thin-layer chromatography (TLC) and DNP-solution² (eg. fig. A.3a). Purity of final product was evaluated by GC/MS-measurements (eg. fig. A.3b and A.4) that showed beside the main product ($\text{d}_{34}\text{-DEHC}$) at ~ 11.6 min (see MS-spectrum in fig. A.4b) a higher boiling compound at ~ 9.6 min (see MS-spectrum in fig. A.4a) which only accounts for 10-area% of the whole GC-spectrum. Nevertheless, whether this component is a side product (eg. chloroformate) of the reaction, or a thermal decomposition product inside the liner of the GC-injector, it could not be sufficiently clarified yet - the alcohol educt phase appears at approx. 7.5 min. For interpretation of the product MS-spectrum detailed analyses of dialkyl carbonates are given elsewhere [85].

²Dilute 30 mL concentrated sulfuric acid with 40 mL distilled water to dissolve 6 g of 2,4-dinitrophenylhydrazine and add then 100 mL ethanol to the final dyeing solution.

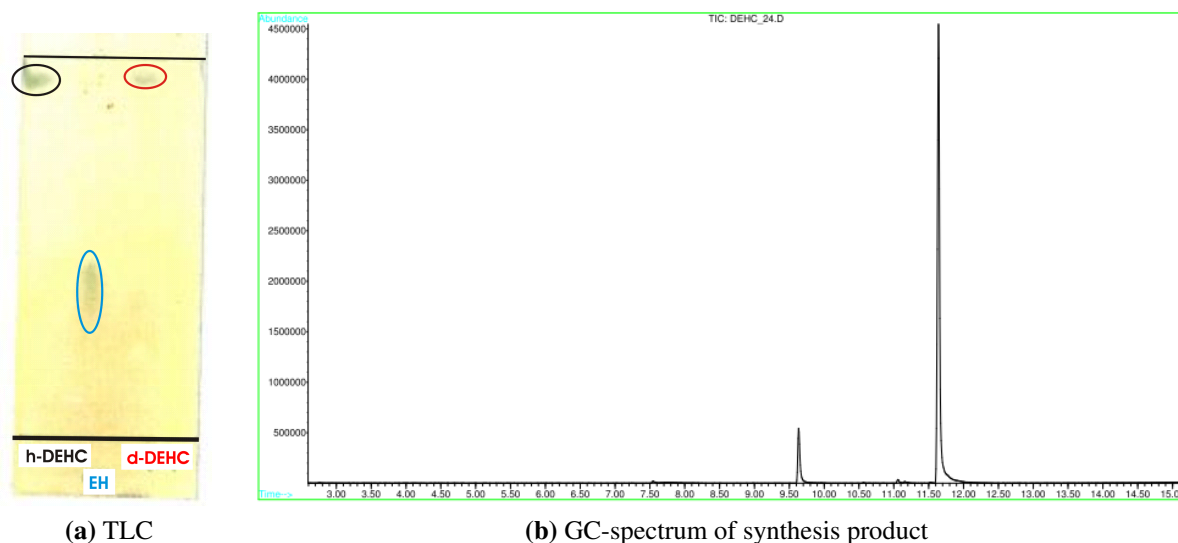


Figure A.3: **a)** shows the dyeing with DNP-solution of a thin-layer chromatogram of the product that was run with methylene chloride and ethanol (99:1) as mobile phase. Left spot belongs to the protonated product 2-ethylhexyl carbonate (h_{34} -DEHC), middle spot marks the protonated 2-ethylhexanol (h_{17} -EH) and right spot belongs to the reaction product of fully deuterated 2-ethylhexyl carbonate (d_{34} -DEHC).

b) shows the time dependent gas chromatogram of the reaction product dissolved in methylene chloride. Peak at 11.6 min belongs to d_{34} -DEHC, whereas the peak at 9.6 min could not be identified by us so far.

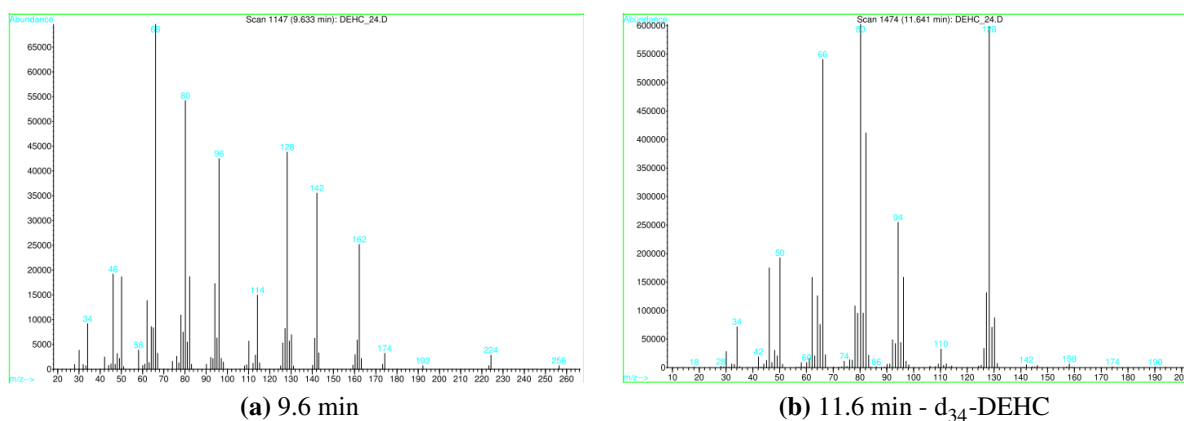


Figure A.4: Mass spectra of reaction product phases separated by gas chromatography and analysed at 9.6 min and 11.6 min by EI-Mass Spectroscopy.

A.2 PIC-method (Tego[®] Wipe DE)

A.2.1 Long-time turbidity measurements

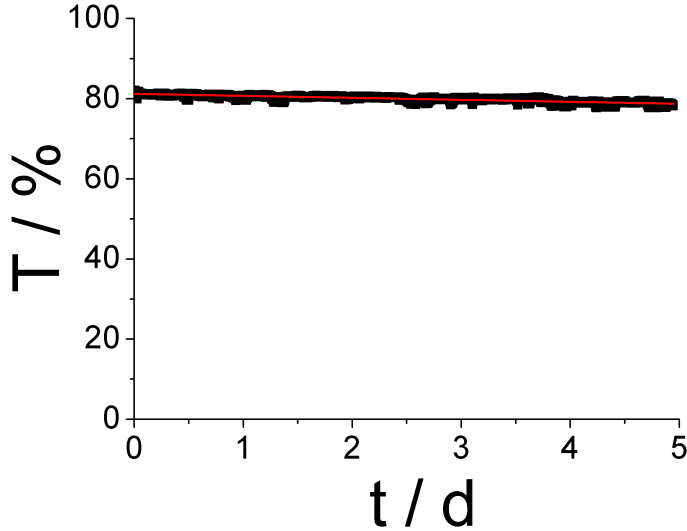


Figure A.5: Transmittance (T) of an o/w-nanoemulsion (95% H₂O) was measured at 25.0 ± 0.1 °C and 633 nm time-dependently (cp. section 3.2.6) in a rectangular 1 mm quartz cell for five days. No significant structural changes (decrease of transmittance T ~ 1.5% per day) could be observed during our typical experimental time window of 2-5 days.

A.2.2 UV/Vis-Transmittance measurements

| H ₂ O | 800 nm | | 700 nm | | 626 nm | | 600 nm | | 500 nm | |
|------------------|--------|------|--------|------|--------|------|--------|------|--------|------|
| | T | R | T | R | T | R | T | R | T | R |
| % | % | nm |
| 80 | 97.1 | 14.5 | 95.1 | 14.6 | 92.5 | 14.5 | 91.2 | 14.5 | 82.7 | 14.5 |
| 85 | 91.7 | 23.7 | 86.7 | 23.4 | 80.2 | 23.3 | 77.1 | 23.3 | 58.5 | 23.2 |
| 90 | 91 | 28.4 | 85.2 | 28.4 | 77.6 | 28.5 | 74 | 28.5 | 53 | 28.7 |
| 95 | 93.5 | 32.3 | 89.3 | 32.1 | 83.8 | 32.1 | 81.1 | 32.1 | 64.4 | 32.3 |
| 98 | 96 | 39.3 | 93.5 | 38.9 | 90.1 | 38.7 | 88.5 | 38.6 | 78.2 | 38.2 |

| H ₂ O | 400 nm | | 350 nm | |
|------------------|--------|------|--------|------|
| | T | R | T | R |
| % | % | nm | % | nm |
| 80 | 60.8 | 14.8 | 39.1 | 15.3 |
| 85 | 26.7 | 23.3 | 10.2 | 23.4 |
| 90 | 20.3 | 29 | 6.58 | 29 |
| 95 | 33.6 | 32.4 | 16.1 | 32.2 |
| 98 | 56.7 | 37.5 | 40.1 | 36.8 |

Table A.6: Approximated particle sizes R for o/w-NE (> 75wt-% H₂O), calculated (eq. (3.4)- (3.6)) from the transmittances T obtained by UV/Vis measurements (fig. 4.5a)

A.2.3 SANS measurements - Teubner Strey analysis (upper phases)

Obtained Teubner-Strey parameters for upper phases of SANS-data treatment using eq. (3.21)-(3.25); scattering length density difference between oil and water was calculated for oil dominated samples as $6.37 \cdot 10^{-4} \text{ nm}^{-2}$ ($5 < x < 40\text{wt-}\% \text{ H}_2\text{O}$) and for water dominated samples as $6.06 \cdot 10^{-4} \text{ nm}^{-2}$ ($50 < x < 98\text{wt-}\% \text{ H}_2\text{O}$); a_2 , c_1 and c_2 are coefficients of various terms of order parameters in Landau free energy. In the case of a microemulsion, c_1 indicates the tendency of forming interfaces between different domains and is usually negative, whereas a positive a_2 favours the microemulsion formation. For a stable morphology the criteria of $4a_2c_2 - c_1 > 0$ with a positive c_2 is required [186]; f_a is the amphiphilicity factor and reaches from 1 for a completely disordered solution to -1 for a superlattice which assumes in case of microemulsions a lamellar structure.

| H ₂ O % | Chi ² | c0 [cm ⁻¹] | c2 [nm ⁴] | V [nm ³] | a2 [] | c1 [nm ²] | ξi [nm] | Ds [nm] | fa [] |
|-----------------------|------------------|---------------------------|--------------------------|--------------------------|-----------|--------------------------|------------|------------|-----------|
| 5 | 0.9990 | 0.89 | 201 | 66979 | 11.2 | 0.778 | 2.9 | 18.4 | 0.01 |
| 10 | 0.9994 | 0.92 | 2.30E+06 | 104401 | 52959 | -219444 | 4.38 | 19.9 | -0.31 |
| 15 | 0.9995 | 0.95 | 1.86E+06 | 124125 | 24368 | -185291 | 5.56 | 21.9 | -0.44 |
| 20 | 0.9991 | 0.98 | 502 | 136081 | 4.05 | -46.1 | 6.75 | 24.1 | -0.51 |
| 25 | 0.9991 | 0.98 | 14036 | 137582 | 73.6 | -1153 | 7.99 | 26.4 | -0.57 |
| 30 | 0.9988 | 1.01 | 240886 | 139747 | 846 | -17309 | 9.26 | 28.8 | -0.61 |
| 35 | 0.9986 | 1.03 | 223197 | 136090 | 493 | -13308 | 10.8 | 32.1 | -0.63 |
| 40 | 0.9978 | 1.06 | 253 | 136936 | 0.356 | -12.2 | 12.3 | 35.8 | -0.65 |
| 50 | 0.9966 | 1.12 | 1.39E+07 | 148370 | 12285 | -541774 | 14.0 | 40.1 | -0.66 |
| 55 | 0.9913 | 1.04 | 3.01E+07 | 127838 | 7912 | -581632 | 17.5 | 55.3 | -0.60 |
| 60 | 0.9897 | 0.75 | 3.82E+08 | 112835 | 44164 | -3.30E+06 | 17.6 | 72.4 | -0.40 |
| 65 | 0.9884 | 0.58 | 4.22E+12 | 96696 | 2.86E+08 | -1.91E+10 | 18.3 | 86.7 | -0.28 |
| 70 | 0.9888 | 0.29 | 1.43E+12 | 15233 | 6.15E+07 | -9.35E+09 | 24.7 | 89.6 | -0.50 |
| 75 | 0.9894 | 0.38 | 2.22E+08 | 41363 | 11560 | -2.17E+06 | 29.3 | 80.7 | -0.68 |
| 80 | 0.9853 | 0.29 | 3.58E+07 | 23764 | 1641 | -395349 | 40.0 | 80.2 | -0.82 |
| 85 | 0.9984 | 0.20 | 4.67E+14 | 44763 | 2.22E+10 | -2.95E+12 | 23.1 | 88.6 | -0.46 |
| 90 | 0.9997 | 0.15 | 8.06E+18 | 41306 | 2.17E+14 | 1.32E+16 | 18.2 | 134 | 0.16 |
| 95 | 0.9994 | 0.08 | 1.04E+08 | 12109 | 344 | 80457 | 30.1 | 235 | 0.21 |
| 98 | 0.9996 | 0.05 | 3.88E+08 | 4057 | 654 | 123223 | 37.1 | 263 | 0.12 |

Table A.7: Teubner-Strey parameters for upper phases of SANS-data treatment section 4.1.2.2

A.2.4 SANS measurements - Teubner Strey analysis (lower phases)

Obtained Teubner-Strey parameters for lower phases of SANS-data treatment using eq. (3.21)-(3.25); scattering length density difference between oil and water was calculated for water dominated samples as $6.06 \cdot 10^{-4} \text{ nm}^{-2}$ ($5 < x < 98\text{wt-}\% \text{ H}_2\text{O}$); a_2 , c_1 and c_2 are coefficients of various terms of order parameters in Landaus free energy. In the case of a microemulsion, c_1 indicates the tendency of forming interfaces between different domains and is usually negative, whereas a positive a_2 favours the microemulsion formation. For a stable morphology the criteria of $4a_2c_2 - c_1 > 0$ with a positive c_2 is required [186]; f_a is the amphiphilicity factor and reaches from 1 for a completely disordered solution to -1 for a superlattice which assumes in case of microemulsions a lamellar structure.

| H ₂ O % | Chi ² | c0 [cm ⁻¹] | c2 [nm ⁴] | V [nm ³] | a2 [] | c1 [nm ²] | ξi [nm] | Ds [nm] | fa [] |
|-----------------------|------------------|---------------------------|--------------------------|--------------------------|-----------|--------------------------|------------|------------|-----------|
| 25 | 0.9956 | 0.18 | 8180 | 175 | 43.2 | -633 | 7.67 | 26.6 | -0.53 |
| 30 | 0.9904 | 0.15 | 1.02E+06 | 95.7 | 3485 | -67869 | 8.91 | 29.3 | -0.57 |
| 35 | 0.9665 | 0.13 | 360280 | 18.5 | 802 | -23941 | 12 | 31.3 | -0.70 |
| 40 | 0.9921 | 0.12 | 2.09E+06 | 26.9 | 2301 | -100109 | 14.7 | 37.2 | -0.72 |
| 50 | 0.9863 | 0.11 | 5.07E+06 | 14.7 | 5002 | -230924 | 15.2 | 38.2 | -0.73 |
| 55 | 0.9976 | 0.09 | 5.58E+15 | 22.3 | 1.16E+12 | -9.37E+13 | 18.2 | 58.8 | -0.58 |
| 60 | 0.9989 | 0.07 | 5.42E+07 | 76.6 | 3856 | -498566 | 22.8 | 77.8 | -0.55 |
| 65 | 0.9651 | 0.34 | 7.61E+07 | 9765 | 4379 | -1.03E+06 | 50.4 | 74.1 | -0.90 |
| 75 | 0.9863 | 0.33 | 1.02E+08 | 30108 | 3744 | -883937 | 34 | 87.2 | -0.72 |

Table A.8: Teubner-Strey parameters for lower phases of SANS-data treatment section 4.1.2.2

A.2.5 SANS-measurements: Residuals for mono- and bimodal data analyses

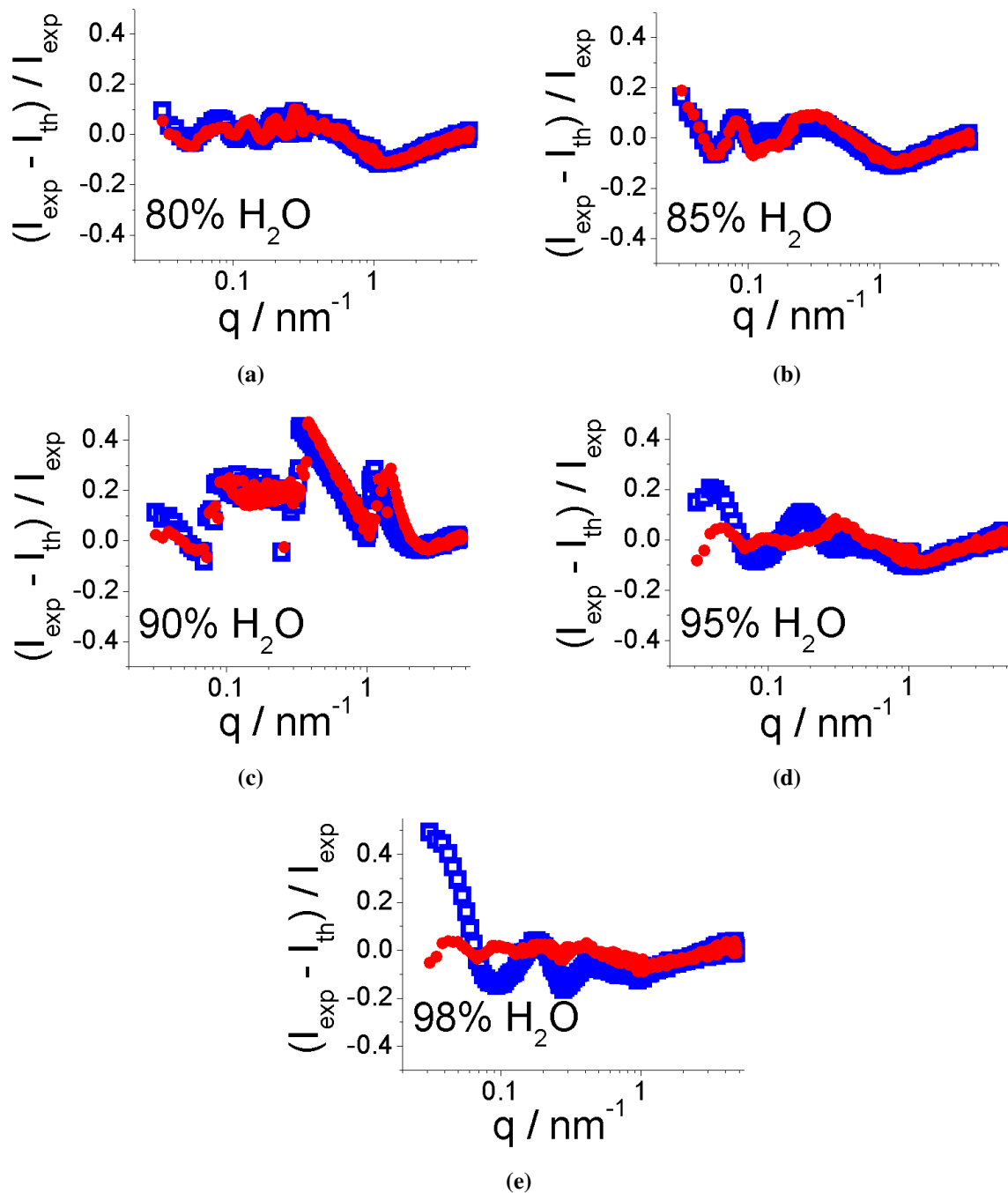


Figure A.6: Residue of SANS-data fits with \square monomodal and \bullet bimodal size distributions for spherical o/w-nanoemulsion droplets (water conc. > 75%)

A.3 PIC-Formulations

A.3.1 Charged surfactant formulations - conductivity-, viscosity- and density data

| H ₂ O wt-% | $\kappa / \mu\text{S/cm}$ | | | | |
|--------------------------|---------------------------|------|------|------|------|
| | DC | EQ | AOT | SCO | SS |
| 0 | 0.03 | | | 0.06 | 0.04 |
| 5 | 0.43 | 0.82 | 1.26 | 0.60 | 0.59 |
| 10 | 2.60 | 0.91 | 4.47 | 1.70 | 2.73 |
| 16 | 9.45 | 0.95 | 13.3 | 3.27 | 7.88 |
| 20 | 14.4 | 0.89 | 28.8 | 5.54 | 14.9 |
| 25 | 20.7 | 0.86 | 57.8 | 6.04 | 22.4 |
| 30 | 24.5 | 0.85 | 94.9 | 6.22 | 29.1 |
| 35 | 28.4 | 0.95 | 138 | 6.15 | 36.6 |
| 40 | 32.9 | 3.91 | 142 | 6.01 | 46.2 |
| 45 | 47.8 | 1.99 | 50.6 | 6.21 | 60.2 |
| 50 | 57.5 | 18.3 | 208 | 6.74 | 72.1 |
| 55 | 116 | 9.28 | 314 | 7.27 | 79.6 |
| 60 | 60.7 | 10.3 | 315 | 15.5 | 116 |
| 65 | 176 | 13.9 | 300 | 21.1 | 164 |
| 70 | 222 | 77.0 | 277 | 15.9 | 217 |
| 75 | 217 | 102 | 247 | 69.3 | 232 |
| 80 | 192 | 108 | 211 | 96.9 | 200 |
| 85 | 165 | 89.4 | 161 | 89.1 | 155 |
| 90 | 109 | 71.5 | 110 | 68.0 | 116 |
| 95 | 64.2 | 45.7 | 72.2 | 41.4 | 65.6 |
| 98 | 27.8 | 24.5 | 28.0 | 21.0 | 33.7 |

Table A.9: Conductivity data κ for oil/water-dilutions of oil/surfactant formulations (2-ethylhexyl carbonate/phenoxy ethanol + parabens/polyglycerol-4 laurate/charged surfactant (66/12/21.1/0.9 wt-%)) with different charged surfactants (DC,EQ,AOT,SCO,SS) at 25°C; values are average determinations of three repeating measurements and of homogenised samples.

| H ₂ O wt-% | $\eta / \text{mPa} \cdot \text{s}$ | | | | |
|--------------------------|------------------------------------|------|-----|------|------|
| | DC | EQ | AOT | SCO | SS |
| 0 | 34.9 | | | | |
| 5 | 29.2 | 28.3 | | 29.6 | 27.1 |
| 10 | 28.9 | 28.9 | | 27.1 | 27.5 |
| 15 | 30.1 | 30.6 | | 29.3 | 28.3 |
| 20 | 29.6 | 33.4 | | 30.5 | 29.1 |
| 25 | 29.8 | 37.7 | | 31.5 | 28.5 |
| 30 | 30.8 | 44.5 | | 32.6 | 28.9 |
| 35 | 32.7 | 55.0 | | 32.1 | 29.2 |
| 40 | 33.6 | 66.9 | | 22.6 | 30.7 |
| 45 | 36.2 | 86.2 | | 13.9 | 30.1 |
| 50 | 37.4 | 84.3 | | 15.1 | 42.9 |
| 55 | 35.8 | 21.4 | | 168 | 54.6 |
| 60 | 21.0 | 415 | | 510 | 15.6 |
| 65 | 5.26 | 99.4 | | 346 | 14.7 |
| 70 | 7.96 | 1647 | | 141 | 15.4 |
| 75 | 19.9 | 46.8 | | 39.4 | 14.7 |
| 80 | 7.42 | 70.9 | | 15.7 | 10.1 |
| 85 | 4.20 | 9.96 | | 5.47 | 2.62 |
| 90 | 1.89 | 3.19 | | 2.36 | 1.88 |
| 95 | 1.30 | 2.50 | | 1.30 | 1.21 |
| 98 | 1.01 | 1.13 | | 1.06 | 0.96 |

Table A.10: Viscosity data η for oil/water-dilutions of oil/surfactant formulations (2-ethylhexyl carbonate/phenoxy ethanol + parabens/polyglycerol-4 laurate/charged surfactant (66/12/21.1/0.9 wt-%)) with different charged surfactants (DC,EQ,AOT,SCO,SS) at 25°C; values are average determinations of three repeating measurements and of homogenised samples.

| H ₂ O wt-% | $\rho / \text{g/cm}^3$ | | | | |
|--------------------------|------------------------|--------|------------------|------------------|--------|
| | DC | EQ | AOT | SCO | SS |
| 0 | 0.9540 | 0.9550 | 0.9560 | 0.9530 | 0.9560 |
| 5 | 0.9572 | 0.9574 | 0.9578 | 0.9565 | 0.9580 |
| 10 | 0.9599 | | | | |
| 20 | 0.9615 | 0.9635 | 0.9639 | 0.9616 | 0.9650 |
| 35 | | | | 0.9821 / 0.9844* | |
| 40 | | 0.9703 | 0.9702 / 0.9796* | | 0.9710 |
| 55 | | | 0.9787 | | |
| 60 | 0.9767 / 0.9824* | 0.9800 | | 0.9800 | 0.9800 |
| 65 | | | 0.9650 / 0.9882* | | |
| 80 | 0.9890 | 0.9869 | 0.9886 | 0.9910 | 0.9870 |
| 90 | 0.9933 | | | | |
| 95 | 0.9952 | | 0.9953 | 0.9966 | |
| 98 | 0.9964 | 0.9965 | | | 0.9966 |

Table A.11: Density data ρ for oil/water-dilutions of oil/surfactant formulations (2-ethylhexyl carbonate/phenoxy ethanol + parabens/polyglycerol-4 laurate/charged surfactant (66/12/21.1/0.9 wt-%)) with different charged surfactants (DC,EQ,AOT,SCO,SS) at 25°C; values are average determinations of three repeating measurements in monophasic samples, * two values indicate densities of biphasic samples (upper/lower Φ).

A.3.2 Studies on the chemical degradation of AOT in O/S-formulations

Samples, formulated with AOT tend to a greater change of physical properties than formulations with other charged surfactants. This is according to its chemical degradation by bacteria. Trials to suppress this degradation have been carried out for an o/w-dilution ratio of 35:65 (o:w), while adding 1wt-% of penicillin to the initial O/S-formulation or exchange the water phase (H₂O) by deuterium oxide (D₂O - taking into account the density difference) according to their antibacterial properties [42,73]. Neither the penicillin addition nor the water exchange sustained the original viscosities obtained for this certain dilution ratio. Thereby the penicillin addition lowers and the water exchange increases the original viscosity by (more or less) a factor of ten. Nevertheless the accomplished antibacterial arrangements reduce the degradation.

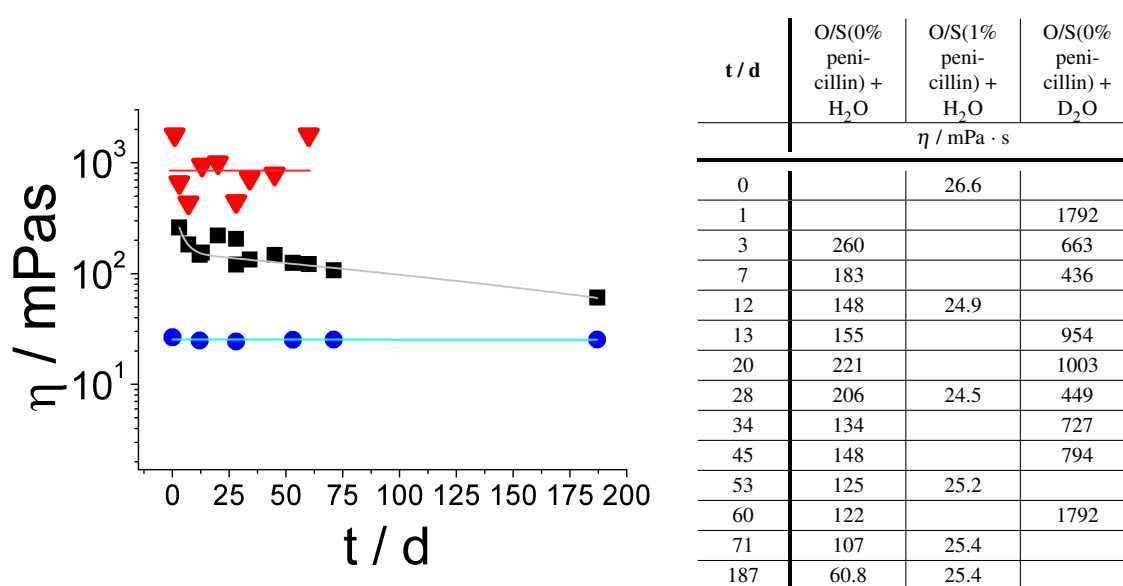


Figure A.7: Measured viscosities η time dependently t for o/w-mixtures (35/65) of O/S-concentrates containing 2-ethylhexyl carbonate/phenoxy ethanol + parabens/polyglycerol-4 laurate/AOT; i) \blacksquare O/S(0% penicillin)+H₂O, ii) \bullet O/S(1% penicillin)+H₂O, iii) \blacktriangledown O/S(0% penicillin)+D₂O

A.3.3 Charged surfactant formulations - fit data of bimodal spherical model log-normal distributed

| wt(H ₂ O) % | A ₁ | R _{1,M_w} nm | σ ₁ | A ₂ = 1-A ₁ | R _{2,M_w} nm | σ ₂ | bkg cm ⁻¹ | R _{1/2,M_w} nm |
|---------------------------|----------------|------------------------------------|----------------|--------------------------------------|------------------------------------|----------------|-------------------------|--------------------------------------|
| DC | | | | | | | | |
| 80 | 0.92 | 12.7 | 0.50 | 0.08 | 31.6 | 0.04 | 0.2900 | 23.8 |
| 85 | 0.72 | 14.3 | 0.45 | 0.28 | 32.0 | 0.19 | 0.2000 | 28.8 |
| 90 | 0.56 | 14.8 | 0.43 | 0.44 | 32.8 | 0.34 | 0.1500 | 30.9 |
| 95 | 0.38 | 15.4 | 0.36 | 0.62 | 35.6 | 0.50 | 0.0800 | 34.6 |
| 98 | 0.28 | 16.0 | 0.35 | 0.72 | 39.4 | 0.54 | 0.0500 | 38.7 |
| AOT | | | | | | | | |
| 80 | 0.64 | 8.59 | 0.35 | 0.36 | 18.7 | 0.34 | 0.5992 | 17.1 |
| 90 | 0.47 | 10.0 | 0.39 | 0.53 | 22.7 | 0.34 | 0.2226 | 21.8 |
| 95 | 0.32 | 11.8 | 0.40 | 0.68 | 23.2 | 0.47 | 0.1207 | 22.5 |
| 98 | 0.31 | 13.8 | 0.50 | 0.69 | 30.7 | 0.46 | 0.0699 | 30.1 |
| EQ | | | | | | | | |
| 80 | 0.99 | 9.87 | 0.58 | 1E-05 | 32.1 | 0.40 | 0.2654 | 9.87 |
| 90 | 0.76 | 12.1 | 0.45 | 0.24 | 31.2 | 0.39 | 0.1461 | 28.3 |
| 95 | 0.59 | 12.7 | 0.56 | 0.41 | 36.0 | 0.38 | 0.0903 | 34.7 |
| 98 | 0.53 | 16.0 | 0.50 | 0.47 | 46.1 | 0.37 | 0.0611 | 44.8 |
| SCO | | | | | | | | |
| 80 | 0.76 | 8.71 | 0.37 | 0.24 | 8.97 | 0.51 | 0.5945 | 8.78 |
| 90 | 0.72 | 12.3 | 0.46 | 0.28 | 30.3 | 0.28 | 0.2303 | 27.7 |
| 95 | 0.56 | 12.8 | 0.46 | 0.44 | 26.8 | 0.31 | 0.1197 | 25.1 |
| 98 | 0.51 | 18.3 | 0.51 | 0.49 | 48.9 | 0.34 | 0.0681 | 47.4 |
| SS | | | | | | | | |
| 80 | 0.49 | 8.30 | 0.25 | 0.51 | 10.0 | 0.43 | 0.5536 | 9.40 |
| 90 | 0.66 | 11.8 | 0.42 | 0.34 | 28.9 | 0.35 | 0.2190 | 26.9 |
| 95 | 0.30 | 12.9 | 0.52 | 0.70 | 31.9 | 0.44 | 0.0926 | 31.4 |
| 98 | 0.40 | 16.1 | 0.53 | 0.60 | 37.7 | 0.42 | 0.0667 | 36.7 |

Table A.12: Fit parameters amplitude A, mass weighed radii R_{1,M_w}, R_{2,M_w} and polydispersity indices σ₁ and σ₂ for population 1 and 2, respectively; in addition mass weighted radius of both size distributions R_{1/2,M_w} in respect to their given polydispersities. For dilutions (wt-% (H₂O)) of nanoemulsion qualified O/S-mixtures containing DEHC/K300/P4L/charged surfactant with different charged surfactant components (dilauryl citrate (DC), 2-ethylhexyl sodium sulfosuccinate (AOT), Rewoquat CR 3099 (EQ), sulfonated castor oil - Na-salt (SCO) and 2-sodium laureth sulfosuccinate (SS)).

A.3.4 Charged surfactant concentration-variation - fit data of bimodal spherical model log-normal distributed

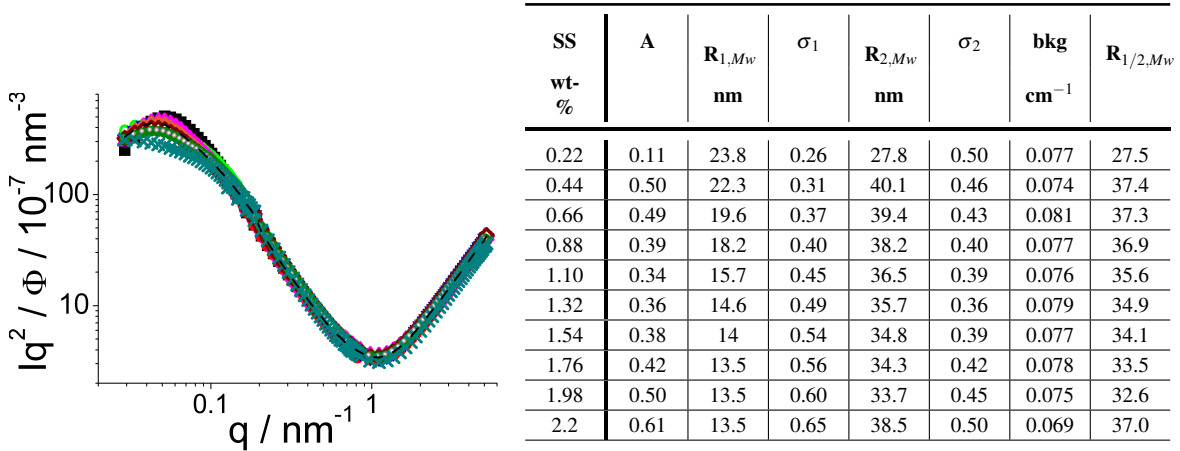


Figure A.8: *left:* SANS-curves in full observed q -range for NEs at 95wt-% (H_2O) formed from oil/surfactant mixtures containing DEHC/K300/P4L/SS (66.6/12.1/21.3 + SS) varying the SS-concentration (\bullet 0.22, \square 0.44, \circ 0.66, $---$ 0.88, \blacktriangledown 1.10, \triangle 1.32, \blacklozenge 1.54, \diamond 1.76, \bullet 1.98, \times 2.20 wt-%). SANS studies were done directly after sample preparation at 25.0 ± 0.1 °C in 1mm cells. *right:* Table of fit parameters using a bimodal log-normal distributed spherical model. Given radii are converted in mass weighted ones.

A.3.5 Charged surfactant concentration-variation - fit data of Teubner-Strey analyses

Obtained Teubner-Strey parameters using eq. (3.21)- (3.25) for nanoemulsions formed from O/S-mixtures based on DEHC/K300/P4L (66.7/12.1/21.2wt-%) and variable SS-concentration (0.22-2.2wt-%). O/S-mixtures were diluted with 95wt-% water. Scattering length density difference was calculated to $6.06 \cdot 10^{-4} nm^{-2}$.

| wt(SS(TW)) % | χ^2 | c_0 [cm^{-1}] | c_2 [nm^4] | V [nm^3] | a_2 [] | c_1 [nm^2] | ξ_i [nm] | D_s [nm] | f_a [] |
|--------------|----------|---------------------|------------------|----------------|-----------|------------------|--------------|------------|-----------|
| 0.22 | 1.0000 | 0.06 | 3.09E+08 | 11597 | 2397 | -378684 | 30.4 | 152 | -0.22 |
| 0.44 | 0.9999 | 0.06 | 1.13E+07 | 15540 | 39.9 | 39861 | 23.4 | 832 | 0.94 |
| 0.66 | 0.9996 | 0.07 | 1.30E+07 | 14738 | 34.2 | 42195 | 24.8 | — | 1.00 |
| 0.88 | 1.0000 | 0.06 | 5.43E+08 | 11471 | 2181 | 506397 | 28.5 | 227 | 0.23 |
| 1.10 | 0.9999 | 0.06 | 1.13E+08 | 10174 | 494 | 12075 | 30.6 | 197 | 0.03 |
| 1.32 | 1.0000 | 0.06 | 3.96E+08 | 11409 | 2075 | 56282 | 29.1 | 189 | 0.03 |
| 1.54 | 0.9999 | 0.06 | 2.51E+07 | 11175 | 105 | 19148 | 28.8 | 218 | 0.19 |
| 1.76 | 0.9999 | 0.06 | 1.92E+08 | 12023 | 712 | 362411 | 26.4 | 284 | 0.49 |
| 1.98 | 0.9999 | 0.06 | 1.14E+06 | 15249 | 4.25 | 4494 | 22.7 | — | 1.02 |
| 2.2 | 1.0000 | 0.06 | 8.64E+07 | 17959 | 32.3 | 826247 | 19.3 | — | 7.82 |

Table A.13: Teubner-Strey parameters and calculated correlation length ξ_i , periodic distance D_s and amphiphilicity f_a obtained from SANS-spectra of nanoemulsions prepared from O/S-mixtures based on DEHC/K300/P4L (66.7/12.1/21.2wt-%) and variable SS-concentration (0.22-2.2wt-%). O/S-mixtures were diluted with 95wt-% water.

A.3.6 Oil formulations - fit data of bimodal spherical model log-normal distributed

| wt(H ₂ O) % | A ₁ | R _{1,Mw} nm | σ ₁ | A ₂ = 1-A ₁ | R _{2,Mw} nm | σ ₂ | bkg cm ⁻¹ | R _{1/2,Mw} nm |
|---------------------------|----------------|-------------------------|----------------|--------------------------------------|-------------------------|----------------|-------------------------|---------------------------|
| DEHC | | | | | | | | |
| 80 | 0.99 | 9.87 | 0.58 | 1E-05 | 32.1 | 0.40 | 0.2654 | 9.87 |
| 90 | 0.76 | 12.1 | 0.45 | 0.24 | 31.2 | 0.39 | 0.1461 | 28.3 |
| 95 | 0.59 | 12.7 | 0.56 | 0.41 | 36.0 | 0.38 | 0.0903 | 34.7 |
| 98 | 0.53 | 16.0 | 0.50 | 0.47 | 46.1 | 0.37 | 0.0611 | 44.8 |
| CC | | | | | | | | |
| 80 | 0.98 | 10.6 | 0.65 | 0.02 | 12.8 | 0.31 | 0.3391 | 10.7 |
| 90 | 0.49 | 11.4 | 0.34 | 0.51 | 24.1 | 0.37 | 0.2118 | 22.9 |
| 95 | 0.50 | 13.3 | 0.46 | 0.50 | 32 | 0.30 | 0.1103 | 30.8 |
| 98 | 0.54 | 18.7 | 0.48 | 0.46 | 40.9 | 0.29 | 0.0674 | 38.8 |
| OO | | | | | | | | |
| 80 | 0.38 | 8.45 | 0.25 | 0.62 | 13.3 | 0.42 | 0.6737 | 12.6 |
| 90 | 0.79 | 12.1 | 0.44 | 0.21 | 33.0 | 0.44 | 0.2216 | 29.6 |
| 95 | 0.63 | 13.6 | 0.48 | 0.37 | 38.8 | 0.40 | 0.1145 | 37.1 |
| 98 | 0.54 | 16.4 | 0.43 | 0.46 | 48.4 | 0.42 | 0.0698 | 46.8 |

Table A.14: Fit parameters amplitude A, mass weighed radii R_{1,Mw}, R_{2,Mw} and polydispersity indices σ₁ and σ₂ for population 1 and 2, respectively; in addition mass weighed radius of both size distributions R_{1/2,Mw} in respect to their given polydispersities. For dilutions (wt-% (H₂O)) of nanoemulsion qualified O/S-mixtures containing oil/K300/P4L/Rewoquat CR 3099 with different oil components (2-ethylhexyl carbonate (DEHC), 2-octyl carbonate (CC) and octyloctanoate (OO)).

A.4 O/S-Variation at constant dilution ratio for the system O: DEHC/K300 S: P4L/SS

A.4.1 Guinier approximated radii for structures in O/S-variation.

Model free analysis for SANS-curves of O/S-variation using the Guinier approximation to obtain an average particle size by the extrapolated zero-angle intensity $I(q=0)$. In contrast we also calculated the radius of gyration $R(R_G)$, as in the range of $qR < 1$ for the presence of individual, non-interacting particles the scattering intensity $I(q)$ depends only it. Further explanations are given in section 3.2.13.1.

The employed system based on DEHC/K300 (85/15) as oil and P4L/SS (96/4) as surfactant phase. The O/S-mixtures were diluted at constant water ratio to 95wt-%.

| O % | S % | I0 1/cm | V_p $10^{24}m^3$ | ΔSLD $10^{-4}nm^{-2}$ | R(I0) nm | B $10^{-18}m^2$ | R_G nm | R(R_G) nm |
|--------|--------|------------|-----------------------|----------------------------------|-------------|--------------------|-------------|------------------|
| 95 | 5 | 6347 | 35.8 | 6.10 | 20.4 | -1202 | 60.0 | 77.5 |
| 90 | 10 | 5432 | 30.8 | 6.09 | 19.4 | -1347 | 63.6 | 82.1 |
| 85 | 15 | 58375 | 332 | 6.08 | 42.9 | -957 | 53.6 | 69.2 |
| 80 | 20 | 38086 | 217 | 6.07 | 37.3 | -566 | 41.2 | 53.2 |
| 78 | 22 | 25467 | 146 | 6.05 | 32.7 | -416 | 35.3 | 45.6 |
| 75 | 25 | 14091 | 81.1 | 6.04 | 26.9 | -262 | 28.0 | 36.2 |
| 65 | 35 | 7327 | 42.4 | 6.03 | 21.6 | -191 | 23.9 | 30.9 |
| 60 | 40 | 2685 | 15.6 | 6.01 | 15.5 | -88.6 | 16.3 | 21.1 |
| 55 | 45 | 1241 | 7.24 | 6.00 | 12.0 | -57.6 | 13.1 | 17.0 |
| 50 | 50 | 1114 | 6.52 | 5.99 | 11.6 | -46.7 | 11.8 | 15.3 |
| 45 | 55 | 728 | 4.28 | 5.98 | 10.1 | -36.6 | 10.5 | 13.5 |
| 40 | 60 | 684 | 4.04 | 5.96 | 9.88 | -41.9 | 11.2 | 14.5 |
| 35 | 65 | 509 | 3.02 | 5.95 | 8.97 | -46.1 | 11.8 | 15.2 |
| 30 | 70 | 4406 | 26.2 | 5.94 | 18.4 | -1000 | 54.8 | 70.7 |
| 25 | 75 | 2598 | 15.5 | 5.92 | 15.5 | -653 | 44.2 | 57.1 |
| 20 | 80 | 2365 | 14.2 | 5.91 | 15.0 | -582 | 41.8 | 54.0 |
| 15 | 85 | 2121 | 12.8 | 5.90 | 14.5 | -563 | 41.1 | 53.1 |
| 10 | 90 | 1868 | 11.3 | 5.89 | 13.9 | -420 | 35.5 | 45.8 |
| 5 | 95 | 1596 | 9.71 | 5.87 | 13.2 | -334 | 31.7 | 40.9 |
| 0 | 100 | 1593 | 9.74 | 5.86 | 13.2 | -250 | 27.4 | 35.3 |

Table A.15: For samples of O/S-variation, Guinier approximated radii from SANS-data using linear extrapolation to zero-angle intensity ($\ln I = \ln I_0 - 1/3R_G^2 q^2$, with $B = -1/3R_G^2$). Average particle size $R(I_0)$ was obtained by eq. (3.17) using the zero angle intensity I_0 , the volume fraction of the aggregates ($\Phi = 0.0476$, assuming all oil and surfactant is contained), the volume of one scattering particle V_p and the contrast of the particles to the matrix ΔSLD (water (D_2O)). The radius of gyration R_G was calculated from the slope B of the Guinier approximation according to equation (3.15) and converted to a radius for spherical particles ($R_G^2 = 3/5 R^2$).

A.4.2 Teubner-Strey analyses for nano- and microemulsions of O/S-variation.

Obtained Teubner-Strey parameters of SANS-curves for O/S-variation using eq. (3.21)- (3.25); a_2 , c_1 and c_2 are coefficients of various terms of order parameters in Landaus free energy. In the case of a microemulsion, c_1 indicates the tendency of forming interfaces between different domains and is usually negative, whereas a positive a_2 favours the microemulsion formation. For a stable morphology the criteria of $4a_2c_2 - c_1 > 0$ with a positive c_2 is required [186]; D_S is the quasiperiodic repeat distance (periodicity) and can be associated with a peak in the SANS spectra at $2\Pi/D_S$ in case of high densities and order; ξ is the correlation length and corresponds to a characteristic length for positional correlation; f_a is the amphiphilicity factor and reaches from 1 for a completely disordered solution to -1 for a superlattice which assumes in case of microemulsions a lamellar structure.

| S(S+O) wt-% | E-type | $\Delta\eta$ 1/nm ² | c_0 1/cm | c_2 nm ⁴ | V nm ³ | a_2 | c_1 nm ² | ξ nm | D_s nm | f_a |
|----------------|---------|-----------------------------------|---------------|--------------------------|------------------------|-------|--------------------------|-------------|-------------|-------|
| 20 | NE | 6.08E-04 | 0.06 | 2.77E+08 | 10167 | 814 | 115644 | 32.3 | 229 | 0.12 |
| 22 | NE | 6.06E-04 | 0.07 | 9.78E+05 | 12712 | 5.26 | 614 | 27.6 | 198 | 0.14 |
| 25 | NE | 6.05E-04 | 0.06 | 1.79E+08 | 13183 | 1892 | -24289 | 25.1 | 154 | -0.02 |
| 30 | μ E | 6.04E-04 | 0.06 | 1.03E+08 | 25273 | 3027 | 446170 | 16.2 | 156 | 0.40 |
| 35 | μ E | 6.03E-04 | 0.06 | 4.20E+05 | 30687 | 42.7 | -2037 | 16.1 | 79.2 | -0.24 |
| 40 | μ E | 6.01E-04 | 0.06 | 5.55E+06 | 12953 | 858 | -93228 | 22.3 | 61.6 | -0.68 |
| 45 | μ E | 6.00E-04 | 0.07 | 6.30E+03 | 30709 | 1.83 | -135 | 17.8 | 53.4 | -0.63 |
| 50 | μ E | 5.99E-04 | 0.06 | 2.73E+06 | 18591 | 1074 | -64592 | 15.8 | 50.0 | -0.60 |
| 55 | μ E | 5.98E-04 | 0.06 | 5.86E+04 | 22475 | 36.3 | -1501 | 12.9 | 45.8 | -0.51 |
| 60 | μ E | 5.96E-04 | 0.07 | 1.29E+06 | 24571 | 868 | -27689 | 11.5 | 46.4 | -0.41 |
| 65 | μ E | 5.95E-04 | 0.06 | 1.20E+05 | 30058 | 116 | -1518 | 8.97 | 45.9 | -0.20 |

Table A.16: Teubner-Strey parameters for nano- (NE) and microemulsions (μ E) of O/S-variation (O: DEHC/K300, S:P4L/SS) at constant dilution ratio (95wt-% water). Scattering length density difference of dispersed aggregates to solvent $\Delta\eta$ was calculated according to the O/S-composition, while assuming that all O/S-mixture is contained in the emulsion droplets.

A.4.3 Igor Pro 6.12A source code for simulations of disk- and vesicle-scattering

Scattering intensities of disk-like and vesicle structures:

```
#pragma rtGlobals=1          // Use modern global access method.

function disk_vs-vesicle ()
  variable ves=1
  variable r,d, phi,dsld
  if (ves==0)
    r=32
    d=3
    phi=0.046
    dsld=5.81e-4
    return phi*pi*r*r*d*dsld*dsld*1e+7
  else
    r=32
    d=3
    phi=0.046
    dsld=5.81e-4
    return phi*(4*pi/3*r^3-4*pi/3*(r-d)^3)*dsld*dsld*1e+7
  endif
end
```

The program calculates the scattering intensity of either disks ($ves = 0$) or vesicles ($ves = 1$). For the calculations we assumed monodisperse particles whose scattering intensity is given by the equations (4.12). The radii r originates from individual model fits of a monodisperse approach to the scattering curve of 100wt-% surfactant of a O/S-mixture diluted with water to 95wt-% (D_2O -respecting the density difference to H_2O). The O/S-mixture contained DEHC/K300 (85/15) as oil and P4L/SS (96/4) as surfactant phase. We assume the surfactant phase, given by the volume fraction ϕ , completely embedded into the structures that show a layer- or respectively shell-thickness of approximately 3 nm at high scattering vector q . Their scattering density difference $dsld$ to the solvent (D_2O) was calculated due to the P4L/SS ratio to $5.81 \cdot 10^{-4} \text{ nm}^{-2}$.

A.5 Nanoemulsion kinetics

A.5.1 Matlab source code of interdroplet exchange dynamics

Simulation for two populations of different contrast merging together in time:

```

q = logspace(log10(0.01),log10(5),80); % scattering vector [1/nm]
SLDSolventVec = linspace(-0.56e-4,6.36e-4,18); % scattering length density solvent [1/nm^2]
vari = linspace(0,1,20); % time increment [arb. units]

%%Calculation of exchange dynamics.
I = zeros(length(vari),length(q));
for n = 1:length(SLDSolventVec)
    for m = 1:length(vari)
        R = 10;
        t = 1.3;
        phi = .05;
        SLDCore1 = 0.10e-4+vari(m)*6.19e-4/2;
        SLDCore2 = 6.11e-4-vari(m)*6.19e-4/2;
        SLDSShell = 0.507e-4;
        SLDSolvent = SLDSolventVec(n);
        IBkg = (SLDSolventVec(n)-SLDSolventVec(1))/(SLDSolventVec(end)-SLDSolventVec(1))*(0.04-1)+1;
        scale = 1e7;
        a1 = [R t phi/2 SLDCore1 SLDSShell SLDSolvent 0 scale];
        a2 = [R t phi/2 SLDCore2 SLDSShell SLDSolvent 0 scale];
        f = @(x,a) coreShellSpheres(x,a(1:8));

        I(m,:) = f(q,a1) + f(q,a2) + IBkg;
    end
end

%%Visualisation.
subplot(3,6,n)
h=mesh(q,vari,I);
axesHandle = get(h,'Parent');
set(axesHandle,'XScale','log');
set(axesHandle,'ZScale','log');
xlim([q(1) q(end)]);
ylim([vari(1) vari(end)]);
zlim([min(min(I)) max(max(I))]);
set(axesHandle,'YDir','reverse');
title(sprintf('SLDSolvent:_%1.3e_nm^{-2}',SLDSolvent));

end

```

Scattering integral of a mono-disperse collection of core-shell spheres:

```

function [val] = coreShellSpheres(q,a)
%% Parameters
R = a(1); % radius [nm]
t = a(2); % shell thickness [nm]
phi = a(3); % shell volume fraction
SLDCore = a(4); % scattering length density: core [1/nm^2]
SLDSShell = a(5); % scattering length density: shell [1/nm^2]
SLDSolvent = a(6); % scattering length density: solvent [1/nm^2]
IBkg = a(7); % background intensity [1/cm]
scale = a(8); % intensity scaling

%% Calculation
RI = R; % inner radius
RO = R + t; % outer radius
deltaSLDI = SLDCore-SLDSShell; % inner scattering length density difference
deltaSLDO = SLDSShell-SLDSolvent; % outer scattering length density difference

volumeSphereShell = 4*pi/3*(RO^3 - R^3); % shell volume
n = phi/volumeSphereShell; % number density

val = n*(kSphere(q,RI,deltaSLDI) + kSphere(q,RO,deltaSLDO)).^2; val = val*scale + IBkg;
end

```

Form factor of a homogeneous sphere:

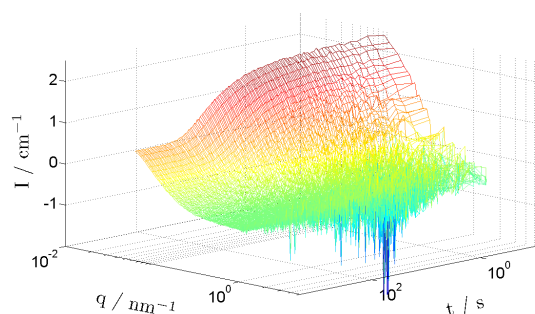
```

function [val] = kSphere(q,R,deltaSLD)
qR = R*q;
volumeSphere = 4*pi/3*R^3;
val = volumeSphere*deltaSLD*3*(sin(qR)-qR.*cos(qR))./qR.^3;
end

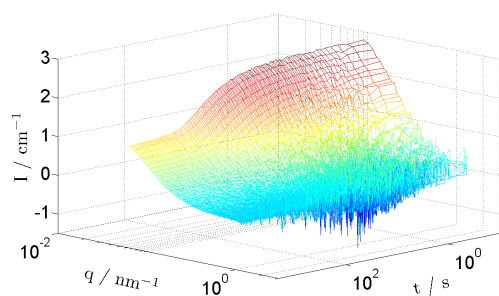
```

A.5.2 NE-interdroplet exchange dynamics - Additives

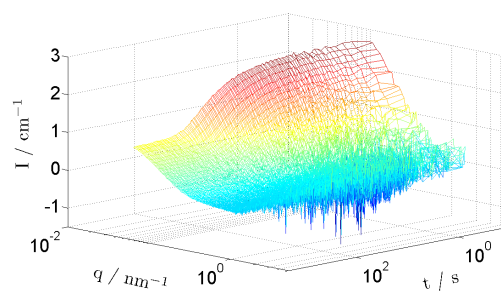
The equilibration dynamics of the interdroplet exchange among nanoemulsion droplets at a dilution ratio of 98wt-% water ($\text{H}_2\text{O}/\text{D}_2\text{O}$ -mixture 40/60) were measured by the stopped-flow SANS method, using the contrast sensibility of neutron experiments. For this purpose hydrogenated and deuterated nanoemulsions based on O/S-formulations containing (h_{34} or d_{34})-DEHC/K300/P4L/AOT (66/12/21.1/ ~ 0.9) were equally mixed and their contrast equilibration traced time-dependently. The influence of additives on the equilibration dynamics was studied, spiking the initial O/S-mixture with either additional AOT to a collective weight fraction of ~ 0.9 , 2 and 5wt-% (A.10a and A.10b); or with the triblock copolymer Pluronic L31 of 0, 1 and 5wt-% (A.10c and A.10d).



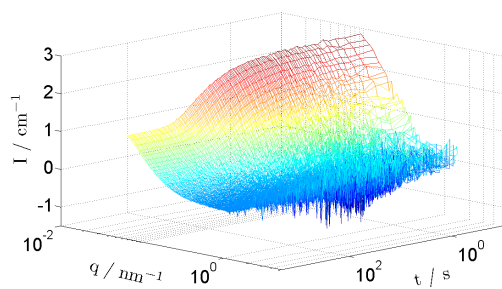
(a) 0.9% AOT or rather 0% L31



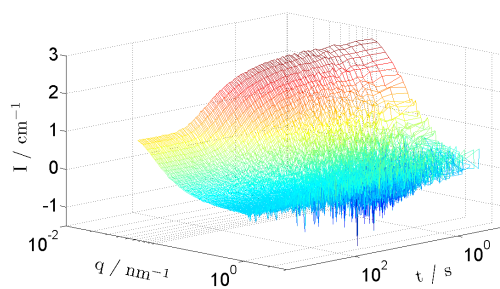
(a) 2% AOT



(b) 5% AOT



(c) 1% Pluronic L31



(d) 5% Pluronic L31

Figure A.9: Equilibration dynamics of interdroplet exchange among nanoemulsion droplets at a dilution ratio of 98wt-% water ($\text{H}_2\text{O}/\text{D}_2\text{O}$ -mixture 40/60). O/S-mixture bases on DEHC/K300/P4L/AOT (66/12/21.1/ ~ 0.9) and was additionally spiked with further AOT (A.10a and A.10b) or triblock copolymer Pluronic L31 (A.10c and A.10d) before dilution.

A.6 PIC-Mechanism

A.6.1 Refractivities of glycerol/H₂O and sugar/H₂O mixtures

| glycerol % | H ₂ O % | n ^{25°C} | sugar % | H ₂ O % | n ^{25°C} |
|---------------|-----------------------|-------------------|------------|-----------------------|-------------------|
| 0 | 100 | 1.3321 | 0 | 100 | 1.3321 |
| 20 | 80 | 1.3568 | 2.5 | 97.5 | 1.3361 |
| 40 | 60 | 1.3834 | 5 | 95.0 | 1.3398 |
| 60 | 40 | 1.4121 | 7.5 | 92.5 | 1.3432 |
| 80 | 20 | 1.4420 | 10 | 90.0 | 1.3472 |
| 100 | 0 | 1.4722 | | | |

Table A.17: Measured refractivities for water/glycerol and water/sugar (D(+)-glucose/galactose) mixtures at 25.0 ± 0.1 °C -unspecific wavelength

A.6.2 Transmittance spectra of glycerol/H₂O and sugar/H₂O mixtures

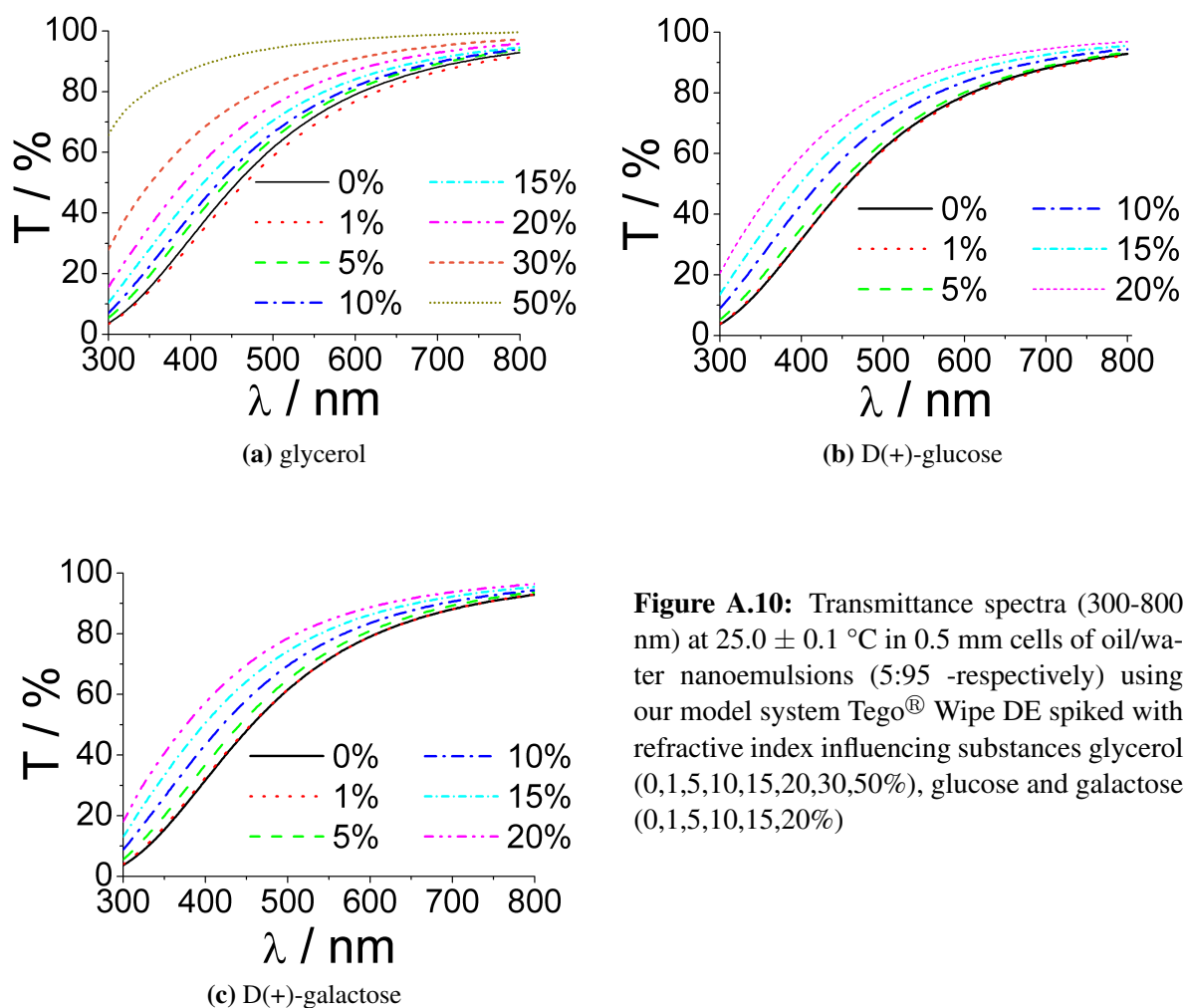


Figure A.10: Transmittance spectra (300-800 nm) at 25.0 ± 0.1 °C in 0.5 mm cells of oil/water nanoemulsions (5:95 -respectively) using our model system Tego® Wipe DE spiked with refractive index influencing substances glycerol (0,1,5,10,15,20,30,50%), glucose and galactose (0,1,5,10,15,20%)

A.6.3 NMR reference spectra of pure components of the nanoemulsion qualified O/S-mixture (DEHC/K300/P4L/AOT)

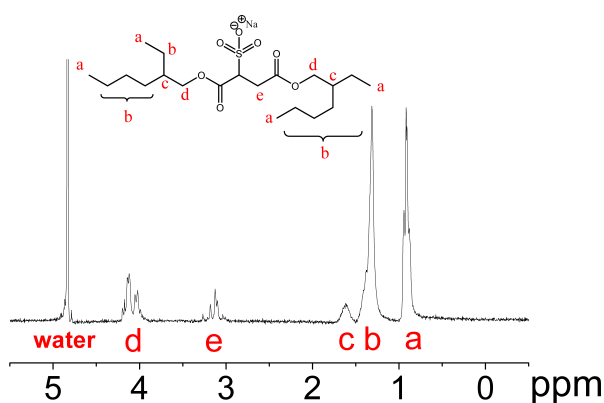
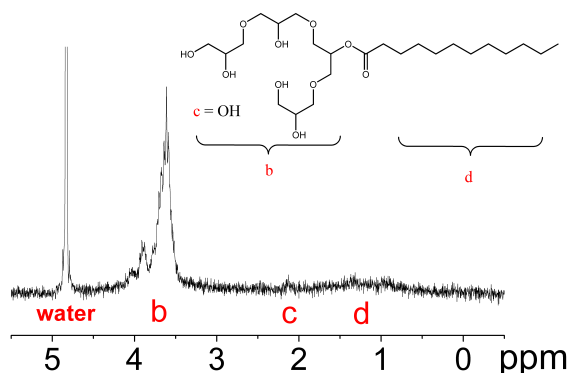
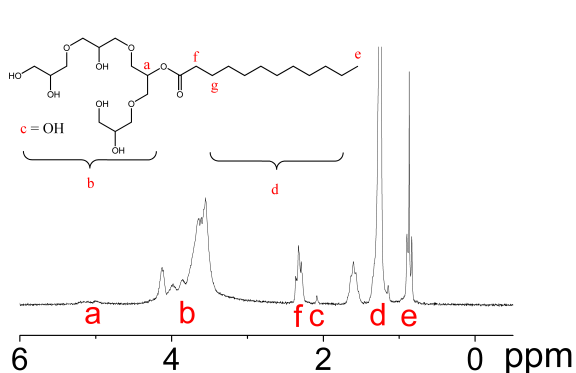
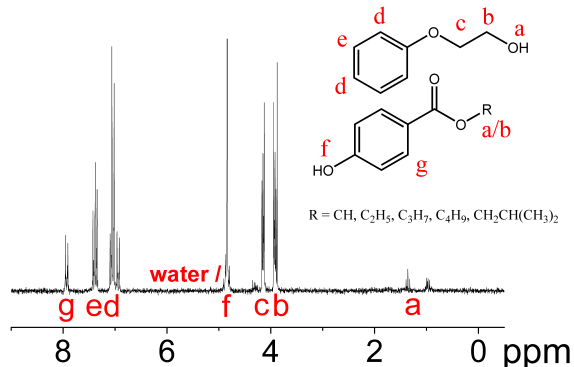
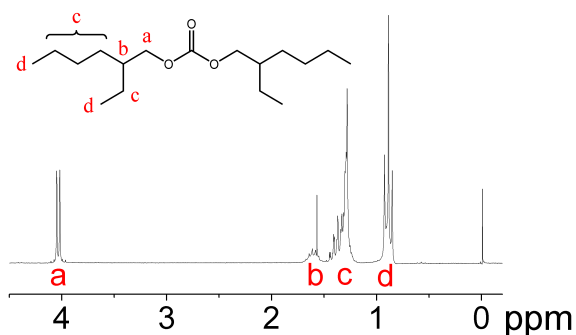


Figure A.11: NMR reference spectra of pure components of the nanoemulsion qualified O/S-mixture (DEHC/K300/P4L/AOT).

A.6.4 Summarised NMR-data for samples upon dilution of nanoemulsion qualified O/S-mixture (DEHC/K300/P4L/AOT)

| | | Peak | | | | | | | | | | | | |
|-----|--|--------------------------|------|----------|------|---------|------|---------|------|---------|------|---------|------|---------|
| | | 1 | | 2 | | 3 | | 4 | | 5 | | 6 | | |
| ppm | signal | H ₂ O / wt- % | ppm | I | ppm | I | ppm | I | ppm | I | ppm | I | ppm | I |
| | doublet | 30 | 7.84 | 4.0E+04 | 7.8 | 3.9E+04 | | | | | | | | |
| | | 60 | 7.84 | 2.3E+04 | 7.82 | 1.6E+04 | | | | | | | | |
| | | 75 | 7.86 | 3.8E+04 | 7.82 | 3.7E+04 | | | | | | | | |
| | | 90 | 7.89 | 1.4E+04 | 7.85 | 1.9E+04 | | | | | | | | |
| | | 95 | 7.91 | 1.1E+04 | 7.87 | 1.4E+04 | | | | | | | | |
| 6-8 | triplet (roof effect) | 30 | 7.19 | 7.2E+04 | 7.15 | 1.5E+05 | 7.11 | 1.0E+05 | | | | | | |
| | | 60 | 7.21 | 5.5E+04 | 7.18 | 6.5E+04 | 7.15 | 3.0E+04 | | | | | | |
| | | 75 | 7.26 | 6.5E+04 | 7.22 | 1.1E+05 | 7.18 | 8.0E+04 | | | | | | |
| | | 90 | 7.34 | 4.3E+04 | 7.30 | 9.4E+04 | 7.26 | 7.3E+04 | | | | | | |
| | | 95 | 7.38 | 3.4E+04 | 7.34 | 6.2E+04 | 7.3 | 5.2E+04 | | | | | | |
| | triplet → multiplet (roof effect) | 30 | 6.85 | 3.1E+05 | 6.81 | 2.7E+05 | 6.78 | 1.6E+04 | | | | | | |
| | | 60 | 6.88 | 1.3E+05 | 6.85 | 1.1E+05 | 6.82 | 2.2E+04 | | | | | | |
| | | 75 | 6.92 | 2.4E+05 | 6.89 | 1.7E+05 | 6.85 | 2.8E+04 | 6.82 | 1.3E+04 | | | | |
| | | 90 | 6.99 | 1.2E+05 | 6.97 | 8.6E+04 | 6.95 | 9.1E+04 | 6.93 | 2.5E+04 | 6.89 | 1.4E+04 | 6.85 | 1.6E+04 |
| | | 95 | 7.04 | 3.8E+04 | 7.03 | 8.4E+04 | 7.01 | 5.8E+04 | 6.98 | 6.5E+04 | 6.92 | 8.1E+03 | 6.87 | 1.0E+04 |
| 4-6 | singlet | 30 | 4.82 | 3.6E+05 | | | | | | | | | | |
| | | 60 | 4.83 | 6.0E+05 | | | | | | | | | | |
| | | 75 | 4.84 | 1.4E+06 | | | | | | | | | | |
| | | 90 | 4.84 | 2.2E+06 | | | | | | | | | | |
| | | 95 | 4.84 | 2.7E+06 | | | | | | | | | | |
| 3-5 | doublet | 30 | 4.00 | 1.43E+06 | 3.97 | 1.5E+06 | | | | | | | | |
| | | 60 | 3.99 | 9.8E+05 | 3.97 | 7.1E+05 | | | | | | | | |
| | | 75 | 4.00 | 8.8E+05 | 3.98 | 8.1E+05 | | | | | | | | |
| | | 90 | 4.00 | 9.3E+05 | 3.98 | 9.3E+05 | | | | | | | | |
| | | 95 | 4.00 | 6.0E+05 | 3.97 | 5.9E+05 | | | | | | | | |
| 0-3 | multiplet (main peak) (roof effect) | 30 | 1.27 | 4.1E+06 | | | | | | | | | | |
| | | 60 | 1.28 | 2.6E+06 | | | | | | | | | | |
| | | 75 | 1.28 | 2.6E+06 | | | | | | | | | | |
| | | 90 | 1.29 | 2.6E+06 | | | | | | | | | | |
| | | 95 | 1.29 | 1.7E+06 | | | | | | | | | | |
| | triplet (roof effect) | 30 | 0.91 | 2.1E+06 | 0.87 | 3.9E+06 | 0.84 | 1.5E+06 | | | | | | |
| | | 60 | 0.90 | 1.8E+06 | 0.88 | 2.2E+06 | 0.84 | 1.0E+04 | | | | | | |
| | | 75 | 0.92 | 1.2E+06 | 0.88 | 2.3E+06 | 0.85 | 9.9E+05 | | | | | | |
| | | 90 | 0.92 | 1.4E+06 | 0.89 | 2.5E+06 | 0.85 | 8.9E+05 | | | | | | |
| | | 95 | 0.92 | 8.6E+05 | 0.89 | 1.7E+06 | 0.85 | 6.2E+05 | | | | | | |

Table A.18: Peak position (ppm) and peak intensities (I - is proportional to the molar concentration of a sample) given of ¹H-NMR spectra of oil/surfactant dilutions (in D₂O) upon emulsification pathway to form nanoemulsions via the phase inversion concentration (PIC) method; density difference of deuterium oxide to water was taken into account. O/S-mixture contained DEHC/K300/P4L/AOT (66/12/21.1/0.9 wt-%).

| wt-% (glycerol) | NE: wt-% (H ₂ O) | | | | | | | | | |
|--------------------|-----------------------------|---------|-------------------|---------|-------------------|---------|-------------------|---------|-------------------|---------|
| | 80 | | 85 | | 90 | | 95 | | 98 | |
| | n ^{25°C} | √τ | n ^{25°C} | √τ | n ^{25°C} | √τ | n ^{25°C} | √τ | n ^{25°C} | √τ |
| 0 | 1.3581 | 0.17192 | 1.3519 | 0.42556 | 1.3455 | 0.4186 | 1.3391 | 0.36191 | 1.3352 | 0.32655 |
| 1 | 1.3589 | 0.17212 | 1.3528 | 0.41722 | 1.3466 | 0.41035 | 1.3399 | 0.35707 | 1.3368 | 0.32034 |
| 5 | 1.3626 | 0.18384 | 1.3568 | 0.39326 | 1.3509 | 0.38783 | 1.3452 | 0.33903 | 1.3418 | 0.29983 |
| 10 | 1.3679 | 0.15198 | 1.3672 | 0.36868 | 1.3564 | 0.35817 | 1.3508 | 0.31071 | 1.3472 | 0.2733 |
| 15 | 1.3734 | 0.13058 | 1.3675 | 0.33838 | 1.3621 | 0.33509 | 1.3565 | 0.29754 | 1.3544 | 0.25732 |
| 20 | 1.3788 | 0.13409 | 1.3729 | 0.31548 | 1.3679 | 0.30598 | 1.3631 | 0.26826 | 1.3595 | 0.22623 |
| 30 | 1.3891 | 0.11997 | 1.3848 | 0.25892 | 1.3798 | 0.25623 | 1.375 | 0.21217 | 1.3722 | 0.19567 |
| 50 | 1.4118 | 0.03732 | 1.4082 | 0.11495 | 1.4042 | 0.13246 | 1.4013 | 0.12444 | 1.3988 | 0.10034 |

Table A.19: Summary of measured refractivities and square root of corresponding turbidity coefficient $\sqrt{\tau}$ (cp. 3.2.5) at $25.0 \pm 0.1^\circ\text{C}$ of nanoemulsions at different dilution ratios (80,85,90,95,98 % H₂O) spiked with refractive index influencing glycerol of 1,5,10,15,20,30 and 50wt-%; to determine the O/S-composition of the nanoemulsion droplets at the different dilution ratios.

A.6.5 SANS-contrast match of NE

| H ₂ O/D ₂ O % | SLD(H ₂ O/D ₂ O) 10^{-6}\AA^{-2} | 80% $\sqrt{\tau} / \text{cm}^{1/2}$ | 85% $\sqrt{\tau} / \text{cm}^{1/2}$ | 90% $\sqrt{\tau} / \text{cm}^{1/2}$ | 98% $\sqrt{\tau} / \text{cm}^{1/2}$ |
|--|--|--|--|--|--|
| 20/80 | 4.98 | 246 | 295 | 152 | 73.1 |
| 40/60 | 3.60 | 172 | 211 | 91.9 | 56.4 |
| 60/40 | 2.21 | 79.4 | 126 | 69.4 | 34.4 |
| 80/20 | 0.83 | 23.5 | 42.5 | 20.5 | 11.7 |

| H ₂ O/D ₂ O % | SLD(H ₂ O/D ₂ O) 10^{-6}\AA^{-2} | 95% $\sqrt{\tau} / \text{cm}^{1/2}$ |
|--|--|--|
| 0/100 | 6.37 | 206 |
| 10/90 | 5.68 | 181 |
| 20/80 | 4.98 | 172 |
| 30/70 | 4.29 | 146 |
| 40/60 | 3.60 | 123 |
| 50/50 | 2.91 | 97.4 |
| 60/40 | 2.21 | 66.4 |
| 70/30 | 1.52 | 47.9 |
| 80/20 | 0.83 | 23.6 |
| 90/10 | 0.13 | 1.16 |
| 100/0 | -0.56 | -22.4 |

Table A.20: Square root of intensities obtained via Guinier approximation (to zero angle q scattering) from SANS-curves of nanoemulsions formed at different dilution ratios (80, 85, 90, 95 and 98wt-% water) and different solvent contrast conditions (H₂O/D₂O). O/S-mixture used for the contrast variation was our model system Tego[®] Wipe DE.

A.6.6 Gibb's Adsorption Isotherm of P4L

The surfactant head group area a_h of polyglycerol-4 laurate was determined by surface tension σ measurements at different surfactant concentrations c_S . From the Gibb's isotherm (σ vs. $\ln(c_S)$) that describes the enrichment and depletion of a solute at the interface of two ideally diluted homogenous phases, the surface concentration γ was derived from the steepest slope of the decreasing surface tension with increasing surfactant concentration. The surfactant head group area is connected with the surface concentration via the Avogadro constant N_A (section 3.2.7.1).

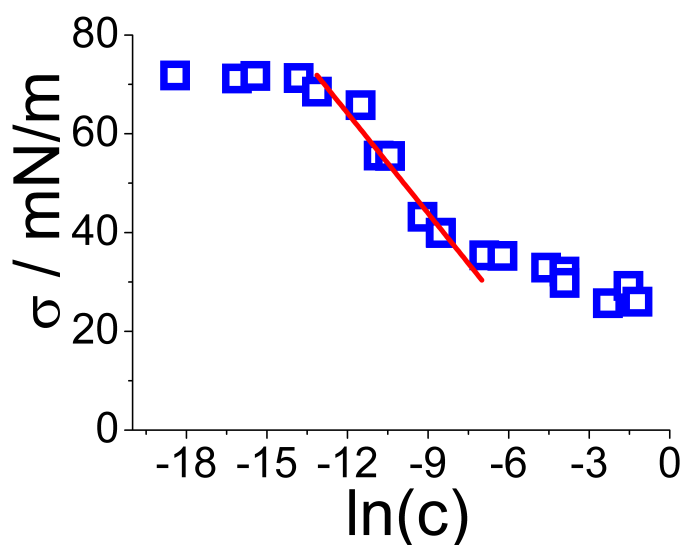


Figure A.12: Gibb's adsorption isotherm of nonionic surfactant polyglycerol-4 laurate P4L, for determination of the surfactant head group area a_h using equation (3.10) and 3.11. The plot visualises the surface tension σ measured with a tensiometer dependent on the employed surfactant concentration c_S given in logarithmic scale $\ln(c_S)$

A.6.7 Individual volume fractions of TW-dilution in nanoemulsion region.

| H ₂ O wt-% | Φ_{theo} | Φ_{actual} | $\Phi_{theo,components}$ | | | |
|--------------------------|---------------|-----------------|--------------------------|--------|--------|--------|
| | | | DEHC | K300 | P4L | DC |
| 80 | 0.2078 | 0.1681 | 0.1372 | 0.0249 | 0.0439 | 0.0018 |
| 85 | 0.1556 | 0.1168 | 0.1027 | 0.0187 | 0.0329 | 0.0014 |
| 90 | 0.1052 | 0.0741 | 0.0694 | 0.0126 | 0.0222 | 0.0009 |
| 95 | 0.0521 | 0.0415 | 0.0344 | 0.0063 | 0.0110 | 0.0005 |
| 98 | 0.0206 | 0.0177 | 0.0136 | 0.0025 | 0.0044 | 0.0002 |

Table A.21: Dilution of Tego[®] Wipe DE concentrate with water H₂O. List of theoretical Φ_{theo} and actual Φ_{actual} volume fraction of the O/S-mixture that is dispersed in water (H₂O). Individual volume fractions $\Phi_{theo,components}$ of the O/S-components (DEHC/K300/P4L/DC (66/12/21.1/~0.9wt-%)).

A.7 NE-encapsulation

A.7.1 Encapsulation of PIC-NE by polycondensation reaction (TDI/DETA).

Analogously to *S. Magdassi et al.* [176] the encapsulation of PIC-formed nanoemulsion droplets was attempted by an interfacial polycondensation reaction using oil-soluble monomer toluene 2,4-diisocyanate (TDI) with water-soluble monomer and crosslinker diethylentriamine (DETA) to form a polymeric shell (polyurea elastomer, eg fig. A.14 -right reaction-arrow) around the nanoemulsion droplets.

As the diisocyanate reacts also non-selectively with hydroxyl groups and hence as well with the surfactant/co-surfactant components in our initial O/S-concentrate (eg. fig. A.14 for isocyanate reactions), we studied the reaction kinetics of the polymerisation processes. For this purpose we added to our model system Tego[®] Wipe DE with 2, 5 and 10wt-% of TDI. Figure A.13a gives an impression about the reaction progress after a couple of minutes (approx. ~ 10 min) after the TDI was added to the O/S-mixture. Their exact kinetics were followed with UV/Vis-turbidity measurements and compared to those of the polycondensation reaction TDI and DETA in pure acetone.

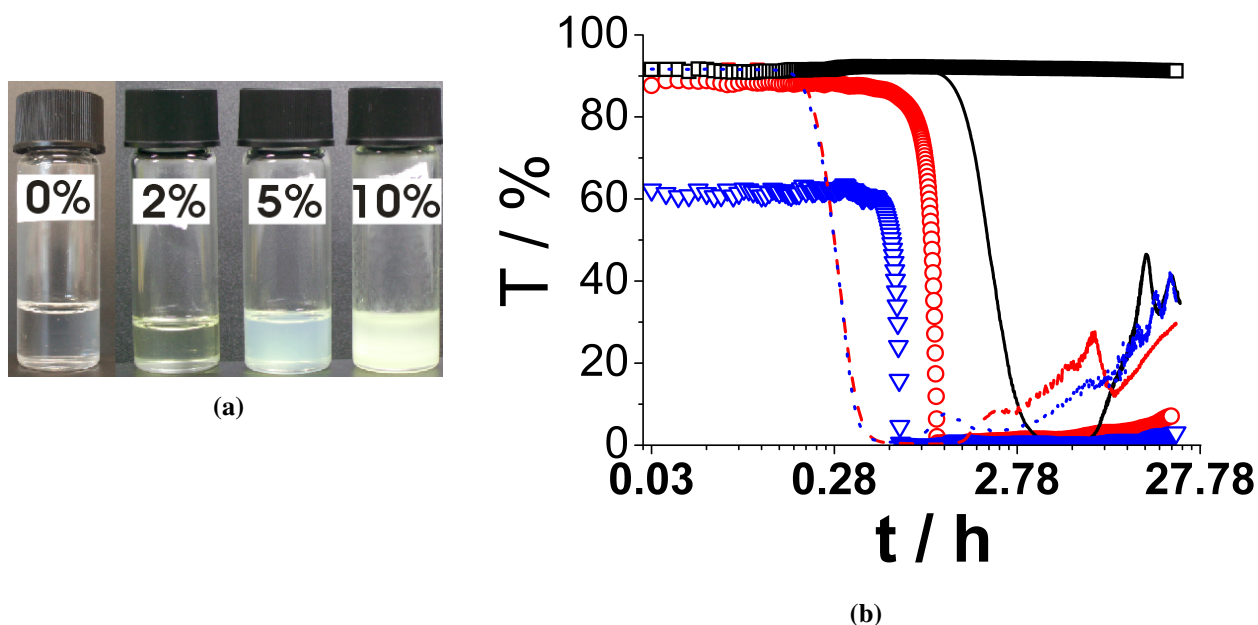


Figure A.13: **a)** Tego[®] Wipe DE (undiluted O/S-concentrate) containing 0, 2, 5 and 10wt-% of toluene 2,4-diisocyanate (TDI). The TDI is reacting with the hydroxyl groups of the surfactant/co-surfactant compounds of the O/S-mixture. Picture was taken approx. 10 min after preparation. **b)** Following the reaction kinetics for the polymerisation of TDI with the hydroxyl groups of the surfactant/cosurfactant compounds employed in the O/S-mixture via UV/Vis-turbidity measurements at $25.0 \pm 0.1^\circ\text{C}$, 626 nm, for 20 hours. O/S-mixture contained \square 2, \circ 5 and ∇ 10wt-% of TDI. Additional measurements for the polyurea condensation reaction of TDI and diethylentriamine (DETA) in acetone. TDI/DETA ratio in acetone was calculated in respect to the relative amounts of the surfactant/cosurfactant employed in the O/S-mixture to fulfill equivalent TDI concentrations of -2 , $-\cdot-\cdot$ 5 and $\cdot\cdot\cdot$ 10wt-%. (TDI in TW symbols, TDI and DETA lines)

The TDI/DETA ratio in acetone was calculated in respect to the relative amounts of the surfactant/cosurfactant employed in the O/S-mixture. From the UV/Vis-measurements we found that the polyurea formation of TDI and DETA proceeds faster than the polymerisation of the diisocyanate with the surfactant/cosurfactant components of the O/S-mixture. Hence, an encapsulation of nanoemulsion droplets formed by the PIC-dilution process might be imaginable, when a rapid dilution of the TDI-spiked O/S-phase with the DETA-solution is intended.

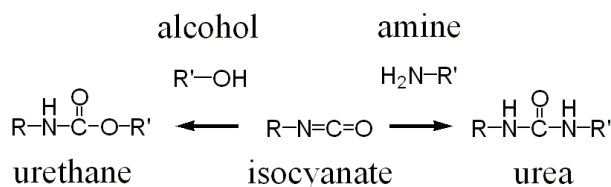


Figure A.14: Possible reactions of isocyanate group in presence of amine and hydroxyl groups.

A.7.2 PH-measurements of NE-encapsulation attempts

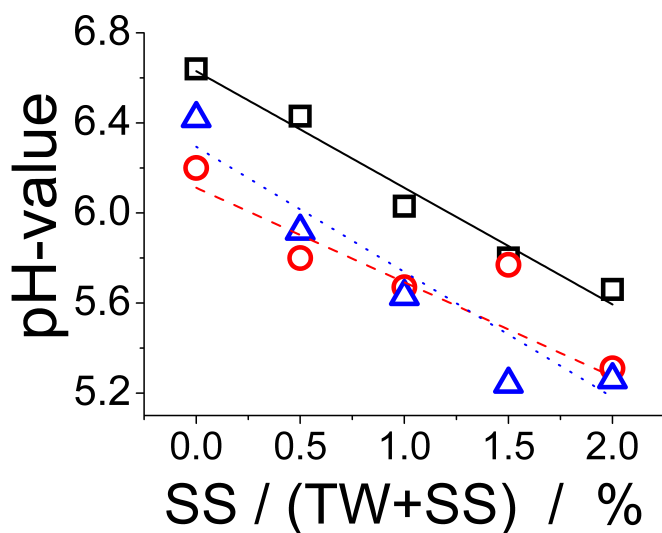


Figure A.15: pH-measurements of nanoemulsion samples based on our model system Tego[®] Wipe DE containing different SS-concentrations that were diluted with an aqueous solution of lysozyme (95wt-% H₂O(lysozyme)) of proper concentrations to obtain charge ratios of $z[\text{cat}^+/\text{an}^-] = \square$ 0.1, \circ 0.2 and \triangle 0.3.

A.7.3 SANS-measurements: Residuals for bimodal data analyses of nanoemulsion encapsulation attempts with surfactant/lysozyme complexes.

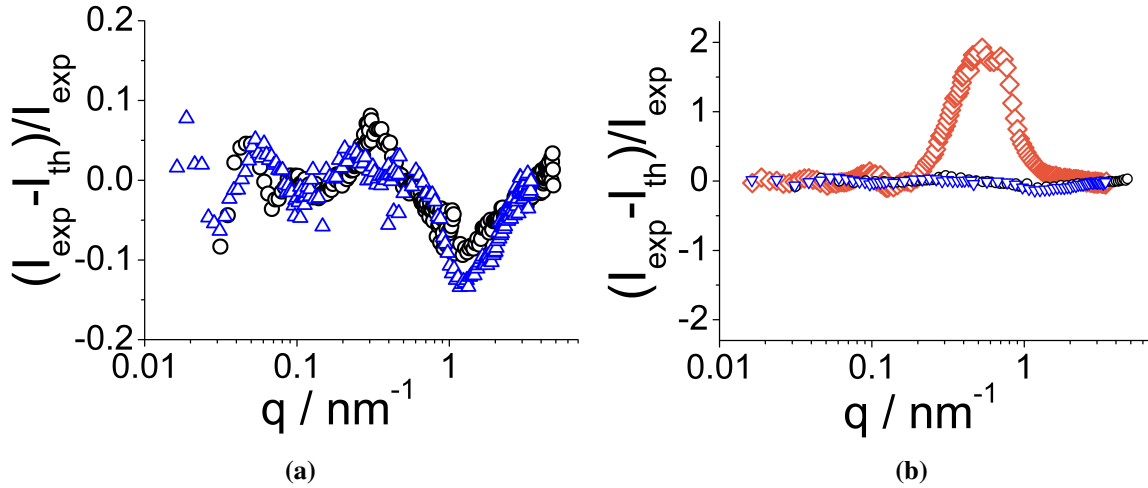


Figure A.16: Residue of SANS-data fits using a bimodal lognormal distributed spherical model for nanoemulsion encapsulation attempts. O/S-mixture (Tego[®] Wipe DE), contained 1wt-% of SS and were diluted with an aqueous lysozyme solution (95wt-% H₂O(lysozyme)) of proper concentrations to obtain charge ratios of $z[\text{lys}^+/\text{SS}^-] = 0.1$ \triangleleft and 0.5 \diamond beside the pure system ($z = 0$ \circ).

A.7.4 SANS - Teubner Strey analysis (SS⁻/lys⁺)

Obtained Teubner-Strey parameters for encapsulation trials of nanoemulsion droplets formed by PIC-dilution process using surfactant/lysozyme interactions to form a shell-like complex at the oil/water interface. For Teubner-Strey SANS-data fit equation (3.21)- (3.25) were used, whereas a_2 , c_1 and c_2 are coefficients of various terms of order parameters in Landaus free energy. Scattering length density difference between oil and water was calculated for the uncapsulated case ($z = 0$) to $6.06 \cdot 10^{-4} \text{ nm}^{-2}$ and also used for the encapsulation trials ($z = 0.1$ and 0.5). fa is the amphiphilicity factor and goes from 1 for a completely disordered solution to -1 for a lamellar structure.

| z | Chi^2 | c_0 | c_2 | V | a_2 | c_1 | ξ_i | D_s | fa |
|------------------------------|----------------|--------------------|-----------------|-----------------|--------|-----------------|---------------|---------------|--------|
| $[\text{lys}^+/\text{SS}^-]$ | | $[\text{cm}^{-1}]$ | $[\text{nm}^4]$ | $[\text{nm}^3]$ | $[\]$ | $[\text{nm}^2]$ | $[\text{nm}]$ | $[\text{nm}]$ | $[\]$ |
| 0 | 0.9994 | 0.074 | 1.04E+08 | 12109 | 344 | 80457 | 30.1 | 235 | 0.21 |
| 0.1 | 0.9987 | 0.106 | 9.11E+06 | 38219 | 51.4 | 150291 | 13.7 | -* | 3.47 |
| 0.5 | 0.9975 | 0.081 | 4.08E+08 | 6109 | 178 | 841070 | 34.4 | -* | 1.56 |

Table A.22: Teubner-Strey parameters for encapsulation trials of nanoemulsions formed via the PIC-process at 95wt-% water, using our model system Tego[®] Wipe DE spiked with 1wt-% of anionic SS and aqueous lysozyme solutions of proper concentrations to reach charge ratios of $z[\text{lys}^+/\text{SS}^-] = 0.1$ and 0.5 . Corresponding SANS-data is given in figure 4.77 of section 4.6. * values result in an non-solvable mathematical expression.

A.8 Mathematical tools

A.8.1 Moments of Log-normal distribution

Naturally particles are rarely uniform in size, shape and mass distribution (monodispersity). A collection of objects with a broad range of these characteristics (polydispersity) can be described by distribution functions (eg. Gaussian, Schulz, Log-normal...).

Following the first four moments (μ) of the Log-normal distribution function, that was used during this work, are given; as they control the most significant characteristics. Thereby the first moment μ_1 represents the mean value of R, the second μ_2 its mean squared-deviation (variance), the third μ_3 and fourth μ_4 its skewness (a measure of the departure from symmetry) and the kurtosis (or flatness) of the distribution. A detailed derivation of all four moments for other distribution functions are given by Clarke *et al.* [205].

$$\int f(x)dx = 1 \quad (\text{A.1a})$$

$$\mu_1 = \int xf(x)dx = \bar{R} \quad (\text{A.1b})$$

$$\mu_2 = \int x^2 f(x)dx = \sigma_s^2 \quad (\text{A.1c})$$

$$\mu_3 = \int x^3 f(x)dx = \frac{\sigma_s}{\bar{R}} \cdot \left(3 + \frac{\sigma_s^2}{\bar{R}^2} \right) \quad (\text{A.1d})$$

$$\mu_4 = \int x^4 f(x)dx = 16 \frac{\sigma_s^2}{\bar{R}^2} + 15 \frac{\sigma_s^4}{\bar{R}^4} + 6 \frac{\sigma_s^6}{\bar{R}^6} + \frac{\sigma_s^8}{\bar{R}^8} \quad (\text{A.1e})$$

$$\text{with } x = R - \bar{R}$$

$$\text{and } \sigma_s = R_M \sigma_0 \left[\exp(4\sigma_0^2) - \exp(3\sigma_0^2) \right]^{1/2} \quad (\text{A.1f})$$

\bar{R} being the number weighted radius obtained during fit of scattering curves with a polydisperse model. R_M is the modal size parameter and is related to \bar{R} by $\ln \bar{R} = \ln R_M + 3\sigma_0^2/2$ with σ_0 the distribution breath parameter and σ_s the standard deviation (eg. eq. (A.1f)).

A.8.1.1 Areas-averaged radii ($R_{Mw,A}$) via the first three moments of Log-normal distribution function.

The averaged squared radius $R_{Mw,A}$ is accessible via the first three moments of a distribution function $f(R)$, due to equation (A.2):

$$\langle R \rangle_{M_w} = \frac{\bar{R}^3 \int f(x)dx + 3\bar{R}^2 \int xf(x)dx + 3\bar{R} \int x^2 f(x)dx + \int x^3 f(x)dx}{\bar{R}^2 \int f(x)dx + 2\bar{R} \int xf(x)dx + \int x^2 f(x)dx} \quad (\text{A.2})$$

A.8.1.2 Volume-averaged radii (R_{M_w}) via the first four moments of Log-normal distribution function.

The mass weighted radii R_{M_w} are accessible via the first four moments of a distribution function $f(R)$, due to equation (A.3):

$$\langle R \rangle_{M_w} = \frac{\bar{R}^4 \int f(x)dx + 4\bar{R}^3 \int xf(x)dx + 6\bar{R}^2 \int x^2 f(x)dx + 4\bar{R} \int x^3 f(x)dx + \int x^4 f(x)dx}{\bar{R}^3 \int f(x)dx + 3\bar{R}^2 \int xf(x)dx + 3\bar{R} \int x^2 f(x)dx + \int x^3 f(x)dx} \quad (\text{A.3})$$

Appendix B

List of abbreviations

B.1 General

| | | |
|-----------|-------|---|
| #C | | number of C-atoms |
| 1D and 2D | | one and two dimensional |
| A | | amplitude <i>or</i> fraction |
| a_h | | surfactant head group area |
| abbr. | | abbreviation |
| Agg. | | aggregate |
| A_s | | specific surface area |
| b | | bound coherent scattering length |
| bkg | | background |
| BB | | berger baller mixer |
| BHS | | bimodal lognormal distributed spherical model |
| c | | concentration |
| C | | solubility |
| cmc | | critical micelle concentration |
| cryo-TEM | | cryogenic transmission electron microscopy |
| d | | thickness |
| db | | doublet |
| D | | diffusion coefficient |
| dn/dc_g | | refractive index increment |
| D_s | | periodicity |
| EI | | electron impact ionization |
| ESRF | | European Synchrotron Radiation Facility |
| fa | | amphiphilicity |
| FWHM | ... | Full Width at Half Maximum |
| G | | Gordon parameter |
| GC | | gas chromatography |

| | | |
|------------------------|-------|---|
| HDS | | high density mixer |
| HLB | | H ydrophilic- L ipophilic- B alances |
| HS | | hard sphere <i>or</i> monomodal lognormal distributed spherical model |
| HZB | | Helmholtz-Zentrum Berlin |
| I | | intensity |
| ILL | | Institut Laue-Langevin |
| ind. | | industrial |
| L | | length |
| LCST | | L ower C ritical S olution T emperature |
| LSS | | Large Scale Structure Group |
| m | | multiple phase region |
| MS | | mass spectroscopy |
| Mw | | molecular weight |
| NE | | nanoemulsion |
| NMR | | nuclear magnetic resonance spectroscopy |
| ^1N | | number density |
| $n^{25^\circ\text{C}}$ | | refractivity at 25°C |
| o | | oil |
| O/S | | Oil-Surfactant |
| o/w | | oil-in-water |
| o/w/o | | oil-in-water-in-oil |
| PIC | | P hase I nversion C oncentration |
| PIT | | P hase I nversion T emperature |
| PSQ | | P hase S hift by Q uenching |
| P(q) | | form factor |
| Q | | invariant |
| q | | scattering vector |
| r <i>or</i> R | | particle radius |
| $R_{n,Mw}$ | | mass weighted radius of population n (n = 1,2) |
| $R_{n,N}$ | | number weighted radius of population n (n = 1,2) |
| R_G | | radius of gyration |
| S | | surfactant |
| SANS | | S mall A ngle N eutron S cattering |
| SAXS | | S mall A ngle X -ray S cattering |
| SF | | stopped flow |
| SD | | Sample-to-Detector distance |
| SLD | | scattering length density |
| solv | | solvent |
| sph | | sphere |

S(q) structure factor
T temperature *or* transmittance
t time
TLC thin-layer chromatography
tp triplet
TS Teubner-Strey
TUB Technische Universität Berlin
UCST **U**pper **C**ritical **S**olution **T**emperature
USAXS **U**ltra **S**mall **A**ngle **X**-ray **S**cattering
V_m molar volume
V_p volume of one particle
w water
w/o water-in-oil
w/o/w water-in-oil-in-water
WAXS **W**ide **A**ngle **X**-ray **S**cattering
xi correlation length
z charge
Z atomic number
ZP zeta potential

B.2 Chemical substances

AOT 2-octyl sodium sulfosuccinate
CC 2-octylcarbonate (Cetiol CC)
DC dilauryl citrate
DEHC 2-ethylhexyl carbonate
DETA diethylentriamine
d-DEHC d₃₄-2-ethylhexyl carbonate
h-DEHC h₃₄-2-ethylhexyl carbonate
EH d₁₇-2-ethylhexanol
EQ 2-oleic acidyl isopropylester 2-methylammonium Methosulfate (Rewoquat CR 3099)
K300 Euxyl[®] K300
L31 Pluronic L31
lys lysozyme
OO Octyloctanoate
P4L polyglycerol-4 laurate
PB parabene
PhOH phenoxy ethanol

| | | |
|-----|-------|---|
| PEO | | polyethylene oxide |
| PGL | | 1,2-diacyl-sn-glycerol-3-phospho-L-serine sodium salt |
| PPO | | polypropylene oxide |
| SCO | | sulfonated castor oil, Na salt (Hydriosul HRN 100) |
| SS | | 2-sodium laureth sulfosuccinate (Rewopol SB FA 30) |
| TW | | Tego [®] Wipe DE |
| TDI | | toluene 2,4-diisocyanate |

B.3 Greek letters and mathematical abbreviations and physical constants

| | | |
|---------------------|-------|---|
| ΔH_{vap} | | energy of vaporization |
| δ | | Hildebrand parameter <i>or</i> chemical shift in NMR |
| η | | dynamic viscosity |
| κ | | conductivity |
| k_B | | Boltzmann constant: $k_B = 1.381 \cdot 10^{-23}$ J/K |
| γ | | surfactant concentration at the interface |
| λ | | wavelength |
| lg | | logarithm to the base 10 |
| ln | | natural logarithm |
| μE | | microemulsion |
| Mw | | molecular weight |
| N_A | | Avogadro constant: $N_A = 6.022 \times 10^{23}$ mol ⁻¹ |
| ν | | kinematic viscosity |
| Φ | | phase <i>or</i> volume fraction of particles |
| R | | Gas constant: $R = N_A \cdot k_B = 8.314$ J/(mol · K) |
| r_e | | electron radius: $r_e = 2.81 \cdot 10^{-5}$ Å |
| $\rho^{25^\circ C}$ | | density at 25°C |
| σ | | polydispersity <i>or</i> surface tension |
| Σ -formula | | sum formula |
| τ | | turbidity coefficient <i>or</i> relaxation time |
| wt-% | | weight fraction |
| ξ_i | | correlation length |

Bibliography

- [1] *BioLogic Science Instruments*: <http://www.bio-logic.info/index.html>, 13.05.2011.
- [2] <http://www.esrf.fr/UsersAndScience/Experiments/SoftMatter/ID02/BeamlineLayout>, 15.06.2011.
- [3] <http://www.esrf.fr/UsersAndScience/Experiments/SoftMatter/ID02/BeamlineLayout/EH2>, 15.07.2011.
- [4] *Large dynamic range small-angle diffractometer D22 (ILL)*: <http://www.ill.eu/instruments-support/instruments-groups/instruments/d22/documentation/stopped-flow/>, 13.05.2011.
- [5] S. Alay, F. Gode, and C. Alkan. Synthesis and thermal properties of poly(n-butyl acrylate)/n-hexadecane microcapsules using different cross-linkers and their application to textile fabrics. *Journal Of Applied Polymer Science*, 120:2821–2829, 2011.
- [6] J. Allouche, E. Tyrode, V. Sadtler, L. Choplin, and J.L. Salager. Simultaneous conductivity and viscosity measurements as a technique to track emulsion inversion by the phase-inversion-temperature method. *Langmuir*, 20:2134–2140, 2004.
- [7] N. Anton, J.P. Benoit, and P. Saulnier. Design and production of nanoparticles formulated from nano-emulsion templates - a review. *J. Controlled Release*, 128:185–199, 2008.
- [8] M. Antonietti and K. Landfester. Polyreactions in miniemulsions. *Prog. Polym. Sci.*, 27:689–757, 2002.
- [9] N.W. Ashcroft and J. Lekner. Structure and resistivity of liquid metals. *Phys. Rev.*, 145:83–90, 1966.
- [10] W.D. Bancroft. The theory of emulsification. i. *J. Phys. Chem.*, 16:177–233, 1912.
- [11] A. Barth, I. Grillo, and M. Gradzielski. Dynamics of formation of vesicles studied by highly time-resolved stopped-flow experiments. *Tenside Surf. Det.*, 47:300–306, 2010.
- [12] L. Belkoura, C. Stubenrauch, and R. Strey. Freeze fracture direct imaging: A new freeze fracture method for specimen preparation in cryo-transmission electron microscopy. *Langmuir*, 20:4391–4399, 2004.

- [13] S. Benita and M.Y. Levy. Submicron emulsions as colloidal drug carriers for intravenous administration - comprehensive physicochemical characterization. *J. Pharm. Sci.*, 82:1069–1079, 1993.
- [14] B.P. Binks. *Modern Aspects of Emulsion Science*. 1998.
- [15] B.P. Binks and J. Dong. Emulsions and equilibrium phase behaviour in silicone oil plus water plus nonionic surfactant mixtures. *Colloids Surf., A*, 132:289–301, 1998.
- [16] K. Bouchemal, S. Briancon, E. Perrier, and H. Fessi. Nano-emulsion formulation using spontaneous emulsification: solvent, oil and surfactant optimisation. *Int. J. Pharm.*, 280:241–251, 2004.
- [17] F. Bracher and T. Litz. The reagent .15. bis(trichloromethyl)carbonate (triphosgene). *J. Prak. Chemie*, 337:516–518, 1995.
- [18] S. Brösel and H. Schubert. Investigations on the role of surfactants in mechanical emulsification using a high-pressure homogenizer with an orifice valve. *Chem. Eng. Process*, 38:533–540, 1999.
- [19] R.M. Burk and M.B. Roof. A safe and efficient method for conversion of 1,2-diols and 1,3-diols to cyclic carbonates utilizing triphosgene. *Tetrahedron Lett.*, 34:395–398, 1993.
- [20] K. Buszello and B.W. Müller. *Pharmaceutical Emulsions and Suspensions*. 2000.
- [21] H.J. Butt, K. Graf, and M. Kappl. *Physics and Chemistry of Interfaces*. 2006.
- [22] L.J. Cayias, R.S. Schechter, and W.H. Wade. Measurement of low interfacial-tension via spinning drop technique. *Adv. Chem. Series*, pages 234–247, 1975.
- [23] S.H. Chen. Small-angle neutron-scattering studies of the structure and interaction in micellar and microemulsion systems. *Annu. Rev. Phys. Chem.*, 37:351–399, 1986.
- [24] S.H. Chen, S.L. Chang, and R. Strey. Structural evolution within the one-phase region of a 3-component microemulsion system - water-n-decane-sodium-bis-ethylhexylsulfosuccinate (aot). *J. Chem. Phys.*, 93:1907–1918, 1990.
- [25] L.Y. Chu, T. Yamaguchi, and S. Nakao. A molecular-recognition microcapsule for environmental stimuli-responsive controlled release. *Adv. Mater.*, 14:386–389, 2002.
- [26] K.D. Collins and M.W. Washabaugh. The hofmeister effect and the behavior of water at interfaces. *Q. Rev. Biophys.*, 18:323–422, 1985.
- [27] P.P. Constantinides and J.P. Scalart. Formulation and physical characterization of water-in-oil microemulsions containing long- versus medium-chain glycerides. *Int. J. Pharm.*, 1:57–68, 1997.

- [28] J.T. Davies and E.K. Rideal. *Diffusion through Interfaces*. Interfacial Phenomena. Academic Press, New York, 1961.
- [29] P. Debye, H.R. Anderson, and H. Brumberger. Scattering by an inhomogeneous solid .ii. the correlation function and its application. *J. Appl. Phys.*, 28:679–683, 1957.
- [30] G. Decher and J.D. Hong. Buildup of ultrathin multilayer films by a self-assembly process: I. consecutive adsorption of anionic and cationic bipolar amphiphiles on charged surfaces. *Makromolekulare Chemie-Macromolecular Symposia*, 46:321–327, 1991.
- [31] B. Deminiere, A. Colin, F. Leal Calderon, and J. Bibette. *Modern Aspects of Emulsion Science*. 1998.
- [32] O. Diat and D. Roux. Effect of shear on dilute sponge phase. *Langmuir*, 11:1392–1395, 1995.
- [33] H. Eckert and B. Forster. Triphosgene, a crystalline phosgene substitute. *Angew. Chem., Int. Ed.*, 26:894–895, 1987.
- [34] M.S. El-Aasser, C.D. Lack, J.W. Vanderhoff, and F.M. Fowkes. The miniemulsification process - different form of spontaneous emulsification. *Colloids Surf.*, 29:103–118, 1988.
- [35] M.S. El-Aasser and E.D. Sudol. *Miniemulsions: Overview of research and applications*, volume 1. Federation Soc Coatings Technology, 2004.
- [36] H. Elias, S. Lorenz, and G. Winner. Das experiment: 100 jahre nernstscher verteilungssatz. *Chem. Unserer Zeit*, 26:70–75, 1992.
- [37] T. Engels, T. Förster, and W. von Rybinski. The influence of coemulsifier type on the stability of oil-in-water emulsions. *Colloids Surf., A*, 99:141–149, 1995.
- [38] H. Essawy and K. Tauer. Polyamide capsules via soft templating with oil drops-1. morphological studies of the capsule wall. *Colloid Polym. Sci.*, 288:317–331, 2010.
- [39] O. Faust. Analysis of birefringence of cellulose containing gels. *Kolloid-Zeitschrift*, 41:54–55, 1927.
- [40] P. Fernandez, V. Andre, J. Rieger, and A. Kuhnle. Nano-emulsion formation by emulsion phase inversion. *Colloids Surf., A*, 251:53–58, 2004.
- [41] P. Finkle, H.D. Draper, and J.H. Hildebrand. The theory of emulsification. *J. Am. Chem. Soc.*, 45:2780–2788, 1923.
- [42] A. Fleming. On the antibacterial action of cultures of a penicillium, with special reference to their use in the isolation of b. influenzae. *Br. J. Exp. Pathology*, 10:226–236, 1929.

- [43] A. Forgiarini, J. Esquena, C. Gonzalez, and C. Solans. Formation and stability of nano-emulsions in mixed nonionic surfactant systems. *Trends Colloid Interface Sci.* Xv, 118:184–189, 2001.
- [44] A. Forgiarini, J. Esquena, C. Gonzalez, and C. Solans. Formation of nano-emulsions by low-energy emulsification methods at constant temperature. *Langmuir*, 17:2076–2083, 2001.
- [45] T. Forster, W. von Rybinski, and A. Wadle. Influence of microemulsion phases on the preparation of fine-disperse emulsions. *Adv. Colloid Interface Sci.*, 58:119–149, 1995.
- [46] T. Förster, F. Schambil, and W. von Rybinski. Production of fine disperse and long-term stable oil-in-water emulsions by the phase inversion temperature method. *J. Dispersion Sci. Technol.*, 13:183–193, 1992.
- [47] N.A. Fuks and A.G. Sutugin. *Rus. Chem. Rev.*, 34:116–129, 1965.
- [48] Gad. *J. Arch. Anat. Phys.*, page 181, 1878.
- [49] S. Gasic, B. Jovanovic, and S. Jovanovic. The stability of emulsions in the presence of additives. *J. Serb. Chem. Soc.*, 67:31–39, 2002.
- [50] W.M. Gelbart, A. Ben-Shaul, and D. Roux. *Micelles, membranes, microemulsions and monolayers*. 1994.
- [51] S. Giessler-blank, R. Scheuermann, J. Venzmer, and D. Lindsay. Nanoemulsions and processes for their preparation, and their use as formulations of plant protection agents and/or pesticides and/or cosmetic preparations, 2010.
- [52] S. Giessler-blank, R. Scheuermann, J. Venzmerand, and D. Lindsay. Nano-emulsions and method of producing them, and their use as formulations for plant protection and/or to fight pests and/or cosmetic preparations, 2010.
- [53] E.S.R. Gopal. *Emulsion Science*. Academic Press, London and New York, 1968.
- [54] L. Goracci, L. Brinchi, R. Germani, and G. Savelli. Easy and efficient procedure for preparation of symmetric organic carbonates in ionic liquid. *Lett. Org. Chem.*, 3:530–533, 2006.
- [55] J.E. Gordon. *The organic chemistry of electrolyte solutions*. 1975.
- [56] M. Gradzielski and H. Hoffmann. *Handbook of Microemulsion Science and Technology*. 1999.

- [57] M. Gradzielski, D. Langevin, and B. Farago. Experimental investigation of the structure of nonionic microemulsions and their relation to the bending elasticity of the amphiphilic film. *Phys. Rev. E*, 53:3900–3919, 1996.
- [58] M. Gradzielski, D. Langevin, T. Sottmann, and R. Strey. Small angle neutron scattering near the wetting transition: Discrimination of microemulsions from weakly structured mixtures. *J. Chem. Phys.*, 104:3782–3787, 1996.
- [59] R.W. Greiner and D.F. Evans. Spontaneous formation of a water-continuous emulsion from a w/o microemulsion. *Langmuir*, 6:1793–1796, 1990.
- [60] I. Grillo. Small-angle neutron scattering study of a world-wide known emulsion: Le pastis. *Colloids Surf., A*, 225:153–160, 2003.
- [61] I. Grillo. Applications of stopped-flow in saxs and sans. *Curr. Opin. Colloid Interface Sci.*, 14:402–408, 2009.
- [62] Y.X. Gu, Y.H. Huang, B. Liao, S. Zhao, and G.M. Cong. The effect of solvent polarity on phase inversion process for emulsification of poly(phenylene oxide) (ppo) ionomer. *Eur. Polym. J.*, 36:1477–1482, 2000.
- [63] A. Guinier and G. Fournet. *Small angle scattering of X-rays*. 1955.
- [64] J. Gummel, M. Sztucki, T. Narayanan, and M. Gradzielski. Concentration dependent pathways in spontaneous self-assembly of unilamellar vesicles. *Soft Matter*, 7:5731–5738, 2011.
- [65] X.M. Guo, Z.M. Rong, and X.G. Ying. Calculation of hydrophile-lipophile balance for polyethoxylated surfactants by group contribution method. *J. Colloid Interface Sci.*, 298:441–450, 2006.
- [66] J.M. Gutierrez, C. Gonzalez, A. Maestro, I. Sole, C.M. Pey, and J. Nolla. Nano-emulsions: New applications and optimization of their preparation. *Curr. Opin. Colloid Interface Sci.*, 13:245–251, 2008.
- [67] C.M. Hansen and K. Skaarup. The three dimensional solubility parameter - key to paint component affinities iii. - independent calculation of the parameter components. *J. Paint. Technol.*, 39:511–514, 1967.
- [68] W. Helfrich. Lyotropic lamellar phases. *J. Phys.: Condens. Matter*, 6:A79–A92, 1994.
- [69] P.C. Hiemenz and R. Rajagopalan. *Principles of Colloid and Surface Chemistry, 3rd Edition*. 1997.
- [70] J.H. Hildebrand. Solubility xii regular solutions. *J. Am. Chem. Soc.*, 51:66–80, 1929.

- [71] J.H. Hildebrand. Order from chaos. *Science*, 150:441–450, 1965.
- [72] J.H. Hildebrand and R.L. Scott. *Solubility of Non-Electrolytes*. Reinhold, Dover, New York, 1964.
- [73] K. Hirai, M. Tomida, Y. Kikuchi, O. Ueda, H. Ando, and N. Asanuma. Effects of deuterium oxide on streptococcus mutans and pseudomonas aeruginosa. *Bull Tokyo Dent Coll*, 51:175–83, 2010.
- [74] S. Hoeller, A. Sperger, and C. Valenta. Lecithin based nanoemulsions: A comparative study of the influence of non-ionic surfactants and the cationic phytosphingosine on physicochemical behaviour and skin permeation. *Int. J. Pharm.*, 370:181–186, 2009.
- [75] W. A. Hoffman. A convenient preparation of carbonates from alcohol and carbon dioxide. *J. Org. Chem.*, 47:5209–5210, 1982.
- [76] H. Hoffmann, C. Thunig, U. Munkert, H.W. Meyer, and W. Richter. From vesicles to the I3 (sponge) phase in alkyldimethylamine oxide heptanol systems. *Langmuir*, 8:2629–2638, 1992.
- [77] H. Hoffmann and W. Ulbricht. Transition of rodlike to globular micelles by the solubilization of additives. *J. Colloid Interface Sci.*, 129:388–405, 1989.
- [78] K. Holmberg, B. Jönsson, B. Kronberg, and B. Lindman. *Surfactants and polymers in aqueous solution*. 2003.
- [79] F.M. Mims III. How to analyze scientific images. *Country Scientist*, 18:42–44, 2009.
- [80] P. Izquierdo, J. Esquena, T.F. Tadros, C. Dederen, M.J. Garcia, N. Azemar, and C. Solans. Formation and stability of nano-emulsions prepared using the phase inversion temperature method. *Langmuir*, 18:26–30, 2002.
- [81] P. Izquierdo, J. Feng, J. Esquena, T.F. Tadros, J.C. Dederen, M.J. Garcia, N. Azemar, and C. Solans. The influence of surfactant mixing ratio on nano-emulsion formation by the pit method. *J. Colloid Interface Sci.*, 285:388–394, 2005.
- [82] B. Jacrot. The study of biological structures by neutron-scattering from solution. *Rep. Prog. Phys.*, 39:911–953, 1976.
- [83] D.D. Joseph, M.S. Arney, G. Gilberg, H. Hu, D. Hultman, C. Verdier, and T.M. Vinagre. A spinning drop tensioextensometer. *J. Rheol*, 36:621–662, 1992.
- [84] U. Keiderling. The new 'bersans-pc' software for reduction and treatment of small angle neutron scattering data. *Appl. Phys. A: Mater. Sci. Process.*, 74:1455–1457, 2002.

- [85] J.A. Kenar, G. Knothe, and A.L. Copes. Synthesis and characterization of dialkyl carbonates prepared from mid-, long-chain, and guerbet alcohols. *J. Am. Oil Chem. Soc.*, 81:285–291, 2004.
- [86] M.M. Kozlov and W. Helfrich. Effects of a cosurfactant on the stretching and bending elasticities - a surfactant monolayer. *Langmuir*, 8:2792–2797, 1992.
- [87] P. M. Kruglyakov. *Hydrophile-lipophile balance of surfactants and solid particles: physicochemical aspects and applications*. Elsevier Science, Netherlands, 2000.
- [88] D.E. Kuehner, J. Engmann, F. Fergg, M. Wernick, H.W. Blanch, and J.M. Prausnitz. Lysozyme net charge and ion binding in concentrated aqueous electrolyte solutions. *J. Phys. Chem. B*, 103:1368–1374, 1999.
- [89] F. Lachampt and R.M. Vila. A contribution to the study of emulsions. *Am. Perfum., Cosmet.*, 82:29–36, 1967.
- [90] S. Lamaallam, H. Bataller, C. Dicharry, and J. Lachaise. Formation and stability of miniemulsions produced by dispersion of water/oil/surfactants concentrates in a large amount of water. *Colloids Surf., A*, 270:44–51, 2005.
- [91] K. Landfester. Polyreactions in miniemulsions. *Macromol. Rapid Commun.*, 22:896–936, 2001.
- [92] K. Landfester, J. Eisenblatter, and R. Rothe. Preparation of polymerizable miniemulsions by ultrasonication. *JCT Res.*, 1:65–68, January 2004.
- [93] L.T. Lee, D. Langevin, and R. Strey. Relationship between microemulsion structure and surfactant layer bending elasticity. *Physica A*, 168:210–219, 1990.
- [94] Z.X. Li, J.R. Lu, R.K. Thomas, and J. Penfold. Neutron reflectivity studies of the adsorption of aerosol-ot at the air-water interface: The structure of the sodium salt. *J. Phys. Chem. B*, 101:1615–1620, 1997.
- [95] H.A. Lieberman and M.M. Rieger. *Pharmaceutical Dosage Forms: Disperse systems*. Marcel Dekker, New York, 1998.
- [96] I.M. Lifshitz and V.V. Slezov. Kinetics of diffusive decomposition of supersaturated solid solutions. *Soviet Physics JETP-USSR*, 8:331–339, 1959.
- [97] R.C. Little. Correlation of surfactant hydrophile-lipophile balance (hlb) with solubility parameter. *J. Colloid Interface Sci.*, 65:587–588, 1978.
- [98] W.R. Liu, D.J. Sun, C.F. Li, Q. Liu, and H. Xu. Formation and stability of paraffin oil-in-water nano-emulsions prepared by the emulsion inversion point method. *J. Colloid Interface Sci.*, 303:557–563, 2006.

- [99] L. Livius and H. Eckert. *Phosgenations - A Handbook*. 2004.
- [100] R.A. Mackay. *Nonionic Surfactants: Physical Chemistry*. M.J. Schick, 1987.
- [101] A. Maestro, I. Sole, C. Gonzalez, C. Solans, and J.M. Gutierrez. Influence of the phase behavior on the properties of ionic nanoemulsions prepared by the phase inversion composition method. *J. Colloid Interface Sci.*, 327:433–439, 2008.
- [102] A. Manosroi, P. Wongtrakul, J. Manosroi, H. Sakai, F. Sugawara, M. Yuasa, and M. Abe. Characterization of vesicles prepared with various non-ionic surfactants mixed with cholesterol. *Colloids Surf., A*, 30:129–138, 2003.
- [103] S. Matsumoto and P. Sherman. A dta technique for identifying phase inversion temperature of o/w emulsions. *J. Coll. Int. Sci.*, 33:294–298, 1970.
- [104] D.J. McClements. Edible nanoemulsions: fabrication, properties, and functional performance. *Soft Matter*, 6:2297–2316, 2011.
- [105] D.J. McClements and S.R. Dungan. Factors that affect the rate of oil exchange between oil-in-water emulsion droplets stabilized by a nonionic surfactant - droplet size, surfactant concentration, and ionic-strength. *J. Phys. Chem. A*, 97:7304–7308, 1993.
- [106] D.J. McClements, S.R. Dungan, J.B. German, and J.E. Kinsella. Factors which affect oil exchange between oil-in-water emulsion droplets stabilized by whey-protein isolate - protein-concentration, droplet size and ethanol. *Colloids Surf., A*, 81:203–210, 1993.
- [107] J.E. McMurry. *Fundamentals of Organic Chemistry*. 5th ed. - Australia ; Pacific Grove, CA, USA : Thomson-Brooks/Cole, 2003.
- [108] J. Meyer, G. Polak, and R. Scheuermann. Preparing pic emulsion with a very fine particle size. *Cosmetics & Toiletries* [®]magazine, 121:1–10, 2006.
- [109] J. Meyer, G. Polak, and R. Scheuermann. Preparing pic emulsions with a very fine particle size. *Cosmetic & Toiletries* [®]magazine, 1:63–68, 2007.
- [110] J. Meyer, G. Polak, R. Scheuermann, and M. Plesch. The easiest way to nanoemulsions: Pic emulsion technology. In *SEPAWA Congress, Würzburg*, 2006.
- [111] J. Meyer, R. Scheuermann, and J. Venzmer. Method of producing finely divided oil-in-water emulsions, 2008.
- [112] M. Minana-Perez, C. Gutron, C. Zundel, J.M. Anderez, and J.L. Salager. Miniemulsion formation by transitional inversion. *J. Dispersion Sci. Technol.*, 20:893–905, 1999.

- [113] D. Morales, J.M. Gutierrez, M.J. Garcia-Celma, and C. Solans. A study of the relation between bicontinuous microemulsions and oil/water nano-emulsion formation. *Langmuir*, 19:7196–7200, 2003.
- [114] M. L. Moya, A. Rodriguez, M. D. Graciani, and G. Fernandez. Role of the solvophobic effect on micellization. *J. Colloid Interface Sci.*, 316:787–795, 2007.
- [115] T. Nakagawa. *Nonionic Surfactants*. M.J. Schick, 1966.
- [116] H. Nakajima. *Industrial Applications of Microemulsions: 8 Microemulsions in Cosmetics*, volume 66. Marcel Dekker, Inc. (New York), 1997.
- [117] F. Nallet, R. Laversanne, and D. Roux. Modeling x-ray or neutron-scattering spectra of lyotropic lamellar phases - interplay between form and structure factors. *J.Phys. II*, 3:487–502, 1993.
- [118] T. Narayanan, O. Diat, and P. Bosecke. Saxs and usaxs on the high brilliance beamline at the esrf. *Nuclear Instruments & Methods In Physics Research Section A-Accelerators Spectrometers Detectors And Associated Equipment*, 467:1005–1009, 2001.
- [119] S. Nave, J. Eastoe, R.K. Heenan, D. Steytler, and I. Grillo. What is so special about aerosol-ot? ii. microemulsion systems. *Langmuir*, 16(23):8741–8748, November 2000.
- [120] S. Nave, J. Eastoe, R.K. Heenan, D. Steytler, and I. Grillo. What is so special about aerosol-ot? part iii-glutaconate versus sulfosuccinate headgroups and oil-water interfacial tensions. *Langmuir*, 18:1505–1510, 2002.
- [121] S. Nave, J. Eastoe, and J. Penfold. What is so special about aerosol-ot? i. aqueous systems. *Langmuir*, 16:8733–8740, 2000.
- [122] S. Nave, A. Paul, J. Eastoe, A.R. Pitt, and R.K. Heenan. What is so special about aerosol-ot? part iv. phenyl-tipped surfactants. *Langmuir*, 21:10021–10027, 2005.
- [123] P. Panine, S. Finet, T.M. Weiss, and T. Narayanan. Probing fast kinetics in complex fluids by combined rapid mixing and small-angle x-ray scattering. *Adv. Colloid Interface Sci.*, 127:9–18, 2006.
- [124] C. Parkinson and P. Sherman. Phase inversion temperature as an accelerated method for evaluating emulsion stability. *J. Coll. Int. Sci.*, 41:328–330, 1972.
- [125] J.K. Percus and G.J. Yevick. Analysis of classical statistical mechanics by means of collective coordinates. *Phys. Rev.*, 110:1–13, 1958.
- [126] J.F. Perez-Benito and C. Arias. Occurrence of colloidal manganese-dioxide in permanganate reactions. *J. Colloid Interface Sci.*, 152:70–84, 1992.

- [127] W.J. Perram. Hard-sphere correlation-functions in percus-yevick approximation. *Mol. Phys.*, 30:1505–1509, 1975.
- [128] J.P. Perrine, M. Thivent, and F.V. Völker. The pulsed power converter and septum magnet system for injection into the electron storage ring at esrf. In *5th European Particle Accelerator Conference*, pages 2394–2396, 1996.
- [129] C.M. Pey, A. Maestro, I. Sole, C. Gonzalez, C. Solans, and J.M. Gutierrez. Optimization of nano-emulsions prepared by low-energy emulsification methods at constant temperature using a factorial design study. *Colloids Surf., A*, 288:144–150, 2006.
- [130] H. Pleiner and H.R. Brand. Flow birefringence in the sponge phase. *Europhysics Letters*, 15:393–397, 1991.
- [131] M. Porras, C. Solans, C. Gonzalez, and J.M. Gutierrez. Properties of water-in-oil (w/o) nano-emulsions prepared by a low-energy emulsification method. *Colloids Surf., A*, 324:181–188, 2008.
- [132] M. Porras, C. Solans, C. Gonzalez, A. Martinez, A. Guinart, and J.M. Gutierrez. Studies of formation of w/o nano-emulsions. *Colloids Surf., A*, 249:115–118, 2004.
- [133] L.M. Prince. A theory of aqueous emulsions .i. negative interfacial tension at oil/water interface. *J. Colloid Interface Sci.*, 23:165–173, 1967.
- [134] H.M. Princen, I.Y.Z. Zia, and S.G. Mason. Measurement of interfacial tension from shape-of a rotating drop. *J. Colloid Interface Sci.*, 23:99–107, 1967.
- [135] Z.E. Proverbio, S.M. Bardavid, E.L. Aranciba, and P.C. Schulz. Hydrophile–lipophile balance and solubility parameter of cationic surfactants. *Colloids Surf., A*, 214:167–171, 2003.
- [136] D. Quemada and D. Langevin. Rheological modelling of microemulsions. *J. Theor. Appl. Mech.*, Num. Spec.:201–237, 1985.
- [137] G. Quincke. *Wied. Ann.*, 35:593–632, 1888.
- [138] M.S. Ramadan, D.F. Evans, R. Lumry, and S. Philson. Micelle formation in hydrazine water mixtures. *Journal Of Physical Chemistry*, 89:3405–3408, 1985.
- [139] G.B. Ray, I. Chakraborty, S. Ghosh, and S.P. Moulik. A critical and comprehensive assessment of interfacial and bulk properties of aqueous binary mixtures of anionic surfactants, sodium dodecylsulfate, and sodium dodecylbenzenesulfonate. *Colloid Polym. Sci.*, 285(4):457–469, January 2007.
- [140] D. Richard, M. Ferrand, and G.J. Kearley. *J. Neutron Res.*, 4:33–39, 1996.

- [141] M.L. Robbins, J. Bock, and J.S. Huang. Model for microemulsions .iii. interfacial-tension and droplet size correlation with phase-behavior of mixed surfactants. *J. Colloid Interface Sci.*, 126:114–133, 1988.
- [142] K. Roger, B. Cabane, and U. Olsson. Emulsification through surfactant hydration: The pic process revisited. *Langmuir*, 27:604–611, 2011.
- [143] H.L. Rosano, T. Lan, A. Weiss, J.H. Whittam, and W.E.F. Gerbacia. Unstable microemulsions. *J. Phys. Chem.*, 85:468–473, 1981.
- [144] M.J. Rosen. *Surfactants and Interfacial Phenomena, 3rd Ed.* 2004.
- [145] K.J. Ruscak and C.A. Miller. Spontaneous emulsification in ternary systems with mass transfer. *Ind. Eng. Chem. Fundam.*, 11:534–540, 1972.
- [146] N. Sadurni, C. Solans, N. Azemar, and M.J. Garcia-Celma. Studies on the formation of o/w nano-emulsions, by low-energy emulsification methods, suitable for pharmaceutical applications. *Eur. J. Pharm. Sci.*, 26:438–445, 2005.
- [147] W. Sager, R. Strey, W. Kühnle, and M. Kahlweit. Aot, influence of impurities on the phase behavior. *Progr. Colloid Polym. Sci.*, 97:141–145, 1994.
- [148] J.L. Salager, A. Forgiarini, and L. Márquez. Nanoemulsions. FIRP BOOKLET No. E237-A, Universidad de Los Andes, 2006.
- [149] S. Sanguasri and MA. Augustin. Nanoscale materials development: a food industry perspective. *Trends Food Sci. Technol.*, 17:547–556, 2006.
- [150] M.M. Santore, D.E. Discher, Y.Y. Won, F.S. Bates, and D.A. Hammer. Effect of surfactant on unilamellar polymeric vesicles: Altered membrane properties and stability in the limit of weak surfactant partitioning. *Langmuir*, 18:7299–7308, 2002.
- [151] M. Schick and W.H. Shih. Simple microscopic model of a microemulsion. *Phys. Rev. Lett.*, 59:1205–1208, 1987.
- [152] K.V. Schubert and R. Strey. Small-angle neutron-scattering from microemulsions near the disorder line in water formamide octane-ciej systems. *J. Chem. Phys.*, 95:8532–8545, 1991.
- [153] K.V. Schubert, R. Strey, S.R. Kline, and E.W. Kaler. Small-angle neutron-scattering near lifshitz lines - transition from weakly structured mixtures to microemulsions. *J. Chem. Phys.*, 101:5343–5355, 1994.
- [154] P.N. Shankar and M. Kumar. Experimental-determination of the kinematic viscosity of glycerol water mixtures. *Proc. Royal Society*, 444:573–581, 1994.

- [155] H. Shinoda and H. Saito. The effect of temperature on the phase equilibria and the types of dispersion of the ternary system composed of water, cyclohexane, and nonionic surfactant. *J. Colloid Interface Sci.*, 26:70–74, 1968.
- [156] K. Shinoda and H. Arai. Correlation between phase inversion temperature in emulsion + cloud point in solution of nonionic emulsifier. *J. Phys. Chem.*, 68:3485–3490, 1964.
- [157] K. Shinoda and S. Friberg. *Emulsion and Solubilization*. 1986.
- [158] K. Shinoda and H. Kunieda. Conditions to produce so-called microemulsions - factors to increase mutual solubility of oil and water by solubilizer. *J. Colloid Interface Sci.*, 42:381–387, 1973.
- [159] K. Shinoda and H. Kunieda. *Encyclopedia of Emulsion Technology*, volume 1. P. Becher, 1983.
- [160] K. Shinoda and H. Kunieda. *Phase properties of emulsions: PIT and HLB*. Encyclopedia of emulsion technology. P. Becher, 1983.
- [161] K. Shinoda and H. Saito. The stability of o/w type emulsions as functions of temperature and hlb of emulsifiers - emulsification by pit-method. *J. Colloid Interface Sci.*, 30:258–263, 1969.
- [162] K. Shinoda and Y. Shibata. Principles for the attainment of minimum oil-water interfacial-tension by surfactants - the characteristics of organized surfactant phase. *Colloids Surf.*, 19:185–196, 1986.
- [163] P. Siddhan, M. Jassal, and A.K. Agrawal. Core content and stability of n-octadecane-containing polyurea microencapsules produced by interfacial polymerization. *J. Appl. Polym. Sci.*, 106:786–792, 2007.
- [164] J.A. Silas and E.W. Kaler. Effect of multiple scattering on sans spectra from bicontinuous microemulsions. *J. Colloid Interface Sci.*, 257:291–298, 2003.
- [165] D. Sinclair and V.K. Lamer. Light scattering as a measure of particle size in aerosols - the production of monodisperse aerosols. *Chem. Rev.*, 44:245–267, 1949.
- [166] N.L. Sitnikova, R. Sprik, G. Wegdam, and E. Eiser. Spontaneously formed trans-anethol/water/alcohol emulsions: Mechanism of formation and stability. *Langmuir*, 21:7083–7089, 2005.
- [167] C. Solans and M.J. GarciaCelma. Surfactants for microemulsions. *Curr. Opin. Colloid Interface Sci.*, 2:464–471, 1997.
- [168] C. Solans, P. Izquierdo, J. Nolla, N. Azemar, and M.J. Garcia-Celma. Nano-emulsions. *Curr. Opin. Colloid Interface Sci.*, 10:102–110, 2005.

- [169] C. Solans, N. Usón J. Esquena, A.M. Forgiarini, D. Morales, P. Izquierdo, N. Azemar, and M.J. García-Celma. *Surfactant and Solutions: Fundamental and Applications*. 2002.
- [170] I. Sole, A. Maestro, C. Gonzalez, C. Solans, and J. M. Gutierrez. Optimization of nano-emulsion preparation by low-energy methods in an ionic surfactant system. *Langmuir*, 22(20):8326–8332, September 2006.
- [171] I. Sole, C.M. Pey, A. Maestro, C. Gonzalez, M. Porras, C. Solans, and J.M. Gutierrez. Nano-emulsions prepared by the phase inversion composition method: Preparation variables and scale up. *J. Colloid Interface Sci.*, 344:417–423, 2010.
- [172] O. Sonneville-Aubrun, D. Babayan, D. Bordeaux, P. Lindner, G. Rata, and B. Cabane. Phase transition pathways for the production of 100 nm oil-in-water emulsions. *Phys. Chem. Chem. Phys.*, 11:101–110, 2009.
- [173] T. Sottmann and R. Strey. Ultralow interfacial tensions in water-n-alkane-surfactant systems. *J. Chem. Phys.*, 106:8606–8615, 1997.
- [174] O. Spalla. *Neutrons, X-rays and Light: Scattering Methods Applied to Soft Condensed Matter*. Elsevier, North-Holland, 2002.
- [175] T.L. Spehr. *Water dynamics in soft confinement*. PhD thesis, Technische Universität Darmstadt, 2010.
- [176] L. Spornath and S. Magdassi. Polyurea nanocapsules obtained from nano-emulsions prepared by the phase inversion temperature method. *Polym. Adv. Technol.*, 21, 2010.
- [177] R. Strey. *Zur Mikrostruktur von Mikroemulsionen*. Habilitationsschrift, 1992.
- [178] R. Strey. Microemulsion microstructure and interfacial curvature. *Colloid Polym. Sci.*, 272:1005–1019, 1994.
- [179] E.D. Sudol and M.S. El-Aasser. *Emulsion polymerization and emulsion polymers*. 1997.
- [180] G. Sukhorukov, A. Fery, and H. Mohwald. Intelligent micro- and nanocapsules. *Prog. Polym. Sci.*, 30:885–897, 2005.
- [181] M. Sztucki and T. Narayanan. Development of an ultra-small-angle x-ray scattering instrument for probing the microstructure and the dynamics of soft matter. *J. Appl. Crystallogr.*, 40:S459–S462, 2007.
- [182] R.F. Tabor, J. Eastoe, and I. Grillo. Time-resolved small-angle neutron scattering as a lamellar phase evolves into a microemulsion. *Soft Matter*, 5:2125–2129, 2009.
- [183] T. Tadros, R. Izquierdo, J. Esquena, and C. Solans. Formation and stability of nano-emulsions. *Adv. Colloid Interface Sci.*, 108:303–318, 2004.

- [184] T.F. Tadros and B. Vincent. *Encyclopedia of Emulsion Technology*. 1983.
- [185] P. Taylor. Ostwald ripening in emulsions. *Adv. Colloid Interface Sci.*, 75:107–163, 1998.
- [186] M Teubner and R. Strey. Origin of the scattering peak in microemulsions. *J. Chem. Phys.*, 87:3195–3200, 1987.
- [187] S. Tomomasa, M. Kochi, and H. Nakajima. *J. Jpn. Oil Chem.*, 37:1012, 1988.
- [188] J. Ugelstad, M.S. El-Aasser, and J.W. Vanderho. Emulsion polymerization - initiation of polymerization in monomer droplets. *J. Polym. Sci., Part B: Polym. Lett.*, 11:503–513, 1973.
- [189] N. Uson, M.J. Garcia, and C. Solans. Formation of water-in-oil (w/o) nano-emulsions in a water/mixed non-ionic surfactant/oil systems prepared by a low-energy emulsification method. *Colloids Surf., A*, 250:415–421, 2004.
- [190] P. van Beurten and A. Vrij. Polydispersity effects in the small-angle scattering of concentrated-solutions of colloidal spheres. *J. Chem. Phys.*, 74:2744–2748, 1981.
- [191] M. Vermeulen and P. Joos. Interfacial-tension during mass-transfer of decanoic acid from hexane to an aqueous-solution containing naoh. *Colloids Surf.*, 36:13–27, 1989.
- [192] M. Vermeulen, P. Joos, and L. Ghosh. Spontaneous emulsification in the system sodium dodecyl-sulfate in water and cholesterol in hexane. *J. Colloid Interface Sci.*, 140:41–47, 1990.
- [193] S.A. Vitale and J.L. Katz. Liquid droplet dispersions formed by homogeneous liquid-liquid nucleation: "the ouzo effect". *Langmuir*, 19:4105–4110, 2003.
- [194] B. Vonnegut. Hydrometer-type float method for measuring surface and interfacial tensions. *Rev. Sci. Instrum.*, 13:82–83, 1942.
- [195] A. Wadle, T. Förster, and W. von Rybinski. Influence of the microemulsion phase-structure on the phase inversion temperature emulsification of polar oils. *Colloids Surf., A*, 76:51–57, 1993.
- [196] C. Wagner. Theorie der alterung von niederschlägen durch umlosen (ostwald-reifung). *Z. Elektrochem.*, 65:581–591, 1961.
- [197] P. Walstra. *Encyclopedia of Emulsion Technology*. 1983.
- [198] P. Walstra. *Encyclopedia of Emulsion Technology*. Marcel Dekker, New York, 1996.
- [199] P. Walstra and P.E.A. Smoulders. *Modern Aspects of Emulsion Science*. 1998.

-
- [200] L.J. Wang, R. Tabor, J.L. Eastoe, X.F. Li, R.K. Heenan, and J.F. Dong. Formation and stability of nanoemulsions with mixed ionic-nonionic surfactants. *Phys. Chem. Chem. Phys.*, 11:9772–9778, 2009.
- [201] T. Warnheim and A. Jonsson. Phase-diagrams of alkyltrimethylammonium surfactants in some polar-solvents. *J. Colloid Interface Sci.*, 125:627–633, 1988.
- [202] J. Weiss, P. Takhistov, and J. McClements. Functional materials in food nanotechnology. *J. Food Sci.*, 71:107–116, 2006.
- [203] J.M. Wiencek and S. Qutubuddin. Solubilization in nonionic microemulsions. *Colloids Surf.*, 54:1 – 23, 1991.
- [204] R.W. Wood. The physical and biological effects of high-frequency soundwaves of great intensity. *Phil. Mag.*, 4:417–436, 1927.
- [205] Y.D. Yan and J.H.R. Clarke. Insitu determination of particle-size distributions in colloids. *Adv. Colloid Interface Sci.*, 29:277–318, 1989.
- [206] H.J. Yang, W.G. Cho, and S.N. Park. Stability of oil-in-water nano-emulsions prepared using the phase inversion composition method. *J. Ind. Eng. Chem.*, 15:331–335, 2009.
- [207] Z.J. Yu and R.D. Neuman. Reversed micellar solution-to-bicontinuous microemulsion transition in sodium bis(2-ethylhexyl) phosphate n-heptane water-system. *Langmuir*, 11:1081–1086, 1995.

This work has been carried out in the Large Scale Structure Group (LSS) at the Institut Laue Langevin (ILL) in Grenoble, France, and the Stranski Laboratory for Soft Condensed Matter in the group of Prof. Dr. M. Gradzielski at the Technische Universität in Berlin, Germany, over a period of three years (11.09.2008 - 23.09.2011).

Acknowledgements

First of all I would like to acknowledge my supervisor Prof. Dr. Michael Gradzielski who always supported and encouraged me during this work and who initiated my participation at the ILL-PhD program. I was always grateful to be part of his scientific group in Berlin and its excellent scientific work. Moreover, I would like to thank him for all the work- and life-related instructional discussions we had and his friendship.

I would like to thank Prof. Dr. Thorsten Ressler for the chairmanship of my PhD-defense. I am also very grateful to my responsables at the ILL Dr. Isabelle Grillo and Dr. Bela Farago for their expert guidance during neutron experiments, their support and trust in my independency. I am additionally very thankful to Isabelle for all her non-work related help and time she spent to me concerning the daily life in France. Moreover I always appreciated that she never gave up speaking in French with me!

Even if Dr. Ralf Schweins never have been one of my responsables at the ILL I always felt like he would be. I am likewise very grateful for all his support during neutron and light scattering experiments; and furthermore his willing to listen and help in case of private problems.

I am also very grateful to the ILL for the doctoral scholarship through the ILL PhD program and all the allocated beamtime I got on IN15, D11 and D22. I also want to thank Dr. Peter Lindner as a local contact during some test-beamtimes.

I would like to thank Dr. Theyencheri Narayanan from the ESRF in Grenoble for the allocated inhouse beamtime at the ID02-beamline. Furthermore I am grateful to the ID02-beamline staff Dr. Michael Sztucki, Dr. Manuel Fernandez Martinez and Dr. Jeremie Gummel as local contacts and all their support during SAXS-beamtimes.

For the possibility to do synthesis lab-work of deuterated compounds and the allocation of laboratory space I would like to thank Prof. Dr. Helmut Schwarz head of the Physical Organic Chemistry of the TU-Berlin (Germany) and Prof. Dr. André Laschewsky of the Fraunhofer IAP in Potsdam Golm (Germany). Special thanks refer to John P. Boyd (AK-Grohman, TUB) and Burkhard Butschke (AK-Schwarz, TUB) for their support and ideas of possible synthesis

pathways; just as to Dr. Michael Päch (IAP, Golm) who finally synthesised the deuterated compound.

Moreover I would like to acknowledge our collaboration Prof. Dr. Dganit Danino and all her students of the Biotechnology and Food Engineering Department of the Israel Institute of Technology (Technion) in Haifa (Israel), who prepared nanoemulsion samples of us and analysed them via the cryo-TEM technique.

During my PhD I also got the chance within two DAAD-projects to experience scientific work in two collaborating groups.

I am therefore very grateful to Prof. Dr. Norman J. Wagner and all his group members of the Chemical Engineering in the Colburn Labs of the University Delaware (USA), I joined for six weeks 2008. I am especially thankful to the cryo-TEM measurements Christina Michelina Marino accomplished during and after my stay there. I am also very grateful for the fruitful discussions and instrumental support I got from Dr. Monica Branco, Dr. Armin Opitz, Dr. Jason M. Mc Mullan, Dr. Aaron P.R. Eberle and Dr. Matthew Helgeson. Additionally I would like to thank Prachi Thereja who hosted me for the first four days of my stay at hers.

Furthermore I would like to thank Prof. Dr. Conxita Solans, Dr. Jordi Esquena and all their group members of the CSIC research center in Barcelona (Spain), I joined twice for six and four weeks 2010/2011. I am especially thankful to the postdocs of this group Marc Obiols-Rabasa and Roland Ramsch for the introduction of cross-correlated DLS measurements. Moreover I am very grateful to Jordi Nolla, Alberto Gonzalez Vilchez, Stefanie Leitner, Kelly Permartin, Camille Paulme, Carolina Aubéry Torres, Silvia Vilchez Maldonado, Neus Vilanova, Shan Singh, Alex Vilches, Dr. Jon Vilasau, Dr. Maria Homs, Dr. Txell Llinas Pons, Dr. Margarita Sánchez Domínguez and Dr. Gabriela Caldero Linnhoff.

As I had the great opportunity to work in two different groups simultaneously I would like to express my acknowledgments and appreciations for both of them: the group of Molecular Material Science of the Stranski Laboratorium at the TU-Berlin (Germany) that is in supervision of Prof. Dr. Michael Gradzielski and the Large Scale Structure (LSS) Group of the Institut Laue-Langevin in Grenoble (France) supervised by Dr. Bob Cubitt (formerly Dr. Peter Timmens and Dr. Albrecht Wiedenmann).

In detail I am very grateful to our postdoc in Berlin Dr. Sylvain Prévost who taught me the main fundamentals of SANS and was supporting me often during beamtimes. I am thankful to all the fruitful discussions we had, his advices and patience. Moreover I am grateful to my PhD-fellows Katharina Bressel and Ingo Hoffmann for their help concerning theoretical questions. Michael Muthig for the development and support concerning his MatLab based data processing and analysis program 'SASET' that was used for static and dynamic SANS/SAXS-data treat-

ment. Ingo Bressler for the improvements on the 'SASfit' analysis software. I also would like to thank Paula Malo de Molina, Raphael Michel, Andreas Klee, Leonardo Chiappisi, Jens Popig, Claudia Opperl and Anina Barth for their help in doing measurements during my absence in Berlin and their support during group-beamtimes at the ILL.

I am also very grateful to my student assistant in Berlin Michael Bernicke who worked with me on this project for 1 1/2 years.

I also acknowledge all the support I got from our technical assistants Sandrine Verdon (LSS), Michaela Dzionara, Gabriele Hedicke, Jana Lutzki and Dr. Rene Straßnick; our secretary Karin Sultan (LSS), Petra Erdmann, Maria Blobel and Christiane Abu-Hani; as alike our radiation protection officer Dr. Daniela Fliegner.

I would like to express my appreciation to all the PhD-students and scientists of the ILL and ESRF, as well as the different trainees I got known during the duration of my thesis and with whom I shared work and life.

I am very grateful to Dr. Stefan Eibl and Julie Bertrando who helped me a lot to settle in during the first months and who always lend themselves generously. I am very grateful for the fruitful discussions I had with Dr. Marcus Hennig and his help during MatLab programming at the ILL. I would like to thank Dr. Marcus Trapp and Dr. Martin Mourigal for their support and commitment during my period as a student representative at the ILL. Furthermore I am grateful to Dr. Garry McIntyre, Dr. Tinka Luise Spehr, Dr. Marco Maccarini, Dr. Bastian Märkisch, Dr. Michael Marek Koza, Dr. Eva Rosenbaum, Dr. Andreas Stadler, Dr. Bachir Auon, Dr. Julia Rasch, Dr. Audrey Schollier, Dr. Stuart Fisher, Dr. Martin Simson, Dr. Michael Baker, Dr. Adrian Hill, Kent Leung, Jessica Valle Oreo, Irene Calvo-Almazan, Jad Kozaily, Wiebke Knoll, Federica Sebastiani, Francesco Piscitelli, Alexis De Ghellinck, Jonathan Correa, Andrew Jones, Christian Dorns, Dominik Werder, Matxalen Rey Abasolo, Rolf Michels, Markus Appel, Marina Kley, Elena Jordan, Fabio Zanini and Marianna Yanez. I also would like to thank my office mate Dr. Mouna Tatou, who spent two years of her thesis at the ILL, for all the discussions and the pleasant time we spent together.

Moreover, I am especially grateful to my closest friends at the ILL Ida Berts and Dr. Yuri Gerelli for all their support and encouragement during these difficult last months and weeks of writing. I will never forget, THANKS!

I am very grateful for the intensive proofreading of my thesis to Anna Angus-Smyth.

There are so many important friends in my life with whom I shared so many good and bad moments during this period. I always appreciated the possibility in making new friends, experiencing new things, travelling around and broaden my horizon by going abroad. I am so grateful to all the people I met and to those who kept contact despite the distances. I am so grateful to all of you! I could continue this list of acknowledgements much longer and would like to apologize to all those I did not name.

I also would like to thank Dr. Jochen Krempel for his patience, love and support. Furthermore, I am very grateful to his amazing abilities in solving any tricky LaTeX-problem I had!

Finally I am very thankful to my whole family who kept encouraging and supporting me through the whole three years. I am so grateful for their love and trust.